Resonant and traveling-wave parametric amplification near the quantum limit

Luca Planat

THÈSE

Pour obtenir le grade de

DOCTEUR DE L'UNIVERSITÉ GRENOBLE ALPES

Spécialité : Physique de la Matière Condensée et du Rayonnement

Arrêté ministériel : 25 mai 2016

Présentée par

Luca PLANAT

Thèse dirigée par **Wiebke GUICHARD**, Université Grenoble Alpes et codirigée par **Nicolas ROCH**, Chargé de recherche, Université Grenoble Alpes

préparée au sein du **Laboratoire Institut Néel**
dans **l'École Doctorale Physique**

Amplification paramétrique en résonance et à ondes progressives proche de la limite quantique

Resonant and traveling-wave parametric amplification near the quantum limit

Thèse soutenue publiquement le **22 juin 2020**,
devant le jury composé de :

Monsieur DAVID B. HAVILAND
PROFESSEUR DES UNIVERSITES, INSTITUT ROYAL DE TECH. (KTH) - SUEDE, Rapporteur
Monsieur PATRICE BERTET
INGENIEUR CHERCHEUR HDR, CEA DE SACLAY, Rapporteur
Madame ANJA METELMANN
PROFESSEUR ASSOCIE, UNIVERSITE LIBRE DE BERLIN - ALLEMAGNE, Examinateur
Monsieur BENOÎT BOULANGER
PROFESSEUR DES UNIVERSITES, UNIVERSITE GRENOBLE ALPES, Président du jury

Acknowledgments

J'ai pu mener à bien cette thèse durant ces quatre années passées à l'Institut Néel grâce à toutes les personnes que j'ai cotoyées et qui m'ont aidé tant par leur talent que par leur disponibilité. Je vais tenter d'exprimer, au cours de ces quelques lignes, toute ma gratitude. Je commencerai par remercier les membres de mon jury qui ont accepté d'évaluer mon manuscrit et ma soutenance de thèse. Dr. Patrice Bertet, merci beaucoup pour les commentaires enthousiastes et l'intérêt porté à ce travail. Prof. David Haviland, thank you very much for your very thorough reading of the manuscript and your numerous notes. I imagine it took a substantial amount of time, but you definitively improved the quality of this manuscript. Merci à vous deux d'avoir accepté d'être rapporteurs. Merci aux examinateurs, Dr. Anja Metelmann et Prof. Benoît Boulanger pour vos commentaires et les discussions très intéressantes que vos questions ont générées.

Je remercie également le personnel de l'Institut Néel. Pour commencer, les personnes qui m'ont aidé dans la fabrication des échantillons et qui, à bien des égards, ont permis l'obtention des résultats présentés dans ce manuscrit. Ainsi, merci au pôle nanofabrication de l'Institut: Thierry Crozes, Sébastien Dufresnes, Gwénaëlle Julie, Bruno Fernandez, Latifa Abbassi et Jean-François Motte, à l'équipe de la PTA et notamment Frédéric Gustavo et Irène Pheng, à Laurent Cagnon pour l'aide sur l'ALD et à Philippe David qui a permis de faire les dépôts de cuivre en sputtering. Je remercie aussi ceux qui rendent possible la mesure de ces échantillons: Christophe Hoarau et Sylvain Dumont pour la conception des PCB, Laurent Del-Rey pour ton aide sur les portes échantillons, mais aussi pour la formation sur les machines-outils avec Gilles Pont, j'en garde un très bon souvenir, et Éric Eyraud pour ton expertise sur les sionludis. Je suis ravi d'avoir vu le sionludi XL avant la fin de ma thèse et de savoir qu'il abrite à présent une très chouette expérience. Je remercie également toutes les personnes qui nous aident dans les tâches administratives. Merci à Angélique Simoes et Otmane Benhamed pour l'aide avec les commandes et les ordres de missions et à Florence Pois pour votre aide sur la plupart des questions administratives résolues avec rapidité.

Il faut aussi saluer les collaborations et les discussions scientifiques grâce auxquelles la thèse a pu avancer. Pour cela, merci Denis Basko de nous avoir aidés sur le modèle des TWPA modulés spatialement. Travailler avec toi est un privilège, et tu nous as permis de dégager une bien meilleure compréhension de notre système. Thank you Kater Murch and Rajamani Vijayaraghavan for your precious

help on the resonant JPA et merci à Daniel Esteve et Michael Selvanayagam pour votre relecture des articles.

Je remercie aussi les chercheurs, post-docs et thésards de l'Institut qui se sont interessés à mon sujet: Franck Balestro pour ta disponibilité et ton aide à toute heure de la journée, Christopher Bauerle pour tes questions pertinentes durant les séminaires, Matias Urdampilleta et David Niegemann de vous être penchés sur la question des TWPA à basses fréquences et Tristan Meunier pour faire confiance à ce projet mais aussi pour avoir rendu le March meeting 2019 aussi drôle. Merci aussi aux thésards que l'on croise au labo et en dehors: Jorge (dont j'ai saisi très vite l'importance et le prestige au sein du labo) pour ton accueil à Madrid, Hugo pour ta bienveillance et Álvaro, Roberto, David, Goutham, Kimon, Thanasis, Francesco, Everton, Junliang. C'était très sympa de se retrouver pour des parties de foot et/ou partager une pinte ou un verre de pastis.

Un grand merci à toute l'équipe des circuits supras. C'est assez vertigineux de voir l'ampleur que cette équipe a pris en quatre ans. Tout d'abord, je ne vous remercierai jamais assez, Rémy et Javier, de m'avoir accueilli aussi gentiment et de m'avoir formé avec autant de patience. J'ai mis un peu de temps à intégrer votre groupe très select des déjeuners du bâtiment D, mais je ne l'ai pas regretté! Merci aux plus anciens encore, Kitti et Étienne. Kitti, for your initiation on the coffee machine (with Rémy's help) during my first months as an intern, et Étienne pour ton interêt et ton soutien au fil des March meetings (et merci pour la retransmission de la soutenance au sein du CEA!). Thanks to the post-docs Yuriy et Farshad, and his legendary nonchalance. Et merci aussi à ceux qui sont arrivés dans l'équipe au cours de ces quatre années, Akanksha with whom I started my internship at the Institut. Doriane, pour tes étonnantes expressions du Québec. Gonzalo for your constant good mood. Thibault, félicitations pour ton polyglottisme: la preuve en est sur les channels Discord. Timothée, bravo pour tes résultats et ta superbe utilisation du JPA. Dorian, fais attention à ne pas non plus trop ressembler à ton boss (le chevelu). Un grand merci aussi à la 'TWPA Team' pour tout le travail que vous avez fourni. Vous avez tous été de surcroît des personnes formidables avec qui travailler. Katia, I wish you the very best in Zurich. Vincent, félicitations pour ton travail acharné, même pendant le confinement. Arpit, it was my pleasure to train you, although it has been pretty short: you mastered the topic in the blink of an eye. Martina, thanks a lot for all your kindness during my redaction time. Both of you, it is incredible how much you have already achieved. Vient ensuite la joyeuse troupe de la salle Z-218. Merci de m'avoir supporté tout ce temps mais surtout pour tous les fous rires. Kazi, congratulations for remaining always so calm in front of the most bizarre and absurd situations. Vladimir, congratulations as well, but for managing to astonish me in so much different ways every single day at the office. Karthick, thank you for your originality and your sense of humour, and congrats for your LoTR viewing record. Et Seb, c'est évidemment impossible de te remercier en une seule phrase, mais je peux essayer de le résumer ainsi: merci pour cette amitié vraiment unique. And finally thank you Jovian: your genuine kindness is simply amazing. I truly hope that you will fulfill your dreams and become a pétanque champion. Pour finir,

merci aux permanents, Cécile Naud, Julien Renard, Wiebke Guichard, Olivier Buisson et Nicolas Roch. Votre gentillesse et votre humanité sont une chance inestimable pour tous les membres de l'équipe. Wiebke, merci pour la liberté et la confiance que tu m'as accordées tout au long de ma thèse, mais aussi pour avoir toujours continué à suivre mes travaux, même jusqu'à la fin de la thèse, malgré les complications. Olivier, merci pour ton ouverture d'esprit, ton expertise tant pratique que théorique, ton humilité mais aussi pour ton sens de l'humour. Tu instilles dans l'équipe une ambiance exceptionnelle. Finalement Nico, je ne sais pas si j'aurai les mots pour t'exprimer toute ma gratitude. Merci d'avoir été toujours là, et d'avoir rendu les choses aussi simples. Merci de m'avoir fait confiance, mais aussi de m'avoir donné confiance en moi-même pendant cette thèse. C'était une belle aventure.

Je remercie toutes les personnes en dehors du labo. Ma famille, mes parents pour m'avoir toujours laissé une liberté totale et en même temps pour avoir toujours été là quand j'en avais besoin. Mes colocs (Titiksha je te compte dedans), plus de trois ans (et un confinement!) à vivre ensemble sans jamais de problème et tout en continuant à se marrer autant. Et les joinvillais. C'est fou de vous avoir tous garder si proche tout ce temps. Merci d'avoir sublimé la soutenance grâce à vos vannes et vos encouragements en direct (et au passage, merci Zach, Tom et Baba pour le logo et l'idée d'un style 'minimaliste' pour la couverture).

Je finirai en remerciant celle qui a toujours été présente, tout au long de cette thèse, et quoi qu'il arrive. Σ'ευχαριστώ πολύ Ιωάννα μου, d'avoir été si compréhensive et patiente avec moi. Merci aussi pour tout ce que tu m'as appris, tout ce que tu m'as apporté durant ces trois dernières années. J'ai hâte d'en découvrir toujours plus avec toi, et te connaissant, je sais qu'il n'en sera pas autrement.

Contents

Introduction, definition of concepts and summary

1

1.1 Introduction

At the time this manuscript was drafted, Google LLC demonstrated their ability to program a 53 quantum bit (qubits) superconducting processor [1]. The dramatic computational speed-up they reported with the Sycamore quantum processor allowed them to claim quantum supremacy [2] for the very first time. Besides the controversies and debates that a major scientific claim naturally generates, the massive frenzy around this breakthrough among the physicists and the general audience shows the tremendous thrill quantum computing is currently generating. Quantum information and quantum computing are obviously stirring minds up with the promises to unlock the next great technologies. However, such technological leaps cannot be confined to only one research field and ask for a cross-disciplinary approach, from abstract quantum algorithm design to material science and engineering. This thesis, dealing with ultra-low noise amplifiers, is a consequence of the association between quantum information and superconducting circuits [3, 4], starting more than 30 years ago. This flourishing combination created a real need to develop ultra-low noise amplifiers working with microwave signals, being able to reach the quantum limit of noise.

Quantum limited amplifiers were not originally intended for quantum information. As Carlton M. Caves explains in 1982 in his seminal article [5], quantum limited amplifiers were first envisaged during the development of masers and theoretical works on the fundamental limits of amplifiers first peaked during the 1960's [6, 7]. Interest in quantum limited amplifiers declined notably because of the technological lock preventing from fabricating amplifiers actually reaching the quantum limit of noise. A renewed interest appeared in the 1980's, when it was realized that quantum amplifiers could be useful in the detection of gravitational waves [8], which eventually happened in 2015. (**Note**: in December 2019 the LIGO team reported they managed to squeeze vacuum states to improve detection of gravitational waves for the first time [9]). This theoretical proposal was supported by John Clark's creative work on DC Superconducting QUantum Interference Device (SQUID) [10] and their first application for low noise microwave amplifiers [11, 12]. They reported gain up to 20 dB with noise temper-

atures down to $T_n = 6\,K(+15/-7)$. After some years, parametric amplifiers based on a single Josephson junctions would reach and eventually go beyond SQUID-based amplifiers performances [13]. They reported gain as high as 13 dB and a noise temperature as low as $3\,K \pm 4\,K$. But one had to wait until Bernard Yurke's pioneering work to have Josephson parametric amplifiers (JPA) operating near the quantum-limited sensitivity [14], squeezing thermal [15] and vacuum [16] noise. Notwithstanding that Josephson-based traveling-wave parametric amplifiers were first proposed in 1985 [17] (and as early as 1958 [18] without using Josephson junctions), one must also acknowledge Bernard Yurke's forward-thinking work on these devices [19]. Regardless a numerous series of exploits, Yurke's work would stay a bit underrated for some years. The dearth of direct applications for quantum limited noise and their relative poor figures of merit (see Section 1.2) compared to cryogenic, transistor-based amplifiers are plausible explanations for this lack of recognition. Nowadays, and for the past ten years, we assist to a regain of interest for quantum limited amplifiers. A wide range of quantum technologies rely now on quantum limited chain of amplification for microwave signals detection at millikelvin temperature. This include nano-electromechanical systems (NEMS) [20], spin qubits [21], electron spin resonance detection [22] but also for more basic research such as axionic dark matter detection [23] and obviously quantum information with superconducting qubits [24]. The modern age of microwave quantum limited amplifiers coincides with the emergence of circuit QED (cQED) [25, 26, 27, 28]. Before reaching their contemporary form, Josephson amplifiers were first thought as metastable switches dubbed Josephson bifurcation amplifiers (JBA) [29, 30] for qubit readout [31]. However, it is Manuel A. Castellanos-Beltran *et. al* work which truly defined what present Josephson amplifier are. They successfully implemented a resonant JPA [32] in 2007 with an array of SQUID. One year later, they experimentally recorded an intrinsic noise below the standard quantum limit (SQL, see Section 1.3) while having more than 20 dB of power gain [33].

From then on, the vast majority of Josephson amplifiers worked with a resonant parametric interaction and routinely reached the quantum limit of noise, thanks to the remarkable progressed in nano-fabrication techniques. Despite years of improvements in improving their bandwidth [34, 35], their saturation point [36, 37], optimizing their pumping schemes [38, 39, 40, 41, 42] and their directionality [43, 44], Josephson amplifiers struggled to leave the resonant paradigm. In 2012 superconducting parametric amplifiers successfully managed to reproduce the physics of nonlinear fiber optics, implemented with high kinetic inductors [45]. It is only three years later that Josephson-based traveling-wave amplifiers finally emerged [46, 47]. With these achievements, superconducting amplifiers could eventually go from a resonant interaction to a traveling-wave process. Since then, few research teams managed to implement a working traveling-wave amplifier [48, 49]. This thesis is in line with this shift from resonant to traveling-wave parametric interactions for amplification purposes.

Before shortly summarizing the principle results of this thesis (Section 1.5), this chapter is devoted to the introduction of three concepts related to (Josephson)

amplifiers. It will also be the occasion to define the quantities used in the rest of this thesis. First, the main quantifiable figures of merit of an amplifier – gain, bandwidth, saturation and noise– are quickly reviewed. Second, a brief review of quantum limit of noise is carried out. Eventually, basic notions on Josephson junctions and SQUIDs are reviewed.

1.2 Figures of merit

An amplifier is a device expected to amplify an input signal on a large frequency span, with little possible signal distortion or added noise. In this section we draw up a non-exhaustive list of what we consider to be the most important figures of merit for our amplifiers. We define the parameters and their notations used throughout the manuscript.

Gain

Obviously gain is the first feature one can think of for an amplifier. Seen as a transfer function with a **signal** amplitude A_{in} at the input and a signal amplitude A_{out} at the output (as shown in Fig. 1.1), the power gain factor G is defined as the output to input amplitude ratio: $\sqrt{G} = A_{\text{out}}/A_{\text{in}}$. The internal process leading to amplification can be of different nature: vacuum tubes (traveling-wave tube amplifiers [50, 51]), field-effect (high electron mobility transistors [52]) or parametric interaction (Josephson parametric amplifiers). The high power source providing the necessary energy to feed this process is called **pump**. Throughout this manuscript, gain will be in general given and plotted as the power signal G, in decibel unit. For instance, whenever we refer to 20 dB gain, it corresponds to a factor 100 in power (or a factor 10 in amplitude), in linear units.

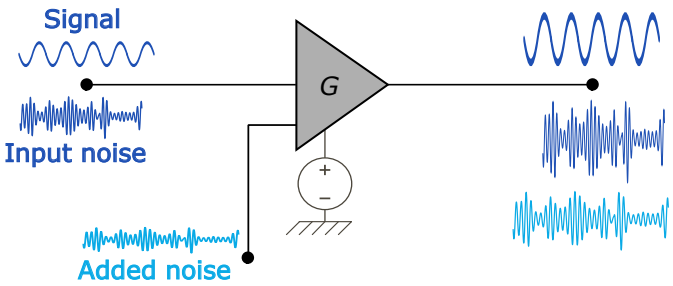

Figure 1.1 – **Schematic of amplification process.** The amplifier is driven by a high energy source called pump. At its input, the signal and noise amplitudes are amplified by a factor $\sqrt{G}$. Noise is coming from the environment (input noise) and the amplifier internal channel (added noise).

Bandwidth

G is a function of the signal angular frequency, denoted ω_s. An amplifier bandwidth is defined as the frequency range where $G(\omega_s)$ is higher than a threshold value. In this thesis, the bandwidth is defined as the full width at half maximum (FWHM), meaning the frequency windows where $G(\omega_s) > G_{max}/2$ in linear units (or $G_{max} - 3\,\text{dB}$ in decibels), and denoted Δ_{bw}. One of the major challenge of this work is to increase the bandwidth of Josephson-based quantum limited amplifiers via a traveling-wave process instead of a resonant one. With SQUID-based amplifiers, it is possible to increase the amplifier bandwidth by tuning its working point with an external magnetic flux.

Dynamic range

In addition to being frequency dependent, the gain is also dependent upon the signal power, denoted P_s. Below a certain input signal power P_s^{min}, amplification cannot occur. Above a certain input signal power threshold P_s^t the amplified signal is distorted and/or the gain is compressed. An amplifier is said linear when P_s is in between P_s^{min} and P_s^t, and the gain is not power dependent. The dynamic range is the difference between these two powers. There are different ways to define P_s^t. In this thesis it was chosen as the input signal power inducing a compression of one decibel of the initial maximum gain G_{max}. The input signal power inducing this compression is called the 1 dB **compression point** and is denoted $P_{1\,\text{dB}}$. A part of this work has been dedicated to **increase** the 1 dB compression point of our quantum limited amplifiers. In decibel units, the dynamic range of an amplifier is defined as $DR(\text{dB}) = P_{1\text{dB}} - P_s^{min}$. For an ultra-low noise amplifier, P_s^{min} can be taken as its noise power $P_s^{min} = k_b T_n \Delta_{bw}$ [19], where k_b is the Boltzmann constant and T_n is the amplifier noise temperature. We precisely define T_n in the following paragraph.

Noise

An amplifier, being an active component generates a finite amount of energy noise, which can be expressed in different units: power spectral density, temperature, number of quanta... in this manuscript, noise will mostly be expressed in temperature (kelvin) or in number of quanta (at a given frequency). During the process of amplification, two sources of noise must be considered: environmental (thermal, quantum fluctuations) and intrinsic to the amplifier (see Fig. 1.1). For microwave amplifiers, the former can be reduced to its minimum by working in a cryogenic environment ($k_b T << \hbar\omega$) to cancel thermal fluctuations (more details in Chapter 5). It is thus sensitive to quantum fluctuations only, and environmental noise is as low as half of a quanta, at the working frequency. Amplifiers intrinsic noise is coming from every non measured amplification channels and contributing to a loss of information. In the rest of this manuscript, we will always speak about **input-referred noise** to characterize the amplifiers noise. It means that the output noise is normalized by the amplifier power gain G. Input-referred noise

is suited to compare the amplifier noise to the energy carried by the signal to be amplified. Quantum limited amplifiers developed during this work are the least noisy cryogenic amplifiers since their intrinsic noise reach the limit allowed by quantum mechanics and their environment noise is dictated by quantum fluctuations only. The next section is dedicated to a more thorough definition of the quantum limit of noise.

1.3 Quantum limit of noise

Let us consider an amplifier with at its input a quantum field whose operator $\hat{a}_{\text{in}}$ is amplified such that the field at the amplifier output $\hat{a}_{\text{out}}$ is defined as:

$$\hat{a}_{\text{out}} = \sqrt{G}\hat{a}_{\text{in}}, \tag{1.1}$$

where G is the amplifier power gain. Both $\hat{a}_{\text{out}}$ and $\hat{a}_{\text{in}}$ are quantum operators, therefore they must respect their commutation relation $[\hat{a}_{\text{out}}, \hat{a}^{\dagger}_{\text{out}}] = 1$ (same for $\hat{a}_{\text{in}}$). The expression of $\hat{a}_{\text{out}}$ in Eq. (1.1) cannot hold with the commutation relations. Thus an extra degree of freedom must be added to Eq. (1.1) to fulfill the commutation relation. The nature of this extra degree of freedom will effectively change the nature of the noise limit. If the extra term is the signal phase, the amplifier is said **phase-sensitive**. Otherwise, the amplifier is said **phase-preserving**.

1.3.1 Phase-preserving amplifier

Caves theorem [5] states that in the case where a (quantum) amplifier is not sensitive to the signal's quadrature (thus phase-preserving), the amplifier must have one or more internal modes to fulfill commutation relations. For an ideal amplifier, there is exactly **one** internal mode, described by its quantum operator $\hat{b}$ that fulfills $[\hat{b}, \hat{b}^{\dagger}] = 1$. This internal mode is commonly called the **idler**, for legacy reasons since we are working with electromagnetic waves in the microwave range. This internal mode interacts with the input signal to produce the output signal. Moreover, the idler mode fluctuations and the amplified input fluctuations are not correlated. From these considerations, Eq. (1.1) becomes:

$$\hat{a}_{\text{out}} = \sqrt{G}\hat{a}_{\text{in}} + \sqrt{G-1}\hat{b}^{\dagger}. \tag{1.2}$$

At the output of the amplifier, at signal frequency, the total noise power spectral density (PSD) is given by $\mathcal{N}_{\text{out}} = \frac{1}{2}\left\langle \left\{ \hat{a}_{\text{out}}, \hat{a}^{\dagger}_{\text{out}} \right\} \right\rangle$[a] [53]. Using Eq. (1.2) we find,

$$\mathcal{N}_{\text{out}} = G\mathcal{N}_{\text{in,s}} + (G-1)\mathcal{N}_{\text{in,id}}, \tag{1.3}$$

where $\mathcal{N}_{\text{in,s}}$ and $\mathcal{N}_{\text{in,id}}$ are signal and idler input noises. In the high gain limit ($G >> 1$), the input-referred noise ($\mathcal{N}_{\text{out}}/G$) is thus given by $\mathcal{N}_{\text{in,s}} + \mathcal{N}_{\text{in,id}}$. The

[a] We assume that $|\langle \hat{a}_{\text{in}} \rangle|^2 = 0$ and $|\langle \hat{a}_{\text{out}} \rangle|^2 = 0$.

noise **added** by the amplification process directly arises from the idler mode and is equal to $\mathcal{N}_{\text{in,id}}$[b]. Therefore, the amplifier added noise is superior or equal to half a quanta. In case of equality, the amplifier is said to be a phase-preserving, quantum-limited amplifier. In the phase-space, phase preservation results in the addition of both environmental and amplifier noise (see Fig. 1.2**(a)**). Phase space volume is not conserved (expansion in both quadratures) and the the standard quantum limit (SQL) of noise is defined as 1 quantum of energy.

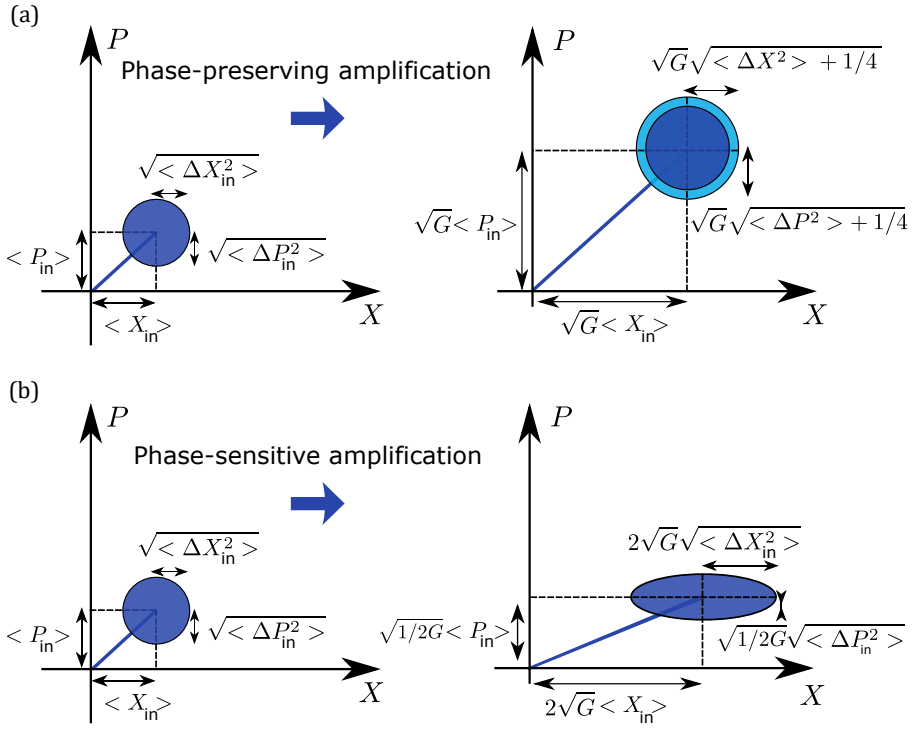

Figure 1.2 – **Contour of Wigner distribution of input and output states. (a)** Phase-preserving amplification. Both signal quadratures are amplified by $\sqrt{G}$. Amplifier intrinsic noise (light blue) is also amplified. **(b)** Phase sensitive amplification. Signal quadratures are unequally amplified. One output quadrature noise is squeezed, its noise is reduced compared to the input one. In the absence of the intrinsic amplifier noise, phase space volume is conserved.

[b] It is interesting to note that the added noise at signal frequency originates from fluctuations at idler frequency.

1.3.2 Phase-sensitive amplifier

Phase space volume can be conserved through the amplification process when the amplifier is sensitive to the input signal phase [53]. In a phase-sensitive amplifier, the input signal mode is degenerated both temporally and spatially with the idler mode: the only remaining degree of freedom to fulfill the commutation relation is the signal phase ϕ (with respect to the pump phase). Eq. (1.1) therefore reads:

$$\hat{a}_{\text{out}} = \sqrt{G}\hat{a}_{\text{in}} + e^{i\phi}\sqrt{G-1}\hat{a}^{\dagger}_{\text{in}}. \tag{1.4}$$

Amplification being sensitive to the signal quadrature, Eq. (1.4) must be written in term of signal's quadrature. For high gain ($G >> 1$):

$$\hat{X}_{\text{out}} \overset{\phi=0}{=} 2\hat{X}_{\text{in}}\sqrt{G}, \tag{1.5a}$$

$$\hat{P}_{\text{out}} \overset{\phi=0}{=} \frac{\hat{P}_{\text{in}}}{2\sqrt{G}}. \tag{1.5b}$$

As shown in Fig. 1.2, one quadrature is attenuated while the other is amplified. Same for the noise, where one quadrature is actually 'squeezed' below the input noise while the other is 'stretched' above it. The total phase space volume is conserved during amplification. If the input noise is originally dictated by quantum fluctuations, the output noise of one quadrature goes below half a quanta, but it does not contradict quantum mechanics since the other quadrature noise is amplified. When an amplifier is phase-sensitive it might be more reasonable to define the SQL to half a quanta.

1.4 Josephson junction: the unit cell for quantum limited amplification

In the previous section we have seen that the minimal extra number of internal modes for a phase-preserving amplifier is one. Amplifiers as simple as parametric amplifiers can have a unique internal mode, called idler. Josephson junctions are a good candidate for quantum limited amplifiers since they foster parametric interactions, work at cryogenic temperatures and are superconducting, thus dissipationless. Josephson junctions are the basic bricks for our quantum limited amplifiers, which are arrays of junctions. In this section, we recall the basic effects and equations of a single Josephson junction and its modeling as a nonlinear LC resonator. In Chapter 2, we will study the physics of an array of junctions.

1.4.1 The Josephson effect

Cooper pair tunneling between two superconductors is generating a supercurrent I, flowing without any voltage drop between the leads. This effect, theoretically

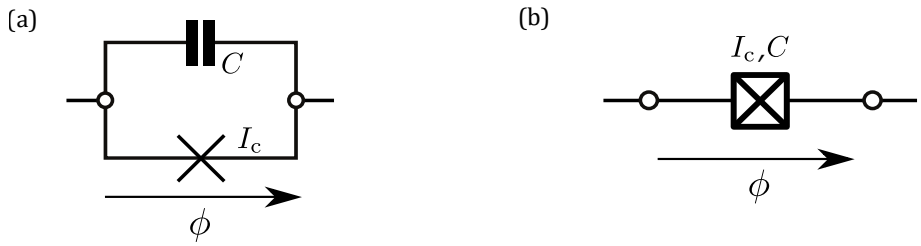

Figure 1.3 – **Sketches of a Josephson junction. (a)** Electrical circuit of a Josephson junction. It can be modeled as a perfect nonlinear element, represented as a cross with a critical current I_c in parallel with a capacitor C. **(b)** Compact representation of **(a)**.

predicted by Brian D. Josephson, is called the Josephson effect. The supercurrent reads:

$$I = I_c \sin\phi, \tag{1.6}$$

where I_c is the critical current, namely the maximum current that can flow through the junction before it transits from a superconductor behavior to a normal behavior. ϕ is the gauge invariant superconducting phase difference. The phase difference of the two macroscopic wave functions between one lead and the other generates the supercurrent. If a voltage drop V is applied between the two leads, the phase difference ϕ varies in time:

$$\frac{\mathrm{d}\phi}{\mathrm{d}t} = \frac{V}{\varphi_0}, \tag{1.7}$$

where $\varphi_0 = \hbar/2e$ is the reduced magnetic flux quantum, $\hbar$ the reduced Planck constant and e the elementary charge. The voltage drop produces an AC supercurrent, whose angular frequency is $\omega = V/\varphi_0$. By combining these effects, we can model the Josephson junction as a nonlinear inductor with an inductance L_j. Taking the general expression of a voltage drop across an inductor, and by considering Eqs. (1.6) and (1.7), L_j reads:

$$L_j = \varphi_0 \frac{\mathrm{d}\phi/\mathrm{d}t}{\mathrm{d}I/\mathrm{d}t} = \frac{\varphi_0}{I_c \cos\phi}. \tag{1.8}$$

Using Eq. (1.6) (and recalling $\cos^2\phi + \sin^2\phi = 1$), the Josephson inductance reads:

$$L_j = \frac{L}{\sqrt{1-(I/I_c)^2}}, \tag{1.9}$$

where $L = \varphi_0 / I_c$ is the linear part of the inductor. The important feature of the junction is the nonlinear dependence of its inductance with respect to power. It is at the heart of the amplification processes since it allows four wave mixing parametric interaction. The linear part of the inductance L is inversely proportional to the junction critical current. The critical current is dependent on the fabrication process of the junction itself, in particular on its tunnel barrier thickness. Given our fabrication facilities and our fabrication recipes, we typically have critical current density of the order of $25\,\mathrm{A\,cm^{-2}}$. Junctions areas are in the order of few micro meters squared. Thus, a junction with an area of $5\,\mu\mathrm{m}^2$ leads to a critical current of $1.25\,\mu\mathrm{A}$ and an inductance $L \approx 250\,\mathrm{pH}$. The nonlinearity of the junctions comes with the price of a very large inductance per unit length. For some purposes, this large inductance is sought (flux qubit, fluxonium) to implement superinductor for instance. As we will see later, large inductances are a burden for low impedance devices such as making $50\,\Omega$ Josephson-based transmission lines.

To finish modeling the Josephson junction as an electrical circuit, the capacitive effect between the two superconducting leads must be accounted. This capacitor, denoted C, is modeled as a parallel plate capacitor. In our facilities, the surface capacitance is around $0.045\,\mathrm{fF\,\mu m^{-2}}$ [54]. A Josephson junction is then modeled as a nonlinear LC circuit (see Fig. 1.3), whose self resonant angular frequency is called plasma and denoted ω_Π reads:

$$\omega_\Pi = \frac{1}{\sqrt{LC}}. \tag{1.10}$$

In first approximation, the plasma frequency is not dependent on the area of the junction since the L is inversely proportional to the area of the junction while C is proportional. Thus, ω_Π only depends on the thickness of the tunnel barrier, controlled by the pressure and time of oxidation of the aluminum during the fabrication of the junction (see Chapter 4 for more details). Given the typical value for L and C we find a plasma frequency in the order of the tens of gigahertz. This motivates that Josephson based amplifiers work in the microwave range. Therefore, they must be in cryogenic environment to work as quantum limited amplifiers.

1.4.2 Flux modulated Josephson junction: DC SQUID

All the devices characterized and measured during this work are actually made of Superconducting QUantum Interference Devices (SQUID). It consists in a superconducting loop wherein lie two Josephson junctions. A SQUID is modeled as a flux-tunable Josephson junction. In the simplest case of two identical junctions of critical current I_c within the superconducting loop, the total current I_{tot} of the loop is written (see Fig. 1.4 for notations):

$$I_{tot} = I_1 + I_2 = 2I_c \cos\left(\frac{\phi_1 - \phi_2}{2}\right) \sin\left(\frac{\phi_1 + \phi_2}{2}\right). \tag{1.11}$$

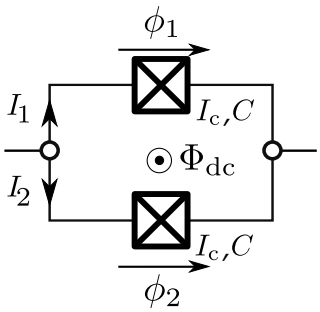

Figure 1.4 – **Schematic of a symmetric SQUID.** Two identical Josephson junctions are in parallel in a superconducting loop. The loop is threaded with an external DC magnetic flux Φ_{dc}.

Given that the phase going around the loop must be modulo 2π, if the superconducting loop is threaded with an external DC magnetic flux Φ_{dc}, we obtain:

$$\phi_1 - \phi_2 = 2\pi \frac{\Phi_{dc}}{\Phi_0}, \tag{1.12}$$

where Φ_0 is the flux quantum. With Eqs. (1.11) and (1.12), the total critical current reads:

$$I_{tot} = 2I_c \cos\left(\pi \frac{\Phi_{dc}}{\Phi_0}\right) \sin\left(\frac{\phi_1 + \phi_2}{2}\right) = I_{c_{squid}} \sin\phi_{tot}, \tag{1.13}$$

with the mean value $\phi_{tot} = (\phi_1 + \phi_2)/2$ and the SQUID critical current $I_{c_{squid}} = 2I_c \cos\pi\Phi_{dc}/\Phi_0$. We eventually define the SQUID inductance:

$$L_{squid} = \frac{\varphi_0}{I_{c_{squid}}} = \frac{L}{2\cos\left(\pi\Phi_{dc}/\Phi_0\right)}. \tag{1.14}$$

A SQUID can be seen as a flux-tunable nonlinear inductor. Therefore, a modulation via an external flux of the junction plasma frequency is possible. For a symmetric SQUID, its linear inductance is two times smaller than the single junction part of it.

1.5 Summary

1.5.1 Thesis overview

Chapter 2 begins with a general description of the different parametric interactions leading to amplification within a quantum optics framework. Four cases are discussed: degenerated and non degenerated parametric amplification and, for

both, the three wave mixing and the four wave mixing processes. We demonstrate that these four parametric interactions have similar Hamiltonians. We then focus on the degenerate case to derive an expression for the gain and for the bandwidth. Eventually, we restrict to the degenerated four wave mixing process to study the saturation in a Kerr-based parametric amplifier. The chapter then gets on with the translation between quantum optics and circuit QED to describe a Josephson parametric amplifier. Eventually, a formal modeling of the $\lambda/4$ resonant JPA into a nonlinear LC series resonator is done. This modeling will be useful to understand the JPA characterized and used for a qubit readout in Chapter 7.

In Chapter 3 we introduce the concept of traveling-wave parametric amplifiers (TWPA); first, nonlinear fiber optics are studied by following the approach of Govind P. Agrawal [55]. Then, a review of the theoretical description of Josephson TWPA is carried out. Similarities between Josephson TWPA and nonlinear fiber optics are pointed out. An attempt to transpose this model to a periodically modulated Josephson TWPA is done. However, this approach turns out to be unsuccessful since it does not take into account the nonlinear dependence of the photonic gap, generated by the periodic modulation. The last part of this section is dedicated to a new model developed by **Denis M. Basko** during this PhD. After a description of this model, the expected features of a Josephson photonic crystal TWPA are shown.

Chapter 4 is entirely dedicated to the fabrication techniques and recipes of the different samples characterized along this thesis. An important time of this work was dedicated to the design and fabrication of $50\,\Omega$ Josephson/SQUID transmission lines with the 'top-ground' deposition technique.

In Chapter 5, we briefly describe the microwave setups and the dilution refrigerators that have been used to measure the samples. We also discuss about the microwave calibrations and the different methods used for precisely infer the phase propagation in the Josephson/SQUID transmission lines.

The last three chapters are dedicated to actual experimental results. Chapter 6 focuses in the linear characterization of the different samples fabricated. Every samples presented have in common that they are SQUID arrays, of various lengths. We classify them with respect to their length and their external quality factor. As for the samples which underwent the top-ground deposition technique, their different source of losses are studied.

In Chapter 7, resonant JPAs performances are shown as well as theoretical data coming from the derivation carried out in Chapter 2 and their agreement. The good agreements allow for an accurate calibration of the microwave setup and *in fine* a quantitative measurement of the amplifiers saturation points. Eventually, we present data coming from the readout of a transmon molecule qubit fabricated and measured in collaboration with **Rémy Dassonneville** done with a SQUID array JPA.

The last chapter is dedicated to Josephson photonic crystal TWPAs. We present their figures of merit. In this chapter we compare experimental data to theoretical data from the model developed in Chapter 3. We again make use of the good agreement between theory and experimental data to calibrate the at-

tenuation line of the setup and extract precisely the saturation and the noise of the TWPA. We demonstrate that our TWPAs have saturation point higher than the previously characterized JPA and are close to be quantum limited.

1.5.2 Results

The results presented in this thesis can be divided in three projects, which lead to three publications. First, the implementation of a high saturation power resonant JPA [56]. Second, setting up a process for the fabrication of reproducible, highly nonlinear, near 50 Ω Josephson transmission lines [57] and the fabrication of a low-footprint, flux-tunable, SQUID-based TWPA [58].

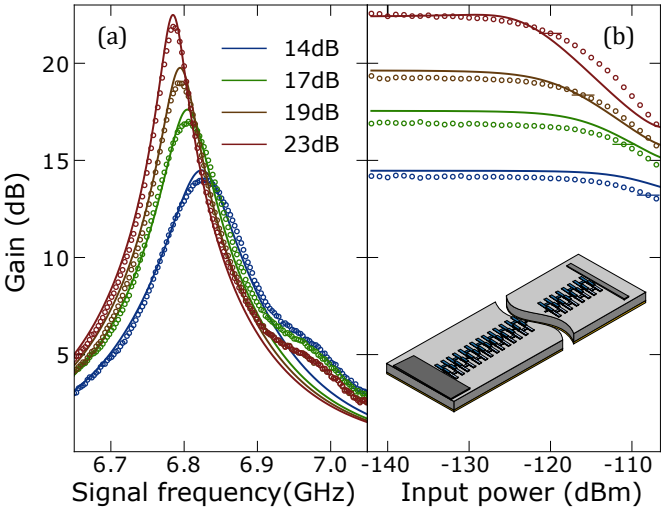

Figure 1.5 – **Resonant JPA performance. (a)** Gain as a function of the signal frequency for different pump power. Hollow points are experimental data while solid lines are theory. Larger pump power leads to higher gain: blue line: −81.65 dBm; green line: −81.12 dBm; brown line: −80.83 dBm; red line: −80.57 dBm. More than 20 dB power gain is found. **(b)** Maximum gain as a function of the signal power. Above a threshold, gain power is compressed. When the linear uncompressed gain is 20 dB, the one decibel compression point is −117 dB. **Inset:** sketch of our SQUID array JPA working in reflection. The only port (input and output) is on the left end of the array.

Resonant Josephson parametric amplifier

The first project carried out during this work was the development and characterization of a resonant JPA designed as a nonlinear $\lambda/4$ resonator. The goal of using a 80 SQUID long array instead of a single junction is to dilute the Kerr

nonlinearity in order to increase the JPA compression point. As it will be thoroughly explained in Chapter 2, Kerr nonlinearity in four wave mixing JPA is in the same time responsible for amplification and saturation. The presented JPA maximum gain can go up to 25 dB power gain. For 20 dB power gain, its bandwidth is 45 MHz with a 1 dB compression point equals to −117 dBm (see Fig. 1.5). This saturation point is a good result for a simple four wave mixing Josephson amplifier. Single junction JPAs based on a four wave gain mixing displays generally 1 dB compression point between −135 dBm and −125 dBm. When this JPA was used in a qubit readout experiment, a fidelity of 97.4% was found with a readout pulse of 50 ns. This state-of-the-art figure is not the result of the JPA only, but it shows its suitability for a proper qubit readout. Moreover, the added noise of the amplifier, in number of quanta, was found to be 0.55 ± 0.25, with a SQL defined at 0.5 quanta. The uncertainty on the calibration prevent us to state that this JPA is actually quantum limited, but it is definitively near it.

Fabrication and characterization of SQUID, low impedance transmission lines

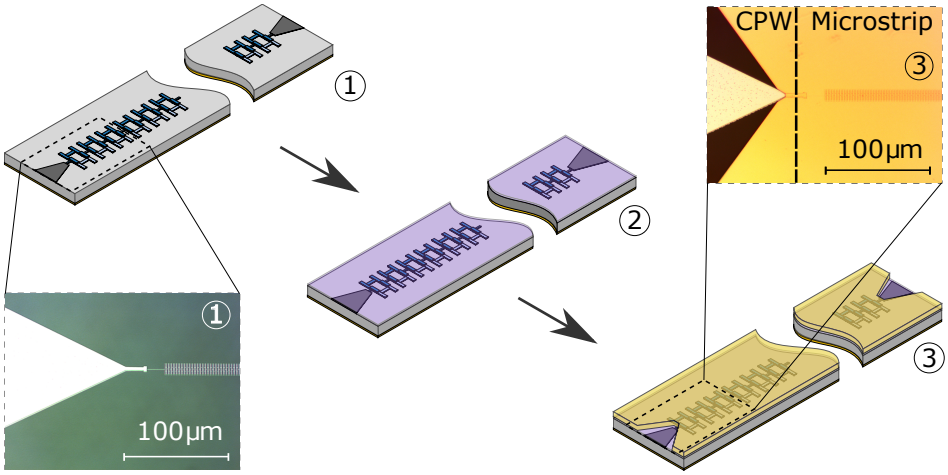

Figure 1.6 – **Fabrication process of the SQUID transmission lines with top-ground geometry.** It is divided in three steps. ①: Two-port 2000-SQUID long array fabrication. ②: Atomic layer deposition of the dielectric. ③: Metallic layer deposition for electric ground purpose. Two spots are cleared from metal for wire bonding.

After demonstrating experimentally that short SQUID arrays were suited for amplification with a very good fabrication yield, the next project was to fabricate much longer SQUID arrays in order to implement traveling-wave amplifiers. The main issue with TWPA is to impedance match the arrays with the low impedance

environment. The second main project was to develop a fabrication process to fabricate 50 Ω SQUID arrays. We completed the existing array fabrication with two more steps (see Fig. 1.6). A thin dielectric layer is deposited on top of the SQUID array via atomic layer deposition. Then, a thick metallic layer is deposited on the dielectric, to work as an electrical ground. This process leads to SQUID-based transmission lines matched with a 50 Ω microwave setup. The highest issue with this fabrication process is the electrical loss undergone by the transmitted signal. Loss study showed they were mainly coming from the top dielectric layer. We reported loss tangents between 5×10^{-3} and 9×10^{-3} and noticed their power dependence. Higher input signal power leads to lower loss tangent. All these considerations lead us to believe that dielectric losses were coming from two-level systems.

Josephson photonic crystal traveling-wave parametric amplifier

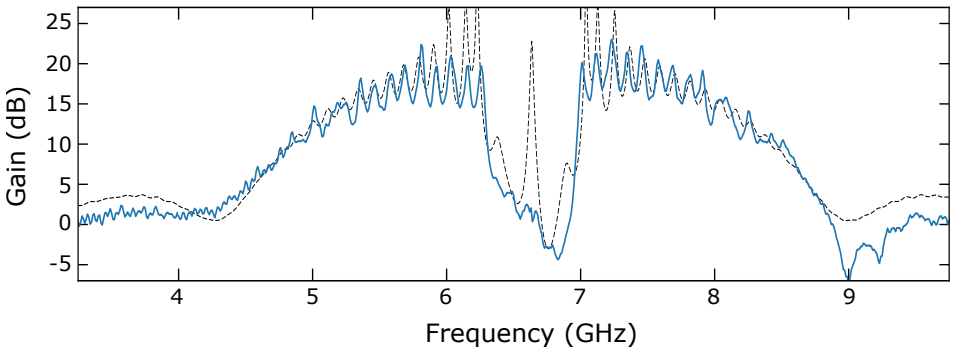

Figure 1.7 – **TWPA gain.** Gain *vs.* frequency. The solid blue line is the experimentally measured gain while the dashed black line is theory. A maximum mean gain around 18 dB is found. We notice the presence of gain ripples close to the maximum gain, due to parasitic reflection. The dip in the middle of the profile is a consequence of the photonic gap, required to get high gain and high bandwidth. We can directly spot the improvement between this figure and Fig. 1.5**(a)**.

Once the top-ground deposition technique developed, we could eventually implement the first periodically modulated, SQUID-based TWPA. Phase matching is enabled by the photonic gap yielded by the periodic modulation. Moreover, TWPA features *in-situ* magnetic flux tunability. It displayed a maximum gain up to 18 dB gain, with a 3 GHz bandwidth from which 750 MHz must be removed because of the photonic band gap (absence of transmission, see Fig. 1.7). However, flux tunability allows to increase this already high bandwidth since the photonic gap position is also flux dependent. Moreover, tunability allows to tune the characteristic impedance of the array and to improve the matching between the TWPA and the environment. Therefore, gain ripples can be partially canceled. As shown

in Fig. 1.7, a good agreement between the theory developed in Chapter 3 and experimental data is found. We took advantage of this good agreement to calibrate the attenuation of the input line. With this calibration, we measured a 1 dB compression point at −103 dBm. We measured a system noise temperature (with the TWPA switched on) between 0.5 K and 2 K, with a mean value around 0.75 K (the 1 quantum SQL being equal to 0.3 K). With the TWPA switched off, the system noise was about ten times higher. The characteristics we have found with the TWPA are dramatically better than the resonant JPA (excepted perhaps for the maximum gain).

Resonant parametric amplification

2

Contents

Link back to Table of contents →

This chapter focuses on parametric amplification in resonant Josephson amplifiers. To be as general as possible, we will use the quantum optics formalism to describe this effect. In quantum optics a parametric interaction is defined as a process happening in a nonlinear medium, where electromagnetic waves of different frequencies can mix and generate new frequencies. A well-known parametric interaction is the spontaneous parametric down conversion (SPDC), which leads to entangled photons generation [59]. SPDC happens when an intense electromagnetic wave (in the sense of high amplitude) of frequency $\omega_p/2\pi$, called **pump**, is sent towards a nonlinear medium and generates two electromagnetic waves, called signal (idler) of frequency $\omega_s/2\pi$ ($\omega_i/2\pi$) such that energy is conserved. These two waves are physically equivalent (except for their frequency). One is called 'signal' because it generally carries the frequency of interest. When dealing with parametric amplification, the spontaneous character of SPDC in the emission is replaced by a stimulated emission when the pump and the signal are simultaneously sent to the nonlinear medium. The key feature to have parametric amplification is that the refractive index depends on the wave amplitude. This dependence can be achieved if, for instance, the polarization field in the medium is a **nonlinear** function of the electric field. Thereby, the pump can make the refractive index vary over time (in this sense, the refractive index becomes a time-varying **parameter** of the equation describing wave propagation, hence the name **parametric**). The pump therefore induces a periodic modulation of the wave velocity. This leads to energy transfer between the pump and the signal, giving rise to gain. In electronics, the analogue of the modulation of the refractive index is the modulation of the inductance (or capacitance) of an electronic circuit, leading to a modulation of the wave velocity of the electronic signal.

2.1 Definition and basics of parametric amplification

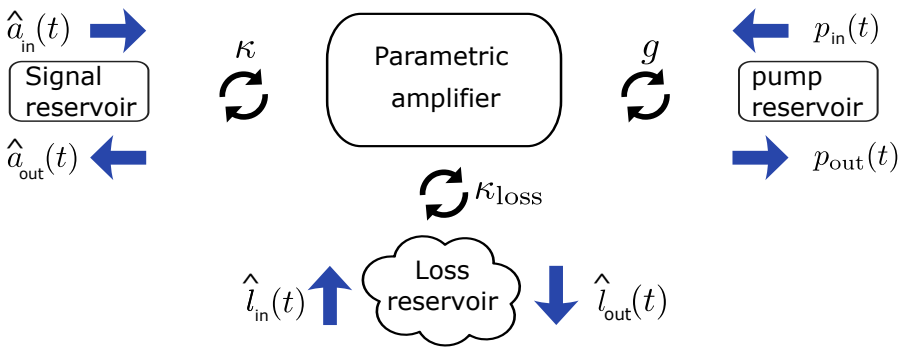

Figure 2.1 – **Illustration of the different incoming and outcoming fields relevant to resonant parametric amplification.**

To maximize the stimulated signal emission, one must increase the interaction time between the pump, the signal and the nonlinear medium. To do so, it is common to put the nonlinear medium in a resonator, of resonant frequency $\omega_0/2\pi$. The ensemble resonator + nonlinear medium is seen as a nonlinear resonator (NLR) of resonant frequency $\tilde{\omega}_0/2\pi$. The tilde denotes a variation of the resonance due to the nonlinear medium, but will be dropped in the rest of the chapter. We consider the case where the amplification occurs in reflection. In that case, input signal field $\hat{a}_{\text{in}}(t)$ and output signal field $\hat{a}_{\text{out}}(t)$ share the same port, coupled to the NLR with a damping rate κ (see Fig. 2.1). Loss ports can be modeled the same way, with a coupling rate κ_{loss}. In Fig. 2.1, the pump is coupled via a third port with damping rate g. In some cases, pump and signal share the same port and $g = \kappa$. To express the signal gain, $\hat{a}_{\text{out}}(t)$ must be compared to $\hat{a}_{\text{in}}(t)$. To do so, we study the dynamics of the intra-resonator field of the NLR, described by its annihilation (creation) operators $\hat{a}$ ($\hat{a}^\dagger$). The standard approach to infer the intra-resonator fields dynamics is to solve the quantum Langevin equation (QLE). It describes, in the Heisenberg picture, the intra-resonator fields evolution of a (nonlinear) resonator coupled to a reservoir of propagating modes [60]. Under the Markov approximation (the system itself does not affect the reservoirs from which the fields are coming [61]) and the rotating wave approximation RWA (*i.e.* only slow fields in the rotating frame of interest are kept, the others are discarded), the QLE for $\hat{a}(t)$ reads:

$$\frac{\mathrm{d}\hat{a}}{\mathrm{d}t} = \frac{i}{\hbar}\left[\hat{H}_{\text{syst}}, \hat{a}\right] - \frac{\kappa + \kappa_{\text{loss}}}{2}\hat{a} + \sqrt{\kappa}\hat{a}_{\text{in}}(t) + \sqrt{\kappa_{\text{loss}}}\hat{l}_{\text{in}}(t), \tag{2.1}$$

where $\hat{H}_{\text{syst}}$ is the Hamiltonian of the system. To relate the output signal field to the input and the intra-resonator field we assume the boundary condition:

$$\sqrt{\kappa}\hat{a}(t) = \hat{a}_{\text{in}}(t) + \hat{a}_{\text{out}}(t). \tag{2.2}$$

To solve the QLE, we need to derive an analytical expression of the system Hamiltonian $\hat{H}_{\text{sys}}$. Its minimal form can be decomposed in three elements. First, the system Hamiltonian involves the nonlinear resonator where amplification occurs, whose Hamiltonian is denoted $\hat{H}_{\text{a}}$. Moreover, the nonlinear resonator must be driven by an intense pump field in order to modulate the refractive index of the medium. Because of its large amplitude, the pump is modeled as a classical drive described by its frequency $\omega_{\text{p}}/2\pi$ and its field amplitude p. Its Hamiltonian is denoted H_{p}. Position and momentum of the pump drive oscillator are defined as:

$$X_{\text{p}} = x_{\text{p}}(p + p^*) \quad , \quad Y_{\text{p}} = -iy_{\text{p}}(p - p^*). \tag{2.3}$$

x_{p} and y_{p} are their respective dimensionless amplitude. The associated potential and kinetic energies are denoted U_{p} and T_{p}, respectively. Eventually, the system must account for the interaction between the nonlinear resonator and the pump, whose Hamiltonian is denoted $\hat{H}_{\text{int}}$. Therefore, the system Hamiltonian is at least a sum of $\hat{H}_{\text{a}}$, H_{p} and $\hat{H}_{\text{int}}$.

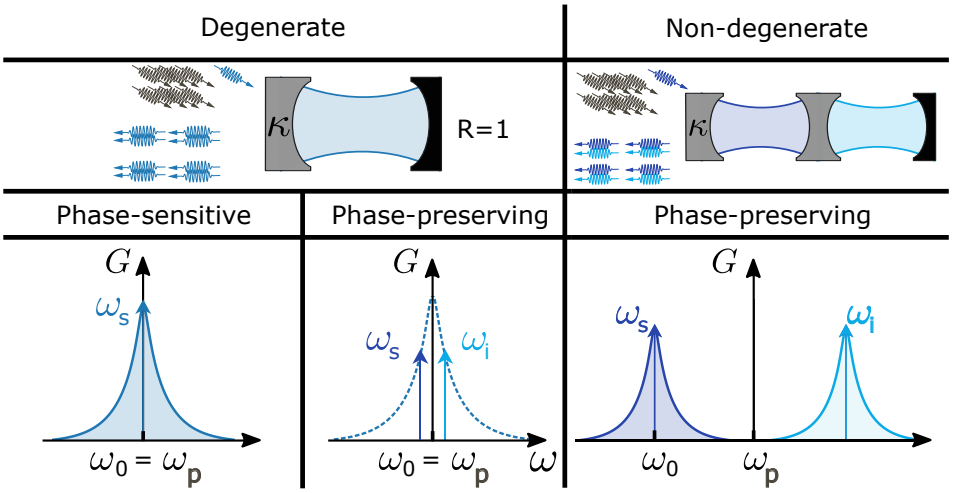

Figure 2.2 – **Four-wave mixing amplification.** The amplification process occurs in a nonlinear resonator (ω_0), pumped by an intense electromagnetic wave (ω_p). The resonator is coupled to the environment with damping rate κ. The other side of the resonator is a perfect mirror with a reflection coefficient R=1. The process can be either spatially degenerate or non-degenerate. Depending whether or not signal (ω_s) and idler (ω_i) have the same frequency the process is said phase-sensitive or phase-preserving.

Before going any further in the derivation of the system Hamiltonian, we must address two questions:

— What is the microscopic nature of the parametric process?

— Does the idler evolve in the same spatial mode than the signal ?

Regarding the first question, we will restrict ourselves to two cases: one pump photon gives one signal photon and one idler photon (**three wave mixing process**, shorted as 3WM) and two pump photons give one signal and one idler photon (**four wave mixing**, shorted as 4WM). The second question has only two answers (yes/no). In the case where the idler evolves in a spatially separated mode from the signal, it is useful to model it as an independent field, with frequency $\omega_\mathrm{i}/2\pi$, annihilation (creation) operators $\hat{b}$ ($\hat{b}^\dagger$) and Hamiltonian $\hat{H}_\mathrm{b}$ and the amplifier is said to be **non-degenerate**. Otherwise, if signal and idler evolve in the same spatial mode, the amplifier is said to be **degenerate**. We take this opportunity to stress the distinction between degenerate/non-degenerate and **phase-sensitive/phase-preserving**. The latter two, defined in the introduction Section 1.3, express whether or not the amplifier gain is sensitive to the phase difference $\Delta\phi$ between the pump and the signal[a]. Phase-sensitivity happens when

[a] We note that other authors might use different choices [62]. However, our conventions will

$\omega_s = \omega_i$ (see Fig. 2.2).

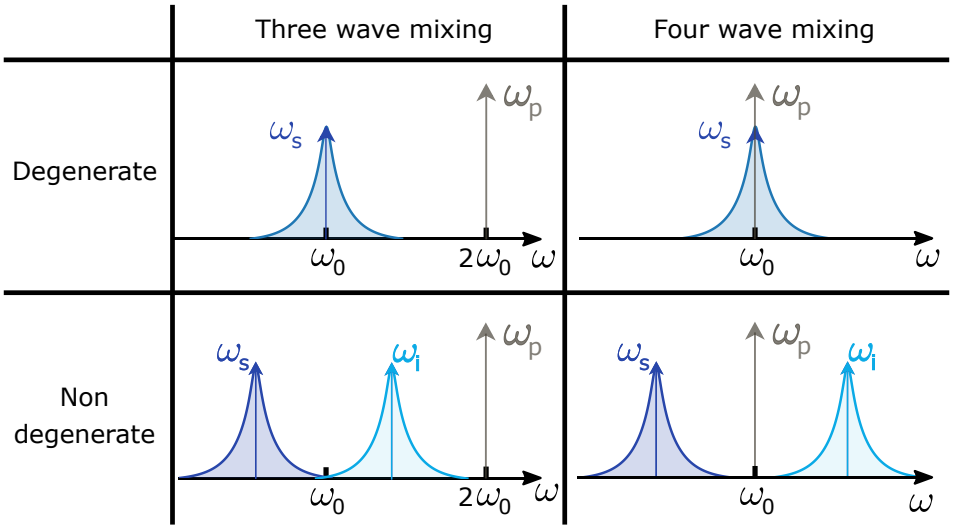

Figure 2.3 – **Four monochromatic pumping schemes with a parametric amplifier.** Frequency landscape of the different schemes. The amplification process is either three wave mixing ($\omega_p = \omega_s + \omega_i$) or four wave mixing ($2\omega_p = \omega_s + \omega_i$). Also, signal and idler modes can be spatially degenerate or not. These four schemes are studied in Section 2.2.

To summarize, there are then four cases to investigate, as shown in Fig. 2.3. Each of these cases will be detailed in the next section. We will show that in the degenerate cases, the system Hamiltonian, after several transformations, can take a canonical form based on the degenerate parametric amplifier model [63, 64] (detailed calculations for the four wave mixing non-degenerate case in Appendix A, Section A.1):

$$\frac{\hat{H}_{\text{sys}}}{\hbar} = \Omega \hat{a}^\dagger \hat{a} + \frac{\lambda}{2}\hat{a}^{\dagger 2} + \frac{\lambda^*}{2}\hat{a}^2, \tag{2.4}$$

where Ω is the frequency of the rotating frame under which the system is studied and λ is the pump strength. For the non-degenerate cases, we will see that the system Hamiltonian takes a slightly different form from Eq. (2.4) due to the idler field.

In Section 2.2, we will get an analytical formulation of the system Hamiltonian $\hat{H}_{\text{sys}}$ for the four cases pictured in Fig. 2.3. As we previously explained, what we call system is the pump oscillator, the nonlinear resonator and their interaction. Then, in Section 2.3, we will connect the system to the environment and the

remain consistent throughout this thesis.

signal reservoir by solving the quantum Langevin equation (Eq. (2.1)) and using the boundary condition (Eq. (2.2)). This will be done in the degenerate case and we will eventually obtain an expression of the signal power gain G.

2.2 Derivation of the different Hamiltonian

In this section we go through the main steps to derive $\hat{H}_{\text{sys}}$ for each pumping scheme. In these derivations, we consider the pump oscillator, the nonlinear resonator and their interaction. Each case concludes with some useful insights on how these schemes are actually implemented in the cQED architecture.

2.2.1 Three wave mixing and degenerate

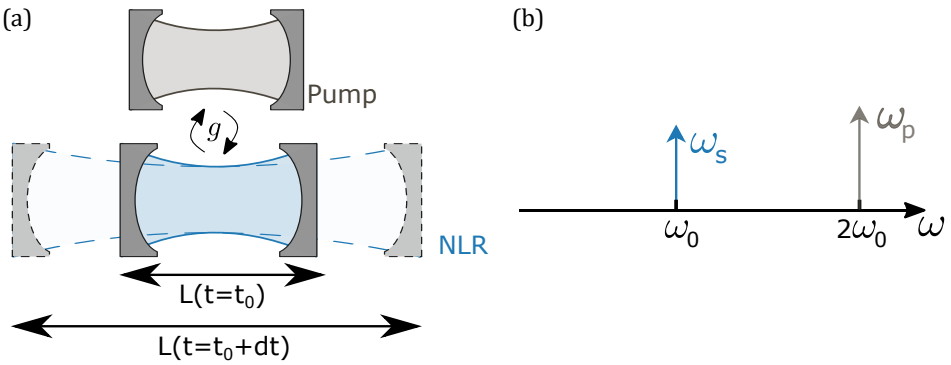

Figure 2.4 – **Three wave mixing degenerate process. (a)** Schematic of the process. The nonlinear resonator is coupled with rate g to the pump oscillator. **(b)** Frequency landscape of the process. Maximum amplification occurs when the pump frequency $\omega_{\text{p}}/2\pi$ is twice the nonlinear resonator frequency $\omega_0/2\pi$ ($\Omega = 0$) and twice the signal frequency $\omega_{\text{s}}/2\pi$. This is the textbook parametric amplification where a drive modulates parametrically the potential of a nonlinear resonator. It is equivalent to modulate periodically its effective length L(t).

We start with the textbook parametric process, namely three wave mixing and degenerate. The position $\hat{X}_{\text{a}}$ and momentum $\hat{Y}_{\text{a}}$ operators of the nonlinear oscillator read:

$$\hat{X}_{\text{a}} = x_{\text{a}}^{\text{zpf}}(\hat{a} + \hat{a}^\dagger) \quad , \quad \hat{Y}_{\text{a}} = -iy_{\text{a}}^{\text{zpf}}(\hat{a} - \hat{a}^\dagger), \tag{2.5}$$

where $x_{\text{a}}^{\text{zpf}}$ and $y_{\text{a}}^{\text{zpf}}$ are their respective zero-point fluctuations. The associated potential and kinetic energies are denoted U_{a} and T_{a}, respectively. Its resonant

frequency is ω_0. The nonlinearity of the oscillator lies in the time dependence of its potential energy and is modeled as:

$$U_{\mathrm{a}}(t) = U_{\mathrm{a}}^0 \left[1 + \gamma \left(p + p^*\right)\right] \quad \text{where} \quad \gamma << 1, \tag{2.6}$$

with U_{a}^0 the mean value of the potential energy. The system Hamiltonian $\hat{H}_{\mathrm{3WMD}}$ is written as the energy of the two oscillators:

$$\hat{H}_{\mathrm{3WMD}} = U_{\mathrm{p}} X_{\mathrm{p}}^2 + T_{\mathrm{p}} Y_{\mathrm{p}}^2 + U_{\mathrm{a}}(t) \hat{X}_{\mathrm{a}}^2 + T_{\mathrm{a}} \hat{Y}_{\mathrm{a}}^2. \tag{2.7}$$

We can reduce the pump Hamiltonian to its drive form $H_{\mathrm{p}} = \hbar \omega_{\mathrm{p}} p^* p$ by applying the RWA. We can do the same with the other oscillator by separating the constant part and the oscillating part of the potential $U_{\mathrm{a}}(t)$. We can define the linear part of the oscillator $\hat{H}_{\mathrm{a}} = \hbar \omega_0 \hat{a}^\dagger \hat{a}$. The Hamiltonian now reads:

$$\hat{H}_{\mathrm{3WMD}} = H_{\mathrm{p}} + \hat{H}_{\mathrm{a}} + \hat{H}_{\mathrm{int}} \quad \text{where:} \quad \hat{H}_{\mathrm{int}} = U_{\mathrm{a}}^0 \gamma (p + p^*) \left(x_{\mathrm{a}}^{\mathrm{zpf}} \left(\hat{a} + \hat{a}^\dagger \right) \right)^2. \tag{2.8}$$

In Eq. (2.8), we see that the nonlinear dependence of the potential $U_{\mathrm{a}}(t)$ generated by the pump can be seen as an interaction between the two oscillators and modeled with $\hat{H}_{\mathrm{int}}$. To get to the general form of the degenerate parametric amplifier, one must change the rotating frame with a unitary transformation $\hat{R}$:

$$\begin{aligned} \hat{H}_{\mathrm{3WMD}} &= \hat{R} H \hat{R}^\dagger + i\hbar \dot{\hat{R}} \hat{R}^\dagger \quad (\hat{R} = e^{i\omega_{\mathrm{p}} t p^* p + i\omega_{\mathrm{p}} t \hat{a}^\dagger \hat{a}/2}) \\ &\overset{\mathrm{RWA}}{=} \hbar(\omega_0 - \frac{\omega_{\mathrm{p}}}{2}) \hat{a}^\dagger \hat{a} + U_{\mathrm{a}}^0 \gamma (x_{\mathrm{a}}^{\mathrm{zpf}})^2 (p \hat{a}^{\dagger 2} + \mathrm{H.c.}), \end{aligned} \tag{2.9}$$

where 'H.c.' stands for Hermitian conjugate. We eventually find the desired form of the Hamiltonian as in Eq. (2.4):

$$\frac{\hat{H}_{\mathrm{3WMD}}}{\hbar} = \Omega \hat{a}^\dagger \hat{a} + \frac{\lambda}{2} \hat{a}^{\dagger 2} + \frac{\lambda^*}{2} \hat{a}^2, \tag{2.10a}$$

$$\Omega = (\omega_0 - \frac{\omega_{\mathrm{p}}}{2}), \tag{2.10b}$$

$$\lambda = \frac{2 U_{\mathrm{a}}^0 \gamma (x_{\mathrm{a}}^{\mathrm{zpf}})^2}{\hbar} p. \tag{2.10c}$$

As expected with a three wave amplifier, the amplification process is fully resonant ($\Omega = 0$) when the pump frequency is twice the resonator frequency (and therefore twice the signal frequency). The interesting feature in this pumping scheme is that the parametric pump strength λ depends on the pump amplitude p and the zero-point fluctuations of the signal. Basically, modulating the potential $U_{\mathrm{a}}^0(t)$ of the resonator at twice the frequency of the resonator is like stretching it back and

forth (as shown in Fig. 2.4) to get the signal amplified.

cQED implementation: The simplest way to implement a 3WM, degenerate Josephson parametric amplifier (JPA) is to embed one or few SQUID in a resonator working in reflection [36]. The flux dependence of the SQUID inductance ($\propto \cos(\pi\Phi/\Phi_0)^{-1}$) is used to modulate periodically the phase velocity of the resonator or, equivalently, its electrical length. For a given pump amplitude, the larger the electrical length modulation, the larger the gain. This is why flux-pumped SQUID-based amplifiers are DC flux biased at a point maximizing the derivative of $\cos(\pi\Phi/\Phi_0)^{-1}$ while a rapid RF magnetic flux (the pump) threads the loop. It is noteworthy that given the DC flux increases the response of the SQUID inductance with respect to the flux, the RF magnetic flux, acting as a pump, has a relatively low power compared to the other pumping schemes for Josephson parametric amplifiers.

2.2.2 Three wave mixing and non-degenerate

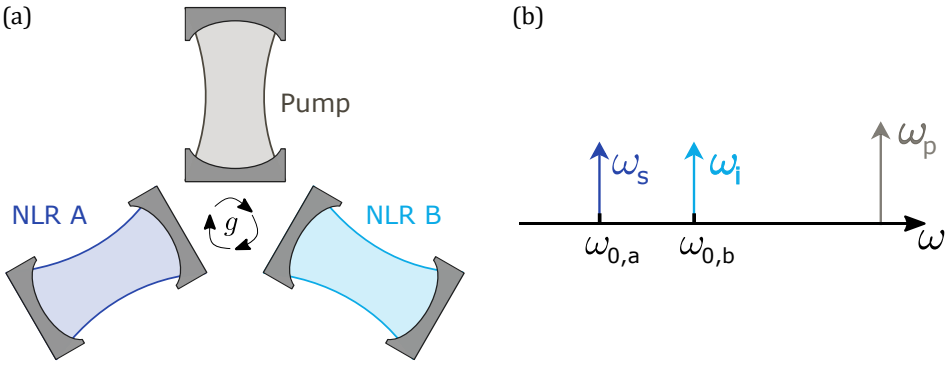

Figure 2.5 – **Three wave mixing non-degenerate process. (a)** Two nonlinear resonators (NLR A and NLR B) and the pump oscillator are coupled with rate g. They have a specific engineered interaction, modeled with the Hamiltonian H_{int}. **(b)** Signal amplification occurs when its frequency $\omega_s/2\pi$ is close to NLR A resonant frequency $\omega_{0,a}$ and fullfill energy conservation $\omega_s = \omega_p - \omega_i$. In this scheme, signal and idler amplifications are also spatially separated.

To get a three wave mixing while being non-degenerate, one must couple two nonlinear resonators (denoted as NLR A and NLR B, see Fig. 2.5) to the pump oscillator. The oscillator NLR B position and momentum operators are defined as:

$$\hat{X}_b = x_b^{\text{zpf}}(\hat{b} + \hat{b}^\dagger) \quad , \quad \hat{Y}_b = -iy_b^{\text{zpf}}(\hat{b} - \hat{b}^\dagger). \tag{2.11a}$$

A clever engineering between these oscillators can lead to a specific interaction,

modeled with $\hat{H}_{\text{int}}$, and allow an amplification process:

$$\hat{H}_{\text{3WMD}} = \hat{H}_{\text{a}} + \hat{H}_{\text{b}} + H_{\text{p}} + \hat{H}_{\text{int}} \quad \text{where:} \quad \hat{H}_{\text{int}} = \hbar g(p + p^*)(\hat{a} + \hat{a}^\dagger)(\hat{b} + \hat{b}^\dagger). \tag{2.12}$$

As said previously, the Hamiltonian for a non-degenerate amplifier is slightly different from the degenerate case in that one considers a third oscillator ($\hat{H}_{\text{b}}$). By expanding $\hat{H}_{\text{int}}$, changing the rotating frame with the unitary evolution operator $\hat{R} = \exp\left(i(\omega_{\text{p}} t p^* p + \omega_{\text{p}} t \hat{a}^\dagger \hat{a}/2 + \omega_{\text{p}} t \hat{b}^\dagger \hat{b}/2)\right)$ and using the RWA, one ends up with:

$$\hat{H}_{\text{3WMND}} = \hbar(\omega_{0,\text{a}} - \frac{\omega_{\text{p}}}{2})\hat{a}^\dagger \hat{a} + \hbar(\omega_{0,\text{b}} - \frac{\omega_{\text{p}}}{2})\hat{b}^\dagger \hat{b} + \hbar g(p a^\dagger b^\dagger + \text{H.c}). \tag{2.13}$$

Eventually, we can write the three wave non-degenerate Hamiltonian as

$$\frac{\hat{H}_{\text{3WMND}}}{\hbar} = \Omega_{\text{a}} \hat{a}^\dagger \hat{a} + \Omega_{\text{b}} \hat{b}^\dagger \hat{b} + \frac{\lambda}{2} \hat{a}^\dagger \hat{b}^\dagger + \frac{\lambda^*}{2} \hat{a}\hat{b}, \tag{2.14a}$$

$$\Omega_{\text{k}} = (\omega_{0,\text{k}} - \frac{\omega_{\text{p}}}{2}) \quad \text{k} = \{\text{a,b}\}, \tag{2.14b}$$

$$\lambda = 2gp. \tag{2.14c}$$

The pump strength depends on the pump amplitude p and on the coupling g between the oscillators. In this case, the nonlinearity of the cavities is hidden in the tri-resonator coupling g.

cQED implementation: Behind the apparent simplicity of the derivations is hidden some very clever resonator engineering to get such three-mode coupling. This amplification scheme in cQED was first implemented with a Josephson ring modulator [39, 40, 60, 65]. These rings of four Josephson junctions give three main normal modes which are linear combinations of flux at the nodes of each junction. A more recent implementation consisted in using highly asymetric SQUID, also known as superconducting nonlinear asymetric inductive element (SNAIL) to play with the nature of the nonlinearity and achieve three wave mixing process [66].

2.2.3 Four wave mixing and degenerate

Four wave mixing degenerate amplification can be understood as a pump oscillator coupled to a nonlinear resonator[b] with rate g, as shown in Fig. 2.6. The nonlinear resonator displays a sinusoidal potential $U_{\text{a}}(t)$ that mimics the Josephson potential (see Sections 1.4 and 2.5). The potential reads (full mathematical

[b] A four wave mixing process could in principle also work with an even more complicated coupling scheme mixing two pump oscillators and nonlinear resonators. Such circuits are not practically implemented.

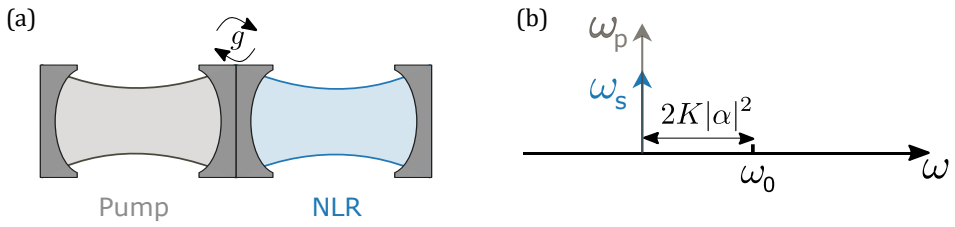

Figure 2.6 – **Four wave mixing degenerate process. (a)** The pump oscillator is coupled to a nonlinear resonator with rate g. **(b)** Maximum amplification occurs when there is a detuning $-2K|\alpha|^2$ between the pump frequency $\omega_\mathrm{p}/2\pi$ and the nonlinear resonator bare frequency $\omega_0/2\pi$. Maximum amplification also requires the signal and the pump to be degenerate ($\omega_\mathrm{s} = \omega_\mathrm{p}$). This small detuning is due to the fourth order nonlinearity coming from the NLR.

treatment done in Appendix A, Section A.1):

$$\begin{aligned} U_\mathrm{a}(t) &= -U_\mathrm{a}^0 \cos\left(x_\mathrm{a}^\mathrm{zpf}\left(\hat{a}+\hat{a}^\dagger\right)\right) \\ &\approx -U_\mathrm{a}^0\left[1-\frac{1}{2!}\left(x_\mathrm{a}^\mathrm{zpf}\left(\hat{a}+\hat{a}^\dagger\right)\right)^2+\frac{1}{4!}\left(x_\mathrm{a}^\mathrm{zpf}\left(\hat{a}+\hat{a}^\dagger\right)\right)^4\right]. \end{aligned} \tag{2.15}$$

We expanded the nonlinear term up to the fourth order. We then use the RWA to keep resonant terms only. As usual, the Hamiltonian can be seen as a sum of the pump oscillator, the nonlinear oscillator and their interaction. In this example, the pump has a large amplitude p and is near-resonant with the nonlinear resonator ($\omega_\mathrm{p} \approx \omega_0$). The pumped Hamiltonian [63, 67] reads:

$$\hat{H}_\mathrm{4WMD} = \hbar\omega_\mathrm{p} p^* p + \hbar\omega_0 \hat{a}^\dagger\hat{a} - U_\mathrm{a}^0 \hat{a}^{\dagger 2}\hat{a}^2 + \hbar g(p+p^*)(\hat{a}+\hat{a}^\dagger). \tag{2.16}$$

We change to a frame rotating at the pump frequency by applying the unitary transformation $\hat{R} = \exp\left(i(\omega_p p^* pt + \omega_p a^\dagger at)\right)$. By applying the RWA, the Hamiltonian reads:

$$\hat{H}_\mathrm{4WMD} = \hbar(\omega_0-\omega_\mathrm{p})\hat{a}^\dagger\hat{a} - U_\mathrm{a}^0\hat{a}^{\dagger 2}\hat{a}^2 + \hbar g(p\hat{a}^\dagger + p^*\hat{a}^\dagger). \tag{2.17}$$

The effect of the pump is to induced a displacement of the field of the nonlinear resonator. To take it into account, we displace the frame of study with the unitary transformation $\hat{D}(\alpha) = \exp(\alpha\hat{a}^\dagger - \alpha^*\hat{a})$, where α is a complex number and the amplitude of the resonator coherent field. The displaced Hamiltonian reads:

$$\hat{H}'_\mathrm{4WMD} = \hat{D}^\dagger(\alpha)\hat{H}_\mathrm{4WMD}\hat{D}(\alpha) - i\hbar\dot{\hat{D}}(\alpha)\hat{D}(\alpha). \tag{2.18}$$

To simplify this equation, we need another condition to link the pump amplitude p to α. The semi-classical evolution of the displaced field, in the Heisenberg picture, makes this link:

$$i\dot{\alpha} = \left(\omega_0 - \omega_\mathrm{p} - \frac{2U_\mathrm{a}^0}{\hbar}|\alpha|^2\right)\alpha + gp. \tag{2.19}$$

In the steady-state, Eq. (2.19) is injected into Eq. (2.18). By dropping constant terms ($\propto |\alpha|^2$ and $|\alpha|^4$), we obtain a simplified expression for the displaced Hamiltonian $\hat{H}'_{\mathrm{4WMD}}$:

$$\begin{aligned}\hat{H}_{\mathrm{4WMD}} = &\hbar(\omega_0 - \omega_\mathrm{p} - \frac{4U_\mathrm{a}^0}{\hbar}|\alpha|^2)a^\dagger a - \frac{U_\mathrm{a}^0}{\hbar}(\alpha^2 a^{\dagger 2} + \alpha^{*2}a^2) - \\ &\frac{U_\mathrm{a}^0}{\hbar}a^{\dagger 2}a^2 - \frac{2U_\mathrm{a}^0}{\hbar}(\alpha a^{\dagger 2}a + \alpha^* a^\dagger a^2).\end{aligned} \tag{2.20}$$

If we only look at the two first terms on the right-hand side of Eq. (2.19), we have the ideal case of a degenerate parametric amplifier as in Eq. (2.4). The next two others could be interesting to investigate as they act as non-ideal terms [63, 67]. For now, we only focus on the ideal case where the signal photon number is very low compared to the pump photon number ($\hat{a}^\dagger\hat{a} << |\alpha|^2$). In Section 2.4.2 we will increment self-consistently the very last term of Eq. (2.20) to study saturation effects in a degenerate, Kerr-based amplifier. We can define the coefficient $K = -2U_\mathrm{a}^0/\hbar$, in hertz, that quantifies the nonlinearity. By dropping the two last terms, the Hamiltonian reads:

$$\frac{\hat{H}_{\mathrm{4WMD}}}{\hbar} = \Omega\hat{a}^\dagger\hat{a} + \frac{\lambda}{2}\hat{a}^{\dagger 2} + \frac{\lambda^*}{2}\hat{a}^2, \tag{2.21a}$$

$$\Omega = \omega_0 - \omega_\mathrm{p} + 2K|\alpha|^2, \tag{2.21b}$$

$$\lambda = K\alpha^2. \tag{2.21c}$$

The pump strength λ is a product of the nonlinearity K and α^2, where α is the pump complex amplitude in the resonator. The former is denoted K because it stands for 'Kerr' as it has a similar effect than the optical Kerr effect namely a power dependent phase-shift (see Section 2.4 for more details). The fact that the pump strength is a product of the two tells us that the more nonlinear the medium is, the lower the required pump power. It is noteworthy that this amplification process is resonant when the pump and the signal are degenerate and resonant with the displaced resonator.

cQED implementation: A JPA that uses the fourth-order Kerr nonlinearity is one of the easiest to implement and fabricate in cQED. It does not require a specific coupling engineering. It can be directly pumped from the same port as

the signal and is hence called current pumped JPA. It proposes an easy way to reach the quantum limit of noise while having large gain (>20 dB). Unfortunately, it suffers from two major drawbacks. First, the pump is close to the signal frequency. Second, it has a poor dynamic range because of the major effect of the K nonlinearity on the saturation (see Section 2.4).

2.2.4 Four wave mixing and non-degenerate

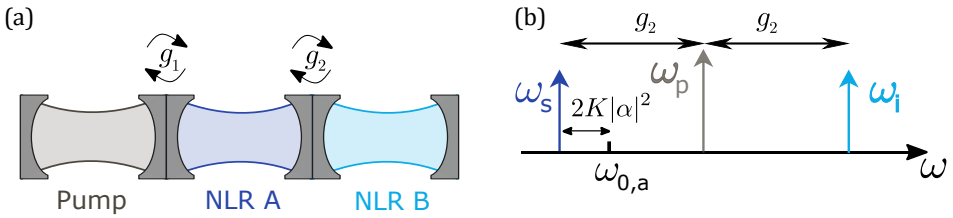

Figure 2.7 – **Four wave mixing non-degenerate process. (a)** Two nonlinear resonators, denoted NLR A ($\omega_{0,a}$) and NLR B ($\omega_{0,b}$) are coupled with rate g_2. The pump oscillator is coupled with rate g_1 to NLR A. **(b)** Signal amplification occurs when there is a small detuning between the signal frequency $\omega_s/2\pi$ and the bare frequency of NLR A. Signal and idler (ω_i) amplifications occur with a detuning $2g_2$ and fulfill the energy conservation $\omega_s + \omega_i = 2\omega_p$. These processes are also spatially separated.

To have a four wave mixing non-degenerate process, the best option is to couple a first nonlinear resonator (NLR A) to another one (NLR B) at rate g_2. NLR B (rightmost in Fig. 2.7**(a)**) resonant frequency is $\omega_{0,b}/2\pi$. $U_a(t)$ and $U_b(t)$ denote the nonlinear potentials of NLR A and NLR B, respectively. We denote the coupling rates as in Fig. 2.7**(a)**. The calculation for the Hamiltonian follows the same logic as in the previous subsection but are a bit heavier as we have to consider two cavities. The Hamiltonian is once again a sum of the pump oscillator, the two nonlinear resonators and their respective interaction.

$$\begin{aligned}\hat{H}_{\text{4WMND}} = {} & \hbar\omega_p p^* p + \hbar\omega_{0,a}\hat{a}^\dagger\hat{a} + \hbar\omega_{0,b}\hat{b}^\dagger\hat{b} - \\ & U_a^0\left(x_a^{\text{zpf}}\left(\hat{a}+\hat{a}^\dagger\right)\right)^4 + \hbar g_1(p+p^*)(\hat{a}+\hat{a}^\dagger) - \\ & U_b^0\left(x_b^{\text{zpf}}\left(\hat{b}+\hat{b}^\dagger\right)\right)^4 + \hbar g_2(\hat{a}+\hat{a}^\dagger)(\hat{b}+\hat{b}^\dagger).\end{aligned} \tag{2.22}$$

We make the two same unitary transformations as in the previous section. We first rotate the frame of study with $\hat{R} = \exp\left(i\omega_p t(p^* p + \hat{a}^\dagger\hat{a} + \hat{b}^\dagger\hat{b})\right)$, at the pump frequency. We then displace the frame of study with $D_a(\alpha) = \exp\left(\alpha\hat{a}^\dagger - \alpha^*\hat{a}\right)$,

where α is the amplitude of the resonator A coherent field and with $D_{\mathrm{b}}(\beta) = \exp\left(\beta\hat{b}^{\dagger} - \beta^{*}\hat{b}\right)$, where β is the amplitude the resonator B coherent field. We define two Kerr coefficients $K_{\mathrm{a}} = -2U_{\mathrm{a}}^{0}/\hbar$ and $K_{\mathrm{b}} = -2U_{\mathrm{b}}^{0}/\hbar$. The Hamiltonian, after the transformation reads:

$$\frac{\hat{H}_{4\mathrm{WMND}}}{\hbar} = \Omega_{\mathrm{a}}\hat{a}^{\dagger}\hat{a} + \Omega_{\mathrm{b}}\hat{b}^{\dagger}\hat{b} + g_2(\hat{a}^{\dagger}\hat{b} + \mathrm{H.c}) + (\frac{\lambda_{\mathrm{a}}}{2}\hat{a}^{\dagger 2} + \frac{\lambda_{\mathrm{b}}}{2}\hat{b}^{\dagger 2} + \mathrm{H.c}), \quad (2.23a)$$

$$\Omega_{\mathrm{k}} = (\omega_{0,\mathrm{k}} - \omega_{\mathrm{p}} + 2K_{\mathrm{k}}|\xi|^2), \quad (2.23b)$$

$$\lambda_{\mathrm{k}} = K_{\mathrm{k}}\xi^2 \quad , \quad \mathrm{k} = \{\mathrm{a,b}\} \quad , \quad \xi = \{\alpha, \beta\}. \quad (2.23c)$$

Here the coupling does not appear in the nonlinear terms (we have two uncoupled nonlinear terms) but in the linear coupling between two resonators.

cQED implementation: Four wave mixing non-degenerate JPAs are relatively new in the cQED community [41, 68]. They consist of two capacitively coupled arrays of Josephson junctions to get a coupling large enough between the two resonators. They manage to overcome one of the drawbacks of degenerate JPAs: the pump is detuned from the signal, which makes four wave mixing amplifiers even more user-friendly.

2.2.5 Conclusion

In this section we showed that the four main types of parametric processes can be described by the same kind of Hamiltonian. The main differences are the origin of the pump strength and whether or not they have a spatial mode associated to the idler. We observed that in the three wave mixing scheme, the interesting terms $(\lambda\hat{a}^2 + \mathrm{H.c})$ come directly from the interaction between the pump and the signal, whereas in the four wave mixing scheme, these terms arise from an additional step of pump induced field displacement. This might explain why three wave mixing is sometimes considered as a more elegant way to reach parametric amplification.

2.3 Gain with an ideal degenerate parametric amplifier

In this section, we will solve the QLE with the degenerate parametric Hamiltonian (as shown in Eq. (2.4)) in the ideal case, without accounting for higher order nonlinear terms for instance. This derivation works for both the 4WM and the 3WM cases.

2.3.1 Gain

To get the expression of the signal power gain G, we must define more precisely the different incoming ports. Loss ports (see Fig. 2.1) with coupling rate κ_{loss} are not considered since, in practice, losses within resonant Josephson parametric

amplifiers are very low. Moreover, we consider the pump and signal reservoir as being connected via the same port with a coupling rate κ. This does not really change the physics, it only simplifies the notations. Since we are looking for the expression of G as a function of the angular frequency ω, we must first Fourier transform the operators:

$$\hat{a}[\bar{\omega}] = \int_{-\infty}^{+\infty} \hat{a}(t) e^{i\bar{\omega}t} \mathrm{d}t \quad , \quad \hat{a}^\dagger[\bar{\omega}] = \int_{-\infty}^{+\infty} \hat{a}^\dagger(t) e^{i\bar{\omega}t} \mathrm{d}t, \tag{2.24}$$

where $\bar{\omega}$ denotes the detuning between the signal and the pump frequency ($\bar{\omega} = \omega_\mathrm{p} - \omega_\mathrm{s}$). It is noteworthy that, in the case where $\bar{\omega} \neq 0$, the two operators $\hat{a}[\bar{\omega}]$ and $\hat{a}^\dagger[\bar{\omega}]$ do commute and describe two independent quantities namely photons at frequency $\bar{\omega}/2\pi$ and $-\bar{\omega}/2\pi$. As a reminder, the case where $\bar{\omega} = 0$ corresponds to the phase-sensitive mode of operation (see Fig. 2.2) whereas for $\bar{\omega} \neq 0$ the amplifier is phase-preserving. To help the reader, the operator $\hat{a}^\dagger[\bar{\omega}]$ will be written as $\hat{a}^\dagger[-\bar{\omega}]$ to emphasize the fact that this operator acts on photons of frequency $-\bar{\omega}$. Now that we have defined frequency domain operators, we can solve the QLE (Eq. (2.1)) with the Hamiltonian in Eq. (2.4) of a degenerate parametric amplifier. After Fourier transform we obtain two coupled equations:

$$\left(i\left(\Omega - \bar{\omega}\right) + \kappa/2\right) \hat{a}[\bar{\omega}] + i\lambda \hat{a}^\dagger[-\bar{\omega}] = \sqrt{\kappa}\hat{a}_\mathrm{in}[\bar{\omega}], \tag{2.25a}$$

$$-i\lambda^* \hat{a}^\dagger[-\bar{\omega}] + \left(-i\left(\Omega + \bar{\omega}\right) + \kappa/2\right) \hat{a}[\bar{\omega}] = \sqrt{\kappa}\hat{a}^\dagger_\mathrm{in}[-\bar{\omega}]. \tag{2.25b}$$

They can be put in a matrix form and we define a 2×2 scattering matrix $\hat{S}[\bar{\omega}]$ such that $\hat{\mathbf{a}}_\mathrm{in}[\bar{\omega}] = \hat{S}[\bar{\omega}]\hat{\mathbf{a}}[\bar{\omega}]$, where $\hat{\mathbf{a}}_\mathrm{in}[\bar{\omega}] = (\hat{a}_\mathrm{in}[\omega], \hat{a}^\dagger_\mathrm{in}[-\omega])^\mathrm{t}$ and $\hat{\mathbf{a}}[\bar{\omega}] = (\hat{a}[\omega], \hat{a}^\dagger[-\omega])^\mathrm{t}$ are vectors of dimension two. As we are interested in having the output signal as a function of the input, we must first inverse the matrix $\hat{S}[\bar{\omega}]$:

$$\begin{pmatrix} \hat{a}[\omega] \\ \hat{a}^\dagger[-\omega] \end{pmatrix} = \sqrt{\kappa}(\det S)^{-1} \begin{pmatrix} \kappa/2 - i(\omega + \Omega) & -i\lambda \\ i\lambda^* & \kappa/2 - i(\omega - \Omega) \end{pmatrix} \begin{pmatrix} \hat{a}_\mathrm{in}[\omega] \\ \hat{a}^\dagger_\mathrm{in}[-\omega] \end{pmatrix}, \tag{2.26}$$

and then use the boundary conditions Eq. (2.2) to get rid of the intra-resonator field from the equations:

$$\begin{pmatrix} \hat{a}_\mathrm{out}[\bar{\omega}] \\ \hat{a}^\dagger_\mathrm{out}[-\omega] \end{pmatrix} = \kappa(\det S)^{-1} \hat{\Sigma}^{-1} \begin{pmatrix} \hat{a}_\mathrm{in}[\bar{\omega}] \\ \hat{a}^\dagger_\mathrm{in}[-\bar{\omega}] \end{pmatrix}, \tag{2.27}$$

with:

$$\hat{\Sigma}^{-1} = \begin{pmatrix} \kappa/4 - i\Omega - (\Omega^2 - \bar{\omega}^2 - |\lambda|^2)/\kappa & -i\lambda \\ i\lambda^* & \kappa/4 + i\Omega - (\Omega^2 - \bar{\omega}^2 - |\lambda|^2)/\kappa \end{pmatrix}, \tag{2.28}$$

and:

$$\det S = \Omega^2 - \bar{\omega}^2 - |\lambda|^2 + \kappa(\kappa/4 - i\bar{\omega}). \tag{2.29}$$

The output $\hat{a}_{\text{out}}[\bar{\omega}]$ is a sum of the incoming signal at detuning $\bar{\omega}$ and idler incoming at detuning $-\bar{\omega}$:

$$\hat{a}_{\text{out}}[\bar{\omega}] = g_{s,\bar{\omega}}\hat{a}_{\text{in}}[\bar{\omega}] + g_{i,\bar{\omega}}\hat{a}^{\dagger}_{\text{in}}[-\bar{\omega}], \tag{2.30a}$$

$$g_{s,\bar{\omega}} = -1 + \frac{\kappa^2/2 - i\kappa(\Omega + \bar{\omega})}{\Omega^2 - \bar{\omega}^2 - |\lambda|^2 + \kappa(\kappa/4 - i\bar{\omega})}, \tag{2.30b}$$

$$g_{i,\bar{\omega}} = \frac{-i\kappa\lambda}{\Omega^2 - \bar{\omega}^2 - |\lambda|^2 + \kappa(\kappa/4 - i\bar{\omega})}. \tag{2.30c}$$

$g_{s,\bar{\omega}}$ and $g_{i,\bar{\omega}}$ are signal and idler gain, respectively. The power gain of the amplifier is defined as $G = |g_{s,\omega}|^2$. In the non-degenerate case, we would follow the same logical steps except that there are four coupled equations to solve.

2.3.2 Gain-bandwidth product

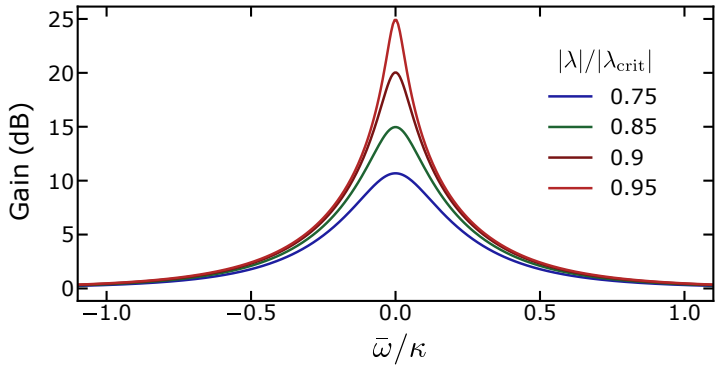

Figure 2.8 – **Signal power gain vs reduced detuning between the pump and the signal frequency.** We display the gain for different pump strength λ.

In most of parametric amplifiers, there is a conservation between the actual maximum gain G_{max} delivered by the amplifier and its dynamic bandwidth Δ_{bw}, in general defined as the -3 dB bandwidth (full width at half maximum, FWHM, defined in Section 1.2). In practice, the higher the gain, the smaller the bandwidth. This can be understood in terms of interaction time between the nonlinear medium inside the resonator and the signal. In order to have a higher gain, the interaction time between the signal and the nonlinear medium must increase; an

increase in the time spent by the signal inside the resonator translates in a decrease of its instantaneous bandwidth. We can derive an analytical expression of this conservation by starting from Eq. (2.30b) and getting an expression of the signal power gain close to its maximum. By considering the pump resonant ($\Omega = 0$) the signal power gain now reads:

$$|g_{s,\bar{\omega}}|^2 = \frac{(\kappa^2/4 + |\lambda|^2 + \bar{\omega}^2)^2}{(\kappa^2/4 - |\lambda|^2 - \bar{\omega}^2)^2 + (\kappa\bar{\omega})^2}. \tag{2.31}$$

The signal gain is greater for very low detuning between the pump and the signal ($\bar{\omega} << \kappa$). Then, it is straightforward that Eq. (2.31) is maximized for $|\lambda_{\text{crit}}|^2 \approx \kappa^2/4$. Therefore, we define a quantity ϵ such that $\epsilon^2 \approx \kappa^2/4 - |\lambda_{\text{crit}}|^2 << \kappa^2$. To have a grasp on the gain/bandwidth product, we must express the signal gain as a Lorentzian (this is experimentally the case for small detuning ($\bar{\omega} \approx 0$)). By taking $\bar{\omega} << \kappa$ and $\lambda \approx \lambda_{\text{crit}}$, the signal gain now reads:

$$|g_{s,\bar{\omega}}|^2 = \frac{(\kappa^2/4 + |\lambda_{\text{crit}}|^2 + \bar{\omega}^2)^2}{(\kappa^2/4 - |\lambda_{\text{crit}}|^2 - \bar{\omega}^2)^2 + (\kappa\bar{\omega})^2} \overset{|\lambda_{\text{crit}}|^2 \sim \kappa^2/4}{=} \frac{\kappa^4/4}{\epsilon^4 + \kappa^2\bar{\omega}^2} = \frac{G_{\max}}{1 + (2\bar{\omega}/\Delta_{\text{bw}})^2}. \tag{2.32}$$

Where $G_{\max} = \kappa^4/4\epsilon^4$ in linear unit. The full width at half maximum ($\bar{\omega} = \Delta_{\text{bw}}/2$) bandwidth reads:

$$\Delta_{\text{bw}} = \frac{2\epsilon^2}{\kappa} = \frac{\kappa}{\sqrt{G_{\max}}}. \tag{2.33}$$

Eq. (2.33) shows that $\Delta_{\text{bw}}\sqrt{G_{\max}}$ is a constant and equals the 'bare' bandwidth of the nonlinear resonator. This result is rather convenient because it allows to know roughly what will be the bandwidth of the amplifier at say 20 dB just by computing the bare bandwidth of a resonator which can be simulated in a electromagnetic simulation software. We can go further by actually plotting different gain profiles at different pump strengths λ. In Fig. 2.8, we plot the gain $|g_{s,\bar{\omega}}|^2$ in logarithmic unit as a function of the reduced detuning between the signal and the pump. We plotted the gain for four different pump strengths λ, between 75% and 95% of $|\lambda_{\text{crit}}|$. As expected, for about 20 dB maximum gain, the bandwidth is a tenth of the bare bandwidth κ. Hence, the bare resonator bandwidth is an important figure of merit.

As said in the introduction, an important figure of merit of an amplifier after its gain and its bandwidth is its dynamic range. It will be the topic of the next section.

2.4 Saturation in a degenerate, Kerr-based amplifier

We now turn to the study of saturation in degenerate, Kerr-based amplifiers working on a 4WM process. This figure of merit is becoming increasingly important in

the field of quantum information. For instance, as scalability is one important parameter for the development of quantum processors, being resource-efficient with qubit measurement is of prime importance. A way to tackle this issue is to perform high-fidelity single-shot frequency multiplexed readout of several qubits [69, 70]. This requires to have a single amplifier per line, able to handle several qubit readout tones without saturating (and with enough bandwidth, but that will be the topic of Chapter 3). Quantifying saturation requires to be specific regarding the amplification process. For example a degenerate, three wave mixing amplifier does not saturate for the same reason than a degenerate, four wave amplifier. In order to be quantitative, we restrict our study to the latter case. During my PhD, I have studied and characterized amplifiers working in a four wave mixing fashion, operated in a degenerate mode as modeled in Section 2.2.3. The next section is devoted to the treatment of the saturation process occurring in such Kerr-based amplifier.

2.4.1 The Kerr fourth order nonlinearity

Optical Kerr effect

As we borrow concepts from nonlinear optics and make analogies between nonlinear optical effects [55] and nonlinear effects in Josephson based circuits, we quickly review basic concepts of nonlinear optics to explain where does the Kerr coefficient defined previously come from. In a nonlinear medium, the response of the polarization $\mathbf{P}$ to a strong electric field can be modeled as:

$$\mathbf{P} = \epsilon_0 \left(\chi^{(1)} \cdot \mathbf{E} + \chi^{(2)} : \mathbf{EE} + \chi^{(3)} \vdots \mathbf{EEE} + ... \right), \tag{2.34}$$

where ϵ_0 is the vacuum permittivity and χ is the dielectric susceptibility. In the general case, $\chi^{(j)}$ is a tensor of rank $j+1$ and the vertical dots are the tensor product. However, in the simplest case where the light is linearly polarized, say in the $\mathbf{x}$ direction, the expression of the polarization $\mathbf{P}$ can be simplified and the different $\chi^{(\mathrm{j})}$ become scalar. For instance, the rank 2 tensor $\chi^{(1)}$ becomes $\chi^{(1)}_{\mathrm{xx}}$. For the sake of simplicity, the 'x' indexes are dropped. For a dissipationless dielectric ($\chi^{(j)}$ is considered as pure real), the linear refractive index is:

$$n_{\mathrm{L}} = \sqrt{\epsilon_{\mathrm{r}}} = \sqrt{1 + \chi^{(1)}}. \tag{2.35}$$

Regarding higher order χ nonlinearities, $\chi^{(2)}$ usually vanishes due to inversion symmetry in centrosymmetric crystals and the first nonlinear coefficient is $\chi^{(3)}$. Josephson junctions or SQUIDs feature analogous inversion symmetries and display only $\chi^{(3)}$ nonlinearities. Using clever engineering tricks, it is possible to obtain $\chi^{(2)}$ nonlinearities in Josephson superconducting circuits [48, 66, 71]. When $\chi^{(2)}$

vanishes, the nonlinear refractive index can be written:

$$\tilde{n} = n_L + n_{\mathrm{nl}}|E|^2 \quad \text{where} \quad n_{\mathrm{nl}} = \frac{3}{8n_{\mathrm{L}}}\chi^{(3)}. \tag{2.36}$$

Thereby, the refractive index of such $\chi^{(3)}$ dielectric is a sum of a linear and a nonlinear refractive index with a dependence with $|E|^2$. The coefficient 3/8 is coming from the full derivation including the nonlinear polarization $P_{\mathrm{nl}} = \epsilon_0\chi^{(3)}\vdots\mathbf{EEE}$ [55]. For a light beam evolving in such $\chi^{(3)}$ medium, a shift of the refractive index will induce a phase shift. If this phase shift is due to the power of the light beam itself, the phase shift is called self-phase modulation (SPM). If this shift is due to the power of another beam, the phase shift is called cross-phase modulation (XPM). These effects will be discussed in the next chapter. Optical Kerr effect is a special case of XPM. It occurs when a birefringence is induced by the two orthogonally electric components of a single beam traveling in a $\chi^{(3)}$ medium.

Kerr as a fuel for amplification in Josephson circuits

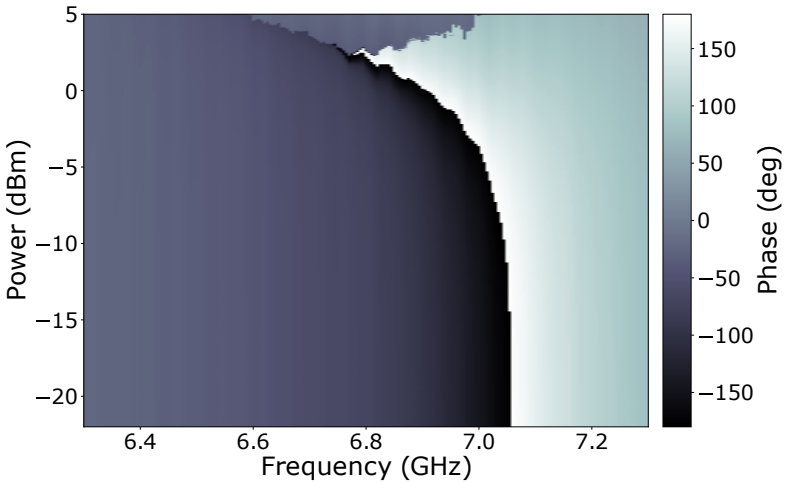

Figure 2.9 – **Experimental self Kerr modulation.** The phase (encoded as a color) of a signal reflected on a nonlinear resonator (Josephson-based resonator) is plotted as a function of its frequency (x-axis) and its power (y-axis). The resonant frequency is visible as the abrupt change of color (2π shift). For low power, the resonance stays around 7.05 GHz. For higher power, the resonance is shifted down to lower frequencies due to the self Kerr effect.

The sinusoidal dependence of the Josephson potential $\left(U \propto U_0 \cos\left[x^{\mathrm{zpf}}\left(\hat{a} + \hat{a}^\dagger\right)\right]\right)$

as introduced at the beginning of Section 2.2.3 for a nonlinear resonator in a four wave mixing process induces a power dependence of its resonant frequency. Without pumping, the associated Hamiltonian reads (after expansion up to the fourth order and RWA):

$$\frac{\hat{H}_{\text{Kerr}}}{\hbar} \overset{\text{RWA}}{=} (\omega_0 - K\hat{a}^\dagger\hat{a})\hat{a}^\dagger\hat{a} \quad , \quad K = 4U_0/\hbar. \tag{2.37}$$

The resonance shift is due to $K\hat{a}^\dagger\hat{a}$ and quantified by K, in Hertz per number of photons. This frequency shift can naturally be seen as a phase shift. There is an analogy between the optical $\chi^{(3)}$ nonlinearity introduced in the previous paragraph and this resonance shift. Since optical Kerr effect is a consequence of the $\chi^{(3)}$ nonlinearity, we speak about **self** and **cross** Kerr effect when referring to a power-induced phase shift of a signal. In Fig. 2.9, we show an experimental plot of the self modulation of the resonance of a nonlinear resonator. In this color plot, we display the phase of a signal as a function of its power (y-axis) and its frequency (x-axis). The abrupt change of color indicates a 2π shift of the phase, which corresponds to the resonance. At low power, it stays around 7.05 GHz whereas for large power, the resonance shifts towards lower frequency (down to ≈ 6.8 GHz). For higher signal power, the resonator enters an unstable region described by the equation of the Duffing oscillator [29, 30].

When pumped by a **second** field, as studied thoroughly in Section 2.2.3, the Hamiltonian is described by Eq. (2.20). The first term on the right-hand side of the equation shows a constant shift of the resonance because of the pump amplitude $|\alpha|^2$ (cross-Kerr) whereas the second term is a modulation of the potential U_0 by the pump amplitude squared α^2. This periodic modulation of U_0 is equivalent to a periodic modulation of the resonator effective length, leading to parametric amplification. It is noteworthy that the potential U_0 is modulated by the pump amplitude **squared**, leading to a four wave mixing process. This is this Kerr-like fourth-order nonlinearity which fuels the amplification process.

Saturation from Kerr effect

An interesting 'paradox' with such Kerr amplifiers is that their fuel is also their weak point as it induces low power saturation. In this short subsection, we will give qualitative arguments to explain it. In the next section, we will treat Kerr-induced saturation in a more formal way.

In Eq. (2.21b), cross modulation of the resonance is induced by the pump amplitude $|\alpha|^2$. Saturation happens when the signal power becomes large enough to actually shift the resonance even further than what is already induced by the pump itself. As a consequence, the pump frequency becomes off-resonant ($\Omega \neq 0$) if no pump correction is applied. This gets worse when the input signal power gets higher. This trend where stronger signal power leads to larger gain drop is by definition a saturation. We qualitatively illustrated this effect in Fig. 2.10. On panel **(a)** we plot the maximum gain ($\bar{\omega} = 0$) encoded as a color as a function of the pump strength (y-axis) and the pump frequency (x-axis). The dimensionless

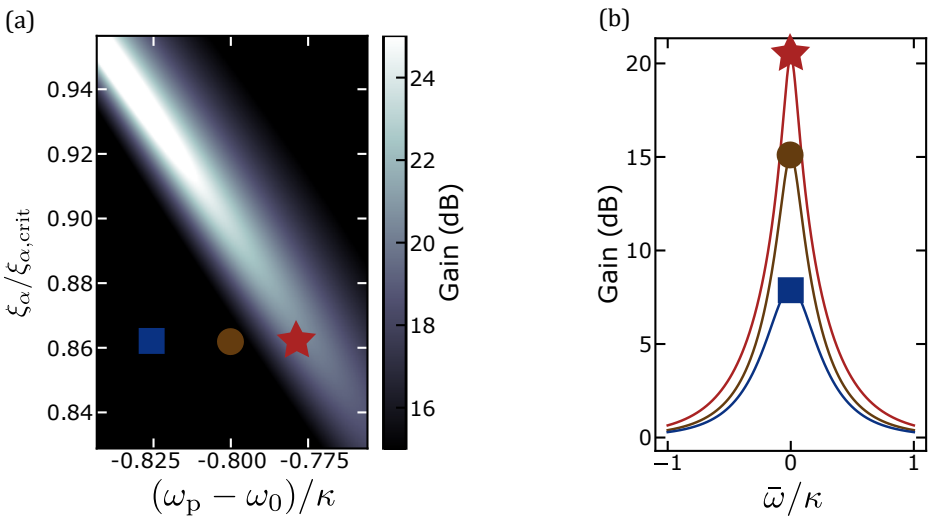

Figure 2.10 – **Effect of pump frequency detuning on gain. (a)** Maximum gain as a function of the pump strength (y-axis) and pump frequency (x-axis). There is a ridge where the the maximum gain is optimized for a specific set of pump (δ^{opti}, $\xi_\alpha^{\mathrm{opti}}$) (diagonal starting from bottom right to top left, the red star is on it). **(b)** Gain profile vs the reduced signal-to-pump detuning. When the pump is off-resonant (brown circle and blue square), the maximum gain decreases from its optimal point (red star). Both plots were obtained by solving equations derived in Section 2.4.2.

quantity ξ_α is the input pump strength and will be properly defined in the next paragraph. The first observation is that higher gain (top-left corner) asks for larger pump power but also for a lower pump frequency ($\omega_\mathrm{p}-\omega_0$ gets more negative). This is expected since the pump frequency must follow the trend of $\omega_0+2K|\alpha|^2$ in order to keep the pump resonant ($\Omega=0$ (Eq. (2.21b)). We highlighted three different pump settings where only the pump frequency gets shifted from the optimal point δ_{opti} (red star on the panel **(a)**). We observe a decrease in the maximum gain G_{max}. As shown in panel **(b)** where we fixed pump settings and only swept $\bar{\omega}$. We clearly see a gain drop when the pump gets off-resonance. This first observation explains partially the origin of gain compression in Kerr-based amplifiers. Recalling the power dependence of a Kerr-based amplifier resonant frequency, we realize that not only the pump power shifts the frequency, but so does the signal power. Therefore, once the pump power and frequency have been correctly set for a low signal power, as the signal power increases, the resonance of the amplifier shifts. If no dynamic correction of the pump frequency is carried out, the pump becomes off-resonance, and a gain drop occurs. Hence we deduce that an increase in the signal power causes a gain drop: this is gain saturation. To obtain quantitative results on what is the actual signal power needed to induce

a given gain drop, we need to precisely compute the total photon number inside the nonlinear resonator. To do so, we need to account for higher order nonlinear terms that were previously dropped in Section 2.2.3.

2.4.2 Total photon number in the resonator

Mean number of pump photons

Up to now, in our analysis the pump strength λ was related to the pump amplitude α **inside** the resonator. Experimentally, we have access to the input pump amplitude α_{in}. To link α_{in} and α we need to solve intra-resonator dynamics for the pump. To do so, we multiply the QLE Eq. (2.1) by its complex conjugate with the pump only [72]:

$$|\alpha_{\text{in}}|^2 = \left(\left(\frac{\omega_{\text{p}}-\omega_0}{\kappa}\right)^2 + \frac{1}{4}\right)|\alpha|^2 - \frac{2\left(\omega_{\text{p}}-\omega_0\right)}{\kappa^2}|\alpha|^4 + \left(\frac{K}{\kappa}\right)^2|\alpha|^6. \tag{2.38}$$

From now on, we will work with dimensionless parameters: the dimensionless drive amplitude $\tilde{\alpha}_{\text{in}}$, signal to pump frequency detuning Δ, pump to resonator frequency detuning δ and the dimensionless pump strength ξ_α

$$\tilde{\alpha}_{\text{in}} = \frac{\alpha_{\text{in}}}{\sqrt{\kappa}}, \quad \Delta = \frac{\bar{\omega}}{\kappa}, \quad \delta = \frac{\omega_{\text{p}}-\omega_0}{\kappa}, \quad \xi_\alpha = \frac{|\tilde{\alpha}_{\text{in}}|^2 K}{\kappa}. \tag{2.39}$$

Eq. (2.38) can be reduced to a cubic equation in n:

$$1 = (\delta^2 + \frac{1}{4})n - 2\delta\xi_\alpha n^2 + \xi_\alpha^2 n^3 \quad \text{where} \quad n = \frac{|\alpha|^2}{|\tilde{\alpha}_{\text{in}}|^2}. \tag{2.40}$$

Here, n is the mean number of pump photons relative to the input pump power.

Mean number of pump photons in the presence of a strong signal

To get the pump photon number inside the resonator when a strong signal is applied, we have to account for both the pump and signal photons in a self-consistent approach. We do so by dealing with non ideal terms in Eq. (2.20) that we previously dropped. First, we compute the dynamics of third order nonlinear terms only:

$$\frac{i}{\hbar}\left[-2U\left(\alpha\hat{a}^{\dagger 2}\hat{a} + \alpha^*\hat{a}^\dagger\hat{a}^2\right), \hat{a}\right] = -iK(2\hat{a}^\dagger\hat{a}\alpha + \hat{a}^2\alpha^*). \tag{2.41}$$

In order to ease the calculation, we simply add these terms self-consistently to the ideal QLE when only the pump is considered

$$\kappa\sqrt{\alpha_{\text{in}}} = \dot{\alpha} - \left(\frac{i}{\hbar}\left[H_{\text{4WMDH}}, \alpha\right] - iK\left(2\langle\hat{a}^\dagger\hat{a}\rangle\alpha + \langle\hat{a}^2\rangle\alpha^*\right)\right) + \frac{\kappa}{2}\alpha$$

$$= \left(i\left(\omega_0 - \omega_{\text{p}}\right) + \frac{\kappa}{2}\right)\alpha + iK\alpha^2\alpha^* + 2iK\langle a^\dagger a\rangle\alpha + iK\langle a^2\rangle\alpha^*. \tag{2.42}$$

If we define the signal strength ξ_{a} and the mean photon number of the input signal n_{a}:

$$\xi_{\text{a}} = \frac{K}{\kappa}n_{\text{a}}, \quad n_{\text{a}} = \langle a_\Delta^\dagger a_\Delta\rangle + \langle a_{-\Delta}^\dagger a_{-\Delta}\rangle, \tag{2.43}$$

we can follow the same mathematical steps with these two new self-consistent terms. We obtain a new cubic equation in n, the mean number of photons inside the resonator, now depending not only on pump parameters but also on the input signal strength:

$$\begin{aligned} 1 = n[\delta^2 + \frac{1}{4} - 4\xi_{\text{a}}\delta + 5\xi_{\text{a}}^2 + \xi_{\text{a}}((2\xi_{\text{a}}^2 + \delta)\cos 2\Delta\phi + \frac{1}{2}\sin 2\Delta\phi)] \\ +n^2[-2\delta\xi_\alpha + 4\xi_\alpha\xi_{\text{a}} + \xi_\alpha\xi_{\text{a}}\cos 2\Delta\phi] + n^3\xi_\alpha^2. \end{aligned} \tag{2.44}$$

where $\Delta\phi$ is the phase difference between the pump and the signal. To consider the terms depending on $\Delta\phi$ we must operate in phase-sensitive mode. We study the case where the signal frequency is very close from the pump but not strictly equals so that the amplifier works in phase-preserving mode and we average these terms to 0. We clearly see the effect of the signal strength on the total number of photon. In Eq. (2.43), the signal strength is proportional to K/κ and this is the important ratio for saturation in a Kerr-based amplifier. To obtain the signal strength, we link n_{a} to the input power using Eq. (2.26), giving the intra-resonator field as a function of the input power. Moreover we neglect the idler input power $\tilde{a}_{in,-\Delta}^\dagger$ and the associated vacuum fluctuations, which leads to:

$$a_\Delta = \frac{i(\delta - 2\xi_\alpha n - \Delta) + \frac{1}{2}}{(i\Delta - \lambda_-)(i\Delta - \lambda_+)}\tilde{a}_{in,\Delta}, \tag{2.45a}$$

$$a_{-\Delta}^\dagger = \frac{i\xi_\alpha n e^{2i\phi}}{(i\Delta - \lambda_-)(i\Delta - \lambda_+)}\tilde{a}_{in,\Delta}, \tag{2.45b}$$

$$\text{with} \quad \lambda_\pm = \frac{1}{2} \pm \sqrt{(\xi_\alpha n)^2 - (\delta - 2\xi_\alpha n)^2},$$

where $\tilde{a}_{\text{in},\Delta} = a_{\text{in},\Delta}/\sqrt{\kappa}$ is the dimensionless signal amplitude of the input field. Once Eqs. (2.45a) and (2.45b) are solved and we get the signal intra-resonator

field, we can compute the signal strength with Eq. (2.43) and solve Eq. (2.44) to obtain n. We can either compute directly the power gain $|g_s|^2$ with this new signal-dependent n **or** compute one more time Eqs. (2.45a) and (2.45b). To obtain a converged result, the signal intra-resonator field needs to be solved self-consistently and this iteration between Eq. (2.45a), Eq. (2.45b) and Eq. (2.44) must be done several times in order to have a more accurate solution as shown in the inset of Fig. 2.11.

2.4.3 Gain saturation

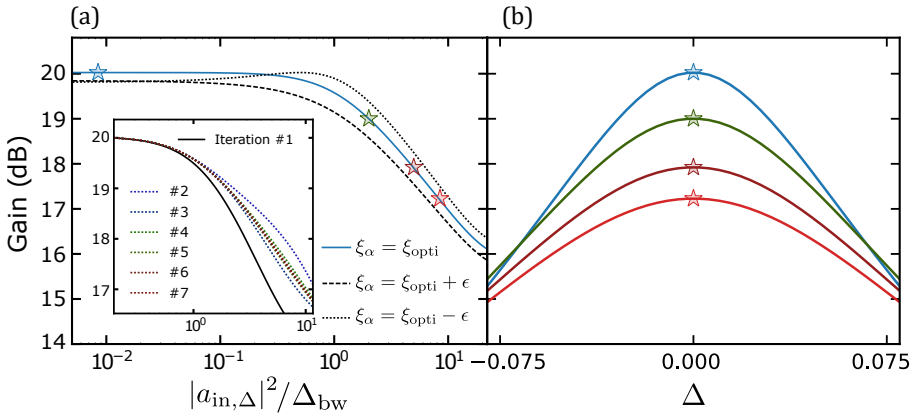

Figure 2.11 – **Effect of signal power on the maximum gain. (a)** Maximum gain vs. reduced input signal photon number. From a certain threshold, the maximum gain starts to drop. A slight detuning from the optimal pump point leads to different saturation power. **Inset:** gain compression when the number of signal photons inside the resonator is being iteratively computed six times. **(b)** Gain profile for a given set of optimal pump parameters and signal strength (δ^{opti}, ξ_α^{opti}, ξ_a).

Now that we can compute the pump photon number n inside the resonator when the input signal increases, we can infer the induced resonator shift and eventually the gain drop. The resonator is chosen weakly nonlinear $\kappa/|K| = 5 \times 10^3$. The signal gain for $\Delta = \Omega = 0$ as a function of the input signal photon per unit time $|a_{\text{in},\Delta}|^2$ and per unit instantaneous -3 dB bandwidth Δ_{bw} is shown in Fig. 2.11**(a)**. In blue, the pump is set optimally to obtain 20 dB of gain ($\delta^{\text{opti}} = -0.77$, $\xi_\alpha^{\text{opti}} = -0.16$) at very low power signal. We can quantify the saturation with the 1 dB compression point. It occurs when the input signal is in the order of few photon per unit time and bandwidth.

An interesting feature of saturation in Kerr-based amplifier is that it depends on the pump settings (δ, ξ_α). When they are a bit detuned from the optimal configuration, saturation point can actually increase or decrease. On the same figure,

we plot saturation for $\xi_\alpha < \xi^{\text{opti}}$ and $\xi_\alpha > \xi^{\text{opti}}$. In the former case, saturation occurs for larger signal. It happens because the pump is slightly detuned from the optimal frequency and the signal photons induce an extra shift, which compensates this detuning. In the latter case, it occurs for lower input signal because the signal-induced frequency shift adds to the initial detuning of the pump.

In the inset of Fig. 2.11**(a)**, we plot the saturation while we iteratively computed the intra-resonator signal field as explained in the previous section. For the initial setting, the saturation is over-estimated. We observe that as we iterate, the saturated gain converges towards a unique solution. After few iterations, we have an accurate solution. Naturally, saturation curves shown in the main panel are converged solution. In Fig. 2.11**(b)**, we plot gain profiles for different signal strengths. The gain is indeed reduced when the signal strength increases.

2.4.4 Pump depletion

Pump depletion describes the situation in which the amplification process has a non negligible effect on the pump power. Up to now, we have been considering the ideal case where the energy exchange between the signal and the pump happens in such a way that signal power does increase but the pump power is so large that the effect of amplification on it can be neglected (in that case, the pump is called **stiff**, see Section 1.2). When the input signal power is too high, the energy exchange between the signal and the pump becomes substantial for the pump, which leads to a power drop (or a depletion of its population) and to a gain drop of the amplifier. Although pump depletion exists in every amplifier, it can be neglected when the difference between the signal power and the pump power is large enough. This is in general the case with a Kerr-based amplifier. This is why to first order, only considering saturation from Kerr effect is reasonable. The study of saturation for even larger signal power would require to consider the actual pump depletion in the amplification process.

2.5 Implementation of a four wave mixing degenerate amplifier

In this section, we will show a way to implement such Kerr-based amplifier for circuit-QED purposes with a Josephson junction. First, we will shift from quantum optics formalism to quantum circuits formalism. Second, a calculation of the Josephson nonlinearity will be done and eventually we will show a way to reduce the Josephson nonlinearity for having a better dynamic range in the Josephson parametric amplifiers (JPA).

2.5.1 Circuit QED translation

As explained in Section 1.4, a Josephson junction (or a SQUID) can be modeled as a simple anharmonic LC circuit where the capacitance and linear inductance

are denoted C and L. The Hamiltonian of such a circuit reads:

$$\hat{H} = \frac{\hat{Q}^2}{2C} + E_{\mathrm{J}} \cos \frac{\hat{\Phi}}{\varphi_0}. \tag{2.46}$$

Where $\varphi_0 = \hbar/(2e)$ is the reduced magnetic flux quantum and $E_{\mathrm{J}} = \varphi_0^2/L$ is the Josephson potential (e is the elementary charge). We define the dimensionless operators $\hat{n} = \hat{Q}/2e$ and $\hat{\phi} = \hat{\Phi}/\varphi_0$. A direct analogy between a nonlinear resonator and a Josephson junction can be made with:

— the generalized flux $\hat{\Phi}$ is analogous to the position $\hat{X}$

— the charge $\hat{Q}$ is analogous to the momentum $\hat{Y}$

Just as momentum and position, charge and generalized flux are conjugate quantum operators, fulfilling the commutation relation $[\hat{\Phi}, \hat{Q}] = i\hbar$. To complete the analogy, these operators are written in terms of ladder operators:

$$\hat{\Phi} = \sqrt{\frac{\hbar}{2\omega_0 C}}(\hat{a} + \hat{a}^\dagger) = \varphi_{\mathrm{zpf}}(\hat{a} + \hat{a}^\dagger), \tag{2.47a}$$

$$\hat{Q} = -i\sqrt{\frac{\hbar\omega_0 C}{2}}(\hat{a} - \hat{a}^\dagger) = -iq_{\mathrm{zpf}}(\hat{a} - \hat{a}^\dagger), \tag{2.47b}$$

where $\omega_0 = 1/\sqrt{LC}$ is the self resonant angular frequency of the junction.

2.5.2 Fourth-order nonlinearity

Compared to transmon qubits [28], Josephson junctions used for JPAs are rather weakly nonlinear [73]. With this consideration in mind, we perform a development up to the fourth order of the cosine potential. The Hamiltonian is then written in term of ladder operators

$$\hat{H}_{\mathrm{jpa}} = E_{\mathrm{c}}\hat{n}^2 + \frac{E_{\mathrm{J}}}{2!}(\phi_{\mathrm{zpf}}(\hat{a}^\dagger + \hat{a}))^2 - \frac{E_{\mathrm{J}}}{4!}(\phi_{\mathrm{zpf}}(\hat{a}^\dagger + \hat{a}))^4. \tag{2.48}$$

Where $\phi_{\mathrm{zpf}} = \varphi_{\mathrm{zpf}}/\varphi_0$ is the reduced flux zero point fluctuations. The charging energy is defined as $E_{\mathrm{c}} = (2e)^2/2C$. We retrieve the standard form for the Hamiltonian:

$$\frac{\hat{H}_{\mathrm{jpa}}}{\hbar} = \omega_0 \hat{a}^\dagger \hat{a} + \frac{K}{2}(\hat{a}^\dagger + \hat{a})^4, \quad \text{where} \quad K = -\frac{2E_{\mathrm{J}}\phi_{\mathrm{zpf}}^4}{4!\,\hbar} = -\frac{E_{\mathrm{C}}}{24\hbar}. \tag{2.49}$$

From an engineering point of view, a single junction JPA displays only two degree of freedom (L and C); whereas an amplifier should meet at least three criteria: a working frequency that can be chosen, a large bandwidth and a high saturation point. For obvious reasons, the working frequency must be fixed by the

user. Thus it leaves one degree of freedom for two parameters. Since saturation is favorably dependent on the bandwidth (signal strength is proportional to K/κ in Eq. (2.43)), a large bandwidth is generally sought. However, in the next subsection we will see that the number of junctions constituting a JPA is a new degree of freedom, allowing for direct control over the Kerr coefficient K, and therefore a control over the saturation of the amplifier.

2.5.3 Josephson arrays

A solution commonly proposed to decrease K is to use arrays [32, 33, 72] of junctions. This will actually 'dilute' the nonlinearity. Even if adding N nonlinear elements instead of one in order to decrease this nonlinearity can appear a bit counter-intuitive, a first qualitative explanation is to recall that nonlinearity expresses itself more when larger powers are at stake. Now, a large phase drop $\Delta\phi$ across one junction or N smaller phase drops $\Delta\phi/N$ across N junctions will not lead to the same nonlinearity. In the latter, the 'effective' nonlinearity seen by each of the junction will be actually smaller. As a second semi-quantitative argument, we can say that the Josephson potential of an array is written $NE_{\mathrm{J}}\cos\frac{\hat{\phi}}{N}$, under the assumption that the phase-drop across the chain is equally divided across each junction- which is not entirely true. The potential is once again developed to the fourth order $NE_{\mathrm{J}}\cos\frac{\hat{\phi}}{N} = NE_{\mathrm{J}} - NE_{\mathrm{J}}\hat{\phi}^2/2N^2 + NE_{\mathrm{J}}\hat{\phi}^4/4!N^4$. The second term is simplified in $E_{\mathrm{J}}\hat{\phi}^2/2N$, and a new Josephson energy is defined as $E_{\mathrm{J}}^* = E_{\mathrm{J}}/N$. Considering that we want to keep the same resonance frequency, it leads to

$$\hbar\omega_0 = \sqrt{8E_{\mathrm{C}}E_{\mathrm{J}}} = \sqrt{8E_{\mathrm{C}}^*E_{\mathrm{J}}^*}, \tag{2.50}$$

this condition gives $E_{\mathrm{C}}^* = NE_{\mathrm{C}}$ and leads to $\phi_{\mathrm{zpf}}^* \propto (E_{\mathrm{C}}^*/E_{\mathrm{J}}^*)^{\frac{1}{4}} \propto N^{\frac{1}{2}}(E_{\mathrm{C}}/E_{\mathrm{J}})^{\frac{1}{4}} \sim N^{\frac{1}{2}}\phi_{\mathrm{zpf}}$. Now the new Kerr term K^* is :

$$\hbar K^* = \frac{NE_{\mathrm{J}}}{4!}\frac{{\phi_{\mathrm{zpf}}^*}^4}{N^4} = \frac{E_{\mathrm{J}}}{4!}\phi_{\mathrm{zpf}}^4\frac{1}{N} = \frac{\hbar K}{N}. \tag{2.51}$$

Thus with an array of N Josephson junctions, while keeping the same resonance frequency and under the assumption that each junction is equally phase-biased in the array, the non-linearity is divided by N compared to the single junction case. To obtain a more accurate value for the Kerr coefficient, we must be careful with the assumption that phase drops are constant all over the array. Indeed, a JPA is in most of the case a junction (or more) coupled to a microwave resonator, $\lambda/4$ or $\lambda/2$. However, phase drops are not constant throughout a distributed resonator, and these position dependent phase drops across each junction must be accounted for. To do so, we will develop a microscopic model taking into account the signal evolution site by site.

2.6 Josephson $\frac{\lambda}{4}$ resonator

This section aims to develop a model accounting for propagating effect in a short Josephson array. The goal is to study the array site by site and obtain its resonant frequencies. Then, following a standard procedure in microwave engineering [74], we will do a mapping between an effective nonlinear LC series oscillator and this nonlinear resonator (close to its resonance). A direct mapping of this effective circuit onto the model described Section 2.4 is possible.

2.6.1 Characterization of the array

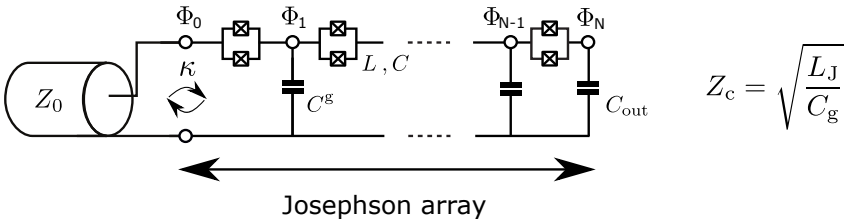

Figure 2.12 – **Electrical sketch of an array of Josephson junctions.** For frequencies below the plasma frequency, the characteristic impedance of the array is defined as $Z_c = \sqrt{L/C^g}$, which is greater than Z_0. This impedance mismatch settles the coupling rate κ between the environment and the array. The array is characterized by three microscopic elements: L, C and C^g. Φ_q is the flux between the q^{th} and $(q+1)^{\text{th}}$ junctions.

The idea is to consider the array itself as a resonator connected to a linear transmission line with a characteristic impedance Z_0. Therefore, the best suited model is to consider the array, as a succession of N identical junctions (L, C), each shunted to ground through a capacitance C^g (see Fig. 2.12). This short array can be seen as a short transmission line of characteristic impedance Z_c. Let us parameterize the array of junctions in order to infer the improvement in the saturation compared to a single junction JPA. The parameters are chosen with realistic values, close to sample that will be characterized in Chapter 6.

The junctions are modeled with the electrical parameters as in Chapter 1: a critical current density $j_c = 25\,\text{A}\,\text{cm}^{-2}$ and a surface capacitance $C = 0.045\,\text{fF}\,\mu\text{m}^{-2}$, while the junctions have a surface $A = 8.8\,\mu\text{m}^2$. Given the boundary conditions of the resonator ($\lambda/4$ resonator), the length of the array L_a reads:

$$L_a = Na = (2i+1)\lambda_i/4 \quad , \quad i \in [0, N-1]\,, \tag{2.52}$$

where a is the size of one junction (in the direction of signal propagation) and i is the mode index. In order to consider the array as a succession of lumped element,

we must have $a << \lambda$. We set $N = L_a/a = 80$. Furthermore, in order to have propagation in the array, the signal frequency ω_s must be smaller than the plasma frequency $\omega_\Pi = (LC)^{-1/2}$ (as defined in Section 1.4). If we consider the signal frequency close to the first resonance ($L_a = \lambda_0/4$), the signal angular frequency is defined as $\omega_s \approx \omega_0 = 2\pi v_\varphi/\lambda_0$ and the condition $\omega_0 < \omega_\Pi$ can be translated in:

$$\frac{C}{C^g} < \left(\frac{2N}{\pi}\right)^2 = 2600, \tag{2.53}$$

where $v_\phi = a/\sqrt{LC^g}$ is the wave velocity. We set the ground capacitance $C^g = 0.25\,\mathrm{fF}$ such that $C/C^g = 1600$. In order to be safer and further away from the plasma frequency, we add a big lumped capacitive element to the array to effectively decrease the resonant frequencies ($\omega \propto C^{-1/2}$). For the sake of design simplicity, this lumped capacitance C_{out} is put at the end of the array (see Fig. 2.12) and set as $C_{out}/C^g = 100$.

Let us check the validity of these parameters. First, we expect to have an external quality factor Q_e between 10 and 20 to get a decent bandwidth. Near resonance, we expect the resonator to behave as a series LC circuit with an inductance L_s. In that case, the external quality factor is defined as [74]:

$$Q_e = \frac{\omega_s L_s}{Z_0}, \tag{2.54}$$

where $L_s = 80 \times L$ as a first rough estimation. We find $Q_e \approx 10$ which is consistent with what we expect. Second, these parameters lead to a ratio $E_J/E_c = 5500$. The junctions are weakly nonlinear in the deep transmon regime, and are therefore well described by the above-mentioned formalism.

2.6.2 Eigenvalues of the array

To get the resonant frequencies of the array, we need to compute the eigen values of the system. We follow the ongoing parametrization of the system by choosing the generalized flux Φ as the best variable to describe the system. We denote Φ_q the flux between the q^{th} and $(q+1)^{th}$ junction as shown in Fig. 2.12 ($\Phi_0 = 0$ since the array is galvanically connected to the environment). Before introducing the nonlinearity as a perturbation in the array, we linearly describe the array by calculating the energy of the system via the Lagrangian, only by considering junctions as linear LC oscillators [75]:

$$\mathscr{L} = \sum_{q=1}^{N-1}\left(\frac{C^g}{2}\dot{\Phi}_q^2\right) + \frac{C_{out}}{2}\dot{\Phi}_N^2 + \frac{C}{2}\sum_{q=0}^{N-1}(\dot{\Phi}_{q+1} - \dot{\Phi}_q)^2 - \frac{1}{2L}\sum_{q=0}^{N-1}(\Phi_{q+1} - \Phi_q)^2. \tag{2.55}$$

To have a better grasp on the linear behavior of such system, the best is to write it as N coupled equations. Eventually the Lagrangian expressed in Eq. (2.55) is

written in a matrix representation:

$$\mathscr{L} = \frac{1}{2}\dot{\mathbf{\Phi}}^T \hat{C} \dot{\mathbf{\Phi}} - \frac{1}{2}\mathbf{\Phi}^T \hat{L}^{-1} \mathbf{\Phi}. \tag{2.56}$$

Where $\mathbf{\Phi}$ and $\dot{\mathbf{\Phi}}$ are vectors of size N and their q^{th} entry are respectively equal to Φ_q and $\dot{\Phi}_q$. The $\hat{C}$ and $\hat{L}^{-1}$ matrices are tri-diagonal matrices:

$$\hat{C} = C \begin{pmatrix} 2 & -1 & 0 & \cdots & \cdots & \cdots & 0 \\ -1 & 2 & -1 & 0 & \cdots & \cdots & 0 \\ 0 & -1 & 2 & -1 & 0 & \cdots & 0 \\ \vdots & 0 & \ddots & \ddots & \ddots & 0 & 0 \\ \vdots & \vdots & 0 & \ddots & \ddots & \ddots & 0 \\ \vdots & \vdots & \vdots & \vdots & \ddots & \ddots & -1 \\ 0 & 0 & 0 & 0 & 0 & -1 & 1 \end{pmatrix} + C^{\text{g}} \begin{pmatrix} 1 & 0 & 0 & \cdots & \cdots & \cdots & 0 \\ 0 & 1 & 0 & 0 & \cdots & \cdots & 0 \\ 0 & 0 & 1 & 0 & 0 & \cdots & 0 \\ \vdots & 0 & \ddots & \ddots & \ddots & 0 & 0 \\ \vdots & \vdots & 0 & \ddots & \ddots & \ddots & 0 \\ \vdots & \vdots & \vdots & \vdots & \ddots & \ddots & 0 \\ 0 & 0 & 0 & 0 & 0 & 0 & \frac{C_{\text{out}}}{C^{\text{g}}} \end{pmatrix}$$

$$\hat{L}^{-1} = \frac{1}{L} \begin{pmatrix} 2 & -1 & 0 & \cdots & \cdots & \cdots & 0 \\ -1 & 2 & -1 & 0 & \cdots & \cdots & 0 \\ 0 & -1 & 2 & -1 & 0 & \cdots & 0 \\ \vdots & 0 & \ddots & \ddots & \ddots & 0 & 0 \\ \vdots & \vdots & 0 & \ddots & \ddots & \ddots & 0 \\ \vdots & \vdots & \vdots & \vdots & \ddots & \ddots & -1 \\ 0 & 0 & 0 & 0 & 0 & -1 & 1 \end{pmatrix}$$

2.6.3 Eigenmodes

In previous work on Josephson junctions arrays, it has been demonstrated [76] that from the two previous matrices $\hat{C}$ and $\hat{L}^{-1}$, the matrix Ω^2 can be defined as:

$$\hat{\Omega}^2 = \hat{C}^{-1}\hat{L}^{-1}, \tag{2.57a}$$

$$\hat{\Omega}^2 \psi_i = \omega_i^2 \psi_i, \quad i \in [0, N-1], \tag{2.57b}$$

where ω_i^2 and ψ_i are the i^{th} eigen values and vectors of $\hat{\Omega}^2$. $\omega_i/2\pi$ and ψ_i define respectively the resonant frequency and the wave profile of each mode i of the

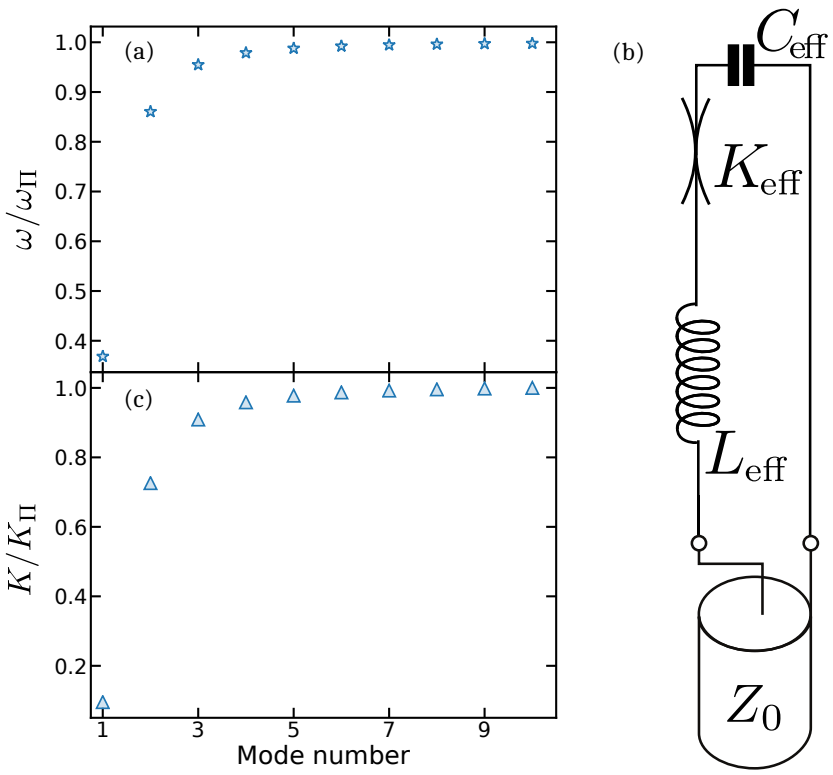

Figure 2.13 – **JPA as a $\frac{\lambda}{4}$ resonator. (a)** Resonant frequencies and **(c)** effective self-Kerr nonlinearities as a function of the modes number. **(b)** Mapping of the array JPA onto a nonlinear LC oscillator.

chain. In Fig. 2.13.**(a)**, we plot ω_i/ω_Π as a function of the mode number. The first resonance is around 30% of the plasma frequency. Given the relatively small number of junctions within the array, the resonant frequencies reach the plasma frequency from mode number $i \approx 5$. No resonance is allowed above it. This is true for any uniform array, no matter its length nor its number of junctions[c] . The computation of the eigen vectors allows the definition of an effective capacitance $C_{\text{eff},i}$ and an effective inductance $L_{\text{eff},i}$ for each mode i:

$$C_{\text{eff},i} = \vec{\psi}_i^T \hat{C} \vec{\psi}_i, \tag{2.58a}$$

$$L_{\text{eff},i}^{-1} = \vec{\psi}_i^T \hat{L}^{-1} \vec{\psi}_i. \tag{2.58b}$$

[c] In a periodic lattice, there can be a second 'optical' branch above the plasma frequency. Also, a simple defect in a uniform array can create a localized state above the plasma frequency.

As explained, we can do a standard mapping from a $\lambda/4$ resonator to an effective series LC circuit ($L_{\text{eff,i}}$ and $C_{\text{eff,i}}$ in Fig. 2.13.**b**) close to its resonance. Moreover, we can define an effective external quality factor Q_{eff} and coupling rate κ_{eff}:

$$Q_{\text{eff}} = \frac{\sqrt{L_{\text{eff}}/C_{\text{eff}}}}{Z_0}, \tag{2.59a}$$

$$\kappa_{\text{eff}} = \frac{\omega_{\text{eff}}}{Q_{\text{eff}}}. \tag{2.59b}$$

This would end the linear mapping between the array and the LC oscillator. However, as convenient it is to model the capacitive effect between the junction and the ground as a single capacitance C^{g} while giving appropriate results, it is not the most accurate way to do it. Actually, a better way to tackle this issue is to use the remote ground model [77]. The next subsection is devoted to its general description.

2.6.4 Remote ground model

In this section, we describe quickly its mathematical treatment as we will use it to treat experimental data in Chapter 7, but a complete treatment can be found in [78]. As it will be shown in Chapter 4 focusing on the the fabrication technique of Josephson arrays, the actual distance between the array and the ground plane is comparable or greater than the modes wavelength λ. Therefore, the screening of the charges by the ground plane cannot be considered as local. Capacitive effects between junctions must be accounted for via the long-range part of the Coulomb interaction. The actual Lagrangian of the system must be written as:

$$\begin{aligned}\mathcal{L} = &\sum_{n=0}^{N-1} \frac{C}{2}(\dot{\Phi}_{n+1} - \dot{\Phi}_n)^2 - \sum_{n=0}^{N-1} \frac{1}{2L}(\Phi_{n+1} - \Phi_n)^2 \\ &+ \sum_{n=1}^{N-1} \frac{C^{\text{g}}_{nn}}{2}\dot{\Phi}_n^2 + \sum_{n=1}^{N-1}\sum_{q\neq n}^{N-1} \frac{C^{\text{g}}_{nq}}{2}(\dot{\Phi}_n^2 - \dot{\Phi}_q^2) + \frac{C_{\text{out}}}{2}\dot{\Phi}_N^2.\end{aligned} \tag{2.60}$$

Where the elements C^{g}_{nq} and C^{g}_{nn} account for the long range interactions between the charges on the junctions between site n and site q. All these coefficients are part of a generalized ground capacitance matrix $\hat{C}_{\text{remote}}$. An analytical expression of these coefficients is found by expressing the voltage at site n as a function of the charge $\tilde{Q}_n$ and the effective dielectric constant of the substrate $\tilde{\epsilon}$ [74]:

$$V_n = \frac{2\tilde{Q}_n}{4\pi\epsilon_0(1+\epsilon_r)} \sum_{n'} \left[\frac{1}{|n-q|a + \delta_{nq} a_0/2} - \sum_{j=1}^{j_{max}} \frac{\tilde{\epsilon}_j}{\sqrt{(n-q)^2 a^2 + (2jd)^2}} \right], \tag{2.61a}$$

$$\text{with} \quad \tilde{\epsilon}_j = \frac{2\epsilon(1-\epsilon_r)^{j-1}}{(1+\epsilon_r)^j}. \tag{2.61b}$$

Where ϵ_r is the substrate relative permittivity, d its thickness, δ_{nq} the Kroenecker symbol and j_{max} the number of neighbors junctions taken into account in this long-range interaction. Finally, a_0 is a fit parameter such that $a_0 \approx a$ and it prevents Eq. (2.61a) from diverging when n=i. We eventually build $\hat{C}^{-1}_{\text{remote}}$, where each coefficient reads:

$$(C^g_{nq})^{-1} = \frac{1}{2\pi\epsilon_0(1+\epsilon_r)} \left[\frac{1}{|n-q|a + \delta_{nq} a_0/2} - \sum_{j=1}^{j_{max}} \frac{\tilde{\epsilon}_j}{\sqrt{(n-q)^2 a^2 + (2jd)^2}} \right]. \tag{2.62}$$

Thanks to this generalized ground capacitance matrix, a more accurate evaluation of the effective parameters can be performed, in better agreement with the experimental results. One drawback of this model is its exponential complexity when the number of junctions increases. However, if it stays low (below ~ 100), this model is still convenient to fit the experimental data.

2.6.5 Nonlinearity as a perturbation

To finalize the mapping between the array and the nonlinear LC series oscillator, we must derive an effective nonlinearity $K_{\text{eff,i}}$ of the i^{th} mode. The procedure is the following [76]: from the Lagrangian $\mathcal{L}$ of the array, the Hamiltonian H_{array} is obtained by performing the Legendre transformation ($H_{\text{array}} = Q^T\dot{\Phi} - \mathcal{L}$). From this linear Hamiltonian, the nonlinearity is added as a perturbation. Using the RWA, the array Hamiltonian reads:

$$\hat{H} = \sum_i \hbar\omega_i \hat{a}_i^\dagger \hat{a}_i - \sum_i \frac{\hbar}{2} K_{ii} \hat{a}_i^\dagger \hat{a}_i \hat{a}_i^\dagger \hat{a}_i - \sum_{i,j} \frac{\hbar}{2} K_{ij} \hat{a}_i^\dagger \hat{a}_i a_j^\dagger \hat{a}_j, \tag{2.63}$$

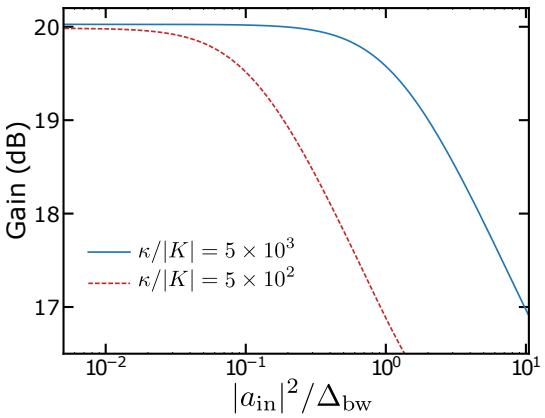

Figure 2.14 – **Maximum gain as function of input signal power.** We observe an improvement in the dynamic range when the ratio $\kappa/|K|$ is increased. These ratio are taken for the same bandwidth κ. The values of $|K|$ are calculated with Eq. (2.64a).

where K_{ii} and K_{ij} are the self and cross Kerr coefficients, respectively:

$$K_{ii} = \frac{2\hbar\pi^4 E_J \eta_{iiii}}{\Phi_0^4 C^2 \omega_i^2}, \tag{2.64a}$$

$$K_{ij} = \frac{4\hbar\pi^4 E_J \eta_{iijj}}{\Phi_0^4 C^2 \omega_i \omega_j}. \tag{2.64b}$$

η_{iiii} takes into account the spatial variation of the phase across the chain for the i^{th} mode. Given that η_{iiii} depends only on circuit parameters of the chain, the Kerr non-linearities of the modes are fully predictable. In Fig. 2.13**(c)**, we plot K_{ii}/K_Π for 10 modes, where K_Π is the self Kerr coefficient of the last mode. We see that the self Kerr increases as the frequency increases. In our goal to have the lowest nonlinearity working at the lowest resonant frequency is the best choice. In this example, the first mode's self Kerr coefficient (denoted as K_{eff}) is about 10% of K_Π.

2.6.6 QLE with an effective mode

Now that we can fully described the junction-based $\lambda/4$ as a nonlinear LC series (Fig. 2.13**(b)**) characterized by ω_{eff}, κ_{eff} and K_{eff}, we can predict its amplifier behavior. From the study performed in Section 2.4, we know that we exactly need the resonance frequency $\omega_0/2\pi$, the coupling rate κ and the nonlinearity K to have its power gain and its saturation point. We can compare saturation in a JPA with a ratio κ/K_Π and a ratio κ/K_1, where K_1 is the self-Kerr coefficient

of the first mode array JPA described in the last section. In Fig. 2.14, we plot the saturation ($G_{\max}$ vs the input signal power) for these two different ratios κ/K. An enhancement in the saturation of a factor 10 comes from that $K_1/K_\Pi = 10\%$.

This observation closes this chapter dedicated on resonant Josephson parametric amplifiers. The core results are that a Kerr-based amplifier can see its dynamic range increased by decreasing its effective nonlinearity. A solution given in this chapter to minimize this nonlinearity is to dilute it using an array of Josephson junctions.

Periodic structure in a traveling-wave parametric amplifier

3

Contents

Link back to Table of contents →

The previous chapter was dedicated to parametric interactions between a pump and a signal in a nonlinear resonant cavity. Resonant cavities for signal amplification are a double-edged solution: they increase drastically the interaction time between the pump and the signal via the nonlinearity but lead to limited instantaneous $-3\,\mathrm{dB}$ bandwidths Δ_{bw}. This is because standard resonant parametric amplification processes must in general satisfy the gain-bandwidth product (see Eq. (2.33)). Some exceptions exist though, *e.g.* the amplification scheme involving reservoir engineering to generate a dissipative amplification process, going beyond the standard gain-bandwidth product [79]. For stability purposes, the bare cavity bandwidth must be equal *or smaller* than a tenth [30] of the signal frequency ($Q_{\mathrm{e}} > 10$). When an amplifier is pumped to reach 20 dB power gain, standard gain-bandwidth imposes that Δ_{bw} decreases to one hundredth of the signal frequency. This is of course not sustainable in the contemporary paradigm of scalability and frequency multiplexed readout in quantum computing, for instance. Throughout intense efforts to escape from the gain-bandwidth product, traveling-wave amplifiers is a successful implementation of the circuit-QED community to overcome it by using impedance engineering. One must wait until 2012 to see the first experimental realization of a superconducting traveling-wave (TW) amplifiers fabricated with high-kinetic inductance superconductors [45] and until 2015 for the first implementation of Josephson-based TW amplifiers [46, 47]. In that case, gain-bandwidth product does not hold anymore. These amplifiers are major achievements, both technically and for their performances – 20 dB gain with 3 GHz bandwidth near the standard quantum limit. However, the underlying idea of using a transmissive, nonlinear medium to get a continuous flow of photons undergoing four wave mixing processes is not, strictly speaking, new. This originally comes from the field of nonlinear fiber optics [55]. The first section will be an introduction to TW amplifier through the prism of nonlinear optics. Following sections will be about parametric amplification in Josephson TW parametric amplifiers with a particular focus on their main issues: **phase matching**; and how we corrected it thanks to periodic structures.

3.1 Traveling-wave amplifiers with nonlinear fiber optics

In Josephson TW parametric amplifiers and nonlinear optical fibers (NOFs) alike, the interaction time between the signal and the nonlinearity is kept high without having to make use of resonant interactions because the signal travels in a medium long enough (see Fig. 3.1). As we saw in Section 2.4.1, in an optical nonlinear medium the polarization $\mathbf{P}(x, y, z, t)$ is expressed as a polynomial tensor product of the electrical field $\mathbf{E}$(x,y,z,t). In this subsection, we concluded that Josephson junctions are analogous to isotropic nonlinear media; therefore, we study NOFs where the second order nonlinearity $\chi^{(2)}$ vanishes, leading to a $\chi^{(3)}$ nonlinear medium whose elementary amplification mechanism is a **parametric four wave mixing process**, studied thoroughly in Chapter 2. In principle, if we extend what we studied in 0D (point like nonlinearity) to distributed 1D nonlinear medium, there should not be any bandwidth anymore: as long as the signal can propagate,

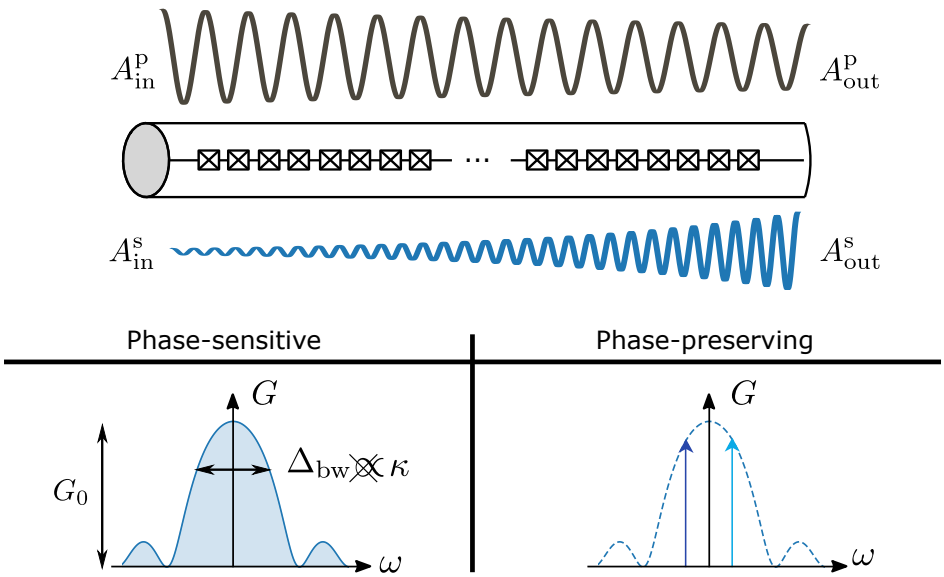

Figure 3.1 – **Schematic of a traveling-wave (TW) amplifier.** The signal is amplified along the nonlinear transmission line. It is co-propagating with the pump, whose amplitude decreases since there is energy exchange between the pump and the signal (Note: this effect is exaggerated for pedagogical purpose). However, most of the time, this effect is neglected and the undepleted pump assumption will be made. A TW amplifier does not have a bandwidth Δ_{bw} limited by resonant effects. It can be operated as a phase-sensitive or as a phase-preserving amplifier.

it should get amplified, no matter the frequency detuning between the pump and the signal. This naive approach is erroneous as we must take into account phase propagation and therefore phase mismatch between the pump and the signal during their propagation due to (i) power dependence of the phase velocity in nonlinear media and (ii) that there is always some dispersion in any medium. To get an analytical expression of the gain and the bandwidth in NOF, we start by studying the dynamics of the electric field in such medium. To simplify the calculation, we study the case where $\mathbf{E}(x, z, t)$ is linearly polarized along the x-axis and propagates along the z-axis. Moreover, we consider a process mixing three continuous waves (CW): the pump (ω_{p}), the signal (ω_{s}) and the idler (ω_{i}). In the terminology of quantum optics, the latter two are also called Stokes and anti-Stokes fields, respectively. The total electric field is modeled as the sum of

the three fields:

$$\mathbf{E}(x,z,t) = \frac{\mathbf{u}_\mathrm{x}}{2} \sum_{\mathrm{j}=\{\mathrm{p,s,i}\}} E_\mathrm{j}(x,z) e^{i(k_\mathrm{j} z - \omega_\mathrm{j} t)} + \mathrm{c.c.}, \tag{3.1a}$$

$$k_\mathrm{j} = \frac{n_\mathrm{j}}{c}\omega_\mathrm{j} \quad , \quad \mathrm{j} = \{\mathrm{p,s,i}\}, \tag{3.1b}$$

where $\mathbf{u}_\mathrm{x}$ is the polarization unit vector (along the x-axis), k_j is the propagation constant, $\omega_\mathrm{j}/2\pi$ is the frequency and n_j the refractive index of mode $\mathrm{j}=\{\mathrm{p,s,i}\}$, while c is the speed of light in vacuum. Each electric field amplitude E_j is decomposed in two parts: its spatial distribution $F_\mathrm{j}(x)$ and its amplitude $A_\mathrm{j}(z)$ such that $E_\mathrm{j}(x,z) = F_\mathrm{j}(x)A_\mathrm{j}(z)$. We make the standard assumptions that (i) the pump field is much more intense than the other fields ($A_\mathrm{s}, A_\mathrm{i} \ll A_\mathrm{p}$) and (ii) that the pump stays undepleted during the whole amplification process. From the Helmholtz equation and after some steps [55], a set of three coupled equations can be written as:

$$\frac{\mathrm{d}A_\mathrm{p}}{\mathrm{d}z} = \frac{i n_\mathrm{nl}\omega_\mathrm{p}}{c}\left[\left(f_\mathrm{pp}|A_\mathrm{p}|^2 + 2\sum_{\mathrm{j}=\{\mathrm{p,s,i}\}} f_\mathrm{pj}|A_\mathrm{j}|^2\right)A_\mathrm{p} + 2f_\mathrm{psi}A_\mathrm{p}^* A_\mathrm{s} A_\mathrm{i} e^{-i\Delta k_\mathrm{l} z}\right], \tag{3.2a}$$

$$\frac{\mathrm{d}A_\mathrm{s}}{\mathrm{d}z} = \frac{i n_\mathrm{nl}\omega_\mathrm{s}}{c}\left[\left(f_\mathrm{ss}|A_\mathrm{s}|^2 + 2\sum_{\mathrm{j}=\{\mathrm{p,p,i}\}} f_\mathrm{sj}|A_\mathrm{j}|^2\right)A_\mathrm{s} + 2f_\mathrm{spi}A_\mathrm{p}^2 A_\mathrm{i}^* e^{i\Delta k_\mathrm{l} z}\right], \tag{3.2b}$$

$$\frac{\mathrm{d}A_\mathrm{i}}{\mathrm{d}z} = \frac{i n_\mathrm{nl}\omega_\mathrm{i}}{c}\left[\left(f_\mathrm{ii}|A_\mathrm{i}|^2 + 2\sum_{\mathrm{j}=\{\mathrm{p,p,s}\}} f_\mathrm{ij}|A_\mathrm{j}|^2\right)A_\mathrm{i} + 2f_\mathrm{ips}A_\mathrm{p}^2 A_\mathrm{s}^* e^{i\Delta k_\mathrm{l} z}\right]. \tag{3.2c}$$

$\Delta k_\mathrm{l} = 2k_\mathrm{p} - k_\mathrm{s} - k_\mathrm{i}$ is the *linear* phase mismatch and n_nl is the same nonlinear refractive index as defined in Section 2.4.1 in $\mathrm{m^2W^{-1}}$. f is the overlap integral between the spatial distribution of the fiber modes; for example, f_spi is the overlap between the signal, pump and idler. For the sake of simplicity, it is considered the same for any of the modes and it is taken as f. From this consideration, f can be factorized and we define the nonlinearity for mode j as:

$$\gamma_\mathrm{j} = \frac{n_\mathrm{nl}\omega_\mathrm{j} f}{c}. \tag{3.3}$$

It can be seen as constant if the difference in frequencies are considered small enough. The first equation for the pump Eq. (3.2a) can be simplified under the strong pump assumption. It can be simplified to

$$\frac{\mathrm{d}A_\mathrm{p}}{\mathrm{d}z} = 3i\gamma|A_\mathrm{p}|^2 A_\mathrm{p}, \quad \text{leading to:} \quad A_\mathrm{p}(z) = A_\mathrm{p0}e^{3i\gamma P_0 z}, \tag{3.4}$$

where $P_0 = |A_\mathrm{p}(z=0)|^2 = |A_\mathrm{p}(z)|^2$ is the incident pump power. The nonlinear phase $3\gamma P_0 z$ is the self-phase modulation (SPM) of the pump. With this compact expression of the pump amplitude and the strong pump approximation, Eqs. (3.2b) and (3.2c) are simplified and we deal with two coupled equations for the dynamics of the signal and idler amplitudes:

$$\frac{\mathrm{d}A_\mathrm{s}}{\mathrm{d}z} = 2i\gamma\left[2P_0 A_\mathrm{s} + A_\mathrm{p0}^2 e^{i\theta z} A_\mathrm{i}^*\right], \tag{3.5a}$$

$$\frac{\mathrm{d}A_\mathrm{i}}{\mathrm{d}z} = 2i\gamma\left[2P_0 A_\mathrm{i} + A_\mathrm{p0}^2 e^{i\theta z} A_\mathrm{s}^*\right], \tag{3.5b}$$

where θ is the nonlinear phase mismatch:

$$\theta = 2(k_\mathrm{p} + \underbrace{3\gamma P_0}_{\text{SPM}}) - k_\mathrm{s} - k_\mathrm{i} = \underbrace{2k_\mathrm{p} - k_\mathrm{s} - k_\mathrm{i}}_{\Delta k_\mathrm{l}} + 6\gamma P_0, \tag{3.6}$$

and is only considering the SPM. To simplify Eqs. (3.5a) and (3.5b) and cancel the first term on their right-hand sides, we introduce the auxiliary $a_\mathrm{j}(z) = A_\mathrm{j}(z)\exp(-4i\gamma P_0 z)$ with j={s,i}. The nonlinear phase shift $4\gamma P_0 z$ is the cross-phase modulation (XPM) produced by the pump on the signal and the idler modes. A difference between SPM and XPM is generic for $\chi^{(3)}$ nonlinear media and is harmful for amplification as we will see later on. The two coupled equations Eqs. (3.5a) and (3.5b) can be written as:

$$\frac{\mathrm{d}a_\mathrm{s}(z)}{\mathrm{d}z} = 2i\gamma A_\mathrm{p0}^2 e^{i\Delta k z} a_\mathrm{i}^*(z), \tag{3.7a}$$

$$\frac{\mathrm{d}a_\mathrm{i}(z)}{\mathrm{d}z} = 2i\gamma A_\mathrm{p0}^2 e^{i\Delta k z} a_\mathrm{s}^*(z). \tag{3.7b}$$

We finally have the total phase mismatch considering pump SPM and signal/idler XPM:

$$\Delta k = \theta - \underbrace{4\gamma P_0}_{\text{XPM signal}} - \underbrace{4\gamma P_0}_{\text{XPM idler}} = 2k_\mathrm{p} - k_\mathrm{s} - k_\mathrm{i} - 2\gamma P_0. \tag{3.8}$$

We clearly see that this slight difference between SPM and XPM is creating a total phase mismatch which grows always larger for higher input pump power. Moreover by exploiting the boundary conditions and assuming that signal and idler are sent from z=0, and for $t = 0$, $a_\mathrm{i}(0) = 0$, we solve Eqs. (3.7a) and (3.7b) (we go particularly fast for this introduction, but this will be explained in the next section for the resolution with Josephson arrays). The signal power $P_\mathrm{s}(z) = |a_\mathrm{s}(z)|^2$ reads:

$$P_{\mathrm{s}}(z) = P_{\mathrm{s}}(0)\left[1 + \left(1 + \left(\frac{\Delta k}{2g}\right)^2\right)\sinh^2(gz)\right], \tag{3.9a}$$

$$g = \sqrt{(\gamma P_0)^2 - \left(\frac{\Delta k}{2}\right)^2}, \tag{3.9b}$$

where g is the parametric gain coefficient. Although a series of assumptions have been made, this expression of the signal power after a distance z is particularly insightful. It shows that total phase mismatch Δk is harmful for signal power gain and it should be kept close to 0. More precisely, g must stay real to expect exponential gain with respect to the distance z. Once more, phase modulation from $\chi^{(3)}$ nonlinearity is harming the amplification performances. Now, if we consider that the signal field traveled a distance $z = L$ in the NOF, we define the signal power gain as:

$$G_{\mathrm{s}} = P_{\mathrm{s}}(L)/P_{\mathrm{s}}(0) = 1 + (\gamma P_0/g)^2 \sinh^2(gL). \tag{3.10}$$

Two limit cases are worth being studied. In the case where no specific engineering is done on phase matching, $\Delta k >> \gamma P_0$ and the parametric gain g becomes imaginary $g = i|\Delta k/2|$. Therefore, the signal gain reads:

$$G_s \approx 1 + (\gamma P_0 L)^2 \frac{\sin^2(\Delta k L/2)}{(\Delta k L/2)^2}, \tag{3.11}$$

which is only a **quadratic** function of $P_0 L$. Otherwise, if the phase mismatch is kept low ($\Delta k << \gamma P_0$), g is real and the signal gain reads:

$$G_s \sim e^{2\gamma P_0 L}, \tag{3.12}$$

which is an **exponential** function of $P_0 L$. This is the core result of this section: an important engineering work to keep phase mismatch low must be done with amplifiers based on a $\chi^{(3)}$ nonlinearity to ensure large gain. Therefore, Josephson junctions being $\chi^{(3)}$-like nonlinearities, same issues will arise in Josephson-based TW amplifiers. Regarding the $-3\,\mathrm{dB}$ bandwidth Δ_{bw}, it also depends on the total phase mismatch between the pump and signal/idler and solving phase mismatch issues will also increase the maximum bandwidth. However, even in the ideal case where $\Delta k_{\mathrm{nl}} \approx 0$, there will always be some residual linear phase mismatch Δk_{l} due to the dispersion of the medium itself. Eventually, if Δk_{l} is modeled as $\Delta k_{\mathrm{l}} \approx \alpha|\omega_{\mathrm{p}} - \omega_{\mathrm{s}}|^2$ (α in $\mathrm{s}^2\,\mathrm{m}^{-1}$), the bandwidth is given by:

$$\kappa \approx \frac{\pi}{L}(2\gamma P_0|\alpha|)^{-1/2}. \tag{3.13}$$

The product $\gamma|\alpha|$ must be minimize in order to maximize the amplifier bandwidth.

This result closes this short review on NOFs used as amplifiers. The next sections will be devoted to the study of Josephson TW parametric amplifiers (JTWPA).

3.2 Traveling-wave amplification in a Josephson metamaterial

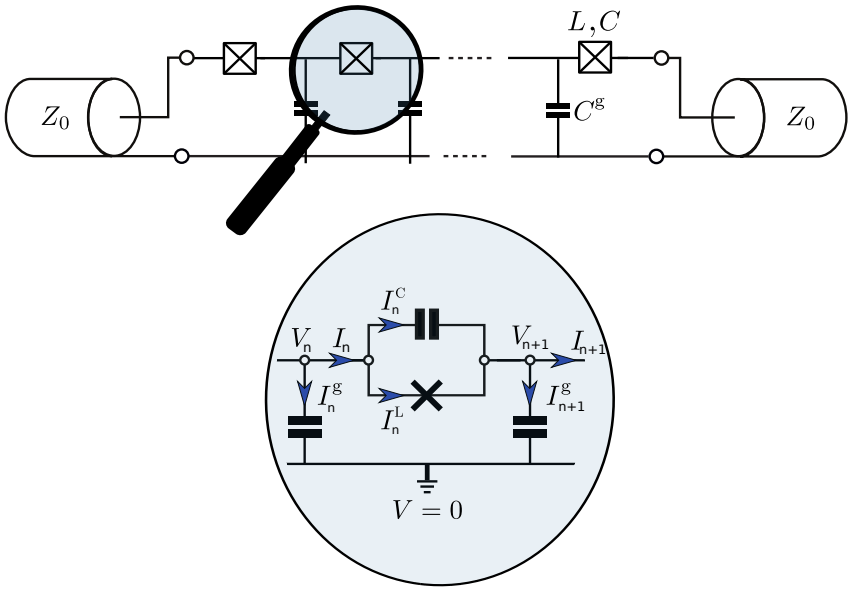

Figure 3.2 – **Electrical scheme of a Josephson TWPA.** The array of Josephson junctions (L, C) is galvanically connected to a $Z_0 = 50\,\Omega$ impedance environment. Each junction is grounded via C^g. **Zoom-in.** The current flowing through the n^{th} junction is denoted I_n and the voltage at the n^{th} island is denoted V_n. Other currents are defined in the main text.

3.2.1 Impedance matched array

The first issue to tackle with traveling-wave amplifiers is a perfect impedance matching between the array of Josephson junctions and the low impedance environment (see Fig. 3.2). The environment has a standard characteristic impedance $Z_0 = 50\,\Omega$. However, a Josephson metamaterial displays a very large inductance per unit length, in the order of 500 pH per square. To reach an impedance as low as $50\,\Omega$, the large inductance must be compensated with a large capacitance per unit length. From a microwave engineering perspective this is not a trivial task. This issue will be thoroughly addressed in Chapter 4, dedicated to the fabrication of our JTWPA.

3.2.2 Configuration of traveling-wave structures

Let us consider an array of $N = 2000$ identical junctions of area $A = 8.8\,\mu\text{m}^2$ and critical current density $j_c = 25\,\text{A}\,\text{cm}^{-2}$. We keep the same notations for the microscopic elements of the array as in the previous chapter: L, C and C^g. Their numerical values are $L = 150\,\text{pH}$, $C = 396\,\text{fF}$ and $C^g = L/50^2 = 59.8\,\text{fF}$. Until the end of the chapter, frequencies are expressed in gigahertz. We parameterize the array as in Fig. 3.2 following the approach from [80]: each junction is seen as an elementary cell of size a where the current I_{n-1}, coming from the previous cell, follows the conservation law:

$$I_{n-1} = I_n + I_n^g \quad , \quad I_n = I_n^L + I_n^C, \tag{3.14}$$

where I_n^L and I_n^C are the currents flowing through the Josephson inductance and the Josephson capacitance, respectively, and I_n^g the current flowing to the ground through the ground capacitance. Let us express all these currents as a function of Φ_n, the generalized flux at node n as defined in Section 2.6, which is still well suited to parameterize such arrays of junctions. We recall that:

$$V_n = \frac{\mathrm{d}\Phi_n}{\mathrm{d}t}, \tag{3.15}$$

where V_n is the voltage at the n^{th} island as shown in Fig. 3.2. The Josephson relation reads:

$$I_n^L = I_c \sin\left(\frac{\Phi_n - \Phi_{n+1}}{\varphi_0}\right), \tag{3.16}$$

with I_c the junction critical current. By taking the temporal derivative of the Josephson relation Eq. (3.16), we have:

$$\begin{aligned}
\frac{\mathrm{d}\left(\Phi_n - \Phi_{n+1}\right)}{\mathrm{d}t} &= L\left(1 - \left(\frac{I_n^L}{I_c}\right)^2\right)^{-\frac{1}{2}} \frac{\mathrm{d}I_n^L}{\mathrm{d}t} \\
&\approx L\left(1 + \frac{1}{2}\left(\frac{I_n^L}{I_c}\right)^2\right)\frac{\mathrm{d}I_n^L}{\mathrm{d}t} + o\left(\frac{I_n^L}{I_c}\right) \\
&= L\frac{\mathrm{d}I_n^L}{\mathrm{d}t} + \frac{L}{6I_c^2}\frac{\mathrm{d}\left(I_n^L\right)^3}{\mathrm{d}t}.
\end{aligned} \tag{3.17}$$

As usual, the nonlinearity is considered weak enough as the ratio I_n^L/I_c is much smaller than one. We integrate the previous relation and we obtain:

$$\Phi_{n+1} - \Phi_n = -LI_n^L - \frac{L}{6I_c^2}\left(I_n^L\right)^3. \tag{3.18}$$

The nonlinear part is considered very small. At first order, we have the standard current phase relation for an inductor:

$$I_n^{\mathrm{L}} \approx -\frac{1}{L}\left(\Phi_{n+1} - \Phi_n\right). \tag{3.19}$$

Next order, we have the current phase relation for the Josephson current:

$$I_n^{\mathrm{L}} \approx -\frac{1}{L}\left(\Phi_{n+1} - \Phi_n\right) + \frac{1}{6I_c^2 L^3}\left(\Phi_{n+1} - \Phi_n\right)^3, \tag{3.20}$$

the current in the Josephson capacitor C reads:

$$I_n^{\mathrm{C}} = C\frac{\mathrm{d}\left(V_n - V_{n+1}\right)}{\mathrm{d}t} = C\frac{\mathrm{d}^2\left(\Phi_n - \Phi_{n+1}\right)}{\mathrm{d}t^2}, \tag{3.21}$$

and for the current flowing through the ground capacitor:

$$I_n^{\mathrm{g}} = C^{\mathrm{g}}\frac{\mathrm{d}V_n - 0}{\mathrm{d}t} = C^{\mathrm{g}}\frac{\mathrm{d}^2\Phi_n}{\mathrm{d}t^2}, \tag{3.22}$$

where we discarded any source of loss coming from the dielectric in between the junction and the ground. From Eq. (3.14) and thanks to Eqs. (3.20) to (3.22), we have the following equation of motion for the generalized flux in its discrete form:

$$\begin{aligned} C^{\mathrm{g}}\frac{\mathrm{d}^2\Phi_n}{\mathrm{d}t^2} =& C\frac{\mathrm{d}^2\left(\Phi_{n+1} + \Phi_{n-1} - 2\Phi_n\right)}{\mathrm{d}t^2} + \frac{1}{L}\left(\Phi_{n+1} + \Phi_{n-1} - 2\Phi_n\right) - \\ & \frac{1}{6I_c^2 L^3}\left(\left(\Phi_{n+1} - \Phi_n\right)^3 - \left(\Phi_n - \Phi_{n-1}\right)^3\right). \end{aligned} \tag{3.23}$$

We make the same assumption than in Section 2.6 by considering a (the unit cell length) very small compared to λ, the signal wavelength. The flux Φ can be seen as a continuous variable and not as a discrete one anymore. Phase differences between two neighbor sites can be expanded as:

$$\Phi_{n+1} - \Phi_n \approx a\frac{\partial\Phi}{\partial x} + \frac{a^2}{2}\frac{\partial^2\Phi}{\partial x^2}, \tag{3.24a}$$

$$\Phi_n - \Phi_{n-1} \approx a\frac{\partial\Phi}{\partial x} - \frac{a^2}{2}\frac{\partial^2\Phi}{\partial x^2}, \tag{3.24b}$$

$$\left(\Phi_{n+1} - \Phi_n\right)^3 - \left(\Phi_n - \Phi_{n-1}\right)^3 \approx 3a^4\frac{\partial^2\Phi}{\partial x^2}\left(\frac{\partial\Phi}{\partial x}\right)^2. \tag{3.24c}$$

By plugging the continuous variables from Eq. (3.24) into the discrete form of the equation of motion Eq. (3.23), we get the continuous equation of motion:

$$C^{\mathrm{g}}\frac{\partial^2\Phi}{\partial t^2}-\frac{a^2}{L}\frac{\partial^2\Phi}{\partial x^2}-Ca^2\frac{\partial^2\Phi}{\partial x^2\partial t^2}=\frac{a^4}{2I_{\mathrm{c}}^2L^3}\frac{\partial^2\Phi}{\partial x^2}\left(\frac{\partial\Phi}{\partial x}\right)^2. \tag{3.25}$$

From the study of $\chi^{(3)}$ nonlinear optical fibers, we know that the solution is composed of the pump, the signal and the idler. This is why we propose as a solution for Eq. (3.25) the following ansatz:

$$\Phi=\frac{1}{2}\sum_{\mathrm{j}=\{\mathrm{p,s,i}\}}\left[A_{\mathrm{j}}\left(x\right)e^{i(k_{\mathrm{j}}x-\omega_{\mathrm{j}}t)}+\mathrm{c.c.}\right]. \tag{3.26}$$

By looking at Eq. (3.1a) and Eq. (3.26), we see that Φ is the circuit equivalent of the electric field in NOFs. We denote A_{j}, k_{j} and $\omega_{\mathrm{j}}/2\pi$ as the slowly varying amplitude, the wavevector and the frequency, respectively, for $\mathrm{j}=\{\mathrm{p,s,i}\}$. We plug this ansatz in Eq. (3.25). Considerable simplification can be made by making the following approximations (in the supplemental materials of reference [81]):

— we discard the second spatial derivative of the amplitude A_{j} by using the slowly varying envelope approximation that translates in $|\frac{\partial^2 A_{\mathrm{j}}}{\partial x^2}|<<|k_{\mathrm{j}}\frac{\partial A_{\mathrm{j}}}{\partial x}|$.

— In the nonlinear part (right-hand side of Eq. (3.25)), the first derivative of the amplitude is neglected. It translates into $|\frac{\partial A_{\mathrm{j}}}{\partial x}|<<|k_{\mathrm{j}}A_{\mathrm{j}}|$.

After several steps (detailed calculations are given in Appendix A, Section A.2.1), and considering as usual the pump amplitude A_{p} much higher than A_{s} and A_{i}, we have the coupled equations:

$$\frac{\partial A_{\mathrm{p}}}{\partial x}=i\frac{a^4k_{\mathrm{p}}^5}{16C^{\mathrm{g}}I_{\mathrm{c}}^2L^3\omega_{\mathrm{p}}^2}|A_{\mathrm{p}}|^2A_{\mathrm{p}}, \tag{3.27a}$$

$$\frac{\partial A_{\mathrm{s}}}{\partial x}=i\frac{a^4k_{\mathrm{p}}^2k_{\mathrm{s}}^3}{8C^{\mathrm{g}}I_{\mathrm{c}}^2L^3\omega_{\mathrm{s}}^2}|A_{\mathrm{p}}|^2A_{\mathrm{s}}+i\frac{a^4k_{\mathrm{p}}^2\left(2k_{\mathrm{p}}-k_{\mathrm{i}}\right)k_{\mathrm{s}}k_{\mathrm{i}}}{16C^{\mathrm{g}}I_{\mathrm{c}}^2L^3\omega_{\mathrm{s}}^2}A_{\mathrm{p}}^2A_{\mathrm{i}}^*e^{i\Delta k_{\mathrm{l}}x}, \tag{3.27b}$$

$$\frac{\partial A_{\mathrm{i}}}{\partial x}=i\frac{a^4k_{\mathrm{p}}^2k_{\mathrm{i}}^3}{8C^{\mathrm{g}}I_{\mathrm{c}}^2L^3\omega_{\mathrm{i}}^2}|A_{\mathrm{p}}|^2A_{\mathrm{i}}+i\frac{a^4k_{\mathrm{p}}^2\left(2k_{\mathrm{p}}-k_{\mathrm{s}}\right)k_{\mathrm{s}}k_{\mathrm{i}}}{16C^{\mathrm{g}}I_{\mathrm{c}}^2L^3\omega_{\mathrm{i}}^2}A_{\mathrm{p}}^2A_{\mathrm{s}}^*e^{i\Delta k_{\mathrm{l}}x}, \tag{3.27c}$$

where we defined the wavevector as:

$$k_{\mathrm{j}}=\frac{\omega_{\mathrm{j}}\sqrt{LC^{\mathrm{g}}}}{a\sqrt{1-\left(\frac{\omega_{\mathrm{j}}}{\omega_{\Pi}}\right)^2}}\quad,\quad\mathrm{j}=\{\mathrm{p,s,i}\}. \tag{3.28}$$

The linear phase-mismatch Δk_l is defined as in Eq. (3.6). This system of coupled equations is very similar to the system derived from the $\chi^{(3)}$ nonlinear optical fiber case in Eqs. (3.4) and (3.5). However, we cannot define a single nonlinear coefficient for the whole system (like the γ coefficient in Eq. (3.3)). Still, we define a common nonlinear parameter for all the three equations in Eq. (3.27). If we consider the first members of the right-hand side of each equation, we define the general nonlinear parameter Ω (in hertz):

$$\Omega = \frac{a^2 k_\mathrm{p}^2}{8 C^\mathrm{g} I_\mathrm{c}^2 L^3} |A_\mathrm{p}|^2, \tag{3.29}$$

which defines nonlinear coefficients related to the pump amplitude:

$$\gamma_\mathrm{pp} = \frac{\Omega k_\mathrm{p}^3 a^2}{2LC^\mathrm{g}\omega_\mathrm{p}^2} \quad , \quad \gamma_\mathrm{sp} = \frac{\Omega k_\mathrm{s}^3 a^2}{LC^\mathrm{g}\omega_\mathrm{s}^2} \quad , \quad \gamma_\mathrm{ip} = \frac{\Omega k_\mathrm{i}^3 a^2}{LC^\mathrm{g}\omega_\mathrm{i}^2}. \tag{3.30}$$

We solve Eq. (3.27a) for the pump amplitude:

$$A_\mathrm{p}(x) = A_\mathrm{p0} e^{i\gamma_\mathrm{pp} x}, \tag{3.31}$$

where every loss associated to the pump have been discarded. Therefore A_p0 is a pure real and is modeled as $A_\mathrm{p0} = Z_\mathrm{c} I_\mathrm{p}/\omega_\mathrm{p}$. Having it purely real allows to simplify the second terms of the right-hand side of Eqs. (3.27b) and (3.27c) since the nonlinear phase of the pump is added to the linear phase mismatch Δk_l. This step is equivalent to the definition of θ in Section 3.1, γ_pp being the SPM coefficient. We rewrite in a simple form the equation of motion for the signal and the idler amplitudes:

$$\frac{\partial A_\mathrm{s}}{\partial x} = i\gamma_\mathrm{sp} A_\mathrm{s} + i\gamma_\mathrm{si} A_\mathrm{i}^* e^{i(\Delta k_\mathrm{l} + 2\gamma_\mathrm{pp})x} \quad , \quad \gamma_\mathrm{si} = \frac{\Omega a^2 \left(2k_\mathrm{p} - k_\mathrm{i}\right) k_\mathrm{s} k_\mathrm{i}}{2\omega_\mathrm{s}^2}, \tag{3.32a}$$

$$\frac{\partial A_\mathrm{i}}{\partial x} = i\gamma_\mathrm{ip} A_\mathrm{i} + i\gamma_\mathrm{is} A_\mathrm{s}^* e^{i(\Delta k_\mathrm{l} + 2\gamma_\mathrm{pp})x} \quad , \quad \gamma_\mathrm{is} = \frac{\Omega a^2 \left(2k_\mathrm{p} - k_\mathrm{s}\right) k_\mathrm{s} k_\mathrm{i}}{2\omega_\mathrm{i}^2}, \tag{3.32b}$$

where γ_si and γ_is are XPM coefficients, generated by the pump, and modulating the signal and the idler, respectively. We eventually simplify Eqs. (3.32a) and (3.32b) by defining the auxiliary $a_\mathrm{s} = A_\mathrm{s} e^{-i\gamma_\mathrm{sp} x}$ (and also for the idler by permuting $s \leftrightarrow i$) as we have done in Section 3.1. It allows to get rid of the first term in the right-hand side of Eqs. (3.32a) and (3.32b):

$$\frac{\partial a_\mathrm{s}}{\partial x} = i\gamma_\mathrm{si} a_\mathrm{i}^* e^{i\Delta k x}, \tag{3.33a}$$

$$\frac{\partial a_\mathrm{i}}{\partial x} = i\gamma_\mathrm{is} a_\mathrm{s}^* e^{i\Delta k x}, \tag{3.33b}$$

where the total phase mismatch reads:

$$\Delta k = \Delta k_{\mathrm{l}} + \underbrace{2\gamma_{\mathrm{pp}}}_{\mathrm{SPM}} - \underbrace{\gamma_{\mathrm{sp}} - \gamma_{\mathrm{ip}}}_{\mathrm{XPM}}. \tag{3.34}$$

As we previously noticed for $\chi^{(3)}$ NOF, γ_{pp} and γ_{sp} (γ_{ip}) are not equal. It is noteworthy that the factor 2 between γ_{pp} and γ_{sp} (γ_{ip}) has the same origin as the one found between the self Kerr and the cross Kerr coefficients as derived in Section 2.6 [76]. In Fig. 3.3, we plot the total phase mismatch defined in Eq. (3.34) as a function of the dimensionless pump current $I_{\mathrm{p}}/I_{\mathrm{c}}$. For large pump current, the phase mismatch becomes larger. In the inset, we plotted the normalized SPM and XPM to stress their different rate with respect to the pump current.

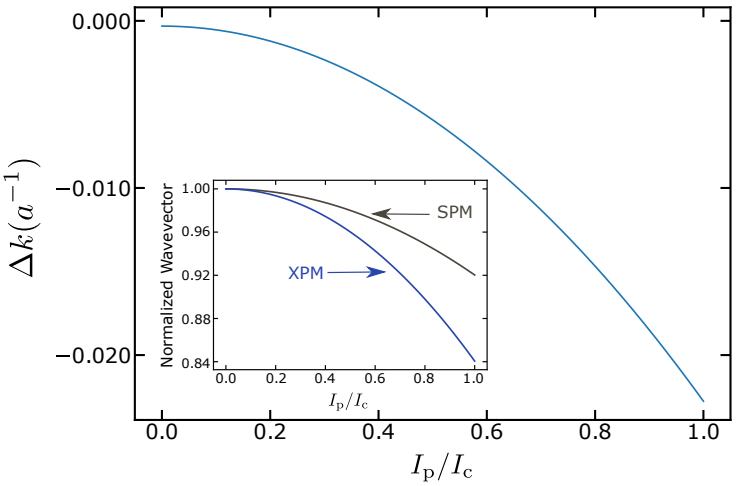

Figure 3.3 – **Pump induced phase modulation.** Wavevector mismatch in a^{-1} unit *vs.* dimensionless pump current. **Inset:** cross-phase and self-phase modulation. In solid blue line, we plot $(k_{\mathrm{p}} - \gamma_{\mathrm{pp}})/k_{\mathrm{p}}$ while in brown, we plotted $(k_{\mathrm{s}} - \gamma_{\mathrm{sp}})/k_{\mathrm{s}}$. The 'rate' difference between SPM and XPM is at the origin of the total phase mismatch Δk growing larger for large pump current.

3.2.3 Gain *vs.* phase-mismatch

The coupled equations between signal and idler in Eq. (3.33) can be written as two differential equations for the signal and the idler. These equations have been solved for optical systems decades ago [82] in three dimensions. In one dimension,

the solution reads (see Appendix A, Section A.2.1 for detailed calculations):

$$a_{\mathrm{s}}(x) = \left(a_{\mathrm{s}}(0) \left(\cosh(gx) - \frac{i\Delta k}{2g} \sinh(gx) \right) + \frac{i\gamma_{\mathrm{si}}}{g} a_{\mathrm{i}}(0)^* \sinh(gx) \right) e^{i\Delta k x/2}, \tag{3.35a}$$

$$a_{\mathrm{i}}(x) = \left(a_{\mathrm{i}}(0) \left(\cosh(gx) - \frac{i\Delta k}{2g} \sinh(gx) \right) + \frac{i\gamma_{\mathrm{is}}}{g} a_{\mathrm{s}}(0)^* \sinh(gx) \right) e^{i\Delta k x/2}, \tag{3.35b}$$

$$g = \sqrt{\gamma_{\mathrm{si}}\gamma_{\mathrm{is}}^* - \left(\frac{\Delta k}{2} \right)^2}. \tag{3.35c}$$

As in the previous chapter, we observe that the signal amplitude is a linear combination of the initial signal amplitude and the initial idler amplitude; and so does the idler. The parametric gain coefficient g is analogous to the one defined in the introduction of this chapter. From these equations, Δk should stay as close to zero as possible so that g is kept real when the pump power increases. We can finally define the signal power gain of the TWPA for $x = N \times a = L$, while considering no idler at its input ($a_{\mathrm{i}}(0) = 0$):

$$G_{\mathrm{s}} = \left| \frac{a_{\mathrm{s}}(x = L)}{a_{\mathrm{s}}(0)} \right|^2 = \left| \cosh(gL) - \frac{i\Delta k}{2g} \sinh(gL) \right|^2. \tag{3.36}$$

To study signal power gain and the effect of mismatch on it, we fix the pump frequency ω_{p} well below the plasma frequency of the junctions $\omega_{\Pi} = (LC)^{-1/2}$. Wavevectors are given by the dispersion relation of the junction array in Eq. (3.28).

In Fig. 3.4 **(a)**, G_{s} is plotted for $\omega_{\mathrm{s}} = \omega_{\mathrm{p}}$ as a function of the pump current. For a given pump current, this is the maximum expected gain since in the degenerate case $\Delta k_{\mathrm{l}} = 0$. In solid blue line, G_{s} is calculated while considering SPM (γ_{pp}) and XPM (γ_{sp} and γ_{ip}). In black dotted line, we calculated G_{s} while artificially discarding XPM and SPM and putting γ_{pp}, γ_{sp} and γ_{ip} equal to 0. This cannot naturally exist but we wanted to show the impact of nonlinear phase mismatch on the expected gain. We can see the huge difference in gain when the pump current starts to be more than 25% of the junctions' critical current. In Fig. 3.4**(b)** and **(c)**, Δk and G_{s} are plotted for fixed pump current I_{p} as a function of the signal frequency. As expected, for fixed pump parameters, when the detuning between the signal and the pump increases, the mismatch Δk increases and G_{s} decreases. It gives the bandwidth of the amplifier, dictated by the dispersion of the junction array. For larger pump currents, the expected maximum gain and Δk are increasing but the expected bandwidth decreases. For G_{max} above 10 dB, the bandwidth is already larger that what we could expect with a resonant JPA. Regarding the maximum signal power gain we theoretically expect, the results we obtained seem to be over optimistic. Even for an array where the phase is not

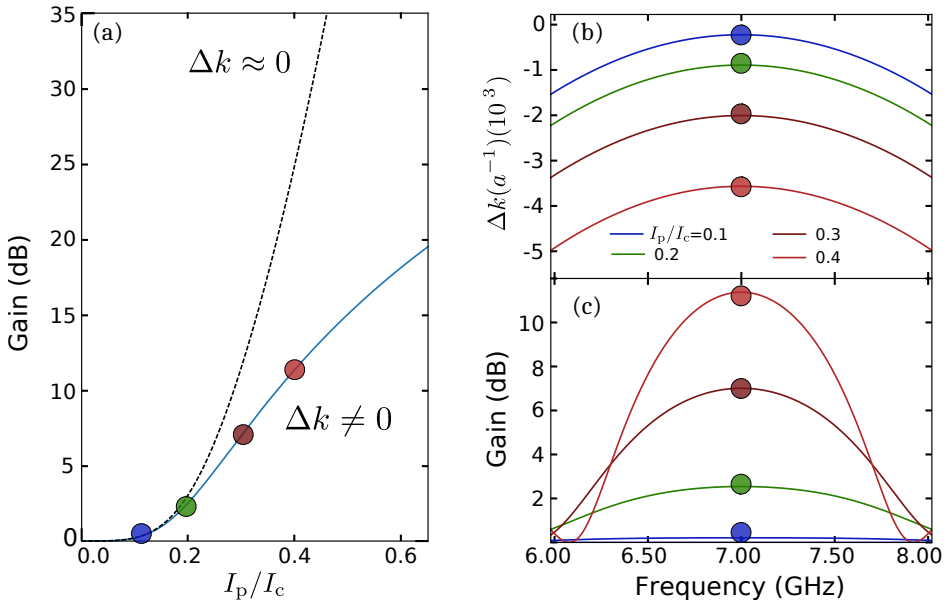

Figure 3.4 – **Effect of phase mismatch on a Josephson TWPA. (a)** Signal power gain as a function of the pump current. It shows that if we could keep the phase matching (black dashed line) to 0, the maximum gain would be orders of magnitude higher than when XPM and SPM are taken into account (blue line). **(b)** Total wavevector mismatch in a^{-1} unit *vs.* signal frequency. **(c)** Signal power gain *vs.* signal frequency. Both plots have the pump current as a parameter encoded as a color. Trivially, the higher the pump current the higher the maximum expected gain and the larger the phase mismatch.

corrected at all, it is in principle possible to reach 20 dB power gain when the pump current is 60% of the critical current. This result should be taken carefully as up to now, we overlooked two issues:

— the electrical losses for both the signal and the pump.

— The AC current at which the TWPA transmission drops by several orders of magnitude is different from the single junction critical current. While the difference between switching current and critical current is well understood in the case of a single junction [83], understanding the quantum dynamics of a driven junction array remains an open theoretical question.

The first point tells that in fact, the pump power is not homogeneous through the whole array and the last junctions do not see the same pump power as the first one. Thus for a given input pump power the total gain is going to be smaller than expected. The second point tells that taking the critical current as the upper bound for the pump current is not the most accurate limit. Indeed, if we define

I_s the current for which the junctions switch from being superconducting to resistive, in principle we have $I_s < I_c$. No signal transmission nor amplification can occur if $I_p > I_s$. Unfortunately, it is very hard to quantitatively calculate I_s as it relies on complex dynamical effect happening within the junction array. A very simple picture would be that if we describe one junction by a fictitious particle of position Φ in a nonlinear potential, we would need to account for its inertia when it is driven by the external pump tone to know whether or not it will be dragged out the potential. However, we do not have for now a better upper bound for the current and we will keep I_c. Panel **(a)** shows anyhow the importance of reducing phase mismatch during the four wave mixing process to get a higher expected maximum gain. Throughout the years, there were many proposals and implementation to fight nonlinear phase mismatch. For instance, opening a stop band in the dispersion relation of a Josephson array [46, 47, 81] or a photonic gap in the dispersion of a high kinetic inductance transmission line [45, 84, 85, 86]. For both techniques, the goal is to correct the pump phase while the amplification occurs. It has also been suggested to change the sign of the Kerr nonlinearity to counter its effect [87, 88]. Or even more dramatically switching from four wave mixing to three wave mixing while neutralizing the fourth order Kerr nonlinearity [48, 71]. We have chosen to open a photonic gap in the dispersion relation of a Josephson metamaterial by periodically modulating the size of the Josephson junctions and therefore its impedance. The next section will focus on the effect of periodic structures on the dispersion relation and how opening a photonic gap can actually help against the detrimental effects of self and cross phase modulation.

3.3 Bloch waves in periodic structures

Waves' physics in periodic structures is very rich and leads to counter intuitive and astonishing results. Bloch theorem and Bloch waves in crystalline structures allowed to anticipate band structures of materials and semi conductors more specifically. The physics describing a periodically modulated Josephson junction array is very similar to the physics describing electronics bands in crystals. In this section, we will briefly review electrons' behavior in a periodic energetic landscape and study their energy band diagrams. For the next two sections we follow N. W. Ashcroft and D. Mermin approach in their solid states physics textbook [89].

3.3.1 Electron in a perfect crystal

Let us consider the case of an electron in a 1D perfect crystal. Each ion is evenly spaced and the potential seen by the electron $U(x)$ must respect the condition :

$$U(x + L_{\text{period}}) = U(x), \tag{3.37}$$

where L_{period} is the length of one period in the crystal. Fig. 3.5**a** shows an example of a crystalline structure where ions are drawn at their equilibrium position with their associated potential and the overall potential seen by the electron. If we

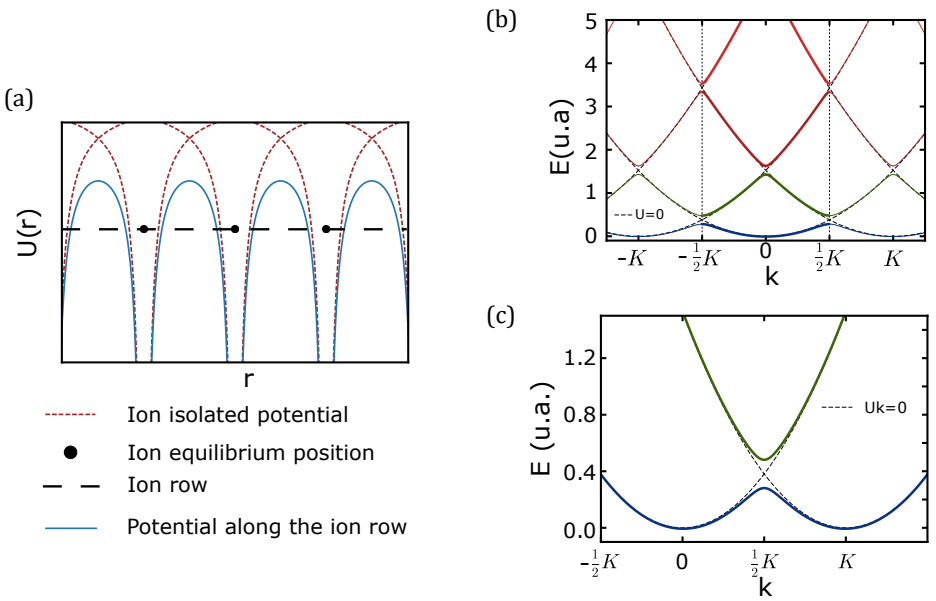

Figure 3.5 – **Crystalline structure and its energy landscape. (a)** Crystalline periodic potential. **(b)** Extended first Brillouin zone. **(c)** Zoom in of the gap.

consider only one electron in such periodic potential, discarding electron-electron interactions, its wave function ψ is solution of the Schrödinger equation:

$$H\psi = \left(-\frac{\hbar^2}{2m}\nabla^2 + U\left(x\right)\right)\psi = E\psi, \tag{3.38}$$

with m the electron mass. Electrons described by this Hamiltonian are called Bloch electrons. Their wavefunctions, solution of Eq. (3.38) can be written as a product of a periodic function of L_{period} and a plane wave:

$$\psi_k(x) = e^{ikx}u_k(x) \quad , \quad u_k(x + L_{\text{period}}) = u_k(x). \tag{3.39}$$

This is the Bloch theorem. Another simple way to state it is:

$$\psi_k(x + L_{\text{period}}) = e^{ikL_{\text{period}}}\psi_k(x). \tag{3.40}$$

It is noteworthy to recall that the wavevector introduced in Eqs. (3.39) and (3.40) is not simply proportional to the electron momentum like for wavevectors of free electrons in a potential well. Eigenstates of the Hamiltonian in Eq. (3.38) are not eigenstates of the momentum operator. However, the wavevector k defined

in Eq. (3.39) is called crystalline momentum and is a natural extension of free electron wavevectors in a crystalline periodic structure.

3.3.2 Band diagram

To compute the energy of an electron in a perfect crystal, we consider the periodic potential to be very weak so that we can treat it as a perturbation. We consider the Hamiltonian eigenstate of Eq. (3.38) as a sum of plane waves:

$$\psi_k(x) = \sum_{K'} c_{k-K'} e^{i(k-K')x}, \tag{3.41}$$

where $c_{k-K'}$ are coefficients of the different plane waves composing the eigenstate and K' are wavevectors of the reciprocal lattice, knowing that the main reciprocal lattice wavevector is defined as:

$$K = \frac{2\pi}{L_{\text{period}}}. \tag{3.42}$$

We define the eigenenergies of the system as E_k, E_{k-K}, E_{k-2K} *etc.* as the energies starting at $K' = 0$, $K' = K$, $K' = 2K$ *etc.* (see Fig. 3.5**(b)**).
If we consider the case where $K' = 0$ and $K' = K$, when these energies are distant from each other ($E_k^0 - E_{k-K}^0 >> U$), they behave like energies of free electrons $E_k^0 = (\hbar k)^2/2m$. However, when k and $k - K$ get closer and their energy get quasi degenerated $E_k^0 - E_{k-K}^0 \approx U$, the energy reads:

$$E = \frac{1}{2}\left(E_k^0 + E_{k-K}^0\right) \pm \sqrt{\left(\frac{E_k^0 - E_{k-K}^0}{2}\right)^2 + |U_K|^2}. \tag{3.43}$$

The energy is lifted at the degeneracy point. In a simple problem like a 1D array of ions, degeneracy happens at $k = K/2 + nK/2$, where n is a positive or negative integer. In Fig. 3.5**(b)** we plotted the energy levels in arbitrary unit for two cases. First with an absence of periodic potential ($U = 0$) and for a finite value of U. The different branches are encoded under different colors. We highlighted the first Brillouin zone, defined between $-K/2$ and $K/2$. In panel **(c)** we zoomed in at the edge of the first Brillouin zone corresponding to a degeneracy point. The curved shape that takes the first branch close to $k = K/2$ is exactly what we are looking for phase correction between the pump, the signal and the idler. If we consider the energy of the electrons being the analogue of the frequency of the electromagnetic waves in our system, then for a frequency close to the gap, its associated wavevector is larger when there is a periodic modulation ($U \neq 0$) than when there is none ($U = 0$). In other words, close to the gap (lower branch), the wavevector has a positive offset. In the previous section, we saw that phase modulation for the pump (γ_{pp}) was twice smaller than for the signal (γ_{sp}) and idler (γ_{ip}). Therefore, the dispersion is engineered in a way that the positive offset

in the pump wavevector will compensate this factor two. In the next section, we model the periodic modulation in a Josephson array with electrical models to be more quantitative on this pump phase offset for phase mismatch correction.

3.4 Periodically modulated Josephson arrays

In this section we present two linear models to get the dispersion relation of a periodically modulated Josephson array. The first one follows the Lagrangian approach while the second relies on ABCD matrices. The total number of junctions is still $N = 2000$. L_{period} is the length of one period, $N_{\text{p}} = L_{\text{period}}/a$ the number of junction per period and $N_{\text{r}} = N/N_{\text{p}} = 50$ the number of period. L_0, C_0, C_0^{g} are the mean values of the respective microscopic parameters and have the same numerical values as in the study of the non modulated arrays.

3.4.1 Periodic modulation – Lagrangian approach

The first approach that comes to mind to get frequencies as a function of the wavevector is to follow the same technique as in Section 2.6. The array can be modeled in the exact same way as for the resonant structure: we build $N \times N$ matrices for the inductances and capacitances and get the eigenvalues of the resonant frequencies matrix $\hat{\Omega}^2$ as defined in the previous chapter. It is noteworthy that given the large ground capacitance needed to have a $50\,\Omega$ Josepson transmission line, no remote ground model is needed. We therefore have only periodic tri-diagonal matrices to deal with. Eventually, we get resonant frequencies as a function of the mode number. To convert mode number in wavelength, one must consider the boundary conditions of the array. In our case, the array is ended on both sides by a galvanic connection with the $50\,\Omega$ environment. Therefore the array can be considered as a $\lambda/2$ 'resonator' (although it is supposed to be matched). Wavelength λ_i can be inferred from mode index i:

$$L_{\text{twpa}} = (i+1)\frac{\lambda_i}{2} \quad , \quad i \in [0, N-1]\,, \tag{3.44}$$

where L_{twpa} is the total length of the TW amplifier and equals to $N \times a$. We compute eigenvalues of $\hat{\Omega}^2$ with microscopic parameters following sinusoidal harmonic modulation:

$$\begin{aligned}
L_n^{-1} &= L_0^{-1}\left(1 + \eta_1 \cos\left(2\pi\frac{n}{N_{\text{p}}}\right) + \eta_2 \cos\left(2\pi\frac{2n}{N_{\text{p}}}\right)\right) \text{ (where } n \in [0, N-1]\text{)}, \\
C_n^{\text{g}} &= C_0^{\text{g}}\left(1 + \eta_1 \cos\left(2\pi\frac{n}{N_{\text{p}}}\right) + \eta_2 \cos\left(2\pi\frac{2n}{N_{\text{p}}}\right)\right), \\
C_n &= C_0\left(1 + \eta_1 \cos\left(2\pi\frac{n}{N_{\text{p}}}\right) + \eta_2 \cos\left(2\pi\frac{2n}{N_{\text{p}}}\right)\right).
\end{aligned} \tag{3.45}$$

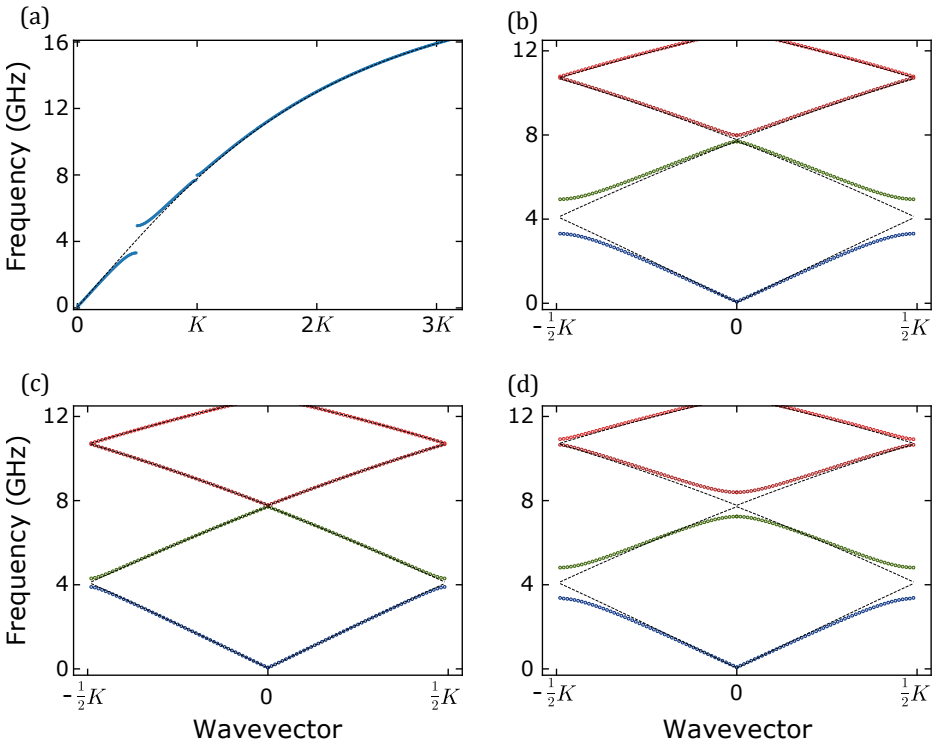

Figure 3.6 – **Dispersion relation calculated with Lagrangian method.** In these four plots, signal frequency is plotted as a function of its wavevector. The numerical value of the plasma angular frequency ω_Π used to plot these dispersions is calculated from the numerical parameters given in Section 3.2.2 and is equal to $\omega_\Pi/2\pi = 20.6\,\text{GHz}$. Colors encode the index of the branch. Only modulation amplitudes are changed throughout the panels. Dashed black lines represent an absence of modulation in the array ($\eta_1 = \eta_2 = 0\%$). **(a)** and **(b)** Same dispersion for $\eta_1 = 40\%$ and $\eta_2 = 0$. In the former, the dispersion is plotted in the extended zone while in the latter dispersion is plotted in the first Brillouin zone. **(c)** $\eta_1 = 10\%$ and $\eta_2 = 0\%$. The gap amplitude is much smaller than in **(a)** and **(b)**. **(d)** $\eta_1 = 40\%$ and $\eta_2 = 20\%$. The second gap ($K = 0$ in the first Brillouin zone) is wider than in **(a)** and **(b)**.

η_1 and η_2 are the modulation amplitudes of the first and second harmonic, respectively, and n is the junction number. Dispersion for $\eta_1 = 40\%$ and $\eta_2 = 0\%$ is plotted in Fig. 3.6 **(a)** in blue dots while in dashed black line is plotted the dispersion for $\eta_1 = \eta_2 = 0\%$. The effect of the periodic modulation on the dispersion is exactly as expected: close to the first gap, for $k \lesssim K/2$, we observe a positive deviation compared to the dispersion without any modulation. For $k = K$, we observe a much smaller gap: this is a second order effect due to the first harmonic

only since $\eta_2 = 0\%$. Hence, the second gap width is smaller than the first one. In panels **(b)**, the same dispersion is plotted on the first Brillouin zone. We kept the same color coding as in Fig. 3.5: colors correspond to the branch index. In panel **(c)**, the dispersion is plotted for the exact same parameters but the modulation amplitude $\eta_1 = 10\%$. We straightforwardly see the difference in the gap amplitudes: the gap in panel **(b)** is almost 4 times larger than in panel **(c)**. On panel **(d)** the dispersion is plotted for $\eta_1 = 40\%$ and $\eta_2 = 20\%$. The first gap is as wide as in panel **(a)** and **(b)** while the second gap is much larger because of the presence of the second harmonic in the modulation. As we will see in the next chapters, we are able to fabricate single and even double harmonic Josephson metamaterials. This model is useful to have a general appreciation on the effect of periodic modulation in the arrays. Moreover, we see that a larger modulation amplitude η allows to have a larger phase deviation from the unmodulated case. It tells us that we will need η to be large enough in order to have the right correction for the pump phase. We do not show it here, but this approach allows to compute self and cross Kerr coefficients for each mode (at the expense of big computation time though) which is convenient to apprehend nonlinear effects happening in the array. Though this model is simple to implement, it is not very accurate as it still consider resonant modes while in principle the array is supposed to be matched with the environment. Moreover, this model does not give any information on the actual signal amplitude within the array.

3.4.2 Periodic modulation – ABCD matrix model

In order to get amplitude **and** phase of the wave being transmitted in the Josephson array, a solution is to compute the complex scattering parameter $S_{21}(\omega)$. To do so, we can model the 1D array of N junctions as a cascade of N two-port networks. Two-port elements can be simply model with ABCD formalism [74], where input voltage and current are related to output voltage and current via a 2×2 transmission (or ABCD) matrix at a given frequency $\omega/2\pi$. There are analytical formulae linking scattering parameters $S_{ij}(\omega)$ to the coefficients of the ABCD matrix. This formalism takes its efficiency from that a cascade of N two-port networks is also modeled as a single ABCD matrix, product of N 2×2 matrices. It is well suited to computer calculations. ABCD coefficients of the array can be translated into scattering parameters and in particular $S_{21}(\omega)$ as we are focused on transmission. Each two-port element is expressed with the microscopic parameters of the chain. The n^{th} two-port element is modeled with parameters in Eq. (3.45). In Fig. 3.7 $|S_{21}(\omega)|$ (in decibels) and $\arg(S_{21}(\omega))$ (in radians) are plotted for the same parameters as in Fig. 3.6**(a)** and **(b)**. The negative slope in the phase is a matter of convention with the minus sign in the complex exponential. First of all, we notice that for $|S_{21}(\omega)|$, the photonic gap induces a big drop in transmission, whose width is directly related to the modulation amplitude η. We also notice the second and third gaps with lower transmission drops as only η_1 is non zero. Regarding the phase, we can multiply it by $-1/L_{\text{twpa}}$ to obtain the dispersion relation $k(\omega)$. Eventually, we plot in Fig. 3.7 **(b)** the dispersion $\omega(k)$ and wrap it

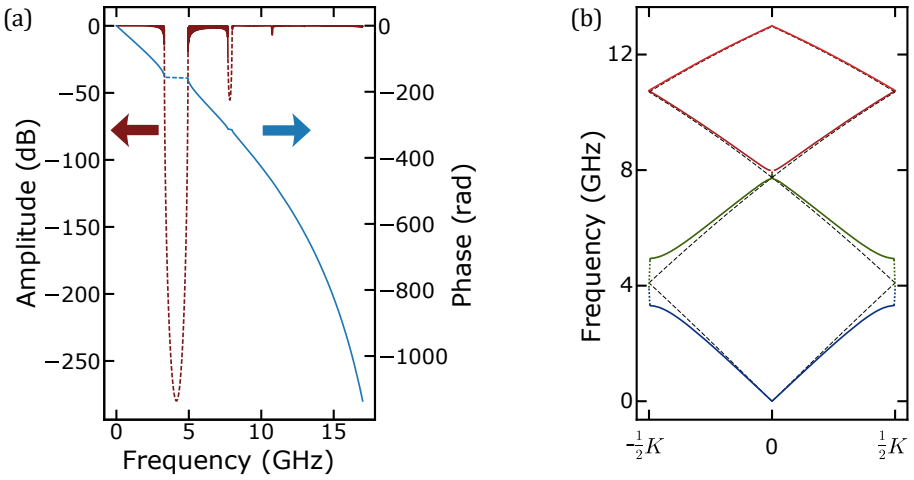

Figure 3.7 – **Transmission and dispersion calculated with ABCD matrices. (a)** In red (to be read with respect to the left axis) is plotted $|S_{21}(\omega)|$ as a function of the frequency. In blue (right axis) is plotted the phase of the signal. The transmission drop is the gap signature. **(b)** The calculated phase is multiplied by $(-1/L_{\text{twpa}})$ and wrapped between $-K/2$ and $K/2$. It follows the same nomenclature as in Fig. 3.6**(b)**, **(c)**, **(d)**.

in the first Brillouin zone. It follows the same convention as in Fig. 3.6**(b)**, **(c)**, **(d)**. We saw in the previous section that a large modulation amplitude allows to have a larger correction on the pump phase but it will lead to a larger 'forbidden' frequency band with no transmission nor amplification allowed. There is then a trade-off between phase mismatch correction and forbidden amplification band. Moreover, as we will see in the next subsection, the forbidden band gap becomes twice bigger during amplification.

3.4.3 Amplification with corrected phase

With the ABCD matrix formalism, we can directly plug the new dispersion relation $k(\omega)$ with the periodic modulation to compute nonlinear coefficients in Eq. (3.30) $(\gamma_{\text{pp}}, \gamma_{\text{sp}}, \gamma_{\text{ip}})$ and Eq. (3.32) $(\gamma_{\text{si}}, \gamma_{\text{is}})$ to finally get the gain coefficient g and the signal gain power G_{s} defined in Eq. (3.36). In Fig. 3.8**(a)**, we plot two gain profiles, for the same pump power and pump frequency, with one modulated dispersion while the other one is not. The modulation amplitude η is equal to 4% in this case, since it provides enough phase correction to have a quantifiable effect on gain. We directly see an improvement in the expected maximum gain and expected bandwidth between the modulated array and the bare one. The gain profile of the modulated array deserves some explanation. In the middle of the amplification band, we can distinguish two dips separated by one

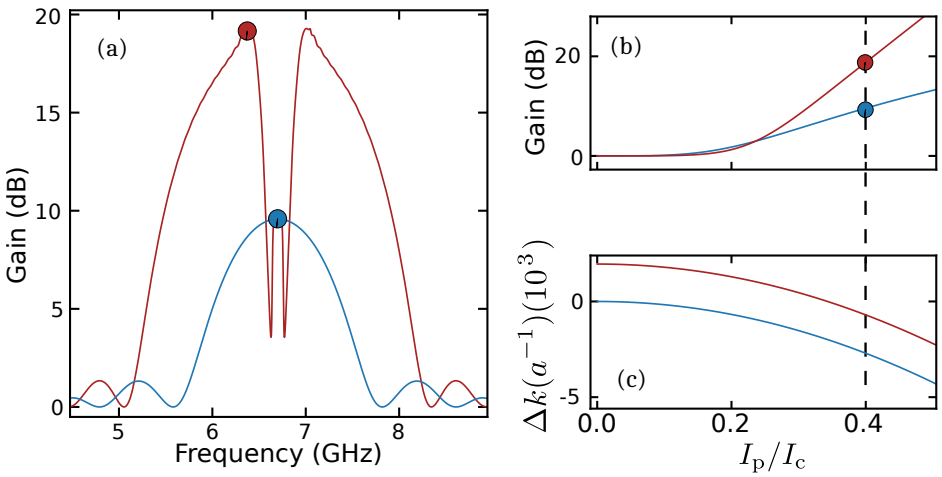

Figure 3.8 – **Calculated gain and phase mismatch for a spatially modulated array with a 4% modulation amplitude.** Red solid lines are for modulated array while solid blue lines encode an absence of modulation (bare arrays). **(a)** Gain *vs.* frequency. The two drops in amplification at the center of the frequency band are the idler gap (left) and signal gap (right). **(b)** Maximum expected gain (taken for points like the red one in **(a)**), function of the pump current. **(c)** Phase mismatch as a function of the pump current. The pump frequency is chosen very close to the gap so that it gets the positive wavevector offset. This is why in the low pump power regime, the mismatch is larger and thus the gain is smaller for the modulated array. At larger power, there is a better phase matching and therefore a larger gain.

local peak. When the signal is degenerated with the pump, there is a small gain of 10 dB only. This is because in that region, phase mismatch does not benefit from the gap correction (this is why it is the same gain as for the bare chain). When the signal goes to higher frequency, the signal is completely in the gap, mismatch is large hence a gain drop until it goes 'out' of the gap. On the other hand, when the signal goes to lower frequency the signal is in the transmission band and in principle there should be amplification. Though, we know that the idler is generated symmetrically with respect to pump, which makes it right in the photonic gap. Hence, again, there is a large phase mismatch and a gain drop. This is detrimental for the amplifier performances since it means the amplifier gap width is actually twice bigger than the 'linear' gap. In panel **(b)**, the maximum gain is plotted as a function of the pump current. For low pump current, the modulated array provides a smaller gain because the pump is on purpose not matched with the signal and idler. For larger pump current, we can tell the effect of modulation on gain. This trend can be explained with panel **(c)** where the total phase mismatch Δk, as defined in Eq. (3.34), is plotted *versus* the pump

current. When the pump current is large enough to provide a decent gain, larger than 5 dB ($I_p \approx 0.25 I_c$), the modulated array has a phase mismatch closer to 0, which makes the amplification more favorable hence a larger maximum gain.

3.4.4 Limitation of the model with periodic modulation

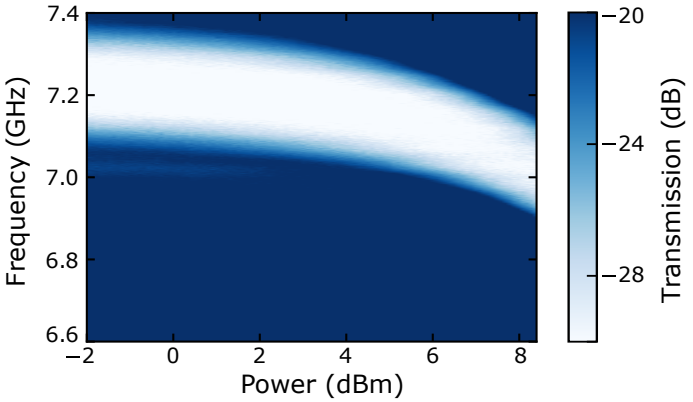

Figure 3.9 – **Experimental frequency shift of the photonic gap due to cross phase modulation in a periodically modulated array of SQUID.** $|S_{21}|$ is plotted in logarithmic unit as a color while signal frequency (y-axis) and pump power (x-axis) are swept. The white region corresponds to a dip in transmission due to the photonic gap. The pump frequency is 6 GHz. For low pump power, the gap region is constant in frequency. For larger pump power, the gap is shifted down to lower frequency.

The theory we used to derive the nonlinear coefficients and model the gain in our TW amplifier was initially developed for Josephson TWPA using the resonant phase matching (RPM) technique [47, 81]. With the RPM technique, every n cell (n is equal to few units), the TWPA is capacitively coupled to a LC resonator to open a stop band at its resonant frequency f_0. Therefore, the frequency position of the gap has nothing to do with the actual value of the microscopic parameters of the Josephson junctions but only with the LC resonator. Thus, it does not have any nonlinear behavior. However, when we adapted the calculation of the nonlinear coefficients in Eqs. (3.30) and (3.32) to the dispersion relation of a periodically modulated Josephson metamaterial calculated with the ABCD matrices, which is a purely linear approach, we missed a major point. In our system, the gap position is dramatically related to the Josephson inductance. When pumped, the Josephson inductance is increased so the photonic gap is shifted to a lower frequency. As shown in Fig. 3.9, we experimentally observe that the gap (dip in transmission) shifts more than its actual width when the pump power increases. In this experimental example, the pump is at 6 GHz. But the same would happen

if the pump frequency was closer from the photonic gap. A theory fully embracing the nonlinear behavior of the photonic gap must be developed. In a way, we should have a model merging the continuity of the ABCD matrices model while accounting for nonlinearities as the Lagrangian approach does. Such model was developed by **Denis Basko** from the laboratoire de physique et de modélisation des millieux condensés (LPMMC). It showed really good agreement with experimental data as we will see in Chapter 8. The next sections are devoted to the description of this theory.

3.5 Nonlinear waves in a Josephson photonic crystal

This section treats nonlinear waves in a periodically modulated Bloch chain. First of all, we must refine the way we parameterized the array in Section 3.2.2.

3.5.1 Finer modeling

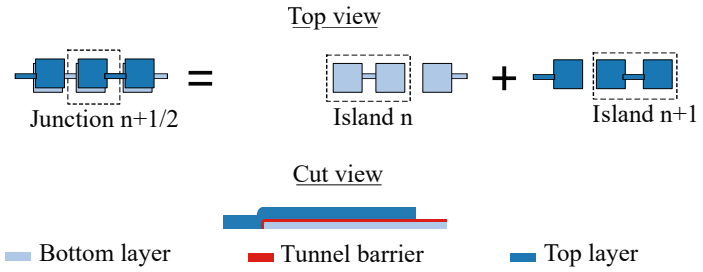

Figure 3.10 – **Simplified scheme of three Josephson junctions.** The junction n+1/2 is defined as the link between the superconducting islands n and n+1.

Up to now, Josephson junctions were considered as point-like inductors. To fully apprehend the model developed by **D.B.**, we must be more precise on the geometry of each junction. As shown in Fig. 3.10, a junction is a superposition of two layers of metal separated by a thin oxide layer – typically 1 nm – forming a tunnel barrier. The tunnel barrier linking the n^{th} island to the $(n+1)^{\text{th}}$ (top view) is the $n+1/2$ junction of the array. The Josephson inductance and capacitance of the junction $n+1/2$ are denoted $L_{n+1/2}$ and $C_{n+1/2}$, respectively. The ground capacitance at the n^{th} island is noted C_n^{g}. To match the array and increase the ground capacitance, we fabricated the ground plane extremely close to the junctions (see Chapter 4). Therefore, one of the two layers of aluminum is fully screened by the other one. In other words, only half of the islands have a substantial capacitive effect with the ground. However, this is not really an issue since we can define a 'meta' cell, with a ground capacitance $\bar{C}_n^{\text{g}}$ being the arithmetical mean of C_n^{g} and C_{n+1}^{g}. By doing so, we totally discard the periodic effect

generated by this two cell periodicity. Fortunately, such effects happen at much higher frequencies than our scope of interest so it can be safely neglected. In the following sections, we drop the bar in $\bar{C}_n^{\mathrm{g}}$.

3.5.2 Equations of motion

Let us start the treatment of the array by calculating site by site, in a discrete fashion, the Lagrangian of the array as we did in Section 2.6 with the superconducting phase $\phi = \Phi/(\hbar/2e)$:

$$\mathcal{L} = \frac{\hbar^2}{(2e)^2}\left[\sum_n \frac{C_{n+1/2}(\dot{\phi}_{n+1}-\dot{\phi}_n)^2 + C_n^{\mathrm{g}}\dot{\phi}_n^2}{2} + \sum_n \frac{1-\cos(\phi_{n+1}-\phi_n)}{L_{n+1/2}}\right]. \tag{3.46}$$

For every site in the bulk of the array, we use the Euler-Lagrange equation to get the equation of motion[a] at site n

$$\begin{aligned}
\forall n \in [1,N]: \qquad & \frac{\partial \mathcal{L}}{\partial \phi_n} - \frac{\mathrm{d}}{\mathrm{d}t}\left(\frac{\partial \mathcal{L}}{\partial \dot{\phi}_n}\right) = 0, \\
\leftrightarrow \forall n \in [1,N]: \qquad & C_{n+1/2}(\ddot{\phi}_n - \ddot{\phi}_{n+1}) + C_{n-1/2}(\ddot{\phi}_n - \ddot{\phi}_{n-1}) + C_n^{\mathrm{g}}\ddot{\phi}_n + \\
& \frac{\sin(\phi_n - \phi_{n+1})}{L_{n+1/2}} + \frac{\sin(\phi_n - \phi_{n-1})}{L_{n-1/2}} = 0.
\end{aligned} \tag{3.47}$$

Sanity check: non-modulated array

As a sanity check, we can briefly discuss the case where we have a homogeneous array without any modulation. When we drop the periodic modulation of the microscopic parameters in Eq. (3.47) (*e.g.* for all n, $L_{n+1/2} = L$), we find back the same equation of motion as in Eq. (3.23). Unlike the previous treatment, we first inject the ansatz into the equation of motion Eq. (3.47) and then treat the waves as continuous variables. The ansatz we choose is naturally a mixture of three monochromatic waves:

$$\phi_n(t) = A_{\mathrm{p}}(n)e^{ik_{\mathrm{p}}n - i\omega_{\mathrm{p}}t} + A_{\mathrm{s}}(n)e^{ik_{\mathrm{s}}n - i\omega_{\mathrm{s}}t} + A_{\mathrm{i}}(n)e^{ik_{\mathrm{i}}n - i\omega_{\mathrm{i}}t} + \mathrm{c.c.}, \tag{3.48}$$

where A_{j} is the wave amplitude, k_{j} the **dimensionless** wavevector ($k_{\mathrm{j}} \leftarrow k_{\mathrm{j}}a$) and ω_{j} the wave frequency (with $\mathrm{j} = \{\mathrm{p},\mathrm{s},\mathrm{i}\}$). When we inject this ansatz in Eq. (3.47) and make the same assumptions (large pump amplitude and slowly varying amplitudes) as in Section 3.2, we naturally find the same solutions for the signal and idler amplitudes. By considering a **large** phase mismatch and assuming the idler

[a] This time, the equation of motion have been found by starting from the calculation of the Lagrangian and used the Euler-Lagrange equation. It is a different starting point than in Section 3.2, where we derived the equation of motion of an array from Kirchhoff's circuit laws.

amplitude to be zero at time $t = 0$ ($A_\mathrm{i}(0) = 0$), it yields for the signal and idler amplitudes (detailed calculations in Appendix A, Section A.2.1):

$$A_s(x) = A_s(0)e^{i\Delta kx/2}(\cos(gx) - \frac{i\Delta k}{2g}\sin(gx)), \tag{3.49}$$

$$A_i^*(x) = A_s(0)e^{-i\Delta kx/2}\frac{\gamma_\mathrm{is}^*}{ig}\sin(gx). \tag{3.50}$$

Here, the nonlinear coefficients are defined slightly differently since the wavevectors are dimensionless and the continuum approximation has been done after injecting the ansatz. They read:

$$\gamma_\mathrm{pp} = \frac{4|A_\mathrm{p}|^2\sin^4(k_\mathrm{p}/2)}{(1-\omega_\mathrm{p}^2LC)\sin(k_\mathrm{p})}, \quad \gamma_\mathrm{sp} = \frac{8|A_\mathrm{p}|^2\sin^2(k_\mathrm{p}/2)\sin^2(k_\mathrm{s}/2)}{(1-\omega_\mathrm{s}^2LC)\sin(k_\mathrm{s})},$$

$$\gamma_\mathrm{si} = \frac{4|A_\mathrm{p}|^2\sin^2(k_\mathrm{p}/2)\sin(k_\mathrm{i}/2)\sin(k_\mathrm{p}-k_\mathrm{i}/2)}{(1-\omega_\mathrm{s}^2LC)\sin(k_\mathrm{s})}, \quad s \leftrightarrow i. \tag{3.51}$$

The parametric gain is defined as $g = \sqrt{\Delta k^2/4 - \gamma_\mathrm{si}\gamma_\mathrm{is}^*}$. Given the large mismatch, it is real. The mismatch Δk is defined as in Eq. (3.34). Again, we see a factor 2 between γ_pp and γ_sp (γ_ip)

Modulated array

We now turn to the case where we have a periodic modulation of the microscopic parameters of the array:

$$\begin{aligned} L_{n+1/2}^{-1} &= L_0^{-1}\left[1+\eta\cos G(n+1/2)\right], \\ C_{n+1/2} &= C_0\left[1+\eta\cos G(n+1/2)\right], \\ C_n^\mathrm{g} &= C_0^\mathrm{g}\left[1+\frac{\zeta}{2}\sum_\pm \cos G(n\pm 1/2)\right], \end{aligned} \tag{3.52}$$

where we kept the same notation defined in Section 3.4.1, except for the reciprocal lattice vector (previously denoted as K) defined now as $G = 2\pi/N_\mathrm{p}$. We changed the notation from K to G to stress that G is dimensionless. As we saw in the previous section, a weak modulation is enough to get a good correction in the mismatch and thus large amplification. In order to be as general as possible, we define two different modulation amplitudes. The modulation amplitude of the Josephson capacitance/inductance is denoted η. The modulation amplitude of the ground capacitance is denoted ζ. They are not necessary equal. We assume both amplitudes to be weak ($\eta, \zeta << 1$). As a recall, the goal of this section is

to have the actual dispersion relation of the array when a strong pump field is propagating by taking into account the nonlinear behavior of the gap. First and foremost, we must obtain the linear dispersion relation. The main ingredient in our approach is to consider that a signal propagating in the Josephson photonic crystal is a mixture of two plane waves:

$$\phi_n(t) = \left(Ae^{ikn} + Be^{i(k-G)n}\right) e^{-i\omega t} + \text{c.c.}. \tag{3.53}$$

Near the photonic gap ($k = G/2$), the two plane waves e^{ikn} and $e^{i(k-G)n}$ are mixed in a non perturbative way, even for a weak modulation. To determine the wavevector as a function of the frequency, we inject the general solution Eq. (3.53) in Eq. (3.47). We assume $0 < k < G$, we apply the RWA and we discard high spatial harmonics. Moreover, we consider $k << 1$, therefore $\sin(k/2) \approx k/2$, $\sin(G/2 - k/2) \approx G/2 - k/2$, $\cos(k/2) \approx \cos(G/2 - k/2) \approx 1$. We consider for now the linear case ($\sin(f) \approx f$, where f is the phase difference $(\phi_n - \phi_{n+1})$, it reads:

$$\left[\frac{\omega_\mathrm{p}^2}{\omega_\Pi^2 \ell_\mathrm{cs}^2} - k_\mathrm{p}^2\left(1 - \frac{\omega_\mathrm{p}^2}{\omega_\Pi^2}\right)\right] A + \left[\frac{\zeta}{2}\frac{\omega_\mathrm{p}^2}{\omega_\Pi^2 \ell_\mathrm{cs}^2} + \frac{\eta}{2} k_\mathrm{p}(G - k_\mathrm{p})\left(1 - \frac{\omega_\mathrm{p}^2}{\omega_\Pi^2}\right)\right] B = 0, \tag{3.54a}$$

$$\left[\frac{\zeta}{2}\frac{\omega_\mathrm{p}^2}{\omega_\Pi^2 \ell_\mathrm{cs}^2} + \frac{\eta}{2} k_\mathrm{p}(G - k_\mathrm{p})\left(1 - \frac{\omega_\mathrm{p}^2}{\omega_\Pi^2}\right)\right] A + \left[\frac{\omega_\mathrm{p}^2}{\omega_\Pi^2 \ell_\mathrm{cs}^2} - (G - k_\mathrm{p})^2\left(1 - \frac{\omega_\mathrm{p}^2}{\omega_\Pi^2}\right)\right] B = 0. \tag{3.54b}$$

Where $\ell_\mathrm{cs} = \sqrt{C_0/C_0^\mathrm{g}}$ is the Coulomb screening length and ω_Π the plasma frequency as previously defined. It is noteworthy that the plasma frequency stays constant from one junction to the other despite the periodic modulation. Eqs. (3.54a) and (3.54b) accept a solution different from the trivial solution $A = B = 0$. We find it by solving the determinant of this system. After calculation, we get a biquadratic equation in the wavevector k. The solution reads (see detailed calculations in Appendix A, Section A.2.2):

$$k = \frac{\mathrm{sign}\,(\kappa_\omega - \kappa_\mathrm{g})}{\ell_\mathrm{cs}} \sqrt{\frac{\left(\kappa_\omega^2 - \kappa_\mathrm{g}^2\right)^2 - u^4}{\kappa_\omega^2 + \kappa_\mathrm{g}^2 - \eta u^2/2 + \sqrt{D}}} + \frac{G}{2}, \tag{3.55}$$

where

$$\kappa_\omega^2 = \frac{\omega_\mathrm{p}^2}{\omega_\Pi^2 - \omega_\mathrm{p}^2} \quad , \quad \kappa_\mathrm{g}^2 = \frac{G\ell_\mathrm{cs}}{2} \quad , \quad u^2 = \frac{\eta}{2}\kappa_\mathrm{g}^2 + \frac{\zeta}{2}\kappa_\omega^2,$$

and

$$D = 4\kappa_\omega^2\kappa_g^2 + u^2(u^2 - \eta\left(\kappa_\omega^2 + \kappa_g^2\right)^2) + \frac{\eta^2}{4}\left(\kappa_\omega^2 - \kappa_g^2\right)^2.$$

Eq. (3.55) gives the linear dispersion relation of the modulated array. We plot it in Fig. 3.11**(a)**. Now, we need to get the nonlinear dispersion seen by the signal and the pump when the latter propagates in the array and shifts the gap. To properly tackle this problem, we assume the pump propagation to be unaffected by signal and idler, so it can be studied separately. The solution for the pump will then determine signal and idler propagation. We therefore focus first on the pump wave propagation while considering the nonlinearity of the array.

3.5.3 Pump wave propagation – SPM

As we saw in Eq. (3.53), the general solution for the pump is given by a non-perturbative mixture of two plane waves:

$$\phi_n^{\mathrm{P}}(t) = \left(A_{\mathrm{p}}e^{ik_{\mathrm{p}}n} + B_{\mathrm{p}}e^{i(k_{\mathrm{p}}-G)n}\right)e^{-i\omega_{\mathrm{p}}t} + \text{c.c.}, \tag{3.56}$$

whose coefficients A_{p} and B_{p} can be significantly affected by the weak nonlinearity. Moreover, both are equally important since the pump is very close to the gap. As a result, the gap position in frequency depends on the amplitudes of both waves. These two amplitudes will depend on the pump power: for a fixed pump input power, some is reflected while the rest is transmitted and is of course sensitive to the array dispersion and in particular to the gap position, which depends, in turn, on the wave amplitude within the array *etc.* The pump propagating inside the array as well as its reflection at the end of it must be determined *self-consistently* for a given input pump power. First, we inject the pump solution Eq. (3.56) into Eq. (3.47) but this time while expanding the nonlinearity up to the third order $\sin(f) \approx f - f^3/6$. Again, we assume $0 < k_{\mathrm{p}} < G$ and we omit high spatial and temporal harmonics, and approximate $\sin(k_{\mathrm{p}}/2) \approx k_{\mathrm{p}}/2$, $\sin(G/2 - k_{\mathrm{p}}/2) \approx G/2 - k_{\mathrm{p}}/2$, $\cos(k_{\mathrm{p}}/2) \approx \cos(G/2 - k_{\mathrm{p}}/2) \approx 1$:

$$\left[\frac{\omega_{\mathrm{p}}^2}{\omega_{\Pi}^2\ell_{\mathrm{cs}}^2}-k_{\mathrm{p}}^2\left(1-\frac{\omega_{\mathrm{p}}^2}{\omega_{\Pi}^2}\right)+\frac{k_{\mathrm{p}}^4}{2}|A_{\mathrm{p}}|^2+k_{\mathrm{p}}^2(G-k_{\mathrm{p}})^2|B_{\mathrm{p}}|^2\right]A_{\mathrm{p}}$$

$$+\left[\frac{\zeta}{2}\frac{\omega_{\mathrm{p}}^2}{\omega_{\Pi}^2\ell_{\mathrm{cs}}^2}+\frac{\eta}{2}k_{\mathrm{p}}(G-k_{\mathrm{p}})\left(1-\frac{\omega_{\mathrm{p}}^2}{\omega_{\Pi}^2}\right)\right]B_{\mathrm{p}}=0, \tag{3.57a}$$

$$\left[\frac{\zeta}{2}\frac{\omega_{\mathrm{p}}^2}{\omega_{\Pi}^2\ell_{\mathrm{cs}}^2}+\frac{\eta}{2}k_{\mathrm{p}}(G-k_{\mathrm{p}})\left(1-\frac{\omega_{\mathrm{p}}^2}{\omega_{\Pi}^2}\right)\right]A_{\mathrm{p}}$$

$$+\left[\frac{\omega_{\mathrm{p}}^2}{\omega_{\Pi}^2\ell_{\mathrm{cs}}^2}-(G-k_{\mathrm{p}})^2\left(1-\frac{\omega_{\mathrm{p}}^2}{\omega_{\Pi}^2}\right)+k_{\mathrm{p}}^2(G-k_{\mathrm{p}})^2|A_{\mathrm{p}}|^2+\frac{(G-k_{\mathrm{p}})^4}{2}|B_{\mathrm{p}}|^2\right]B_{\mathrm{p}}=0. \tag{3.57b}$$

We recognize the linear system where nonlinear terms proportional to $|A_{\mathrm{p}}|^2$ and $|B_{\mathrm{p}}|^2$ have been added. We have two equations to get three parameters A_{p}, B_{p} and k_{p}. To close the system, we need a boundary condition relating the input power, denoted P_{in}, in principle known by the experimentalist, to the pump amplitudes. To do so, we must consider the left part of the circuit, before the island n=0. This linear, $50\,\Omega$ environment is formally modeled by considering the linearized version of Eq. (3.47) $\sin(\phi_n-\phi_{n+1})\to(\phi_n-\phi_{n+1})$ and by setting the Josephson capacitance $C_{n+1/2}$ to 0 while the Josephson inductance $L_{n1+1/2}$ and ground capacitance C_n^{g} are set to L_{TL} and C_{TL} such that the characteristic impedance Z_{TL} is $50\,\Omega$. We expect as a solution:

$$\phi_{n<0}^{\mathrm{P}}(t)=\left(A_{\mathrm{in}}e^{ik_{\mathrm{TL}}n}+A_{\mathrm{r}}e^{-ik_{\mathrm{TL}}n}\right)e^{-i\omega_{\mathrm{p}}t}+\mathrm{c.c.}, \tag{3.58}$$

where $k_{\mathrm{TL}}=\omega_{\mathrm{p}}\sqrt{L_{\mathrm{TL}}C_{\mathrm{TL}}}$ is the transmission line wavevector. The boundary condition at n=0 for Eq. (3.47) and the continuity of the superconducting phase between Eq. (3.56) and Eq. (3.58) give respectively:

$$\frac{i\omega_{\mathrm{p}}L_{1/2}}{Z_{\mathrm{TL}}}(A_{\mathrm{in}}-A_{\mathrm{r}})=$$

$$\left[\left(1-\frac{\omega_{\mathrm{p}}^2}{\omega_{\Pi}^2}\right)(1+\eta)-\frac{|kA_{\mathrm{p}}+(k-G)B_{\mathrm{p}}|^2}{2}\right]\left[ikA_{\mathrm{p}}+i(k-G)B_{\mathrm{p}}\right], \tag{3.59a}$$

$$A_{\mathrm{in}}+A_{\mathrm{r}}=A_{\mathrm{p}}+B_{\mathrm{p}}. \tag{3.59b}$$

Pump reflection at the last site $n = N$ are neglected. We link the input pump amplitude to its input power by recalling $\mathrm{d}\phi_n/\mathrm{d}t = V_n\Phi_0$:

$$P_{\mathrm{in}} = \frac{V_{\mathrm{in}}^2}{Z_{\mathrm{TL}}} = \frac{2\omega_{\mathrm{p}}^2}{Z_{\mathrm{TL}}}\frac{\hbar^2}{(2e)^2}|A_{\mathrm{in}}|^2. \tag{3.60}$$

In this model, the pump power is directly set in watt in the equations. In our experiment, the pump is also set in watt, making it straightforward to compare with the theoretical pump power. By modeling boundary conditions we have added two more unknown parameters, making now five unknowns to find: $A, B, A_{\mathrm{in}}, A_{\mathrm{r}}$ and more importantly k_{p}. On the other hand, we have three more equations: Eqs. (3.59a), (3.59b) and (3.60), closing effectively the system. However, we cannot just solve it as a set of linear equations because of its nonlinear terms ($|A_{\mathrm{p}}|^2$ and $|B_{\mathrm{p}}|^2$). Actually, solving this system is not trivial since it might have no solution (pump within the nonlinear gap), one solution or several solutions. Among these solutions, some can propagate in the right direction but also in the *wrong* direction since the pump wave (Eq. (3.56)) contains both positive and negative wavevectors. The trick here is to infer for every set of solutions $A_{\mathrm{p}}, B_{\mathrm{p}}, k_{\mathrm{p}}$ in which direction energy is flowing. This can be done by checking the sign of P, the power carried by the pump wave within the array of junctions. P can be found by calculating the time derivative of the Lagrangian in Eq. (3.46) and using Eq. (3.47), it can be demonstrated that (see detailed calculations in the Appendix A Section A.2.3):

$$\begin{aligned} P = 2\omega_{\mathrm{p}}E_{\mathrm{J}}&\left[(k-\frac{G}{2})|A+B|^2 + \frac{G}{2}(|A|^2-|B|^2)\right] \\ &\times\left[\left(1-\frac{\omega_{\mathrm{p}}}{\omega_{\Pi}}\right)(1+\eta) - \frac{|kA+(k-G)B|^2}{2}\right]. \end{aligned} \tag{3.61}$$

After estimation of the sign of P, solutions leading to $P < 0$ are discarded for their unphysical character since they represent an energy flowing in the wrong direction. We see that setting the upper limit for the pump as the critical power ($P_{\mathrm{c}} = Z_{\mathrm{c}}I_{\mathrm{c}}$) is not accurate. Power upper limit should be defined as the power from which there is no physical solution for the pump. However, with this definition, upper limit would be dependent on pump frequency ω_{p} (the closer the pump is from the gap, the lesser power is required to enter in the gap.) Therefore, for the rest of the chapter, pump power will be directly expressed in watt. Now, we can solve the system of equations by sweeping either the pump frequency $\omega_{\mathrm{p}}/2\pi$ or the pump wavevector k_{p} with P_{in} as a parameter and obtain $A_{\mathrm{p}}, B_{\mathrm{p}}$ and k_{p} (or ω_{p}). We can either sweep 'up' or 'down' ω_{p} or k_{p}. Since these equation are solved self-consistently, solution might depends on the initial conditions of calculation. Eventually, we have the dispersion relation for any input power P_{in}. We can therefore reconstruct the dispersion relation and observe the effect of input power on the dispersion and on the photonic gap. In other words, we have access to

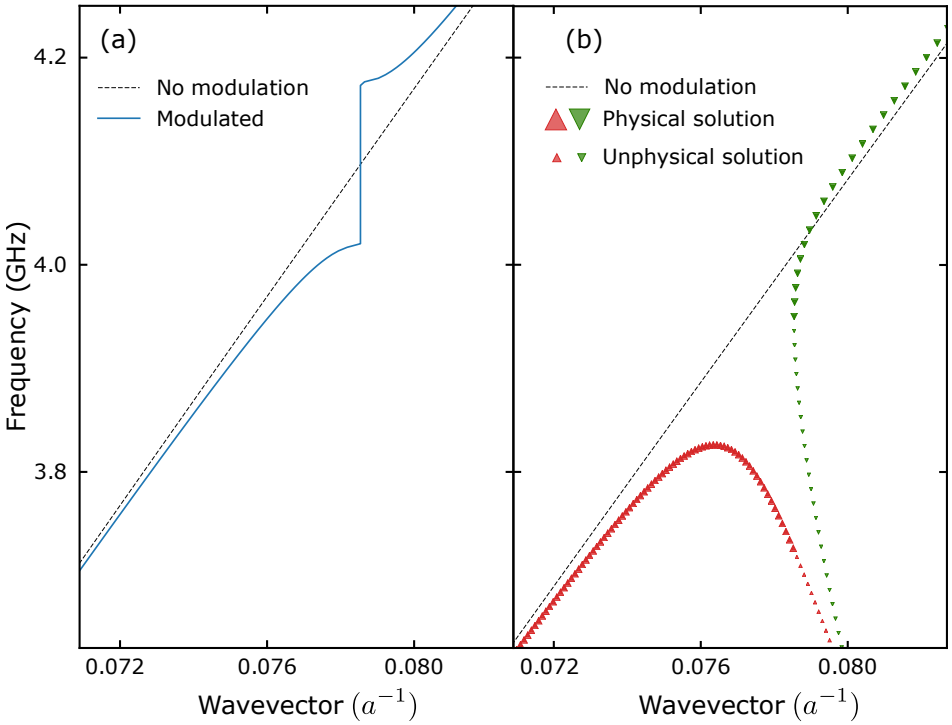

Figure 3.11 – **Effect of pump power on the photonic gap. (a)** Dispersion relation for very low power. **(b)** Dispersion relation after solving the pump wave propagation for $P_{\text{in}} = -74.5\,\text{dBm}$. Red triangles are pump frequencies ω_{p} found by solving the equations with the pump wavevectors k_{p} as the sweeping parameter while doing an upsweep. Green triangles are the opposite: k_{p} are found with ω_{p} as the sweeping parameter while doing a downsweep. The case where k_{p} is solved while upsweeping ω_{p} returns the same solution than when k_{p} is upswept and ω_{p} is calculated. Therefore solutions are superposed with the red triangles, but only up to 3.85 GHz (apex of the lower branch). For higher frequencies, there is no solution in k_{p}.

the self-phase modulation of the pump in the nonlinear photonic crystal while considering the effect of the pump on the gap itself, which is part of the final goal. These results are compiled in Fig. 3.11. In panel **(a)**, we plotted the linear dispersion relation with Eq. (3.55). In panel **(b)** we plotted the dispersion for larger input power ($P_{\text{in}} > 0$). Four situations are plotted: the dispersion of a non modulated array (i). The dispersion of a modulated array where the frequency is the sweeping parameter (upsweep (ii) and downsweep (iii)). The dispersion of a modulated array where the wavevector is the sweeping parameter (only upsweep (iv)). Situations (ii) and (iv) give the same results (see caption of Fig. 3.11). First

and foremost, the photonic gap is indeed shifted down to lower frequency when the pump power is increased. Indeed, this shift is comparable to the gap width itself. We also notice that depending whether the sweep goes up or down, the solutions found are not the same: this comes from the self-consistency of the calculation carried out. Finally, we notice that while we sweep up k_p to get ω_p we have, sometimes, in the lower branch, two solutions. Also, we do have these unphysical solutions where the energy actually flows in the opposite direction as the input pump power. The stability of these solution have not been studied during my PhD but this might lead to interesting phenomenon to understand both theoretically and experimentally.

3.5.4 Signal and idler wave propagation – XPM

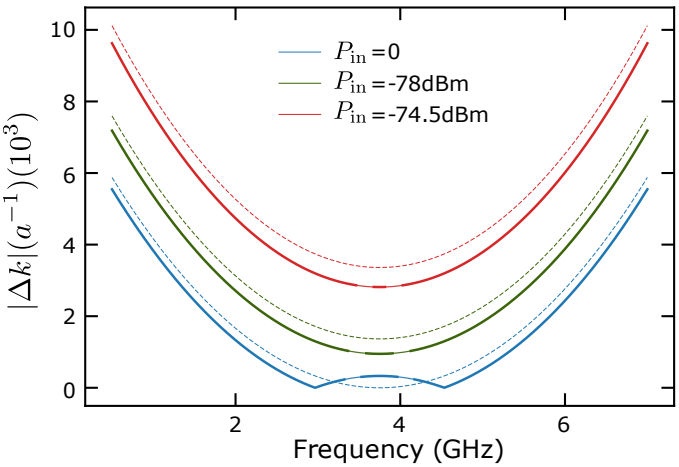

Figure 3.12 – **Total phase mismatch.** $|\Delta k|$ *vs.* frequency with the pump power as a parameter and pump frequency set to 3.75 GHz. We use Eq. (3.64) to calculate $|\Delta k|$. Since this formula is only valid for k_s far enough from the gap, we 'removed' the gap regions by plotting it with a thin line.

Now that we have found the solution for the pump wave $\phi_n^\mathrm{P}(t)$, we can include the signal and the idler as a weak perturbation of the total superconducting phase $\phi_n(t)$:

$$\phi_n(t) = \phi_n^\mathrm{P}(t) + (\phi_n^\mathrm{s}(t)e^{i\omega_\mathrm{s}t} + \text{c.c.}) + (\phi_n^\mathrm{i}(t)e^{i\omega_\mathrm{i}t} + \text{c.c.}). \tag{3.62}$$

The idea is the same as in Section 3.2: we insert Eq. (3.62) into Eq. (3.47) while we linearize it with respect to the signal and idler. We introduce the notation

$\bar{\omega}_\mathrm{j} = \omega_\mathrm{j}/\omega_\Pi$ where $\mathrm{j} = \{\mathrm{s}, \mathrm{i}\}$. For $n \in [1, N-1]$:

$$\frac{\bar{\omega}_\mathrm{s}^2}{l_\mathrm{cs}} \left(1 + \zeta \cos\left(Gn\right)\right) \phi_n^\mathrm{s} + J_{n+1/2}^\mathrm{s} - J_{n-1/2}^\mathrm{s} = 0, \tag{3.63a}$$

$$\frac{\bar{\omega}_\mathrm{i}^2}{l_\mathrm{cs}} \left(1 + \zeta \cos\left(Gn\right)\right) \left(\phi_n^\mathrm{i}\right)^* + \bar{J}_{n+1/2}^\mathrm{i} - \bar{J}_{n-1/2}^\mathrm{i} = 0, \tag{3.63b}$$

$$J_{n+1/2}^\mathrm{s} = \left(1 + \eta \cos\left(G\left(n + \frac{1}{2}\right)\right)\right) \times \left[\left(1 - \bar{\omega}_\mathrm{s}^2 - |\partial\phi_{n+1/2}^\mathrm{P}|^2\right) \partial\phi_{n+1/2}^\mathrm{s} - \frac{1}{2}\left(\partial\phi_{n+1/2}^\mathrm{P}\right)^2 \left(\partial\phi_{n+1/2}^\mathrm{i}\right)^*\right], \tag{3.63c}$$

$$\bar{J}_{n+1/2}^\mathrm{i} = \left(1 + \eta \cos\left(G\left(n + \frac{1}{2}\right)\right)\right) \left[\left(1 - \bar{\omega}_\mathrm{i}^2 - |\partial\phi_{n+1/2}^\mathrm{P}|^2\right) \left(\partial\phi_{n+1/2}^\mathrm{i}\right)^* - \frac{1}{2}\left(\left(\partial\phi_{n+1/2}^\mathrm{P}\right)^*\right)^2 \partial\phi_{n+1/2}^\mathrm{s}\right]. \tag{3.63d}$$

We denoted $\partial\phi_{n+1/2} \equiv \phi_{n+1} - \phi_n$. It makes in total $N-1$ equations for the signal and so does for the idler. It misses at least one equation for each to close the linear set of equations. However, before closing it, we can show that Eq. (3.63) is enough to get the signal and idler wavevectors. Making the assumption that they are far enough from the gap, we can assume that their $e^{i(k-G)n}$ component can be discarded. In that case, signal and idler wavevectors can be written:

$$k_\mathrm{s}^2 = \frac{\bar{\omega}_\mathrm{s}^2/l_\mathrm{cs}^2}{1 - \bar{\omega}_\mathrm{s}^2 - k_\mathrm{p}^2|A_\mathrm{p}|^2 - \left(k_\mathrm{p} - G\right)^2|B_\mathrm{p}|^2} \qquad (s \leftrightarrow i). \tag{3.64}$$

In the denominator of the right-hand side of Eq. (3.64), the two first terms are standard for a dispersion relation with a plasma frequency ω_Π and we find back Eq. (3.28). The next two terms are less conventional and account for the pump effect on the signal and idler phase. They typically are **cross-phase modulation** terms: pump amplitude generates an increase of the signal (idler) phase, which is expected. However, this formula does not take into account the gap position nor its displacement because of the pump power. With this expression for signal/idler wavevectors and with the derivation made in Section 3.5.3 to get the pump parameters $(A_\mathrm{p}, B_\mathrm{p}, k_\mathrm{p})$, we can now calculate easily the phase mismatch Δk while taking into account SPM **and** XPM effects. In Fig. 3.12, we have plotted $|\Delta k|$ for various pump powers for the same pump frequency ω_p, very close to the gap. For $P_\mathrm{in} = 0$, around the pump frequency, the phase mismatch is actually

worse with a periodic modulation, as expected. As soon as P_{in} starts to be large enough, we observe an improvement in this region. Moreover, when P_{in} increases, the mismatch is decreased on the whole frequency band. The region where the solid lines are thinner is where the gap lies. They are symmetric with respect to the pump frequency to account for the gap seen by the signal **and** by the idler (as explained in Section 3.4.3). We have artificially 'removed' these gap regions. We simply reported the shifted gap region (see Section 3.6) as a thin line in the plot. However, the TWPA bandwidth is much larger than the actual width of the photonic gap so it is only a small region.

3.5.5 Phase matching of various non-linear processes

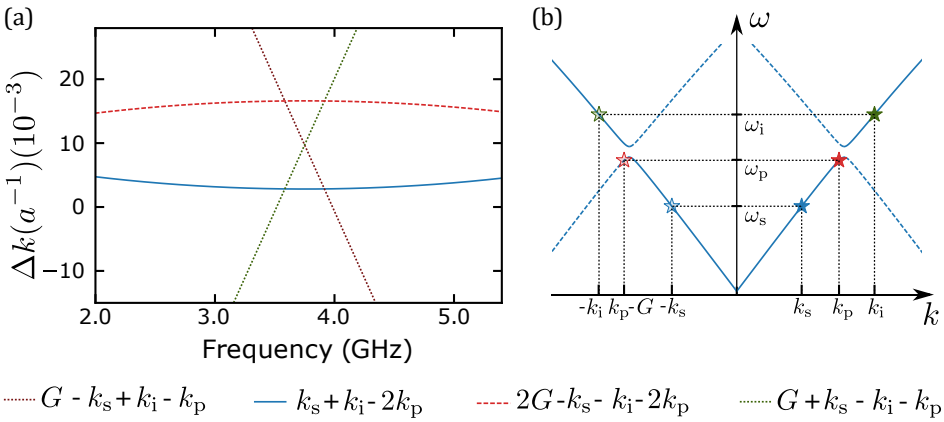

Figure 3.13 – **Mismatch for different wavevectors combinations. (a)** Approximate mismatch for four different combinations as a function of the signal frequency. The pump frequency is set to 3.75 GHz while its power is set to −74.5 dBm. Overall, the standard 'forward' process ($k_s + k_i - 2k_p$) has the lowest phase mismatch compared to 'backward' processes ($2G - k_s - k_i - 2k_p$ for instance). It makes the forward process the most favorable one among the different processes. **(b)** Cartoon of the dispersion relation with an exaggerated modulation amplitude to emphasize the effect of the gap. For the forward amplification process (plain stars, positive wavevectors), wavevectors are evenly spaced, hence guarantying a proper phase matching. For the same frequency, the backward amplification process is not matched since wavevectors are not evenly spaced.

Having an analytical expression for the signal/idler wavevectors accounting for cross phase modulation is also useful to calculate mismatch for different combinations between signal, idler, pump and the reciprocal lattice wavevectors. Indeed, as O'Brien *et. al* pointed out [81], with a periodic lattice, dispersion relation can be defined modulo G, the reciprocal lattice wavevector ($\omega(k) = \omega(k + G)$). Thus, if the relation $2k_p \approx k_s + k_i$ is true, while knowing that $k_p \approx G/2$, then the

relation $2\,(k_\mathrm{p} - G) \approx -k_\mathrm{s} - k_\mathrm{i}$ should hold as well. This would mean that a signal propagating in the opposite direction as the pump could be amplified. This could be very detrimental for the amplifier since any noise coming from the output of the amplifier could 'leak' towards the input of the amplifier, be amplified and scramble the device under measurement. In other words, it cancels the directionality of the amplifier, which is something we want to avoid. However, using the approximate formula Eq. (3.64), we calculated the phase mismatch of such event (and others involving G) in order to check to which extent these events are favorable. In Fig. 3.13**(a)**, we plotted four matching combinations. Pump parameters (P_in and ω_p) are chosen to give a good amplification profile as we will see in the next section (20 dB of maximum gain). Among the four calculated phase mismatch, the 'forward' amplification process shows the best phase matching. We can explain that with 'geometrical' arguments. We plotted the dispersion relation with an exaggerated gap and highlighted counter propagating and forward propagating wavevectors (and corresponding frequencies) in Fig. 3.13**(b)**. We can see that for the forward process, k_s and k_i are evenly separated from k_p leading to Δk close to 0 while for the counter propagating case (negative wavevectors) $-k_\mathrm{s}$ and $-k_\mathrm{i}$ are not evenly separated from $k_\mathrm{p} - G$ making this process less likely to happen. Despite the pump being indeed close to the gap, the assumption $k_\mathrm{p} \approx G/2$ is not entirely correct. For instance, in this particular case where pump parameters are chosen close to the gap to give 20 dB, k_p is still $\approx 6\%$ away from $G/2$, which is a substantial difference. These observations are reassuring for the future TWPA performances. Even though having simple analytical expressions for the XPM is useful to understand the power dependence of Δk and to investigate the phase-matching of various non-linear processes, we still need to fully solve the set of linear equations (Eqs. (3.63a) and (3.63b)) to get the gap shift seen by the signal. To do so, we need to consider the complete expression for the signal and idler waves (*i.e.* considering the $e^{i(k-G)n}$ component) and add the boundary conditions.

3.6 Parametric amplification in a Josephson photonic crystal

3.6.1 Boundary conditions

To close the linear set of equations in Eq. (3.63), we must consider boundary conditions for both signal and idler. The idea is *in principle* the same as for the pump wave propagation: we consider that on the left and right side of the junctions array we have linear 50 Ω transmission lines and conservation of the amplitudes. We have the following situations: the signal is injected from the left side of the array, a major part is transmitted and some is reflected. There is no idler injected. At the end of the array ($n = N$), we **do** consider signal and idler reflection (unlike the pump wave). We model signal reflection despite the good impedance matching since we investigate counter-propagating amplification. We denote A^s_in the incoming signal amplitude at $n = 0$ and $A_\mathrm{in} - \phi^\mathrm{s}_0$ the reflected one; at site $n = N$, the outgoing signal amplitude is denoted ϕ^s_N. For the idler,

there is no incoming wave and the outgoing idler amplitudes are denoted ϕ_0^{i} and ϕ_N^{i} at site 0 and N, respectively. To take into account these boundary conditions, it amounts to define four new entities, noted $J_{-1/2}^{\mathrm{s,i}}$ and $J_{N+1/2}^{\mathrm{s,i}}$, to be injected in Eqs. (3.63a) and (3.63b):

$$J_{-1/2}^{\mathrm{s}} = \frac{\partial \phi_{-1/2}^{\mathrm{s}}}{L_{\mathrm{TL}}\omega_{\Pi}^2 l_{\mathrm{cs}} C^{\mathrm{g}}} = \frac{i\omega_{\mathrm{s}}}{\omega_{\Pi} l_{\mathrm{cs}}} \frac{Z_{\mathrm{c}}}{Z_{\mathrm{TL}}} \left[2A_{\mathrm{in}}^{\mathrm{s}} - \phi_0^{\mathrm{s}}\right], \tag{3.65a}$$

$$\bar{J}_{-1/2}^{\mathrm{i}} = \frac{\left(\partial \phi_{-1/2}^{\mathrm{i}}\right)^*}{L_{\mathrm{TL}}\omega_{\Pi}^2 l_{\mathrm{cs}} C^{\mathrm{g}}} = \frac{i\omega_{\mathrm{i}}}{\omega_{\Pi} l_{\mathrm{cs}}} \frac{Z_{\mathrm{c}}}{Z_{\mathrm{TL}}} \left(\phi_0^{\mathrm{i}}\right)^*, \tag{3.65b}$$

$$J_{N+1/2}^{\mathrm{s}} = \frac{\partial \phi_{N+1/2}^{\mathrm{s}}}{L_{\mathrm{TL}}\omega_{\Pi}^2 l_{\mathrm{cs}} C^{\mathrm{g}}} = \frac{i\omega_{\mathrm{s}}}{\omega_{\Pi} l_{\mathrm{cs}}} \frac{Z_{\mathrm{c}}}{Z_{\mathrm{TL}}} \phi_N^{\mathrm{s}}, \tag{3.65c}$$

$$\bar{J}_{N+1/2}^{\mathrm{i}} = \frac{\left(\partial \phi_{N+1/2}^{\mathrm{i}}\right)^*}{L_{\mathrm{TL}}\omega_{\Pi}^2 l_{\mathrm{cs}} C^{\mathrm{g}}} = -\frac{i\omega_{\mathrm{i}}}{\omega_{\Pi} l_{\mathrm{cs}}} \frac{Z_{\mathrm{c}}}{Z_{\mathrm{TL}}} \left(\phi_N^{\mathrm{i}}\right)^*. \tag{3.65d}$$

A convenient point is that the system is entirely symmetric and counter-propagating amplification can also be studied by setting the input signal at site $n = N$ while the pump is still injected from $n = 0$. The system is now closed, and the amplitude at each site can be brute force numerically calculated. Moreover, every amplitude is proportional to the input signal amplitude $A_{\mathrm{in}}^{\mathrm{s}}$, so the gain $\phi_N^{\mathrm{s}}/A_{\mathrm{in}}^{\mathrm{s}}$ can be straightforwardly calculated (see the Appendix A, Section A.2.4 to see how we numerically calculated it.)

3.6.2 Modeling the amplification site by site

The strength of this model is the absence of any assumptions on the signal and idler shapes. The $2(N+1) \times 2(N+1)$ set of linear equations is brute force solved numerically. Solution at each site n is proportional to A_{in}. Signal gain is therefore easily defined for each site n and we can follow how the signal amplitude evolve site by site. In Fig. 3.14**(a)**, the signal gain $|\phi_n^{\mathrm{s}}/A_{\mathrm{in}}^{\mathrm{s}}|$ is plotted as a function of the site number n. We plotted two cases where the signal is propagating in the same direction and in the opposite direction, with respect to the pump propagation direction. In both cases, the mean value of the signal gain increases as the signal progresses in the array. We have chosen frequencies close to the pump frequency in order to get high gain in both cases. The backward gain starts from the right side of the array but is very small compared to the forward amplification. Since we have the wave profile site by site, we can perform a spatial Fourier transform to see the wavevectors composition of the signal:

$$\phi^{\mathrm{s}}(k) = \sum_{n=0}^{N} \phi_n^{\mathrm{s}} e^{-ikn}. \tag{3.66}$$

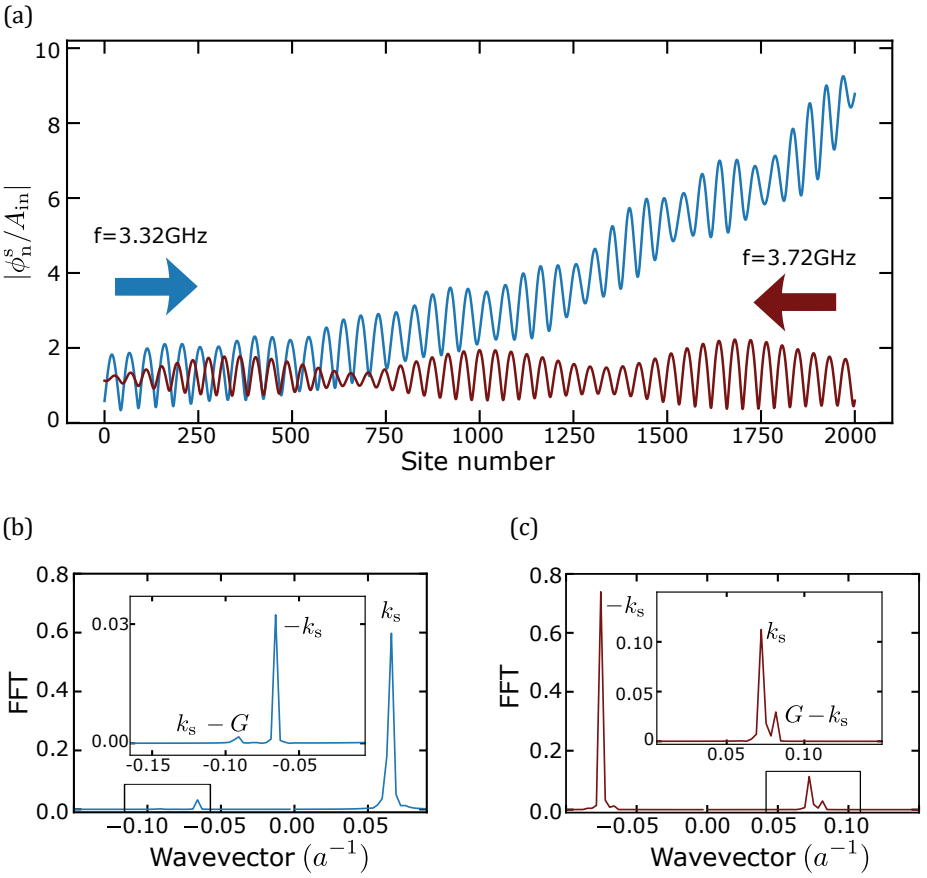

Figure 3.14 – **Forward and backward signal amplification. (a)** Signal gain as a function of the site number when co-propagating (solid blue line) and counter-propagating (red solid line) with respect to the pump wave ($P_{in} = -74.5\,\text{dBm}$, $\omega_p = 3.75\,\text{GHz}$). We see in both case an increase in the mean value. The co-propagating wave is much more amplified than the counter-propagating one. **(b)** and **(c)** Fourier transform (as defined in Eq. (3.66)) of the signals (same color code as in **(a)**).

In Fig. 3.14**(b)** and **(c)** we plotted $\phi^s(k)$. In both cases (forward and backward), we observe three peaks. For the 'forward' wave, the three peaks correspond to $k_s, -k_s$ and $k_s - G$ which is negative ($\omega_s < \omega_{gap}$, $\omega_{gap}/2\pi$ is the gap frequency). The $k_s - G$ component is indeed low. This is explained because the signal is far enough from the gap ($k_s = 0.85 \times G/2$) and therefore the $e^{i(k-G)n}$ component is very low. This proves that our assumption was correct in Section 3.5.4 when we discarded the $e^{i(k-G)n}$ component to get the analytical expression of k_s

in Eq. (3.64).

3.6.3 Gap displacement

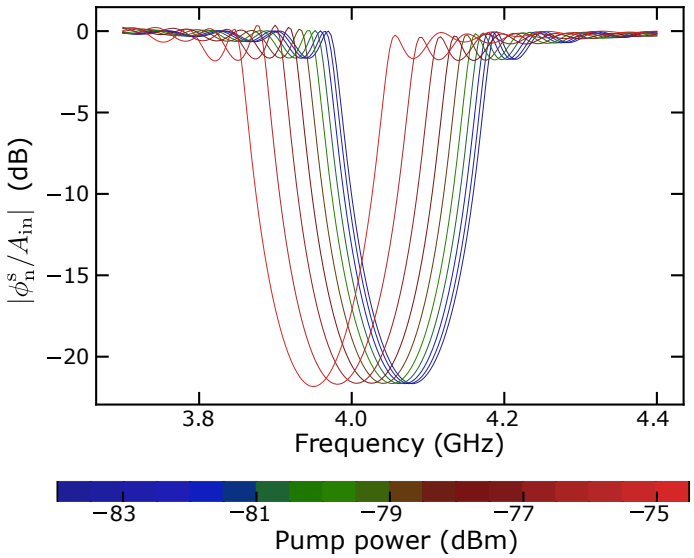

Figure 3.15 – **Expected cross phase modulation of the photonic gap.** Signal transmission as a function of its frequency. Color encodes the pump input power P_{in}. Pump frequency is fixed at $\omega_{\text{p}} = 2.0\,\text{GHz}$. P_{in} shifts the gap position and drag it to lower frequencies as it was experimentally shown in Fig. 3.9. Between the blue and red transmission, the gap shifts more than its own width.

Before showing an actual gain profile calculated with the brute force numerical calculation, we can check the expected effect of the pump power on the gap position. What we showed in Fig. 3.11 is the impact of the self-phase modulation on the gap position. We are now showing cross phase modulation of the gap. The protocol is the following: we set ω_{p} far away from the gap position, while we solve the linear equations for the signal close the gap frequency. We solve it for several pump amplitude P_{in} while we keep ω_{p} constant. In Fig. 3.15, we show signal transmission $|\phi_N^{\text{s}}/A_{\text{in}}^{\text{s}}|$ on a frequency band centered around the gap. Pump is far detuned so there is no amplification effect in this window. This plot is the theoretical counterpart of the experimental plot shown in Fig. 3.9. For larger pump power we can indeed see that the gap position goes towards lower frequencies. This model successfully managed to predict the nonlinear effect of pump power over the gap at least, for now, qualitatively. As we will see Chapter 8, there is a quantitative agreement and we can use this gap shift to have an actual calibration of the setup attenuation. It allows to compare the experimental pump

power sent from room temperature with the unknown pump power received by the TWPA at cryogenic temperature for the same gap displacement.

3.6.4 Amplification *vs.* frequency

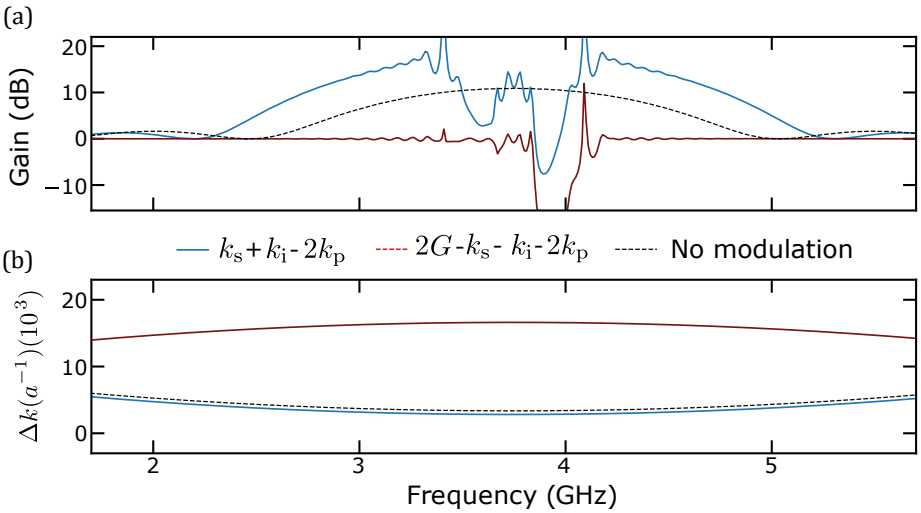

Figure 3.16 – **Gain and mismatch.** The legend between the two panels refers to both panels. **(a)** Signal power gain *vs.* frequency. Pump parameters are $P_{\text{in}} = -74.5\,\text{dBm}$ and $\omega_{\text{p}} = 3.75\,\text{GHz}$. We see the improvement between a modulated and a bare array. **(b)** Phase mismatch versus signal frequency. From this perspective, we can see how much mismatched the backward amplification is.

We finally close this chapter by showing the expected gain profile for a photonic crystal Josephson TWPA. Pump parameters are chosen such that the maximum gain is 20 dB ($P_{\text{in}} = -74.5\,\text{dBm}$ and $\omega_{\text{p}} = 3.75\,\text{GHz}$). The chain parameters are the ones used along this chapter, $N = 2000$, $N/N_{\text{p}} = 50$ and $\eta = \zeta = 4\%$. First, pump propagation is self consistently solved and its parameters are injected in the set of linear equation Eq. (3.63). Eventually, we solve this system and find the gain $|\phi_N^{\text{s}}/A_{\text{in}}|$. The computation time is about 20 s for 800 points. This computation time includes calculation of the transmission and reflection of both signal and idler. In Fig. 3.16, we have plot the forward gain with a modulated and a non modulated array. We also plot the counter-propagating gain, for the same pump parameters. The gain profiles look like what we have found in the previous section but this time with the correct gap position. Of course we observe a great enhancement of the amplifier performance thanks to the periodic modulation. More than 5 dB in the maximum gain with a larger bandwidth. Except for some sporadic peaks, there is almost no gain for a signal propagating backward. To explain these different gain profile, we also plot in Fig. 3.16**(b)**, the corresponding

phase mismatch for each process. A difference in the phase mismatch as little as the one between the modulated and the bare array leads to almost 5 dB difference in the maximum gain. Hence, it is not surprising that a difference in the phase mismatch as large as there is between the forward and backward gain leads to a complete absence of gain for the latter

To conclude, we managed to quantitatively take into account the gap shift during the amplification process by first solving the pump wave propagation and then solving the signal and idler propagation as perturbations. This chapter covers the different theoretical treatments for a Josephson traveling-wave parametric amplifier and what are our expectations. The next chapter will be dedicated, *inter-alia*, to the actual fabrication of traveling-wave parametric amplifiers.

Circuit design and fabrication 4

Contents

This chapter aims to describe the design and the fabrication process of the samples measured throughout this PhD thesis. In the first section we will present a short review of the bridge free fabrication (BFF) technique, used to obtain long Josephson arrays. What we call Josephson arrays in this chapter includes both Josephson junctions and superconducting quantum interference devices (SQUID) arrays. We will highlight what we consider to be important points to fabricate Josephson arrays. The next sections will be dedicated to the top ground deposition (TGD) technique, used to drastically increase the ground capacitance per unit length of the arrays. After discussing microwave simulations and design of very low impedance Josephson arrays transmission lines (TL), we will detail the actual fabrication recipe of the TGD technique.

Link back to Table of contents →

4.1 Josephson array fabrication

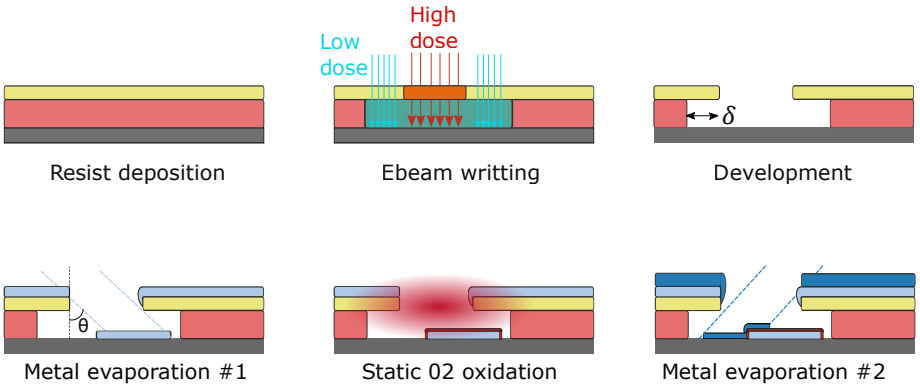

Figure 4.1 – **Steps of the BFF technique** From left to right, top row to bottom row. **Spin-coating:** two layers of resist are spin-coated on each other. **Writing:** the resist is then exposed to the electron beam (ebeam). The bottom one is more sensitive to the ebeam than the top one. **Development:** after development of the resist, an undercut of length δ is carved in the resist. **Evaporation 1:** A first layer of aluminum is deposited via metal evaporation with an angle $+\theta$. **Oxidation:** the first layer of aluminum is oxidized. **Evaporation 2:** a second layer is evaporated with an angle $-\theta$.

Every sample fabricated and measured during this PhD – whether they were resonant amplifiers, traveling-wave amplifiers or even test resonators – were all arrays of SQUID. From relatively short $\lambda/4$ resonators made of 80 SQUIDs to 2000-SQUID-long transmission lines, their common characteristic was they were all distributed Josephson materials. Such non-trivial systems, composed of repeated and complex unit cells, ask for a dramatic control over their uniformity or, in other words, **disorder**. Disorder in an array of repeated cell comes from the spread of one or more characteristic parameters around the targeted value, inherent to any fabrication process. In a first approach, what characterizes a Josephson junction or a SQUID is its inductance L and its capacitance C. These electrical characteristics are related to physical parameters: the tunnel barrier thickness t_t of the junction and its area A. To obtain very low disorder on both t_t and A in Josephson arrays, we must perform a single step electron beam (shorted as ebeam) lithography followed by a double angle metal evaporation with an *in-situ* oxidation. Ebeam lithography allows for a good homogeneity over A because of its remarkable spatial resolution. On the other hand, *in-situ* oxidation allows for a good homogeneity over t_t since all the tunnel barriers are grown at the same time and pressure is supposed to be homogeneous in the deposition chamber. In the next subsection, we describe a fabrication technique allowing for low disorder: the bridge free fabrication (BFF) technique (see Fig. 4.1). This technique was

initially developed by **Florent Lecocq** [90] and recently optimized for arrays fabrication by another PhD student of the SCG group, **Javier Puertas-Martinez**. He thoroughly described the BFF process in his PhD thesis [91]. Even though this present PhD work is not the one which implemented it for the first time, an important part of the fabrication of resonant JPAs and TWPAs relies on this process. In order to be fully consistent and to provide a stand-alone PhD thesis, we will review what we consider to be of prime importance for the realization of Josephson arrays for quantum limited amplifiers.

4.1.1 The bridge free fabrication technique

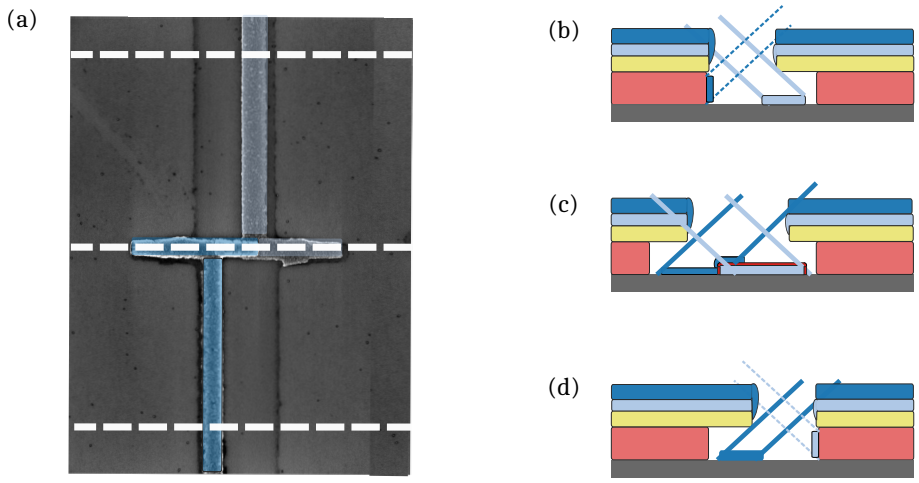

Figure 4.2 – **Fabrication of a of a single Josephson junction with the BFF technique. (a)** Scanning electron microscope (SEM) picture of a single Josephson junction. It does not correspond to the actual design used for our arrays, but it illustrates perfectly the BFF technique. **(b)** Asymmetric undercut to allow the $+\theta$ metal evaporation. **(c)** Symmetric undercut for metal overlapping. **(d)** Asymmetric undercut to allow the $-\theta$ metal evaporation. Pictures taken from reference [91] with the courtesy of **J. Puertas-Martinez**.

The BFF technique solves the three principal problems of the most well-known and commonly used fabrication technique for small-area Josephson junctions known as Niemeyer-Dolan technique [92]. First of all, it avoids shadow patterns. Second of all, it avoids suspended bridge, which allows a cleaner region where the metal is deposited. Lastly, it enables large junction fabrication without having a collapse of the suspended bridge. The latter is the most important regarding our devices since the junctions we use for our amplifiers have particularly large areas (few μm^2).

e-beam lithography & double angle evaporation

As for any lithography, the resist on which patterns are written reacts for a certain type of electronic of electromagnetic beam shone on it. The precision of the writing process will come from the wavelength of the beam used. Structures smaller than the wavelength of the beam itself are almost impossible to fabricate. Electronic wavelength is smaller than electromagnetic wavelength used in the microelectronic field. Not only finer structures can be written, but the overall precision on the structures is also enhanced, which is sought to cancel the disorder in the area A. Given the dimension of one SQUID needed to fabricate Josephson amplifiers – between $3\,\mu m^2$ and $5\,\mu m^2$ for standard conditions of oxidation – a laser lithography is already enough. For instance, in a collaborative work with the group of Ioan Pop in Karlsruhe, we managed to fabricate non-degenerate, four-wave mixing amplifiers made of Josephson arrays with an optical lithography process [68]. However, obtaining even longer arrays up to few **millimeter** long and getting the precision required to make periodic modulation with an amplitude of few percent without an ebeam writer would be, in our opinion, highly difficult. To sum up, doing an ebeam lithography help to keep low disorder over A, the area of the junction. During this step, two resists are used: PMMA-MAA (9%) as the bottom layer and PMMA (4%) as the upper layer, shown in Fig. 4.1 and in Fig. 4.2. They differ by their sensitivity with respect to the ebeam (the lower layer is more sensitive). Difference in sensitivity makes possible to obtain *undercut* structures. During the lithography, we distinguish two kind of undercuts:

— the symmetric undercut as shown in Fig. 4.1 and in Fig. 4.2**(c)** have controlled undercut on both sides. It allows to create the tunnel junction *per se*, because symmetric undercuts allow to have superposition of two metallic layers.

— The asymmetric undercut as shown in Fig. 4.2 **(a)** and **(c)**. It allows to fabricate the connecting wires between the junctions since there is no metal overlap.

This alternation between symmetric and asymmetric undercuts makes possible the fabrication Josephson arrays. Moreover, undercut areas are accessible by an isotropic reactive ion etching, made with a low power oxygen plasma, to remove remaining resist after its development.

In-situ oxidation

Regarding the thickness of the tunnel barrier, its homogeneity throughout the whole Josephson array is also of prime importance. Making it homogeneous all over an array of few millimeter long is possible if the oxidation of all the junctions is done during the same step. Since the BFF is a single step lithography, the first metallic layer is deposited and oxidized *in-situ* (Fig. 4.1) in the same chamber and without venting it. Hence, there is a very good homogeneity of the tunnel thickness

t_t. Using this process **J. P-M.** could demonstrate a 3% homogeneity [91]. One of the major concern about it is the exponential dependence of the Josephson inductance L with respect to t_t.

4.1.2 Focus

The BFF technique is well suited to low disorder and to have a homogeneous array of Josephson junctions. Another issue when fabricating such long arrays is managing to connect all the junctions and avoid opens. The connecting wires between each junction have width below the micron and length in the one micron range. Writing such structures with an ebeam asks for (i) a precise motion of the writing tool and (ii) a perfect focus of the beam on the resist. To fulfill (i), the 2 inch wafer is divided into 300 µm × 300 µm squares. This division is called the main field (each of these square is itself divided into 20 µm × 20 µm squares and called 'sub field'). To go from one main field to the other, the wafer chuck is moving; whereas within a mean field square, a higher precision is sought and the beam itself is moving with magnetic deflection coils. About point (ii), a perfect focus of the beam must be maintain over the 2" wafer in order to avoid 'stitching' errors. Focus problems come from for the unavoidable tilt of the wafer in the chamber. To take this tilt into account, the wafer is locally fitted as a tilted plan. For instance, if the wafer is divided into 16 chips (see Fig. 4.4), the whole writing process will undergo 16 local fits, one for each chip. Then, within one chip, the beam will dynamically change its focus – with respect to the fitted plan – for each sub field (20 µm × 20 µm squares).

4.1.3 Sample design

All the sample designs have been drawn on a CAD software called KLayout which exports in .gds. These .gds are themselves exported in .npf extension, read by the ebeam writer.

Design of the array

For all the fabricated samples (mainly resonant JPAs and TWPAs), the design used for the SQUIDs was the same. This design is shown in Fig. 4.3(**a**), (**b**) and (**c**), where three SQUIDs (six junctions) are drawn. Two junctions, their two bridges and one connecting wire make one unit cell of length a. The width w and height H of one junction are chosen in order to have $A \approx 5\,\mu m^2$, which is above the average area for junctions in cQED. w is chosen to be between 400 nm and 450 nm while H is between 10 µm and 12 µm. We have chosen H to be larger than w in order to maximize the number of junctions per unit length. BFF technique is therefore relevant because it avoids long bridges to collapse. For the 'bulk' of the array, the pattern shown in the three first panels can be repeated up to thousand times [93, 94]. In the previous chapter, we saw that a periodic modulation of the Josephson array could help the phase matching issue that Josephson traveling-wave parametric amplifiers (J-TWPA) are facing. We must periodically modulate

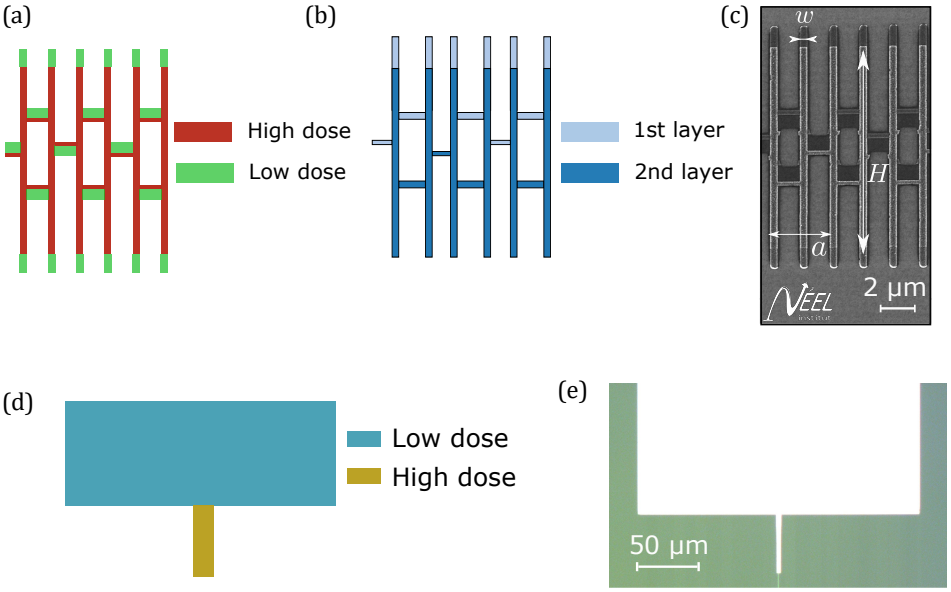

Figure 4.3 – **SQUIDs and bonding pads design. (a)** Dose diagram used for the SQUIDs. The exact numbers are reported in Table 4.1. **(b)** Aluminum layers. **(c)** SEM picture of 3 SQUIDs and their characteristic lengths. We stress that the height H corresponds to the **overlap** of the two aluminum layers. **(d)** Dose diagram of a bonding pad for a resonant JPA. The narrower wire (yellow) is a buffer to protect the SQUIDs from proximity effects due to the large pads. **(e)** Optical picture of a pad. the bright white parts are the deposited aluminum.

the area of the junctions/SQUIDs along the array to open a photonic gap. (**Note**: naturally, two junctions within the same SQUID are identical). To implement it, we have decided to modulate periodically their height H only. Their width and the length of the unit cell remain therefore constant throughout the array. We use Python scripts to automatically generate gds files of arrays where the height is modulated with an amplitude η of few percents. The height of the n^{th} SQUID reads $H_n = H_0(1 + \eta \cos 2\pi n/N_\text{p})$, where H_0 is the mean height and N_p is the number of junctions/SQUIDs per period. Our long arrays for TWPA are typically 2000 SQUIDs long, with N_p between 40 and 50 SQUIDs.

Design of the bonding pads

Let us turn to the boundary conditions of the array. To do everything in a single step, bonding pads must be written and deposited during the same steps as the junctions. Bonding pads, in addition to receiving wire bonds, must have the right microwave geometry in order to transmit correctly the signal and avoid impedance

mismatch with the setup. Given their large areas, proximity effects should be taken care of to avoid that they scramble the fine structures of the junctions. This is why we always write 'buffer' wires (see Fig. 4.3**(d)**) and **(e)**) between the pads and the array, with much smaller areas. Since they are narrower, these wires are written with larger dose for a better development.

4.1.4 Fabrication recipe

The fabrication recipe for a Josephson array is summarized in Table 4.1.

Preparation of the wafer

A batch is written on a 2 inch, single side polished, 275 µm ± 25 µm thick, intrinsic silicon wafer (see Fig. 4.4). Prior to any step, the wafer is gold plated on its unpolished side to ensure good electric and thermal contacts between the chip and the chip-carrier. Before the fabrication of the array, we pattern markers on the wafer. These markers are necessary to align the wafer within the frame of the ebeam writer but also for focus purposes. For marks, it follows the usual scheme: writing ⇨ development ⇨ metal deposition ⇨ lift-off.

Writing

The wafer is first covered by one layer of PMMA-MAA (9%, thickness≈ 250 nm) and PMMA (4%, thickness ≈ 800 nm). Small structures (junctions) are written first with the ebeam followed by large structures (pads) because high current makes the column hotter and requires some time for proper thermalization of the machine. The wafer is then developed in a mix of MIBK-IPA (1:3) and rinsed in IPA.

Aluminum evaporation

Prior to evaporation, undercut areas are cleaned with a reactive ion etching (RIE) based on a low power oxygen plasma (10 W) in order to be isotropic enough. This is possible because of the undercut structures. Aluminum is evaporated with a Plassys® e-gun evaporator. To get some reproducibility in the junctions' electrical parameters, the Plassys's loadlock is pumped overnight with a cryo pump in order to get a vacuum on the order of about 8×10^{-8}mbar. The aluminum is deposited at a rate of 0.1 nm/s. The oxidation lasts 5 min at 4 Torr (except for one batch but we will point it out when the time comes). The lift-off in NMP lasts for at least 4 h at 80 °C.

DC test

After lift-off, Josephson junctions can be tested by measuring their tunnel resistance R_N at room temperature before cooling them down. It allows: (i) to know

Step	Parameter
Resist spin coating	Resist 1:PMMA-MAA 9% ■ 30 s/ 4000 rpm / 4000 rpm s^{-1}
	Baking: 200 °C for 600 s
	Resist 2: PMMA 4% ■ 30 s/ 5000 rpm / 5000 rpm s^{-1}
	Baking: 150 °C for 300 s
Exposure	Pad ■ Dose: 10 C m^{-2} (High current)
	Pad arm ■ Dose: 12 C m^{-2} (High current)
	Junction ■ Dose: 10 C m^{-2} (Low current)
	Undercut ■ Dose: 3 C m^{-2} (Low current)
Development & cleaning	Dev1 : MIBK-IPA 1:3 for 60 s
	Dev2 : IPA for 30 s
	RIE with O_2 for 15 s @ 10 W and 7×10^{-2} mbar
Evaporation	Aluminum 1 ■ : 20 nm @ 0.1 nm s^{-1}
	Oxidation : 300 s @ 5.3 mbar
	Aluminum 2 ■ : 50 nm @ 0.1 nm s^{-1}
Lift-off	Bath of NMP for 4 hours @ 80 °C (US for 60 s)
	Rinsing : Shower of acetone/ethanol/IPA + blow dry

Table 4.1 – **Fabrication recipe for Josephson arrays developed by J. Puertas-Martinez and optimized for large SQUIDs.**

if the junctions are working (no short nor open) and (ii) inferring their critical current I_c as R_N is related to I_c via the (simplified) Ambegaokar-Barratoff relation [95]:

$$I_c R_N (T > \approx T_c) = \frac{\pi}{2} \frac{\Delta_{al}}{e}, \tag{4.1}$$

where Δ_{al} is the superconducting aluminum gap and e the absolute value of the electron charge. Since we are dealing with thin films of aluminum, we take $\Delta_{al}/e = 210\,\mu V$ (not the bulk value). R_N is measured with a two probe station. To get rid of the resistance offset of the measurement apparatus, we measure in general a set of several short test arrays while varying the number of junctions N_j in the array. The slope of $R_N(N_j)$ gives the resistance per junctions and therefore the critical current of one junction. For actual data, see Section 4.3.2.

4.1.5 Wafer overview

We have described a fabrication process that allows to fabricate very long Josephson arrays in a reproducible way with a relatively high fabrication yield. We do not have strong statistics to support this claim since we did not measure systematically each of the 16 long arrays from every batch we have fabricated. However, we can roughly estimate the fabrication yield to be between 8 and 12 working arrays out of 16 fabricated. Depending on which regime we want to make these arrays work, their boundary conditions will not be the same. In Fig. 4.4, we show a cartoon showing three chips with different design: the array are noticeably the same but their boundary conditions differ. With the BFF technique, in a single batch, we can fabricate galvanically coupled resonators to get small external quality factors (top-right). This design is used for resonant JPAs working in reflection and theoretically described in Chapter 2. We can also fabricate capacitively coupled junctions arrays to get larger quality factors (top-left). In the next section, it will be explained why such high external quality factor resonators can be useful. Eventually, we can connect a millimeter long Josephson array from the two sides to work in transmission. Such design can be the starting point for traveling-wave parametric amplifiers as theoretically described in Chapter 3. However, as it is, this design could not work as a TWPA because of a bad impedance matching. This is the topic of the next section.

4.2 Design and simulation of the top-ground plane

The main microwave engineering problem for Josephson TWPAs is to match them to $50\,\Omega$. Let us estimate the characteristic impedance Z_c of the arrays presented in the previous section. If we consider one SQUID made of two identical junctions with an area $A \approx 5\,\mu m^2$ (the area of **one** junction), our fabrication process gives typically junction with a critical current density $j_c \approx 25\,A\,cm^{-1}$. This leads to a Josephson inductance of $L \approx 0.15\,nH$. On the other hand, estimating the ground capacitance per SQUID is not straightforward, given its characteristic lengths $H \sim 10\,\mu m$ and $w \sim 400\,nm$ compared to its distance from the ground $d = 275\,\mu m^2$. A way to experimentally measure it is to fit the array dispersion relation with the Lagrangian model as explained at the end of Chapter 2. We find a ground capacitance $C^g = 0.1\,fF$ for one SQUID. Considering one SQUID as the unit cell of the Josephson transmission line (J-TL), $Z_c = (L/C^g)^{1/2} = 1.3\,k\Omega$. Therefore, we need to either decrease L or increase C^g by a factor 600 to reach $50\,\Omega$.

4.2.1 Rule of thumb to increase the ground capacitance per unit length

Since our process for arrays fabrication has a good yield, the design constraint was to avoid changing the array fabrication step. This means limited freedom on the Josephson inductance. Therefore, the only room left for decreasing the impedance is the ground capacitance. Two solutions arise (see Fig. 4.5): (i) decreasing the substrate thickness while keeping the same dielectric constant (panels **(a)** and

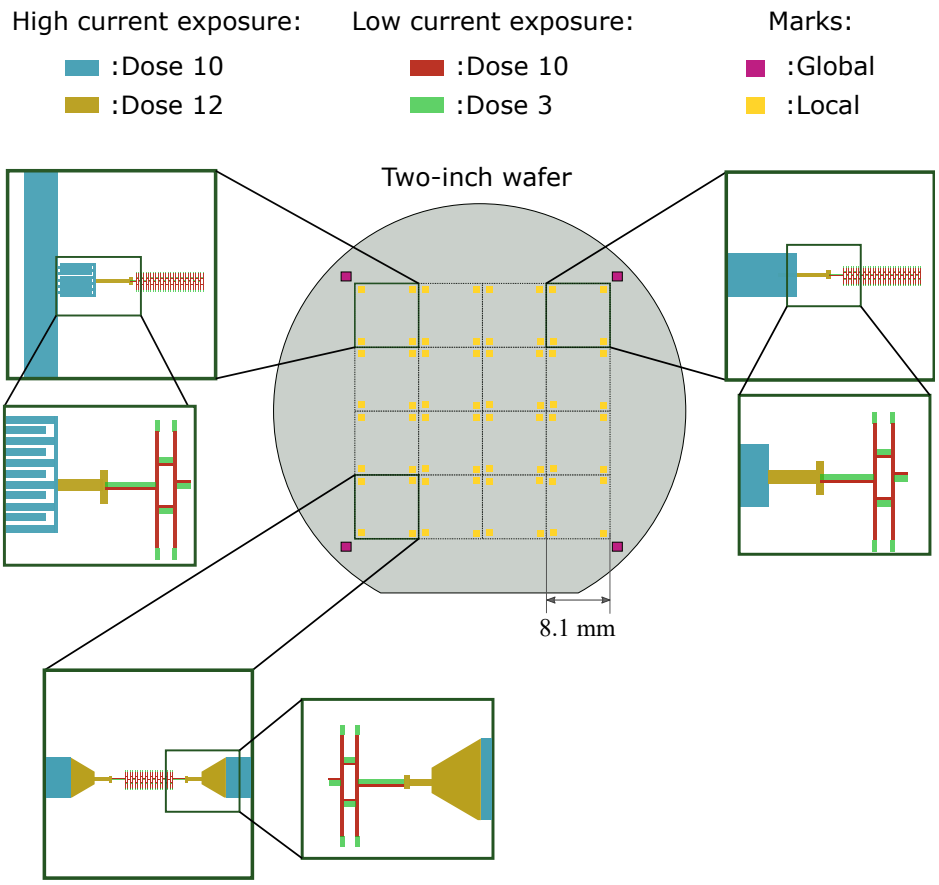

Figure 4.4 – **Cartoon of a 2 inch wafer.** We have chosen to divide it in 16 chips of 8.1 mm×8.1 mm squares. Each of these chips has local golden marks for dynamical focus purpose (Section 4.1.2). The wafer has global marks for alignment purposes with the ebeam writer. In this cartoon, we show three different designs. Drawings do not respect the actual scaling **Top-right:** short array galvanically connected to one bonding pad. The bonding pad and the buffer wire are written with high current, while the array is written with low current. **Top-left:** array coupled to a inter digit capacitor and a transmission line written with high current. **Bottom-left:** array working in transmission, galvanically connected to two taper-shaped bonding pads. The two latter designs will be the starting point before TGD technique.

(b)) or (ii) increasing the dielectric constant of the substrate (panels **(a)** and **(c)**). High dielectric constant ϵ' comes with large losses ϵ'' [74] since $\epsilon'' = \epsilon' \tan\delta$. If $\tan\delta$ is standard and in the order of few 10^{-3}, losses can be very large. For

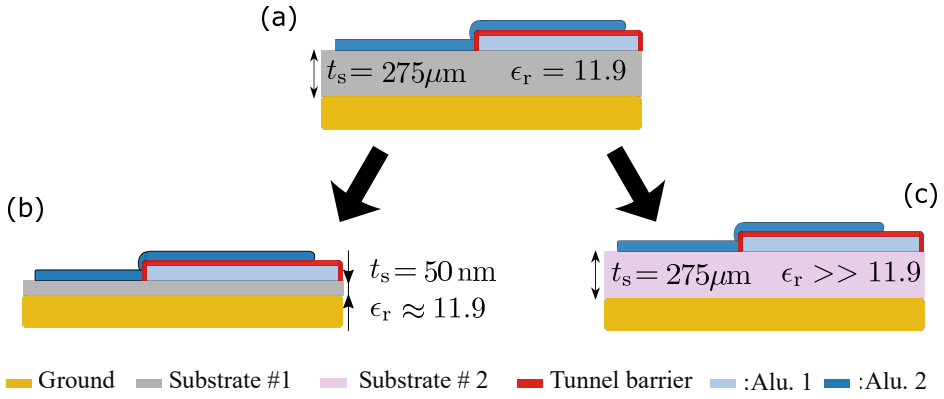

Figure 4.5 – **Impedance matching the SQUID array. (a)** We start from SQUIDs being 275 µm away from the ground. We either have the choice to **(b)** Carve the dielectric in order to be thin enough (50 nm) or to switch to dielectric with a much larger dielectric constant ϵ_r. Both techniques should lead to the same impedance but the former should be lower loss. It is the solution followed in this PhD thesis.

that reason, we have chosen solution (i). To have a good estimation of the substrate thickness, we can first model the ground capacitance as a simple planar capacitance. With this simple model, $t_s \approx 50\,nm$ is the expected substrate thickness to get an impedance of $50\,\Omega$. Obviously, no commercially available substrate that thin can be bought. The idea is to deposit a dielectric **on top** of the array followed by a metal deposition to create a ground with an arbitrary distance from the SQUID array. We nicknamed this 'inverted' microstrip geometry [74] top ground (TG) geometry.

4.2.2 Sonnet simulation for the highly inductive lines

To go further in the characterization of this geometry, we ran some electromagnetic simulations with Sonnet®. Sonnet is a simulation software which solves Maxwell equation in 2D for 3D structures. We mostly used it to calculate scattering parameters to check whether or not our geometry shows high transmission. We subdivided the simulations in two parts: first, we only considered the J-TL then we focused on the transition between the array and the rest of the setup.

High L line

We modeled the J-TL as a very high kinetic inductance material. As we said, we estimated the inductance of the array to be 150 pH for a nominal junction height $H = 11\,\mu m$ and a unit cell $a = 3.2\,\mu m$. Therefore, the simulations were run with a square inductance $L_\square = 500\,pH\ \square^{-1}$ (grey/purple line in Fig. 4.6 **(a)**

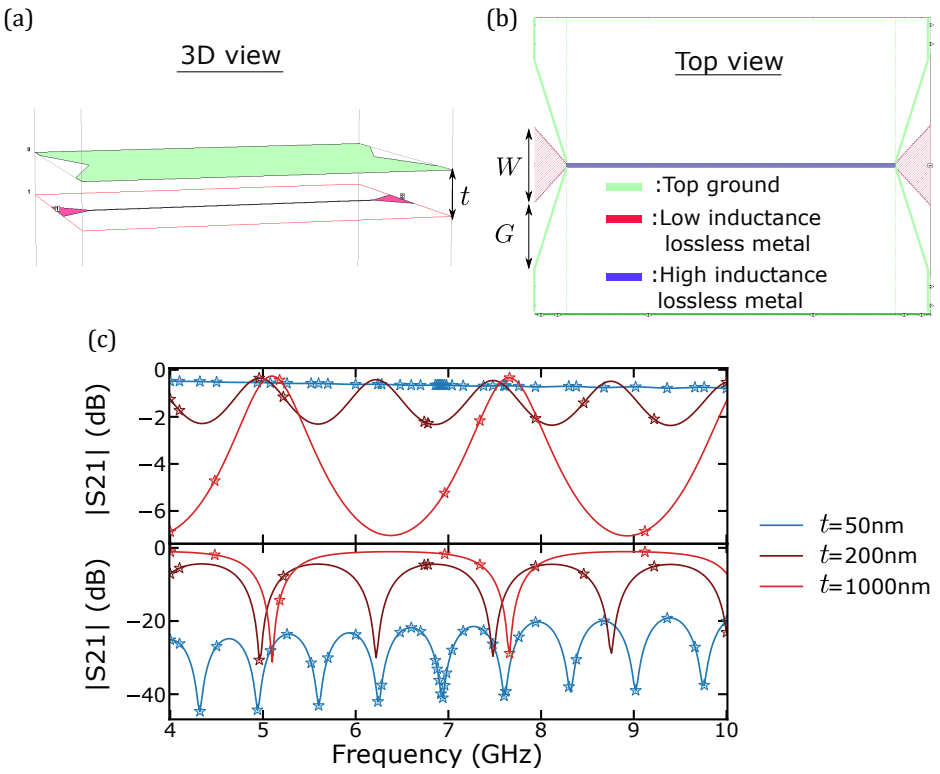

Figure 4.6 – **Sonnet simulation of a transmission line in a top ground geometry. (a)** 3D view of a highly inductive transmission line with a top ground in green. The dielectric is invisible in the picture but its thickness is indicated with t. **(b)** Top view. The two ends of the transmission line are terminated with a tapered bonding pad made from low kinetic metal. **(c)** Transmission and reflection of the transmission line while sweeping t. Stars are calculated points, while the solid lines linking them are the adaptive fits from Sonnet.

and **(b)**). In the actual simulation, the mesh in the signal propagation direction had to be very small (0.2 µm); otherwise, the simulations could not work properly. On the other hand, in order to simulate a transmission line, the total length of the line must be at least several wavelength. If we estimate the wave velocity being $v_\phi = 1.2 \times 10^6 \mathrm{m\,s^{-1}}$, at 10 GHz the wavelength is 120 µm; therefore, we made the line 7 times longer than one wavelength and took 840 µm. For having fast simulations, the mesh in the direction orthogonal to the propagation was taken as large as possible. We have chosen a mesh of 10 µm; thus the array is 10 µm wide. The dielectric (invisible in the pictures, since it lies between the transmission line and the ground plane, in green) is chosen as a layer of alumina. It is modeled with zero conductivity, a dielectric constant $\epsilon_\mathrm{r} = 9.9$ and a loss

tangent $\tan\delta = 10^{-3}$ [96]. Its thickness t is swept to find the optimal ground capacitance. Above it (green plane on panel **(a)**), there is a metallic layer acting as the top ground. We chose it to be a gold thin film, with a conductivity of $\sigma_g = 410\,\mathrm{GS\,m^{-1}}$ and a thickness $t_{tg} = 0.2\,\mu\mathrm{m}$. In the simulation, every edge of the top ground is connected to the 'true' ground (beneath the array) to avoid having a floating mass. In Fig. 4.6(**a**), these connections are not shown for visibility purposes.

CPW to strip-line transition

Once the array is correctly modeled and the optimal dielectric thickness t is set, the question is now how to correctly connect the array to the setup and more precisely to the printed circuit board (PCB) that interfaces the chip (the PCB geometry will be studied in the next chapter). We want (i) a smooth, *on-chip* transition and (ii) pads with enough room for three or four bonding wires. We have chosen a transition that goes from co-planar wave guide (CPW) to top ground. The transition is ensured with taper-shaped bonding pads. On the PCB side, the taper is $W = 200\,\mu\mathrm{m}$ wide and the gap between the taper and the ground is $G = 200\,\mu\mathrm{m}$ in a CPW geometry (see Fig. 4.6(**b**)). On the other end, the taper is in TG geometry, with a line width of $10\,\mu\mathrm{m}$ and the ground above the line (see Fig. 4.6**(b)**). This is a sane transition for the electric field since it smoothly changes from one geometry to the other. We raise here a small detail: the geometry for the tapers is not strictly speaking co-planar waveguide since the ground and the taper are **not** in the same plane. The taper is few tens of nanometers below the TG (see panel **(a)**). Actually, it can be considered as CPW since $t \ll G$.

Results of the simulation

The results of the simulation are plotted in Fig. 4.6**c**. The dielectric thickness is swept from $1\,\mu\mathrm{m}$ to $50\,\mathrm{nm}$. For large thicknesses, the system can be seen as a Fabry-Pérot cavity with large resonances. As t decreases, the system is more matched and resonances disappear. For $t = 50\,\mathrm{nm}$, the transmission $|S_{21}|$ is mostly flat while the reflection is kept under $-20\,\mathrm{dB}$, which is enough, meaning that the array is matched. The negative slope in the transmission is mostly due to **dielectric losses** and also, to a lesser extent, to **conductor losses** from the top ground plane. This will be discussed in Chapter 6. It is interesting to point out that the free spectral range Δf decreases as t_s decreases because wave velocity v_ϕ decreases and Δf is proportional to v_ϕ. On the other hand, v_ϕ is decreasing with t_s because the ground capacitance per unit length C_l increases ($v \propto 1/\sqrt{C_l}$).

4.2.3 Purpose and design of resonators

As we saw in the previous simulations, losses affect the transmission within the devices. Characterizing them in order to understand their origin to *in-fine* mitigate them is of prime importance, especially for amplifiers. As a mater of fact, losses degrade both the maximum gain of an amplifier **and** also increase its intrinsic

noise, because signal loss can be seen as lost information, which translates into noise. The slope in the transmission is naturally a good way to quantify these losses within our structures. However, in addition to that we fabricated resonators based on the same TG geometry to directly probe the internal quality factor Q_i of the resonators and therefore infer the loss tangent within our devices since $Q_i = 1/\tan(\delta)$. These resonators amount to be control samples to check the agreement between the loss tangent measured with the Josephson transmission lines and the internal quality factors measured with the resonators.

4.2.4 Sonnet simulation for the resonators

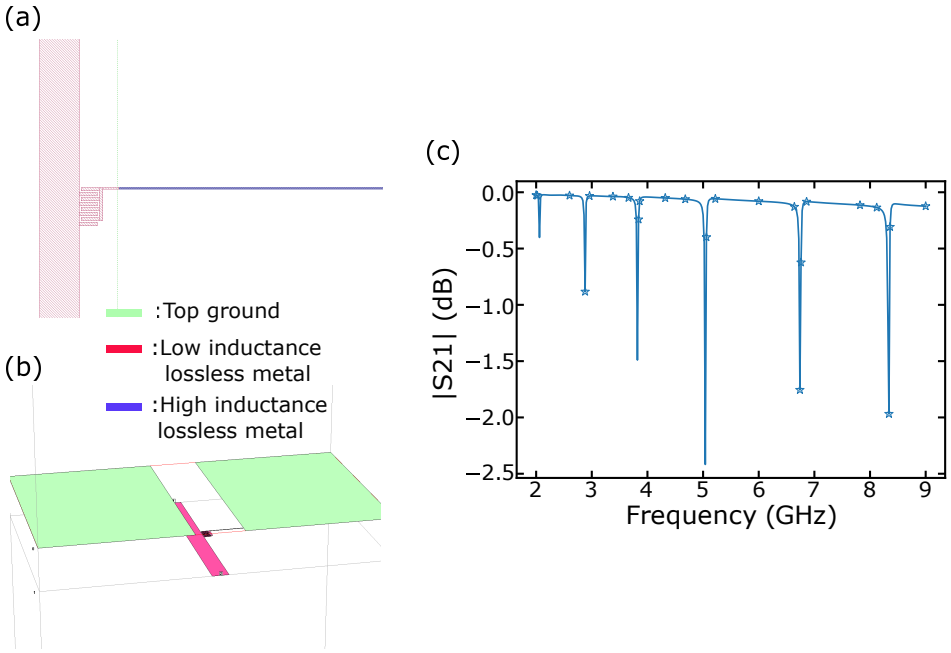

Figure 4.7 – **Sonnet simulation for a hanger resonator in a top ground geometry (a)** Top view. The left red rectangle is the 50 Ω TL that brings the signal. It works in a quasi-CPW geometry. The coupling capacitor is in the middle and has an inter-digital design. Only the high inductance resonator is below the top ground. **(b)** Top view. **(c)** Simulated transmission. The free spectral range is ≈ 750 MHz.

To design a good Q_i-meter, we follow the idea developed in **Etienne Dumur**'s PhD thesis, namely hanger resonators[a]. Hanger resonators' design are shown in Fig. 4.7 **(a)** and **(b)**. They consist in a 50 Ω transmission line, connected to

[a] In the litterature, it is sometimes referred to as a 'notch measurement configuration'.

the environment from both ends, and connected to the resonator via a coupling capacitance. In order to be consistent, we designed the high inductance resonator with the exact same geometry as the above described Josephson-TL; namely: few millimeters long, highly inductive and with an ultra close ground ($t = 50\,\text{nm}$). Then, these resonances will be fitted with a standard transmission model [97] to obtain, among other parameters, the internal quality factor Q_i in Chapter 6. Better will be the precision of the fit if external and internal quality factors have similar order of magnitude. As mentioned before, we expect the dielectric to show loss tangent on the order of 10^{-3}. We thus expect for the internal quality factor to be in the 1000 range. Likewise the Josephson-TL, the structure can be simulated with Sonnet to infer what the resonances will look like. We can thus optimize the capacitive coupling and the resonator length to get the most accurate value for Q_i. A large capacitance is needed to reach the expected external quality factor Q_e. Therefore, we have chosen an inter-digital capacitance design as shown in panel **(a)**. We can also chose the appropriate length for the resonator – 2 mm, or 600 SQUIDs – to get the resonances in the right frequency range. We show the outcome of the simulation in Fig. 4.7**(c)**. There is a free spectral range of 750 MHz . We therefore have several resonances in our measurement windows (typically between 3 GHz and 12 GHz). Each of these resonances can be fitted and return a value for Q_i. Thus a single resonator allows to have some statistics over Q_i .

4.3 Top ground deposition (TGD)

This section is dedicated to the fabrication process of the top-ground. We will first explain how we deposit the dielectric layer and its effect on Josephson junctions. In a second time, we will focus on the proper ground plane deposition. Finally, we will simply highlight the last steps of the process, requiring small tips to correctly mount the chip in the setup.

4.3.1 Dielectric deposition

Characterization of the losses in Chapter 6 will show that the main source of loss comes from the dielectric itself. In our top ground configuration, the Josephson array is completely surrounded by dielectrics: below, the substrate; above, the alumina. However, they will not participate equally to the losses. To quantify this difference we can define a filling factor [74], which takes into account that the electric field is in different dielectrics with different loss tangent and with different amplitude. In our case, the electric field is much more intense between the array and the top ground since the latter is about 10,000 times closer from the array than the bottom ground, hence the losses are completely dominated by the top-deposited dielectric. Therefore, the deposition of the top substrate is the most critical step for our devices. In our current understanding, two main factors will influence the dielectric loss: the nature of the dielectric and the deposition method. In the following, we present two deposition methods.

Atomic layer deposition

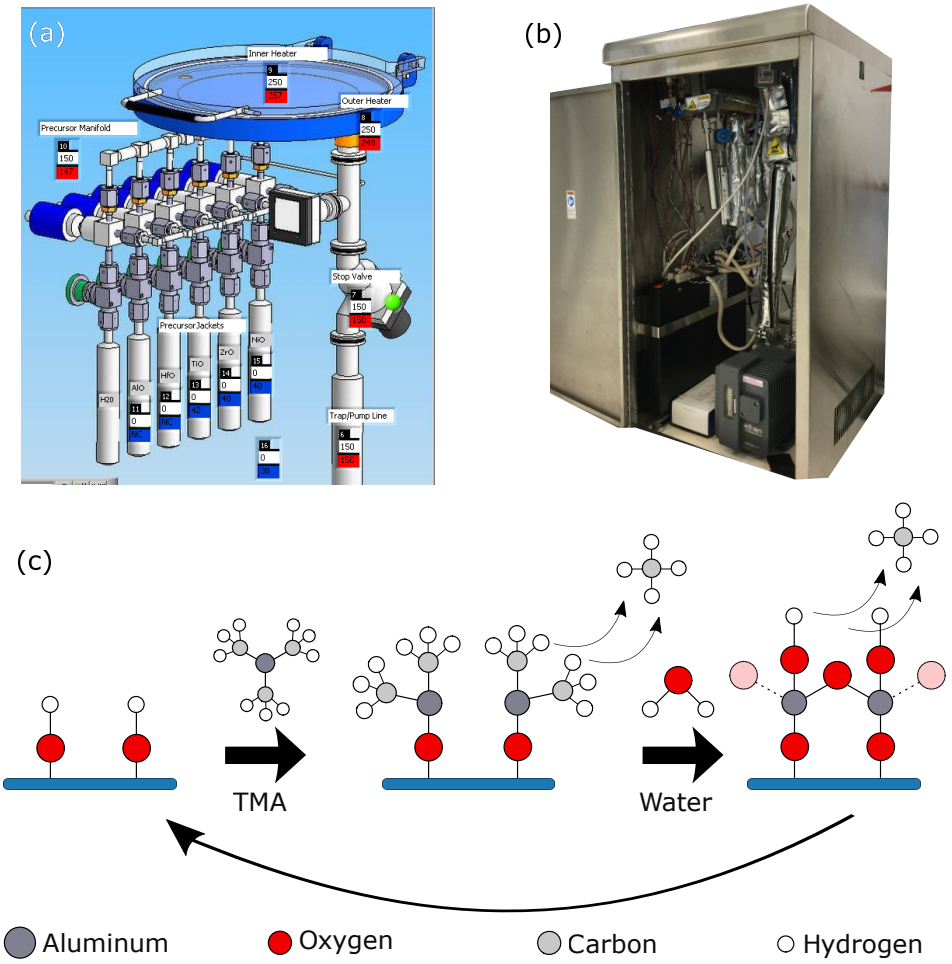

Figure 4.8 – **Principle of the atomic layer deposition (ALD). (a)** Scheme of the Savannah system used for the deposition. The wafer is put in the chamber, which can be heated up to 250 °C. **(b)** Picture of our Savannah system. **(c)** Simplified cycle for alumina deposition with ALD. The substrate has an initial layer of native oxide. A precursor of trimethylaluminum (TMA) is injected in the chamber. It reacts with the oxide layer to give a layer of di-methyl aluminum oxide. A pulse of water is injected to get rid of the methyl groups. One layer of alumina has been deposited. This layer ends with an oxide layer, which can itself react with a new pulse of TMA.

All the samples presented in the thesis with the TG geometry use a dielectric

deposited via atomic layer deposition (ALD). This process allows the deposition of a given material atomic layer by atomic layer. The strengths of this deposition method are many: it gives high quality dielectric, conformal deposition (avoids the shorts to the ground) and a very good control over the deposited thickness (≈ 1 Å). ALD has been studied for decades and can be routinely done in clean/gray room. Such machine is available at the Néel Institute and is under the supervision of **Laurent Cagnon**. It is a Savannah 100 system from Cambridge Nanotech (see Fig. 4.8 **(a)** and **(b)**). One single cycle can be simply summarized as in Fig. 4.8**(c)**. A cycle is then repeated N_c times to deposit N_c layers of dielectric. The recipe used for our dielectric deposition is summarized in Table 4.2. For each sample, we used alumina (Al_2O_3) as a dielectric. The deposition chamber pressure was $P = 0.3$ mbar. Through the different batches, N_c varied between 280 and 380. For every batch, cycles were kept identical: they last 30 s and are a succession of a 15 ms trimethylaluminum (TMA) pulse and a (30 ms) water pulse. During this PhD, we have tried several ways to enhance the alumina quality to decrease dielectric loss. Prior to the deposition a reactive ion etching with O2 plasma can be done on the wafer to clean the junction array on the surface. I did not test it myself, but **Ekaterina Al-Tavil**, a former master intern, did [98]. It did not break nor affect the junctions in a detrimental way. However, a conclusive effect on the dielectric quality could not be seen. The deposition temperature can also play a role in the dielectric quality. We tried two temperatures, 150 °C and 200 °C. Here again, we could not see a clear trend between these two temperatures. Nonetheless, this Savannah system can go up to 250 °C and it would be interesting to try it out. Anyhow, one of the main limiting factor for the dielectric quality seems to be the use of water during the deposition. According to **E.A-T.** and **L.C**, the water pulse time (30 ms) was too long. After reducing it to 15 ms, the loss tangent was lowered. Loss tangents between 2.3×10^{-3} and 4.1×10^{-3} have been found by measuring resonant structures as described in Section 4.2.3. Anyway, according to literature [99], it will be very difficult to reduce alumina $\tan\delta$ below 10^{-3}. In the next section, we will briefly discuss about a deposition technique that does not rely on water.

Plasma enhanced chemical vaporous deposition

A solution to avoid water during the dielectric deposition is to use a different reactant after the precursor injection. This is what plasma enhanced chemical vapor deposition (PE-CVD) does. We have been lucky enough to have one of these deposition tool in Grenoble in the CEA's cleanroom. This deposition technique is much faster since it does not deposit single atomic layers per cycle but between 1 and 4.5 nanometers per second. The deposition thickness ranges between 50 nm and 2 µm. For PE-CVD, the deposition temperature is always 250 °C. No sample presented in this thesis incorporated PE-CVD dielectric. However, **E.A-T.** and **Arpit Ranadive**, the new PhD student taking over this project, have fabricated devices with this deposition technique. Naturally, the point was to compare the loss between the ALD and the PE-CVD techniques and conclude whether or

not there is an improvement with the PE-CVD. Unfortunately, the experimental protocol was not rigorous since we also changed the dielectric material when we tested the PE-CVD. The only available materials in the PE-CVD machine are: SiO_2, SiN and a-Si (amorphous silicon). In their paper reporting the loss tangent of various material, A. D. O'Connell *et. al* [99] measured a 10^{-6} loss tangent for hydrogenated amorphous silicon *i.e.* three order of magnitudes lower than what we measured for Al_2O_3. Thus we decided to deposit a-Si with PE-CVD. However, despite the promise of decreasing the dielectric loss from a factor 1000, we only measured a decreasing from a factor 2 (loss tangents between 1.5×10^{-3} and 2.5×10^{-3} were measured). A more thorough study should be done to conclude on why we could not see a greater improvement in the dielectric quality. Actually, we always find the same level of loss in our structure, whatever the material or the deposition method, in the order of 10^{-3} (from 1.5×10^{-3} to 9.0×10^{-3}). My personal opinion is that we may have one (or several) step(s) in our fabrication process limiting the dielectric quality. This may come from the fact the whole procedure is not exclusively done in a clean room. For instance, the ALD instrument is in a gray room. Also, DC tests (mentioned in Section 4.1.4) are done in a normal room, before and after the dielectric deposition. This might alter the quality of the surface where the dielectric is deposited and also its interface with the top ground, thus increasing the dielectric loss tangent. However, we did not perform enough tests nor fabrication runs to have enough perspective on this issue. This is a personal assumption which needs to be confirmed or invalidated with experimental data. We now turn to the DC measurement of the test arrays.

4.3.2 DC test before and after ALD

Performing DC current measurement after ALD or PE-CVD allows to know if the deposition step altered the Josephson junctions in some way. Temperature can affect Josephson junctions and their tunnel barrier. As we pointed out in the last paragraphs, the junctions stay up to few hours in a chamber heated up to 200 °C. We therefore expect to see an effect on the junctions. We performed systematic DC tests on the same samples before and after ALD. On each fabricated sample, there are 9 small arrays (from 20 SQUIDs to 100 SQUIDs, with an increment of 10 SQUIDs for each array). We can then obtain the resistance per SQUID before and after the deposition. These systematic measurements are shown in Fig. 4.9 for the four different batches that have been fabricated. There is a clear trend where we observe a systematic drop in the junctions' resistance after ALD. This drop is between 10% and 15% of the initial resistance. A simple mechanism that could explain this feature would be the diffusion of aluminum inside the tunnel barrier, reducing the effective thickness of the tunnel barrier and hence reducing the tunnel resistance. This effect naturally translates into an increase in the critical current and a drop in the Josephson inductance when it will be measured at cryogenic temperature. This effect should be considered in the final calculation of the impedance and dielectric thickness to have a $50\,\Omega$ array. Apart from the aforementioned effect on the junctions, we did not observe any other effect nor

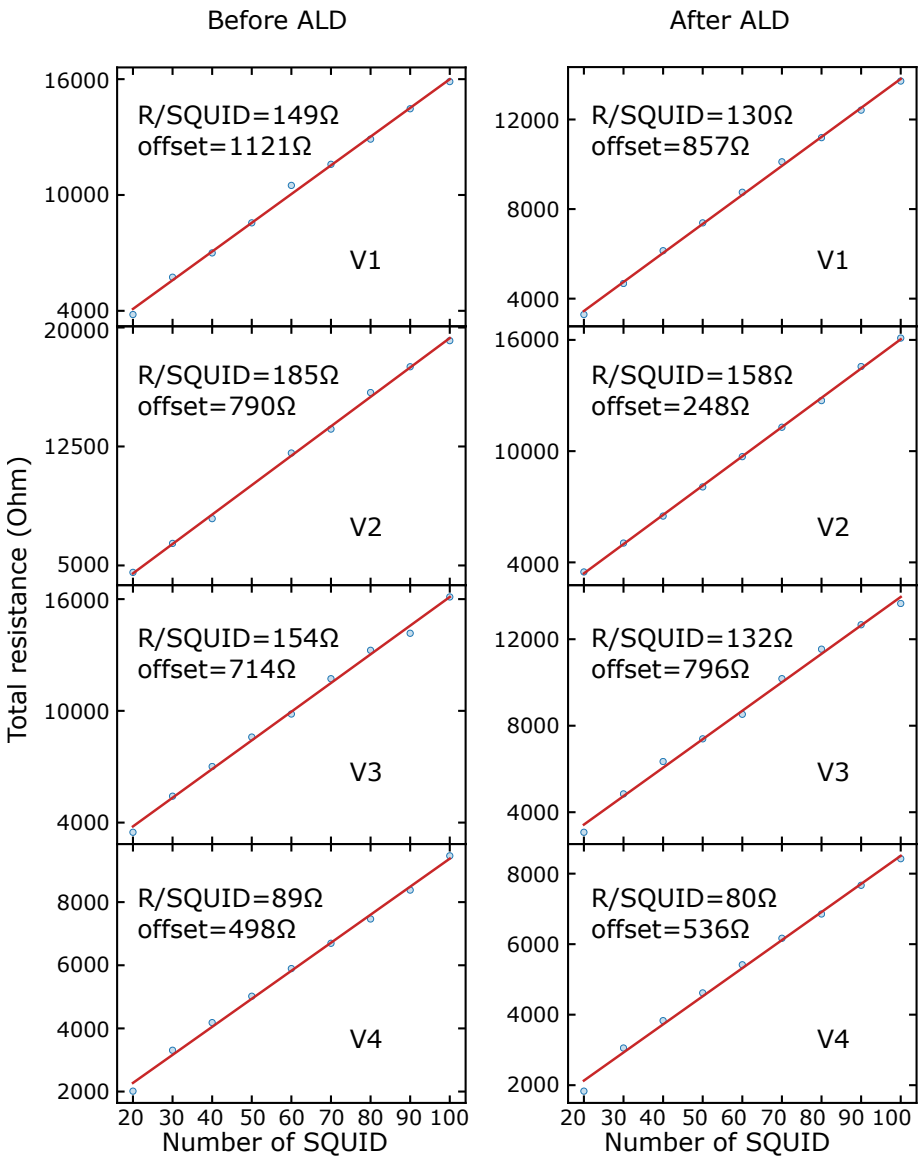

Figure 4.9 – **Resistance of test arrays *vs.* the number of SQUIDs for four samples from four different batches.** The slope gives the resistance per SQUID R/squid. There is a clear trend where R/squid decreases after the ALD process because of the temperature during the deposition process.

particular degradation on the junctions because of heating. As mentioned in the previous subsection, ALD might as well be detrimental to the dielectric quality. That being said, DC measurement after ALD is not as important as measurement before ALD. Indeed, DC measurement before ALD allows to get a direct estimation of the Josephson inductance therefore to set the dielectric thickness. Whereas the measurement after ALD is more to check whether the junctions survive the ALD step and can be done after the top ground deposition.

4.3.3 Ground deposition

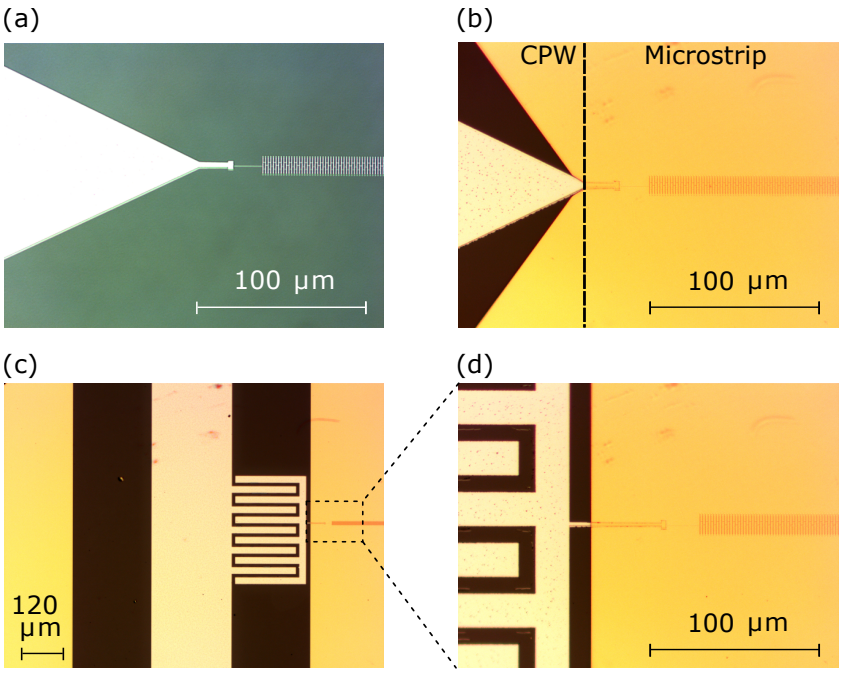

Figure 4.10 – **Picture from two samples before and after gold deposition** Pictures **(a)** and **(b)** display SQUID-based transmission lines whereas **(c)** and **(d)** are showing details of resonant structures **(a)** Input of the SQUID-based transmission line after the first step. Left side of the picture: bonding pad with tapered shape. Right side of the picture: few dozens of SQUID. **(b)** Same structure but with a TG geometry. The gold layer is deposited everywhere but on the bonding pad. SQUID are still distinguishable from below the alumina and gold layers. **(c)** Picture of the resonant structure after ground deposition. The feed-line is visible in the middle. On the right side: inter-digital capacitor coupling the feed-line to a section of SQUID-based transmission line (623 unit cells). **(d)** Zoom in.

The ground deposition requires a lithography step to avoid covering the bonding pads. We pattern the resist using a lithography step. The choice of the resist deposited on the wafer and its thickness depends on the thickness of the ground that we aim at. Importantly, conductor loss are associated with conductor thickness: the thicker a conductor, the lower the associated loss [100, 101] (this will be discussed in Chapter 6). Up to several hundreds nanometers, conductor loss in the top ground are still substantial. From a fabrication point of view, this is somehow challenging. A common rule of thumb in nano-fabrication states that during a standard development/deposition/lift-off process, the thickness of the deposited film should be one third (or less) of the resist thickness. Of course this rule can be overcome, but it gives an order of magnitude. To get the conductor loss negligible, a 1 µm thick top ground is enough, but it asks for a few microns thick resist, which is not the norm in electronic lithography. However, there are optically sensitive resists reaching that thickness range. Obviously, this is a non-existing problem if one is ready to deposit a superconducting top ground. Nonetheless, if we want to fully use the SQUIDs' flux tunability, we cannot use superconducting ground planes. In the following paragraphs, we describe two recipes to deposit the metallic ground: the first one involves electron beam lithography while the second involves laser lithography.

Electron beam lithography & metal evaporation

The thickest e-beam sensitive resist we could find is a negative resist called **ARN-7700-18**. In its optimal condition, this resist is about 400 nm thick. With the help of **Thierry Crozes**, we could push this resist to its limit and with a very slow spin-coating (500 rpm, see Table 4.2 for more details) reach a thickness up to 900 nm. Prior to development and after exposure, the resist must be baked for 90 s on a hot plate set at 105 °C. Afterwards, to develop this large quantity of resist, the development time must be increased to 440 s in the **AR-300 47** instead of 60 s. With that resist thickness, thin films as thick as 400 nm could be deposited (with 20 nm of titanium, as an adhesive layer). To help the lift-off, the wafer can be put inside an ultra-sonic batch, up to 100%, without breaking the junctions or the dielectric. The pros for this ground deposition is that it can be done using electron beam lithography and all benefits that go with it: it is fast, very precise and overall this deposition method is highly reproducible with a high fabrication yield. The drawback is that we can only deposit a 400 nm thick metallic ground (maybe more, but we did not push it). Pictures in Fig. 4.10 show the sample before and after the ground deposition obtained using electronic lithography. The obtained precision is very good.

Laser lithography & metal sputtering

One of the thickest optically sensitive resist we could find in our clean room is called **AZ 4562** and is surprisingly viscous: it can reach up to 6 µm. When this resist is patterned using laser lithography, care should be taken with the refraction of the laser light inside the resist. It has been measured an offset of 8 µm between

the expected insulated spot and the actual insulated spot. Of course, this offset can be adjusted numerically. Development must be done for at least 150 s, given the great quantity of resist to be developed. To be safe, the resist at the bottom of the structures can be suppressed by doing a RIE with an $\mathbf{O_2}$ plasma at 10 W. Given the price of gold, we preferred to deposit 1 µm of copper via sputtering, (with few nanometer of tantalum as an adhesive layer). We have chosen sputtering deposition for two reasons: first, because there was not copper inside our Plassys evaporation system at that time. Second, because sputtering seems to be more stable when a large thickness is deposited than with metal evaporation. The advantages of this technique is a top metallic ground thick enough to get negligible conductor loss. The disadvandtage is that we need to write the structures with laser lithography, which is inherently less precise. But the largest drawback is that after 1 µm deposited, the top ground is not so stable anymore. Powerful ultrasonic agitation during the lift-off can cause the gound plane to peel off, which makes the samples unusable and reduces the fabrication yield. This might come from the association between sputtered deposition and resist lift off.

4.3.4 Packaging

This small subsection aims to give some tips after the fabrication process of the devices to correctly mount them in the chip carrier. Given the unconventional structure of the devices (compared to resonant JPA), some steps must be considered more carefully.

Dicing

For resonant JPA, we conventionally dice the 2 inch wafer into 16 chips with a precise diamond saw with about 10 µm accuracy. The top ground deposition technique based on 400 nm gold preceded with the ALD of alumina never encountered issues during the dicing step. We did though faced some severe issues during the saw dicing of the 1 µm copper thick top ground devices, when the ground started to peel off from some chips. I see two main reasons in these different behaviors: the association titanium and gold is stickier than tantalum and copper and thick depositions are maybe less likely to be steady. At the very end of my PhD, we investigated laser dicing that should be less agressive than diamond saw. Laser dicing produced very clean dicing. Up to now, no device has been properly measured after going through laser dicing.

Bonding

Since ALD happens on the whole wafer surface, it also grows on bonding pads. We observed that for thin alumina deposition (up to 40 nm), the wire bonding machine had no issue piercing the alumina layer and reach the aluminum pads. However, for larger dielectric deposition (70 nm of amorphous silicon) **A.R.** has noticed that bonding was hardly working. A simple etch with SF_6 for 1 min, to

remove the dielectric layer everywhere but under the top conducting layer, worked well and no subsequent issues have been reported.

4.3.5 Full recipe

This subsection summarized the fabrication process with a table (Table 4.2) summarizing the recipe and a figure (Fig. 4.11).

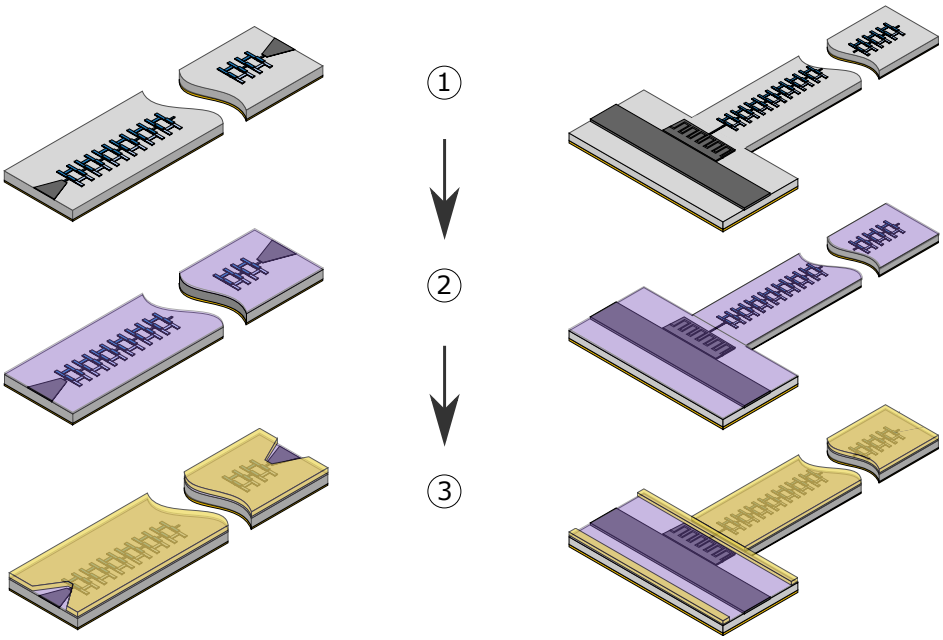

Figure 4.11 – **Fabrication flow for SQUID-based transmission lines and resonators.** Step 1: fabrication of long SQUID arrays using electron-beam lithography and double angle evaporation of aluminium. Step 2: Deposition of a conformal alumina layer via Atomic Layer Deposition (ALD). Step 3: Evaporation of a thick metallic layer (gold or copper) acting as an electrical ground. This layer is patterned using a combination of electron-beam lithography and lift-off.

① Array Fabrication see Table 4.1

② Atomic layer deposition

Step	Parameter
Chamber preparation	Temperature: 150 °C to 200 °C Pressure: 0.29 mbar
ALD	TMA pulse (0.015 s) Wait (10 s) Water pulse (0.030 s) Wait (10 s) # of cycles: 280 to 380
Cleaning	RIE for 120 s @ 20 W and 7×10^{-2}mbar

③ Top ground

Step	Parameter 1	Parameter 2
Resist spin coating	ARN 7700-18 90 s/500 rpm/750 rpm s^{-1} Baking: 85 °C for 90 s	AZ 4562 30 s/ 4000 rpm / 4000 rpm s^{-1} 95 °C for 120 s
Exposure	Ebeam lithography Negative resist Post bake: 105 °C for 90 s	Laser lithography Positive resist No post bake
Development	AR-300-47 240 s DI water 60 s	Micro. Dev 150 s DI water 60 s
Deposition	Ti evap. (10 nm @ 0.25 nm s^{-1}) Au evap. (400 nm @ 0.50 nm s^{-1})	Ta sputt. (5 nm @ ∼0.1 nm s^{-1}) Cu sputt. (1 µm @ ∼0.5 nm s^{-1})
Lift-off	AR 300-76 4 hours	Acetone 1 hour

Table 4.2 – **Fabrication recipe of the top ground deposition.**

Experimental setup 5

Contents

This chapter aims to give information about the experimental setups used to measure the different devices. The first section will be a quick review on the important matters with cryogenic experiments carried out in dilution refrigerators. The second section presents the microwave setups and their calibration.

Link back to Table of contents →

5.1 Requirement for cryogenic experiment

5.1.1 General presentation

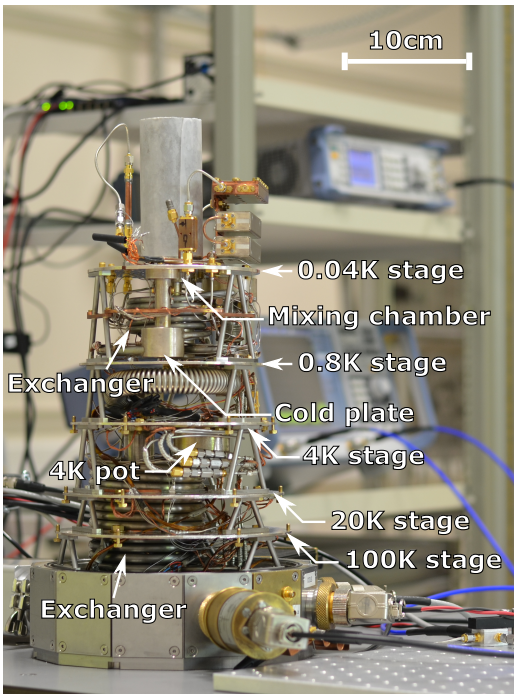

Figure 5.1 – **Photography of the inverted dilution refrigerator (IDR).** All stages are visible. On top, in the gray monolith, the sample holder is anchored to the mixing chamber.

To reach the standard quantum limit of noise, Josephson amplifiers must be cooled down cryogenic temperatures so that input noise is only dictated by zero-point fluctuations. I have therefore carried out my experiments in dilution refrigerators reaching routinely base temperature as low as 25 mK.

Throughout my PhD, I used two wet dilution refrigerators. They essentially only differ by their size and therefore by their full cycle time that is the time required to warm up the fridge, change the sample and cool it back down. Chronologically, the first one was the large dilution refrigerator (LDR). It has eight microwave lines, can handle two independent measurements in parallel and has the necessary microwave setup to perform time domain measurement. It was in the LDR that resonant JPAs have been characterized, measured, and used for fast high-fidelity single-shot qubit readout [102]. Its full cycle time is about five days. Whereas the second one, called inverted dilution refrigerator (IDR, shown

in Fig. 5.1), has a cycle time of one day. At the time of my PhD, the IDR only had the setup to perform continuous wave (CW) measurements. It was in the IDR that the successive batches of traveling-wave parametric amplifiers (TWPA) (and hanger resonators) were measured. The incredibly low cycle time of the IDR naturally allowed to be particularly fast between each improvement of the TWPA.

I had the chance to arrive in the team when both fridges were fully operated, calibrated and working (almost) perfectly. Moreover, both fridges were under the 'jurisdiction' of incredible PhD students, **Rémy Dassonneville** for the LDR and **Javier Puertas-Martinez** for the IDR, which made my experimentalist job much easier.

5.1.2 Cryogenic temperature

Having an amplifier with an intrinsic added noise at the quantum limit would be useless if the input noise is not itself limited by quantum mechanics as well. Therefore, Josephson amplifiers must be in contact with a thermal bath leading to a mean number of thermal photons $n(\omega, T)$ well below one half. This mean number is given by the Bose-Einstein distribution $n(\omega, T) = (\exp(\hbar\omega/k_\mathrm{b}T) - 1)^{-1}$. This distribution predicts that at 25 mK, in our measurement windows ($\omega/2\pi$ between 2 GHz and 20 GHz), $n(\omega, T)$ is, at least, two orders of magnitude below one half. It is therefore safe to consider that at 25 mK we are not sensitive to thermal noise and only limited by quantum noise. To reach that ultra low temperatures, a dilution refrigerator is thus required. For details on their working principles, the reader may refer to Pobell's textbook[103]. Dilution refrigerators are nowadays widespread and commercial dilution refrigerators became very user-friendly. A cooling cycle is now almost fully automatized. We however show one picture of the IDR in Fig. 5.1 because of its originality and remarkable small size. It is about 50 cm high and subdivided in six stages, going from 100 K (lower-most stage) to 25 mK (mixing chamber, upper-most stage). The sample is anchored to the latter for being well thermalized. In their thesis, **J. P-M.** [91] and **R. D.** [104] describe the working principles of the IDR and LDR, respectively, and their different upgrades.

5.1.3 External thermal noise

Anchoring the device under test (DUT) to the coldest stage of a dilution fridge is not enough to get rid of fluctuations, both thermal and electrical. Since the DUT is electrically connected to a thermal bath at room temperatures (RT), the Wiedemann Franz law implies that the thermal conductivity is non zero and therefore the DUT is also thermally connected to a 300 K bath. To avoid that the heat load from 300 K warms up the DUT, we must either use extremly long cables with standard electrical (or equivalently thermal) conductivity or shorter coaxial cables with poor thermal conduction. This is why we do not use copper coaxial cables but stainless steel cables in order to have coaxial cables in the centimeter range instead of the kilometer range inside the cryostat. These cables must be

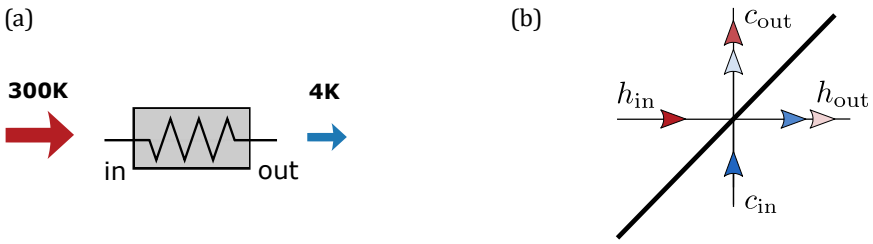

Figure 5.2 – **Attenuator as a beam splitter. (a)** Microwave attenuator reducing the noise power spectral density (PSD) coming from 300 K. **(b)** Modeling of an attenuator as an optical beam splitter with a transparency t. It illustrates Eq. (5.1).

anchored to the different stages in order to progressively decreased the heat load coming from RT to the DUT. However, anchoring coaxial cables do thermalize outer conductors but do not thermalize the inner conductors of the coaxial cables. This is why the coaxial cables are connected to attenuators, themselves anchored to the different temperature stages. This is twice beneficial: the inner conductor is thermalized, but also electrical noise coming from RT instruments is reduced. This can be understood by considering the attenuator as a beam splitter (BS) with a transparency t.

This model is convenient to understand how an attenuator works and it will be useful later on when we will have to compute the expected noise of the TWPA. We consider the electronic noise coming from hot environment at the input of the attenuator anchored to a cold stage. We denote its amplitude h_{in}. The amplitude at the output of the attenuator is denoted h_{out}. We use the same notations for the electronic noise generated by the attenuator itself : c_{in} and c_{out}. The variances of the output noise power are straightforwardly understood by considering Fig. 5.2:

$$\begin{aligned}\langle|h_{\text{out}}|^2\rangle &= t\langle|h_{\text{in}}|^2\rangle + (1-t)\langle|c_{\text{in}}|^2\rangle,\\ \langle|c_{\text{out}}|^2\rangle &= t\langle|c_{\text{in}}|^2\rangle + (1-t)\langle|h_{\text{in}}|^2\rangle.\end{aligned} \tag{5.1}$$

We see that each output channel is a sum of the two input channels. For an attenuator, the transparency is very low. For instance, let us consider the noise coming from 300 K, passing though an attenuator anchored to a 4 K stage and with a 20 dB power attenuation (t=0.01). The power spectral density (PSD) can be approximated to a Johnson-Nyquist white noise $\langle|h_{\text{in}}(\omega)|^2\rangle/4Z_0 \approx k_{\text{B}}T$, where Z_0 is the 50 Ω impedance of the microwave circuit. The PSD at the output of the attenuator is equivalent to a 50 Ω load thermalized at the effective temperature $T_{\text{eff}} \approx \langle|h_{\text{out}}(\omega)|^2\rangle/4Z_0k_{\text{B}} = 7\,\text{K}$. We must thus anchor several attenuators all along the route between the RT instruments and the DUT to get the lowest PSD (or equivalently to the lowest effective temperature generated by a 50 Ω load).

Though, this calculation of the PSD as a Johnson-Nyquist white noise is valid only when the frequencies at stake (2 GHz to 20 GHz) are well below the frequency given by the environment temperature. (25 mK is equivalent to 417 MHz). Thus, for the coldest stage, this approximation does not hold and we must take into account quantum corrections. The reader can refer to **R. D.**'s PhD thesis for these calculations. For both setup, we have about 20 dB attenuation at 4 K and about 40 dB between the 4 K and the 25 mK stage (depending on the room available). Naturally, this problem of attenuating the noise PSD coming from 300 K also concerns the output line, since it connects the DUT to measurement devices. However, in the output lines, we cannot afford to attenuate the signal generated by the DUT; we obviously want the highest possible signal noise ratio (SNR). We instead use non reciprocal devices. From RT to 4 K (see Fig. 5.3), the microwave amplifiers we use are non reciprocal devices: they amplify in the direction 4 K $\rightarrow$ RT but attenuate the opposite direction. Between 4 K and the DUT, there is no (for now) commercially available cryogenic non reciprocal amplifiers. We use instead circulators and/or isolators. These magnetic devices do attenuate in one direction (RT $\rightarrow$ DUT) but do not attenuate in the other direction (DUT $\rightarrow$ RT). These components are in general bulky and have significant insertion loss. Finally to keep the highest SNR we use dissipationless superconducting coaxial cables between the isolators/circulators and the cryogenic amplifier. After the 4 K amplifier, the SNR is already good enough so that standard coaxial cables can be used.

5.1.4 IR filters and shielding

Another source of noise is nonequilibrium quasiparticles, *i.e.* unpaired electrons in a superconductor, created in aluminum and tunneling through the Josephson junctions. They are created by infrared radiation (IR) guided by the coaxial cables or coming from the seams of the sample holder which break the bonding of Cooper pairs. Quasiparticles have a strong impact on lifetime and decoherence time of superconducting qubits and take a prominent place in the current literature [105, 106] but are not a major concern for parametric amplifiers. The two setups I worked with had components to avoid the creation of quasiparticles. For IR in the cables, low-pass filters are placed in the microwave setup, in general between the 4 K stage and the 25 mK. For IR radiations coming from flawed shielding, the solution to stop them is to use highly reflective mirrors and/or by using a black coating (carbon powder and silicon beads mixed in a black epoxy resist called Stycast®). This black coating can absorb IR radiations ans is usually spread on a copper shield at the lowest temperature stage and enclosing the DUT. Often, a second shield is put on top of the aforementioned one, which can protect the samples from external magnetic fields. This shield is called mu-metal shield, where mu refers to the magnetic permeability. It protects the SQUIDs from stray magnetic fields including the one of the circulators or from the Earth itself. It essentially allows to have zero magnetic flux when no external magnetic field is applied.

5.2 Microwave measurement

This section presents the microwave setup inside the inverted dilution refrigerator.

5.2.1 IDR measurement setup

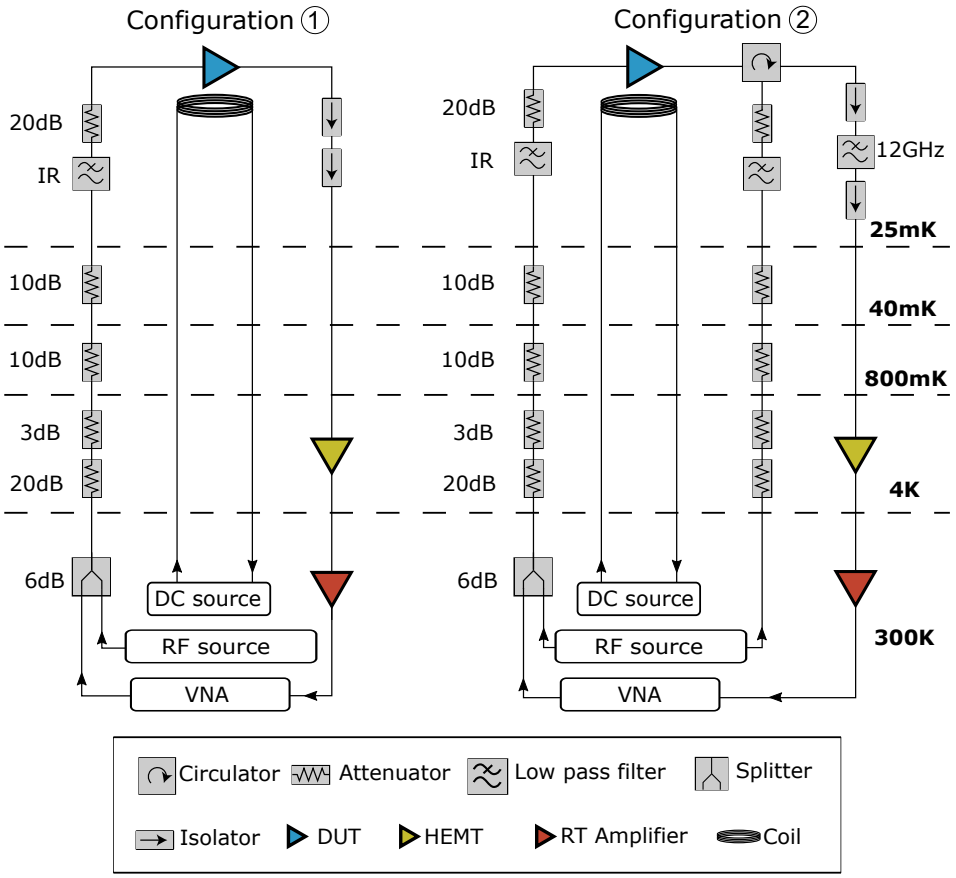

Figure 5.3 – **Experimental setup in the IDR.** Configuration ① is standard for transmission measurement. Configuration ② is meant to probe backward amplification process. The DC source is a HP 3245A and is used to biased the coil. The RF source is a R&S SMB 100A and is used as pump or a second tone for two-tone spectroscopy. The VNA is a R&S ZNB 20 and is used to probe the DUT.

In this subsection we will focus more on the IDR microwave setup than the LDR. The microwave setup of the LDR can be find in Appendix B; it consists in a setup for qubit measurement with a resonant JPA working in reflection. The full

diagram of the microwave setup inside the IDR is shown in Fig. 5.3. As we said, the setup in the IDR is only meant for spectroscopy as we did not have at that time the instruments to carry out time resolved measurement. For this setup, the measured samples were either TWPAs or hanger resonators. The DUT is probed with a vector network analyzer (VNA). A radiofrequency (RF) source is used to pump the TWPA or as a second tone for two-tone spectroscopy of the hanger resonator. Signals from the VNA and the RF source are sent to a room temperature microwave combiner. The unique coaxial cable then goes towards the DUT via several attenuators, each anchored to the corresponding temperature stage for thermalization as explained in the previous subsection. Configuration ① is a standard microwave transmission setup. The output line goes through the isolators and the amplification chain. The high electron mobility transistor (HEMT) amplifier anchored to the 4 K has a 3 GHz to 15 GHz bandwidth for 39 dB maximum gain. It is followed by a room temperature amplifier. When the DUT is passive (no amplification), the SNR is set by the HEMT amplifier. In Chapter 8 we measure the SNR improvement when the device is a TWPA and its pump is on. For configuration ②, the pump is connected to the two ends of the TWPA. This configuration was done to compare the gain whenever the pump is propagating in the same direction (left-most route) or in the opposite direction (right-most route) with respect to the signal. We can experimentally verify if backward amplification (explained in Chapter 3) happens or not in our periodic structures. Apart from that, configuration ① and ② are similar. The superconducting coil used to DC flux tune the SQUIDs is directly anchored to the sample holder (itself being anchored to the mixing chamber). The coil is biased with a DC current source at room temperature. Each instrument is connected to a computer running the software QT lab.

5.2.2 Printed circuit board

The printed circuit board (PCB) has the unique function to route the microwave signal from the subminiatures A (SMA) connectors to the samples. The substrate used for the PCB is a material coming from Rogers Corporation® called TMM10i. Its dielectric constant $\epsilon_{r,pcb} = 9.88$ and its thickness $t_{pcb} = 380\,\mu m$ are very close to the ones of the silicon wafers we used for samples fabrication ($\epsilon_{r,w} = 11.9$ and $t_w = 275\,\mu m$). These very close characteristics provide a very good impedance matching between the PCB and the chip and therefore avoid spurious reflections. For resonant JPA such fine-tuning may be a bit excessive. It is however necessary for TWPA since the impedance matching is crucial for their general performances. One of the drawbacks of this material is its fragility: it breaks easily.

For JPA

The PCBs designed for JPAs are the simplest possible: a microstrip line going straight from the SMA to the chip. The SMA connector is soldered from one end while the micro bonding are done on the other end. The microstrip is 350 µm

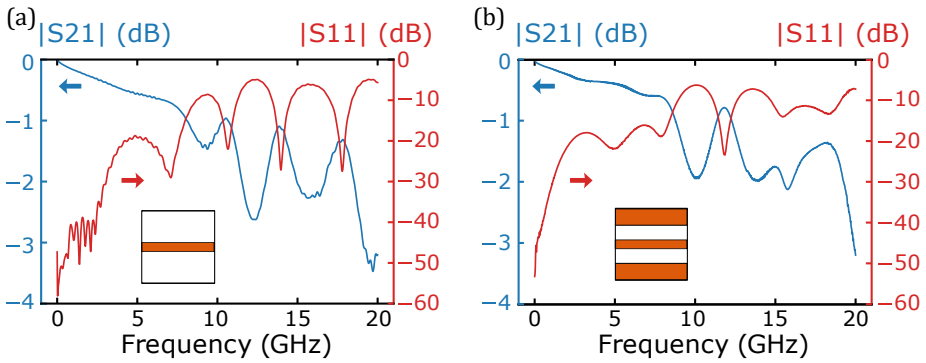

Figure 5.4 – **Transmission and reflection of the printed circuit boards (PCB). (a)** Scattering parameters of the PCB dedicated to the JPA. It is a microstrip line geometry. **(b)** Scattering parameters of the PCB dedicated to the TWPA. It is a co-planar waveguide geometry. Scales for S_{21} and S_{11} axis are not the same.

wide on the PCB (and 238 µm wide on the chip). A sketch of its design and its microwave response are shown in Fig. 5.4**(a)**.

For TWPA

We have seen in the chapter dedicated to device fabrication (Chapter 4) that given the top ground geometry, the best suited transition to provide a good electric field continuity is CPW → top ground. The geometry used for the PCB is thus CPW. It is very important to have vias connecting the upper ground to the lower ground (in contact with the sample holder) all over the PCB to avoid parasitic modes. Microwave response of the CPW geometry is shown in Fig. 5.4**(b)**. Our criteria for a PCB are: a transmission better than −1 dB ($20\log|S_{21}| > -1\,\text{dB}$) and a reflection better than −20 dB ($20\log|S_{11}| < -20\,\text{dB}$). From Fig. 5.4, we see that these criteria are only respected between 0.1 GHz and 8 GHz. For frequencies above 8 GHz, it seems that a parasitic resonance occurs for both geometry (microstrip and CPW). Other team members using the same general designs for the sample holders noticed the same. It seems that this parasitic resonance comes from boundary conditions of the sample holder itself, but its exact origin is not yet understood.

5.2.3 Calibration of the setup

Calibration of the microwave setup gives additional information necessary to fully characterize the DUT. Essentially, the full setup can be divided in three parts (see Fig. 5.3 configuration ①): the input line from the instruments to the DUT, the DUT itself and the output line from the DUT to the instrument. For a resonant

JPA, internal losses can be discarded but not for TWPAs.

For amplifiers in general, calibration of the output line **gain** is crucial because it leads *in-fine* to the amplifier noise T_n. The uncertainty on T_n will depend on the quality of the calibration method for the output line. For instance, a calibration done with two calibrated sources [33] allowed to infer the exact added noise of a resonant JPA (thus experimentally demonstrating the standard quantum limit (SQL) of amplification). A calibration [35] using a shot noise tunnel junction [107] allowed to have a precision on the order of 5% on the total noise of the Josephson amplifier. A poor-man calibration technique consists in measuring the different lines at room temperature and extrapolate this calibration to cryogenic temperature. This calibration as precise as it may be at room temperature will hardly have an uncertainty better than 3 dB.

To a lesser extent, calibration of the **phase** propagation in the setup allows to characterize the microscopic parameters of the TWPA via the measurement of their dispersion relation. In the next chapter, we will give the precise experimental protocol.

Room temperature calibration

We performed a room temperature calibration of the input line of configuration ① and ② (they are identical) just before the noise measurement of the TWPA presented in Chapter 8. At 6 GHz, we measured between the IDR input (represented by the 4 K dashed line in Fig. 5.3) and the 25 mK stage 46 dB of attenuation. Given the 43 dB of discrete attenuators, and the nature of the coaxial cable (SC-219/50-SSS-SS from Coax Co®), we concluded that the coaxial cable is 79.4 cm long and has 1.5 dB attenuation when the IDR is cold. We also have measured 2 dB attenuation for the IF filter at 25 K (between two cooldowns, we only removed the filter). We also considered the 20 dB attenuator on the 25 K stage. Eventually, we directly measured the attenuation of room temperature components (microwave combiner and coaxial cables) at 6 GHz and found 9.1 dB. When the IDR is cold, we thus estimate the total attenuation between the RT instruments and the DUT to −75.6 dB. We round it to $-76\,\text{dB} \pm 3\,\text{dB}$.

In-situ calibration

In-situ calibration allows to measure the transmission of the microwave setup when the refrigerator is cold when there is no device to measure. It allows to calibrate the phase propagation within the microwave setup and the loss within the DUT (in that present case the TWPA). During the course of the different TWPA batches measurement, we have tested two different *in-situ* calibration techniques. Chronologically, the first one was with a four-port microwave switch as shown in Fig. 5.5**(a)** (left part) shunting the TWPA. It allows a calibration during the same cooldown. Unfortunately, this calibration scheme adds uncertainty in the transmission because of the extra cables in between the switch and the TWPA. Regarding loss, it does not really matter as the copper cables, 30 cm in total, hardly attenuate. However, for phase calibration, these extra centimeters of wave

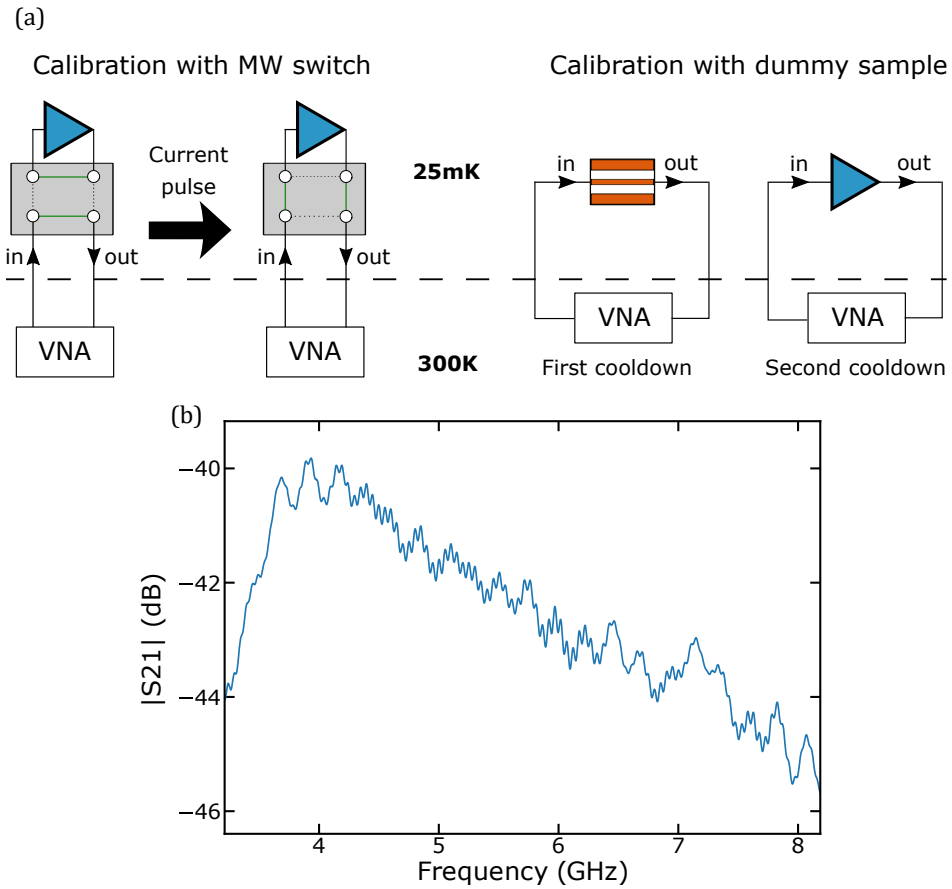

Figure 5.5 – **Calibration of the microwave setup. (a)** Two calibration methods. Either using a microwave switch or a dummy sample measured in a dedicated cooldown. **(b)** Transmission of configuration ① (Fig. 5.3) with a dummy sample. 32 dB of attenuation are added at the output of the VNA in comparison with what is shown in Fig. 5.3.

propagation must be accounted for, by measuring, prior to the cooldown, the phase turning in the cables at room temperature. The difference in the phase propagation whether the cable is at room temperature or cryogenic temperature adds up to the total uncertainty. To overcome this uncertainty, we can follow the method shown in Fig. 5.5**(a)** (right part). In a first time, we perform a first cooldown fully dedicated to measure the dummy sample presented in Section 5.2.2. In a second time, we carry out a cooldown with the TWPA only. By subtracting their amplitude, we obtain the losses of the TWPA. By subtracting their phases, we obtain the phase propagating in the TWPA only. Due to the large kinetic

inductance and low velocity of wave propagation in the TWPA, its total length is much less than the wavelength for propagation through the dummy sample. We can therefore safely neglect the small phase shift due to the propagation through the dummy sample. This second technique is perhaps heavier to carry out since it requires two cooldowns; but this calibration is more accurate and asks for less corrections than the first one. In Fig. 5.5**(b)** we show the transmission of the dummy sample in configuration ① (as in Fig. 5.3) at 25 mK.

Linear characterization of the Josephson arrays

6

Contents

This chapter aims to characterize the linear properties of the different samples measured throughout my PhD. All measured and presented devices are SQUID arrays. To differentiate them, the short arrays used for resonant parametric amplification are denoted $\lambda/4$-Res (after $\lambda/4$ resonator). The medium size arrays with hanger geometry, fabricated using the top ground geometry used for loss calibration, are denoted S-Res (after SQUID resonator). Finally, the long SQUID arrays used as traveling-wave amplifiers are denoted S-TL (after SQUID transmission line). Since four S-TLs will be presented, they will be discriminated with letters A to D. The linear characterization of the $\lambda/4$-Res and the S-TLs will be useful for the two next chapters where they will be operated as amplifiers. The purpose of the S-Res is mainly to be a control sample with respect to the S-TLs.

Link back to Table of contents →

6.1 SQUID $\lambda/4$ resonator

6.1.1 Presentation of the SQUID $\lambda/4$ resonator

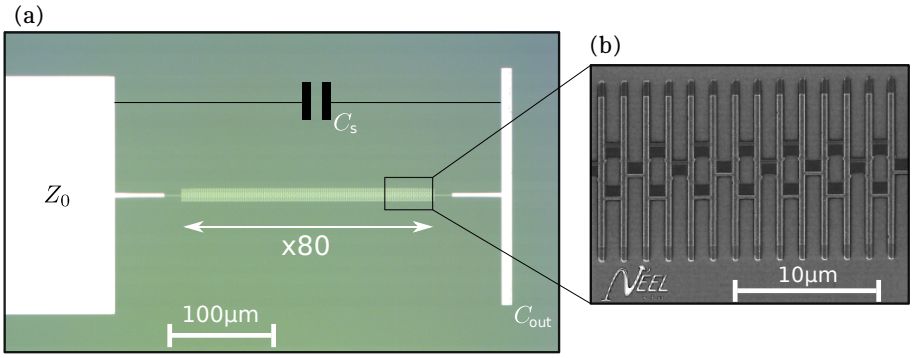

Figure 6.1 – $\lambda/4$ **resonator. (a)** Optical microscope picture. The leftmost pad is the bonding pad, the right-most thin pad is the shunt capacitance denoted C_{out}. In between, there is the array of 80 SQUIDs. **(b)** Scanning electron microscope (SEM) picture of seven SQUIDs where a single junction has a $10.7\,\mu\text{m} \times 0.37\,\mu\text{m}$ area.

The $\lambda/4$-Res characterized in this chapter is a short SQUID array, galvanically coupled to a $Z_0 = 50\,\Omega$ transmission line via only one port. The device works in reflection. The transition between the transmission line and the SQUID array does not require a great care: as shown in Fig. 6.1, the transition between the leftmost pad and the array is step-like. The array is made of 80 identical SQUIDs. Each SQUID is made of two identical Josephson junctions with dimensions $H = 10.70\,\mu\text{m}$ and $w = 0.37\,\mu\text{m}$, with the same notations as defined in Fig. 4.3. The area of the SQUID loop is $4\,\mu\text{m} \times 1.2\,\mu\text{m}$. The size of the unit cell is denoted $a = 3.2\,\mu\text{m}$ therefore the array is $256\,\mu\text{m}$ long. The coil threading the array has a radius of 2 cm, 400 turns and is centered with respect to device. The magnetic flux is therefore supposed to be homogeneous over the rectangle of area $256\,\mu\text{m} \times 4\,\mu\text{m}$.

The array is characterized by five microscopic parameters: L, C and a_0 for each SQUID (as explained in Section 2.6), C_{out} for the large shunt capacitance at the end of the array and C_{s} for the stray capacitance between the input pad and the thin pad as shown in Fig. 6.1.

6.1.2 Linear response

The first and simplest characterization to carry out is to measure the reflection of a low-power signal with a VNA. No useful information can be inferred from the featureless reflected power (Fig. 6.2**(a)**), due to the absence of resonance. Yet, the reflected phase leads to the extraction of the external quality factor Q_{e}. The fit of

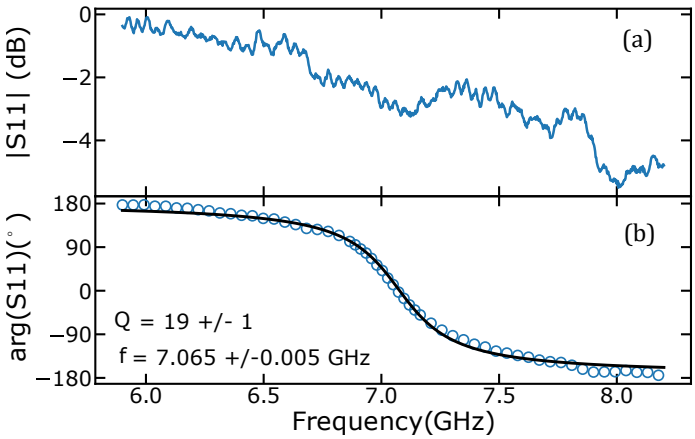

Figure 6.2 – **Amplitude & phase of the reflection coefficient measured with a VNA. (a)** Measured amplitude of the reflected signal. Since the array is strongly over-coupled to the transmission line, the dip in reflection is very weak and hard to resolve above the background ripples. **(b)** Measured phase of the reflected signal (blue hollow points). The experimental data are fitted (solid black line) with an arctangent which gives the external quality factor $Q_e = 19 \pm 1$ and the resonance $f_0 = 7.065\,\text{GHz} \pm 0.005\,\text{GHz}$.

the phase with an arctangent function gives $Q_\text{e} = 19 \pm 1$. No reliable value of the internal quality factor Q_i can be extracted from such fit. However, internal quality factors of resonators fabricated with a similar process (same nominal wafer, recipe, BFF technique) have been measured [77]. From these measurements, internal quality factors in the order of 10^4 were extracted. It is in agreement with the absence of resonance in the reflected power as $Q_\text{i} >> Q_\text{e}$. The 2π phase shift fit also allows to extract the resonance of the $\lambda/4$-Res $f_0 = 7.065\,\text{GHz}$ (at zero magnetic flux).

6.1.3 Dispersion of the array

Power and phase reflection measurement allowed for characterizing the macroscopic parameters of the $\lambda/4$ resonator. Let us find now the microscopic parameters of the resonator. To infer them, we need its dispersion relation and thus more than a single resonant frequency. Then, we must probe higher resonant frequencies. Since we are probing in reflection, it requires a circulator as shown in Appendix B. Microwave circulators are pass-band components since they rely on interferometric. The one used in this experiment has a 4 GHz-8 GHz band. Therefore, we cannot simply probe the higher resonant frequencies with a single-tone spectroscopy as in Fig. 6.3. We have seen in Chapter 2 and Chapter 3 that in a $\chi^{(3)}$ nonlinear medium, the incoming power on one mode affects the reso-

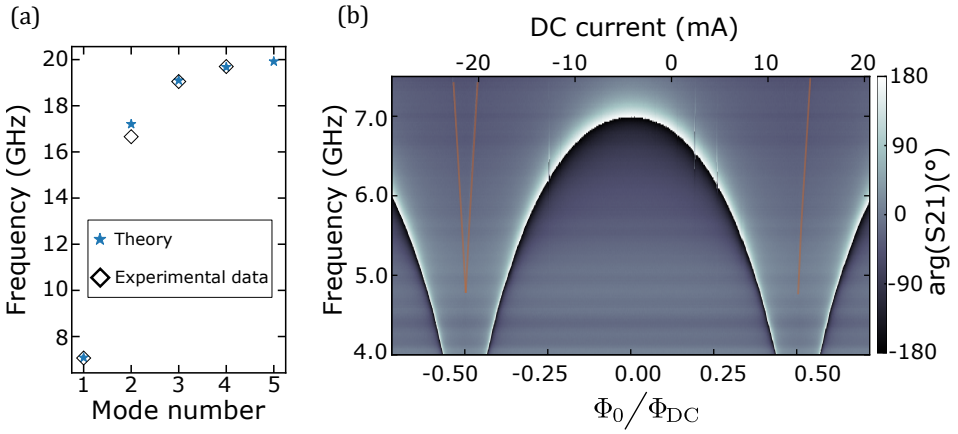

Figure 6.3 – **Resonances of the $\lambda/4$-Res. (a)** Two-tone spectroscopy. We can detect up to 4 modes. We fit this dispersion with the Lagrangian approach and the remote ground model as described in Chapter 2. Fitting parameters are in the text. **(b)** Flux modulation of the resonator close to its first resonance indicated by the abrupt change of color. In orange, we highlighted the second mode resonance going down to 4.5 GHz close to $\Phi/\Phi_0 = \pi/2$.

nant frequencies of the other modes. Having concluded that single junctions or symmetric SQUID behave as $\chi^{(3)}$ nonlinear medium, we can perform a so-called two-tone spectroscopy [75, 108] to detect resonant frequencies higher than 8 GHz. We do as follow: we lock a first tone (called probe) on the first resonance of the short SQUID array. We sweep the frequency of a second tone while recording the probe's phase. A mode is detected whenever there is a dip in the measured phase. In Fig. 6.3**(a)**, we plot the outcome of the two-tone spectroscopy. The second mode frequency is already close to the plasma frequency $\omega_\Pi/2\pi$ and higher modes are in the vicinity of $\omega_\Pi/2\pi$ (see Fig. 6.3**(a)**). A longer array with a lower free spectral range would allow to have more resonant modes [68, 109] and thus more frequencies available for amplification.

The dispersion relation has two features: a linear section and a plateau. The slope of the linear part gives the wave velocity while the plateau sits at the plasma frequency. The array being described by five parameters, we need to reduce the number degrees of freedom to fit the dispersion. The final large capacitance C_{out} and the stray capacitance C_{s} can be inferred using Sonnet. We found $C_{\text{out}} = 24.7\,\text{fF}$ and $C_{\text{s}} = 1\,\text{fF}$. The Josephson capacitance C is obtained from fabrication consideration [54] and set to $C = 370\,\text{fF}$. There are then two parameters left for two independent equations. We fit the experimental points with the Lagrangian approach detailed in Section 2.6. We finally extract $L = 165\,\text{pH}$ and $a_0 = 4.3\,\mu\text{m}$. The former gives a critical current density of $25\,\text{A}\,\text{cm}^{-2}$ and the latter is close to the unit cell length $a = 3.2\,\mu\text{m}$. Both extracted values are in the expected range.

6.1.4 Flux response

The SQUID array can be entirely and homogeneously threaded with an external DC magnetic flux generated by a small coil on top of the device. As shown in Fig. 6.3**(b)**, the magnetic thread is pretty smooth with some exceptions where the phase jumps for some flux. In this figure, the 2π shift is highlighted by the abrupt change of colors, for instance close to 7 GHz for zero magnetic flux. We hardly see any hysteretic jumps close to $\Phi/\Phi_0 = \pi/2$ which would be caused by stray inductance in the loop. But in the other hand we did not measure down to zero frequency because of the circulator pass band (starting from 4 GHz). Hence we cannot exclude hysteretic jumps below this frequency. Also close to $\Phi/\Phi_0 = \pi/2$, for frequency between 6 GHz and 7 GHz, we can spot the second resonant frequency also going down to 4.5 GHz.

6.2 SQUID $\lambda/2$ resonator

6.2.1 Presentation of the SQUID $\lambda/2$ resonator

This section is dedicated to the presentation and the characterization of the SQUID $\lambda/2$ resonator (S-Res) (shown in Fig. 6.4**(a)** and **(b)**) whose design and fabrication have been explained in Section 4.2.3. The device is a $Z_0 = 50\,\Omega$ transmission line in coplanar waveguide (CPW) geometry coupled to a 600 SQUID long array in a hanger geometry. The coupling is capacitive, via an interdigital capacitance. The SQUIDs are nominally identical to the ones presented in the previous section. The main difference naturally comes from the top-ground geometry of the resonator that boosts drastically the ground capacitance C^{g} of each SQUID. Given the geometry, a simple planar capacitance model is enough to describe C^{g}. X_e is the reactance of the wire bonds and reproduces the asymmetry in the resonance dip (see Fig. 6.4**(c)**). Unlike the previous $\lambda/4$-Res, the S-Res external and internal quality factors (Q_{e} and Q_{i}, respectively) are designed to be close from one another. Fits of the S_{21} scattering parameter allow to extract both Q_{e} and Q_{i}.

In this thesis, the results associated to one S-Res are presented. During her internship, **Ekaterina Al-Tavil** measured several resonators, with different top dielectric (amorphous silicon and alumina) as presented in her master thesis [98]. The S-Res presented here is the one I measured during the second year of my PhD.

6.2.2 Extraction of the quality factors

The SQUID array being much longer than the previous $\lambda/4$ resonator, the free spectral range is much smaller and is about 350 MHz. Given the microwave setup, we could measure well resolved resonant dips between 3.5 GHz and 8.5 GHz. It amounts to about twelve resonances for one sample. The fit of the scattering parameter S_{21} (transmitted amplitude and phase) relies on **Étienne Dumur**'s

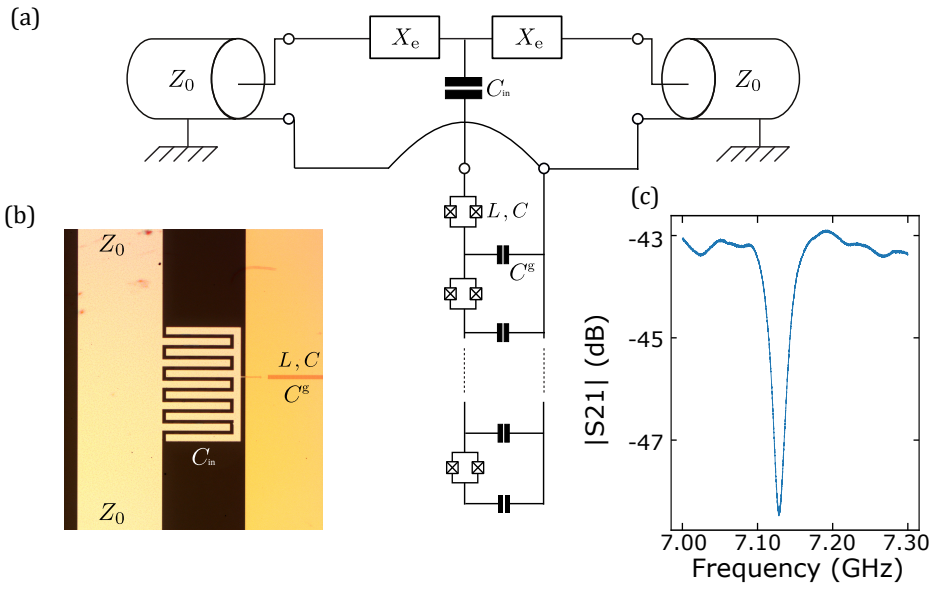

Figure 6.4 – **Hanger $\lambda/2$ resonator with a top ground geometry.** **(a)** Electrical circuit of the S-Res. SQUIDs are characterized by L, C^g and C. The S-Res is coupled to a $Z_0 = 50\,\Omega$ transmission line via a capacitance denoted C_{in}. The wire bonds reactance is denoted X_e. **(b)** Picture taken with an optical microscope: on the left side the Z_0 impedance transmission line in coplanar waveguide geometry, in the center the interdigital capacitance, and on the right the 600 SQUID long resonator covered by a 400 nm gold sheet. **(c)** Transmission measured with the VNA close to a resonance. Fit of such resonance allows to extract quality factors (internal and external).

PhD thesis [97]:

$$S_{21} = \frac{Z_0}{Z_0 + iX_e} \frac{1 + 2iQ_i(\frac{\omega-\omega_0}{\omega_0})}{1 + \frac{Q_i}{Q_e Z_0}(Z_0 + iX_e) + 2iQ_i(\frac{\omega-\omega_0}{\omega_0})}, \tag{6.1}$$

where ω is the signal frequency and ω_0 is the resonance frequency. In Fig. 6.5**(a)-(b)** we plot five resonances with their respective fits. In panel **(c)** we plot an histogram of all the extracted Q_i from S_{21} fits at very low input signal power P_s, close to single photon regime. We estimate the signal power as $P_s = -136\,\text{dBm}$, where $-76\,\text{dB}$ come from the setup (see Chapter 5), $-30\,\text{dB}$ from discrete attenuators at room temperature while the VNA sends $-30\,\text{dBm}$. Signal power at the

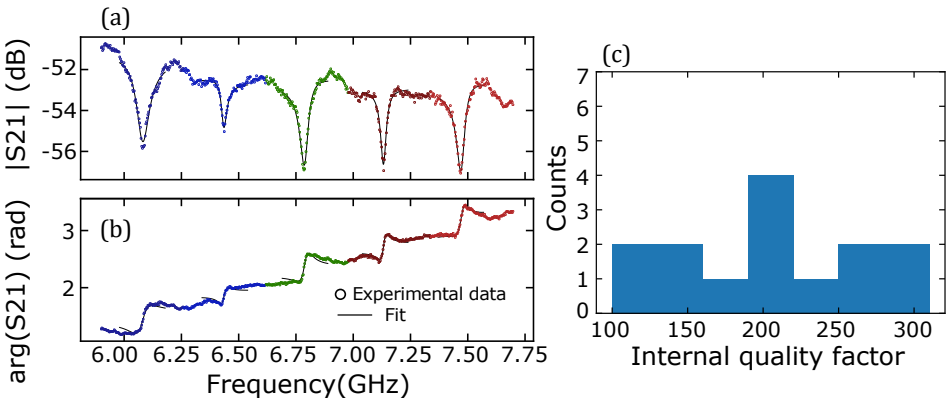

Figure 6.5 – **Extraction of the quality factors. (a)-(b)** Experimental scattering parameter S_{21} (amplitude **(a)** and phase **(b)**) of the S-Res and their fit close to resonances between 6 GHz and 7.75 GHz. **(c)** Counts of internal quality factors extracted from the fit of 14 modes as in panel **(a)** between 3.8 GHz and 8.46 GHz at input power $P_s = -136\,\text{dBm} \pm 3\,\text{dBm}$, corresponding to the single-photon level. We observe a spread of the internal quality factor of around 200 at this power.

input of the S-Res can be translated in photon number [97]:

$$\bar{n} = \frac{2\omega_0/Q_e}{\hbar\omega_0(\omega_0/Q_e + \omega_0/Q_i)^2} P_s. \tag{6.2}$$

For $P_s = -136\,\text{dBm}$, we reach $\bar{n} < 1$ and thus are in the single photon regime. In this power range, we extract internal quality factors centered around $Q_i = 200$ with a maximum spread of $\pm$ 100 as sown in Fig. 6.5**(c)**. These internal quality factors can be translated into a loss tangent $\tan\delta = 0.005 \pm 0.002$ which is a little worse from what we initially expected in Chapter 4 ($\tan\delta = 0.001$) for an alumina dielectric. It is the right order of magnitude, but losses are five times higher than expected. We can believe that the discrepancy between what we have found in the literature and what we have measured comes from fine tuning in the fabrication process. Improving the loss tangent from a factor five seems doable, since, so far, the process has not been optimized to minimize alumina loss.

6.2.3 Power dependence of the internal quality factors

As discussed in Chapter 4, losses are very detrimental to traveling-wave amplifiers. In Chapter 8, te influence of TWPA loss on its intrinsic noise will be formally calculated. A widely acknowledge explanation in the literature for these electrical losses is the presence of two-level systems (TLS) [110] at the superconductor dielectric interface [96, 111, 112]. One of the TLSs signature is the dependence

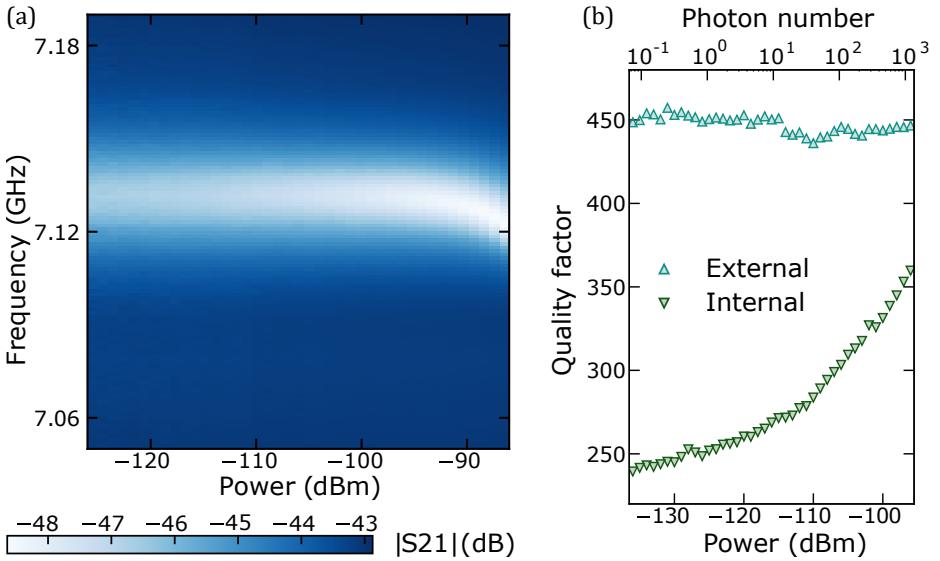

Figure 6.6 – **Power dependence of the internal quality factor. (a)** Color plot of the signal transmission as a function of its frequency and its power. The frequency shift of the resonance due to the self-Kerr effect is visible through the shift of the transmission dip for large input power. **(b)** Extracted quality factors from S_{21} fits. Saturation of internal losses is observed for very low input power. It is around 200, as shown in Fig. 6.5**(c)**. For higher input power, internal losses decrease (it is not visible in this figure) but they also saturate for very large input power.

of losses with respect to the input signal power. To check the power dependence of losses, the experimental protocol is straightforward: we keep measuring one resonance of the S-Res while increasing the input signal power P_s of the VNA. We then fit each resonance and extract the quality factors. In Fig. 6.6**(a)** we plot the signal transmission as a function of its frequency and power close to one resonance. It is noteworthy that for large input power, the resonance actually shifts towards lower frequency because of the self Kerr effect. For each power, we extract Q_e and Q_i and plot them in Fig. 6.6**(b)** as a function of P_s. For very low input power, the internal quality factor somehow saturates (for this frequency, it is around 250). We believe it corresponds to the single photon regime (see upper x-axis of the figure **(b)**). For larger input power, the internal quality factor increases, which is equivalent to a drop in the dielectric losses. This feature is explained by the saturation of the TLSs for large power. For very high input power, all TLSs could be saturated and another plateau should be visible, giving a S-shape to the curve $Q_i(P_s)$. Unfortunately, during the measurement run I did not go to high enough input power and it cannot be seen in Fig. 6.6**(b)**. However, these

high power measurements have been carried out by **E. A-T** on similar devices and the S-shape is recovered. These figures are reported in her master thesis [98]. This S-shape and more precisely this double saturation for very low and very high input power place TLS as the best candidate to explain our dielectric losses. Moreover, the proximity of the experimental values extracted from the fits with the aforementioned literature reporting the presence of TLSs led us to the same conclusion.

6.2.4 Dispersion with two-tone spectroscopy

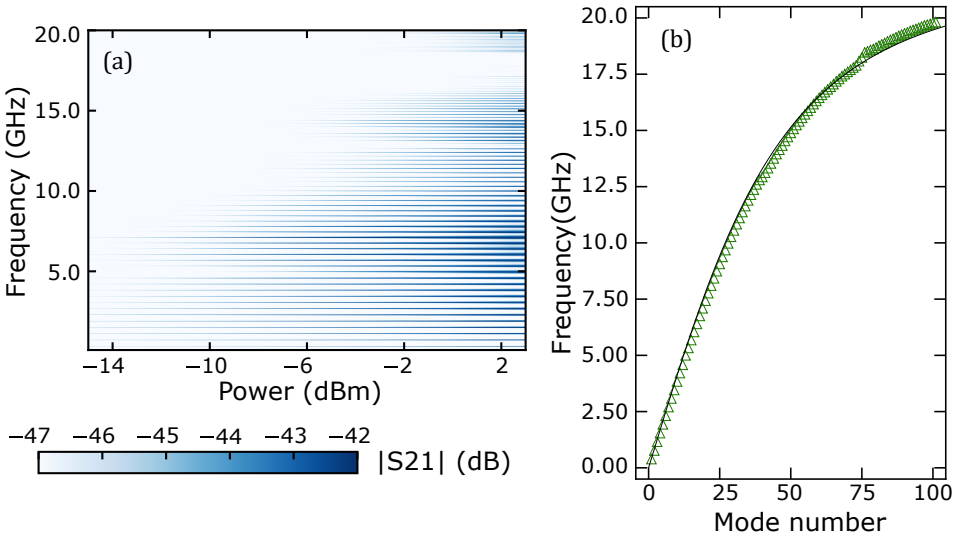

Figure 6.7 – **Two-tone spectroscopy. (a)** Color plot of the two-tone spectroscopy. Each peak in transmission corresponds to a resonant mode of the S-Res. **(b)** Experimental dispersion relation obtained from two-tone spectroscopy and its fit. We see that the free spectral range is smaller compared to the much shorter $\lambda/4$-Res. Extracted Josephson inductance from the fit is reported in Table 6.1.

We can perform the same two-tone spectroscopy as carried with the $\lambda/4$-Res but this time with the S-Res array in order to get its dispersion relation, and to extract its microscopic parameters (in particular the Josephson inductance L). The principle is the same, we lock the probe on a resonant frequency (dip in transmission) while we sweep the second tone frequency and power (shown in Fig. 6.7**(a)**). A resonant mode is recorded by a peak in transmission. All peaks are then reported in Fig. 6.7**(b)** as a function of their respective mode number n. The latter is then translated into a wavevector k thanks to the boundary condition of a $\lambda/2$ resonator where $k = n\pi/N_{\mathrm{j}}a$, with a the unit cell length and N_{j} the number of SQUIDs in the array. The experimentally recorded frequencies are then

fitted with a standard formula for the dispersion relation of a Josephson junctions array [76]:

$$\omega(k) = \omega_p \sqrt{\frac{1-\cos ka}{1-\cos ka + C^{\mathrm{g}}/2C}}. \tag{6.3}$$

As we previously mentioned, C^{g} can be modeled as a planar capacitance given the top-ground geometry. We know the nominal dimensions of the junctions, the dielectric thickness and the value for the dielectric constant of the alumina $\epsilon_{\mathrm{r,Al_2O_3}}$, which might be a bit off given the cryogenic conditions, but the error is limited to a narrow range. To sum up, the S-Res system is simpler to model than the previous short array: there are only three microscopic parameters, and two out of three can be inferred from geometrical and design considerations. There is then only one free parameter, the Josephson inductance L. The fit of the experimental dispersion is shown in Fig. 6.7**(b)**. From this fit, we extract an inductance $L = 137\,\mathrm{pH}$ which is 20% lower from what we have found with the short SQUID array characterized in Section 6.1 ($L = 165\,\mathrm{pH}$). To explain this discrepancy, three points must be kept in mind:

— they have been fabricated twenty-five months apart.

— They were fabricated in two different evaporators.

— After the atomic layer deposition of the dielectric layer the junction tunnel barrier gets thinner (because the whole sample is heated to favor atomic layer deposition) and therefore L drops (see Fig. 4.9 in Chapter 4).

It shows the consistency of the extracted values we find along the different characterization techniques. However, the most important step is to compare the extracted values between the current S-Res and the SQUID transmission line (S-TL) that will be characterized in the next section. All data related to the characterization of the different samples are reported in Table 6.1.

6.3 SQUID transmission line

In this section we will present SQUID transmission lines (S-TL) coming from four different batches fabricated between November 2017 and July 2018, labeled 1 to 4 following the chronological order. The previously characterized S-Res device was coming from batch 2. In Chapter 8, a S-TL from batch 4 will be operated as a SQUID-based traveling-wave parametric amplifier.

6.3.1 Dispersion with a single-tone spectroscopy

All S-TLs are naturally fabricated with the top-ground deposition technique to have the right impedance matching. With a S-TL, the first feature to check is whether or not the array has a characteristic impedance $Z_{\mathrm{c}} = \sqrt{L/C^{\mathrm{g}}}$ close to $50\,\Omega$. Up to now, we have inferred microscopic parameters with a fit of the

dispersion relation, experimentally measured via a two-tone spectroscopy. Unfortunately, in the absence of resonant modes, it is not possible to carry such measurements with a S-TL. To circumvent this issue we instead measured directly the phase propagating inside the S-TL to infer the experimental wavevector. The experimental protocol is to first measure the phase of the scattering parameter S_{21} of the whole setup **with** the S-TL and subtract from it the same quantity measured **without** the S-TL. To obtain the latter we used the two techniques presented earlier in Chapter 5: either with a microwave switch shunting the S-TL or with a dummy sample. Once the calibrated phase obtained, we divide it by the total length of the S-TL $L_{\text{s-tl}} = N_{\text{j}}a$ (same notation as previously defined) to eventually obtain the experimental wavevector. We thus have the experimental dispersion relation $\omega(k)$. Next, we use the standard approach: we fit the dispersion with Eq. (6.3) where k is taken as a continuous experimental variable. The S-TL having also a top-ground geometry, all microscopic parameters (C and C^{g}) are fixed but the Josephson inductance L. We extracted L from the different batches. We can compare two extracted inductances of nominally identical SQUID arrays coming from the same batch. For batch 2, we compared the extracted L between a S-TL and the previous S-Res. For the former we find 127 pH while for the latter we found 137 pH. We find less than 10% discrepancy for two SQUID arrays fabricated on the same two-inch wafer. This discrepancy can be mainly explained by the relative difficulty to keep a good homogeneity in the tunnel barrier thickness over such areas [113]. However, we obtained close values for two different samples taken with two different protocols. We can hence have a good confidence in our characterization methods. For the four batches, all parameters are reported in Table 6.1. Among the different batches, the impedance of all the arrays is close to 50 Ω.

6.3.2 Losses characterization

A more straightforward way to check whether or not the arrays are correctly impedance matched to the 50 Ω environment is to measure the transmitted power within the S-TL. An absence of peaks in transmission (as with a Fabry-Péro cavity would do [93, 94]) is the signature of a correctly matched array. Studying the calibrated transmission also allows to study transmission losses within the S-TL. Calibrated transmission of S-TL are shown in Fig. 6.8**(a)-(d)**, where samples from batch 1 to 4 are presented. The different fabrication parameters for each batch are reported in Table 6.1. Despite some differences in the fabrication recipes (Atomic layer deposition temperature, dielectric thickness), losses are given by the following general trend: −1 dB per gigahertz. As discussed in Chapter 4 dedicated to the fabrication process, we can discriminate two sources of electrical loss in the S-TL: from the dielectric and from the conductor. To model them, we follow the standard microwave engineering approach where we consider the signal amplitude to be [74]:

$$A_{\text{s-tl}} = e^{(\alpha_{\text{d}}+\alpha_{\text{c}})L_{\text{s-tl}}}, \tag{6.4}$$

Device	$\lambda/4$-Res	S-TL A	S-TL B	S-Res	S-TL C	S-TL D
Batch	0	1	2	2	3	4
Type	Res	TL	TL	Res	TL	TL
Phase calib. method	x	Switch	Switch	N/A	Dummy	Dummy
Ox. Pressure (Torr)	4	4	4	4	4	1
ALD temperature (°C)	x	150	150	150	200	150
Dielectric thickness (nm)	x	38	38	38	28	28
Top Ground thickness (nm)	x	200	400	400	400	1000
Top Ground Material	x	Au	Au	Au	Au	Cu
Josephson junction size L(µm)xW(µm)	10.7 x 0.37	12.0 x 0.45	10.5 x 0.40	10.5 x 0.40	12.0 x 0.45	12.0 x 0.45
L(pH)	165	88.1	127	137	140	58.7
C(fF)	370	490	380	380	485	485
C^{g}(fF)	~ 0.1	31	25	25	43	43
$Z_{\mathrm{c}}(\Omega)$	$\sim 10^3$	53	71	74	57	37
Ph. velocity (10^6 m.s^{-1})	~ 25	1.96	1.76	1.62	1.32	2.06
$\tan\delta$ (10^{-3})	0.1*	6.5	6.0	5.0	4.0	6.5
L_{c} (10^{-4}) ($\mathrm{m}^{-1}.\mathrm{Hz}^{-\frac{1}{2}}$)	x	2.5	1.0	x	0.8	<0.1

Table 6.1 – **Summary of the samples characterized in this chapter ($\lambda/4$-Res, S-Res and S-TL).** Main fabrication characteristics, SQUID characteristics and loss coefficients are summarized. The values of flux-dependent parameters are reported at zero flux bias. Calibration methods are also reported. For recall, ALD stands for atomic layer deposition (* = not directly measured with this sample).

.

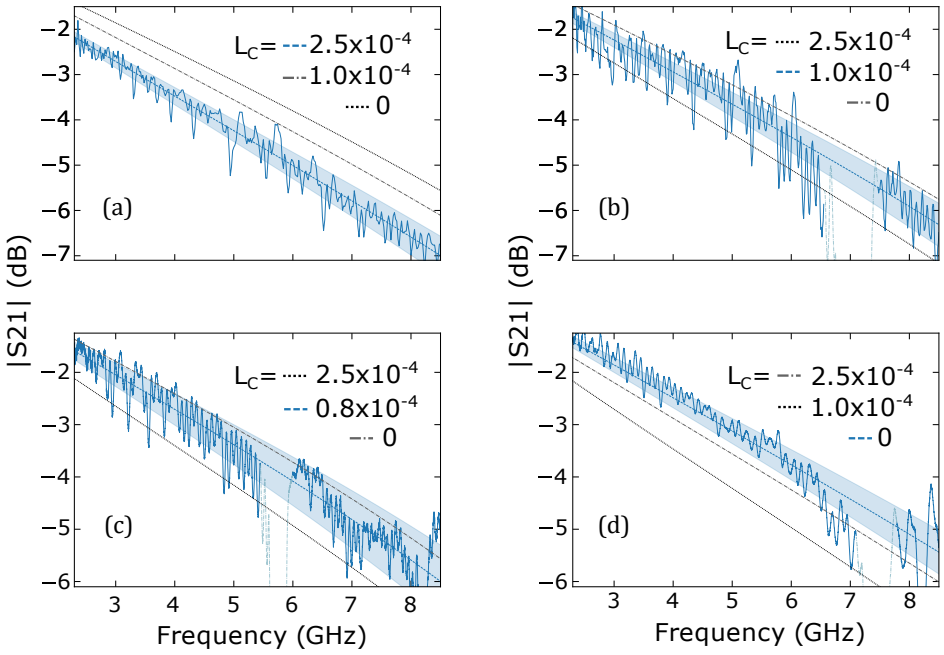

Figure 6.8 – **Calibrated losses within the S-TL.** Panels **(a)** to **(d)** shows calibrated transmission of samples S-TL A to S-TL D, respectively, in solid blue line. For each, we show the calculated attenuation from Eq. (6.4) (dashed lines) with different coefficients α_c as defined in Eq. (6.7) where L_c (in unit of per meter per square root hertz) takes different values reported on the top-right corner of the figures. Blue dashed line is the calculated attenuation with L_c that fits the best experimental data while gray and black dashed lines show the interval of confidence in L_c. Shaded blue areas represent the 5×10^{-4} uncertainty on $\tan\delta$. All data are taken with signal power $P_s = -106 \pm 3$ dBm except for S-TL A (panel **(a)**) taken with $P_s = -101 \pm 3$ dBm.

where α_d (α_c) are real coefficients modeling dielectric (conductor) losses. In our microstrip line geometry, it is safe to assume that the electrical field is confined within the top dielectric between the array and the top-ground. Thus, α_d reads:

$$\alpha_d = k \tan\delta / 2, \tag{6.5}$$

where $\tan\delta$ is the loss tangent and is defined as the ratio of the imaginary part over the real part of the complex permittivity of the medium. Since we previously inferred the experimental dispersion relation $k(\omega)$, we can express α_d as a function of the signal frequency. Regarding the conductor loss, we can rightfully neglect it within the SQUID array since it is superconducting. However, the top ground

being non superconducting, its conductor loss must be accounted for. Given the micro strip geometry of the S-TL where the width of the transmission line is much bigger than the dielectric thickness, the fringing fields can be neglected and conductor loss can be modeled as [74, 100]:

$$\alpha_c = \frac{R_s}{Z_c W}, \tag{6.6}$$

where R_s is the surface resistivity of the conductor. In a normal conductor, surface resistivity is related to its skin depth $\delta_s = \sqrt{2/\omega\mu_0\sigma}$ where μ_0 and σ are the vacuum permeability and the metal conductivity, respectively. On the one hand, if a conductor is much thicker than its skin depth, the surface resistivity is independent of its thickness and is taken as $R_{s,0} = \sqrt{\omega\mu_0/2\sigma}$. On the other hand, if the conductor thickness it comparable or smaller than the skin depth, AC current flows through a narrower area, which increases the effective surface resistivity compared to $R_{s,0}$ [100]. We can leave the resistivity as a free parameter and simply model the conductor losses from Eq. (6.6) as:

$$\alpha_c = L_c\sqrt{f}, \tag{6.7}$$

with f the signal frequency and L_c a prefactor accounting for the conductor loss. To infer the value of $\tan\delta$ and L_c, we fit the experimental calibrated transmission shown in Fig. 6.8. Although S-TL attenuation shows a monotonous trend *versus* frequency, we managed to fit independently these two parameters. Indeed surface resistivity depends on the square root of the signal frequency and dielectric loss varies linearly with frequency. In other words, dielectric loss sets the slope of the insertion loss at high frequencies, while conductor loss affects the lower frequencies. All the obtained fitting parameters are reported in Table 6.1. We observe loss tangent in between $6.5 \times 10^{-3} \pm 5 \times 10^{-4}$ and $4.0 \times 10^{-3} \pm 5 \times 10^{-4}$ for low power measurements, which is again a bit worse from what we could expect. Regarding conductor loss, we observe that as the top-ground thickness increases, L_c drops. We have plotted what we consider to be the best fit (in dashed blue) for each version as well as other values of conductors (in dashed gray) loss to give insights on the confidence interval as shown in Fig. 6.8. We observe that conductor loss decreases as the top-ground gets thicker as expected [100, 101]. We observe that conductor loss is already low for top-ground being 400 nm thick (samples S-TL B and S-TL C) and can be fully neglected when it is 1 µm thick (sample S-TL D).

6.3.3 Flux response

Obviously, having a superconducting top-ground for the S-TL would allow to deposit a very thin top ground without having to suffer from any conductor loss. However, having a superconducting top-ground would not allow to flux bias the SQUID line. On the other hand, a normal metallic top-ground requires a greater care during the fabrication process as explained in Chapter 4, but allows proper threading of the SQUID. The main perk of the flux tuning is the ability to tune,

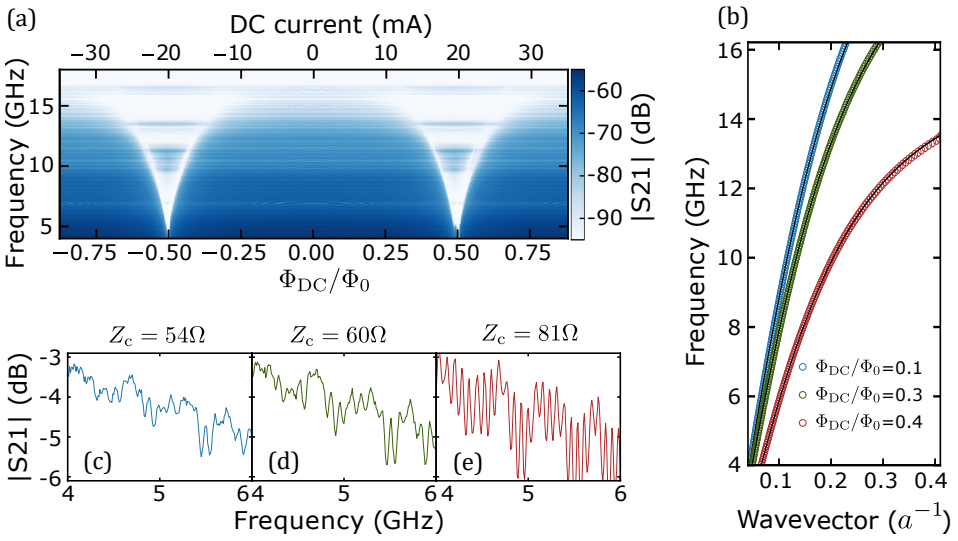

Figure 6.9 – **Flux dependence of the sample S-TL A.** Raw transmission as a function of flux and frequency. **(b)** Experimental dispersion relation and fits taken at three different magnetic fluxes. **(c)**-**(e)** Calibrated transmission. The colors correspond to the same color coding as in **(b)**. The characteristic impedances displayed in the top-right corners are extracted from the fits in **(b)**.

in-situ, the Josephson inductance and thus the characteristic impedance of the array Z_c. It allows to mitigate the inherent uncertainty of any fabrication process. Of course, the flux only allows to increase the Josephson inductance since $L \propto |\cos\Phi|^{-1}$ and therefore increases the characteristic impedance of the S-TL. It is thus necessary to target a lower value for the expected inductance and then to tune it. In Fig. 6.9 we show the flux response of the sample S-TL A. In panel **(a)**, we show a color plot of the transmitted power as a function of the signal frequency and the external magnetic flux Φ_{dc}. The plasma frequency can be spotted by the sudden change in color between blue (transmission) and white (absence of transmission). As $|\Phi_{dc}|$ comes closer from $|\Phi_0/2|$, we can clearly see that plasma frequency drops, until reaching, in the ideal case, zero for $|\Phi_{dc}| = |\Phi_0/2|$. This figures also shows the relative smoothness of the flux modulation on the S-TL: as for $\lambda/4$-Res, no jumps or big dip in transmission occur in a large span of magnetic flux. We can go further into details by studying traces of this color plot, either in phase or in amplitude. In Fig. 6.9**(b)**, three dispersion relation $\omega(k)$ are plotted for three different magnetic fluxes. Fits of the experimental relation are done using Eq. (6.3). As detailed in Section 6.3.1, by calibrating the signal phase inside the S-TL, we can convert it into its wavevector and plot frequency *vs.* wavevector. As expected, as we increase the magnetic flux closer to $\Phi_0/2$, the wave velocity of the S-TL decreases, and therefore the slope of the dispersion drops.

For each of the dispersion shown in panel **(b)** we can plot the transmission and the extracted characteristic impedance as shown in panel **(c)-(e)**. For a flux close to 0, the impedance is close to $50\,\Omega$ and the ripples due to impedance mismatch have an overall low amplitude. For larger magnetic flux, as we extract higher characteristic impedance, we observe an increase in the ripples amplitude. This proves more quantitatively our control over L with external magnetic flux. In Chapter 8 we will show the presence of a magnetic flux sweetspot where the impedance $Z_c \sim 50\,\Omega$ for a flux $\Phi_{dc} \neq 0$ with a sample coming from batch 4.

6.4 Josephson photonic crystal

6.4.1 Presentation

We end this chapter treating on linear characterization of the arrays by emphasizing one of the major feature of our S-TL fabricated with the top-ground deposition technique. Since all microscopic parameters of the array are proportional or inversely proportional to the junctions/SQUID areas, it is possible to turn the S-TL into a photonic crystal and engineer the dispersion relation directly at the lithography stage (detailed in Section 4.1). This is a clear benefit compared to the Lincoln laboratory's traveling-wave parametric amplifiers [47, 114] since it does not require a supplementary fabrication step to implement resonators for phase-matching since photonic gaps can also solve the phase-matching issue. However, on a broader picture, photonic crystals working in the microwave regime have already drown some attention [115] since they could reproduce some very interesting physics coming from the quantum optics field such as frequency translation of single photons [116] or could also be useful in a more applied way to act as cryogenic microwave high-pass or low-pass filters. In Fig. 6.10**(a)-(c)**, we detail one example of a Josephson photonic crystal with a single harmonic modulation of the SQUID areas. The photonic crystal as shown in panel **(a)** will be used as a phase-matched traveling-wave amplifier in Chapter 8. In panel **(a)** the schematic of the photonic crystal and in panel **(b)** a picture of two periods are shown. In the latter, the amplitude of modulation is 60% for clarity purposes whereas actual samples used as amplifiers have an amplitude of modulation of less than 5%. In panel **(c)** an electrical sketch of the photonic crystal is shown with the same notation as defined in Section 3.5. A larger SQUID leads to a larger Josephson and ground capacitance (C and C^g) and to a smaller Josephson inductance L. As mentioned in Section 3.5.2 is not necessary the same for the Josephson parameters (L and C) than for C^g. This is the case for our Josephson photonic crystals. The explanation is related to the fabrication of one junction: the overlap between the two aluminum layers (effectively giving L and C) with height H and width w (as defined and shown in Fig. 4.3) of one junction has a smaller area than the whole surface covered by both the bottom layer and the top layer (effectively giving C^g). As a consequence, the nominal modulation of L, C denoted η is bigger than the modulation of C^g, denoted ζ. This will not have any incidence in the rest of this chapter, but will be considered in Chapter 8.

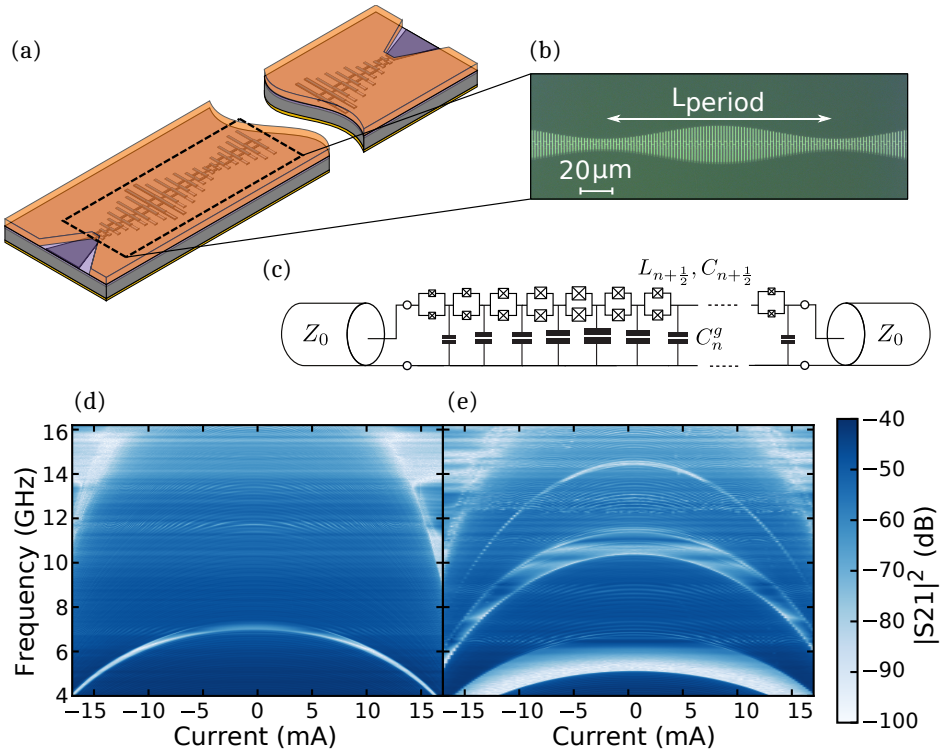

Figure 6.10 – **Periodic modulation in a Josephson photonic crystal. (a)** 3D sketch of a S-TL turned into a Josephson photonic crystal with a top-ground geometry. The orange layer represents the copper top-ground while the purple layer is the alumina layer. Below the orange layer, a sinusoidal modulation of the SQUID height H (as described in Fig. 4.3) can be seen. It is more visible in panel **(b)** where a picture taken with an optical microscope of two periods is shown. In this picture, the modulation is exaggerated (60%) in order to clearly show the modulation. The actual modulation amplitudes used for phase-matched traveling-wave amplifiers are around $\sim 5\%$. **(c)** Electrical circuit of a S-TL with periodic modulation of the electrical components. A larger SQUID area leads to larger C_n^{g} and $C_{n+\frac{1}{2}}$ but smaller $L_{n+\frac{1}{2}}$. **(d)** Flux modulation of the transmission in sample S-TL B. The modulation of the frequency position of the photonic gap is visible. The sinusoidal modulation is 35 SQUID long for 6% modulation amplitude. **(e)** Flux modulation of the transmission for a sample nominally identical to S-TL B (and from the same batch) but with two modulation harmonics. The fundamental harmonic is 42 SQUID long. First harmonic has an amplitude of 36% while the second is 17%.

The property of the photonic crystal can be changed at will: the modulation amplitude defines the gap width while the length of one period L_{period} sets the reciprocal lattice vector and therefore the frequency position of the photonic gap. The frequency position of the latter is also flux-tunable since it is related to L. Likewise the plasma frequency, the gap frequency position can only be shifted down to lower frequency. To illustrate it, we plotted the transmitted power for two Josephson photonic crystals as a function of the external flux in Fig. 6.10**(d)-(e)**.

Single harmonic periodic modulation (sample S-TL B)

In panel **(d)** we plot the flux modulation of transmission for a single harmonic photonic crystal as represented in panel **(a)**. Here, one period is $N_{\text{p}} = 35$ SQUID long with a 6% modulation amplitude. We see that the gap, at zero flux, is roughly 500 MHz wide and positioned at ~ 7 GHz. Naturally, we can tune its position with flux, and fix it, in principle, to zero frequency when the external flux corresponds to half a fluxoid.

Double harmonic periodic modulation

In panel **(e)** we plot a similar figure for a Josephson photonic crystal with nominally identical SQUID but with two modulation periods: the fundamental ($N_{\text{p}} = 42$) and its first harmonic. The fundamental has a 36% modulation amplitude while the first harmonic has 17% modulation. We see two gaps: below 6 GHz and above 10 GHz. Regarding the first gap, it has a lower frequency position compared to the one show in panel **(d)** because its period is longer. It is also wider given its larger modulation amplitude as expected. However, data for the double harmonic crystal are less clean than for the single harmonic one. This could come from the double harmonic or perhaps from the larger modulation amplitude leading to a greater disorder in the characteristic impedance. We did not invest a lot of time in the double harmonic photonic crystal as this sample was simply meant to be a proof of concept. Spending more time on their design could lead to cleaner data.

6.4.2 Characterization

When it comes to characterize a S-TL gap engineered as a Josephson photonic crystal, meaning accounting for the photonic gap in the characterization, it is consistent to use the model developed in Section 3.5 since the same model will be used to describe amplification. To fit experimental linear dispersion relations featuring gaps (see Fig. 6.11), we use Eq. (3.54) from Section 3.5 that links the signal wavevector to its frequency. As previously done, we fix every parameters but the Josephson inductance. As it is shown, the wave velocity and the gap position are well reproduced by only letting L_0 free. As a reminder, the subscript '0' refers to the mean value of the modulated parameters. The gap width being very small (few hundreds of megahertz), if the fit is done on the full measurement frequency windows (more than ten gigahertz), it is hard for a standard fitting

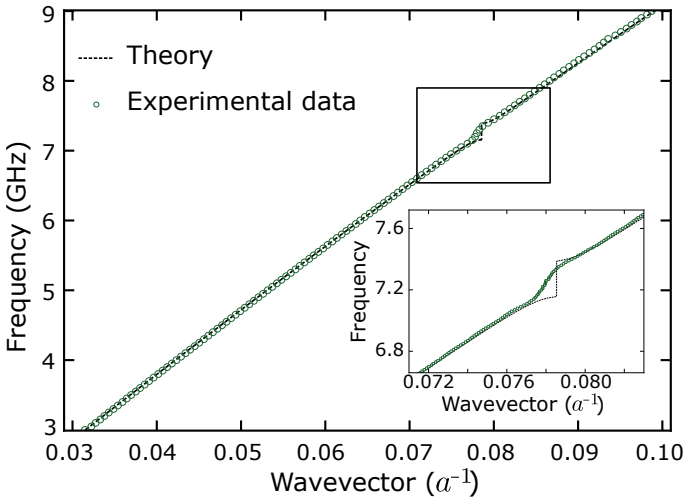

Figure 6.11 – **Linear characterization with the complete model.** Dispersion relation of sample S-TL D measured at very low magnetic flux ($\Phi/\Phi_0 = 0.1$). Theoretical curve is a fit to the linear dispersion relation with L_0 (mean value of the modulated L) as a fit parameter. The kink at 7 GHz is the photonic gap created by spatial modulation. **Inset:** close-up of the photonic gap. Theory agrees with experimental data and reproduces gap position with a 0.6% error.

procedure to really take the gap into consideration. Thus, after fitting on the whole measurement windows, an adjustment on L_0 of about 1 pH is required to get a perfect match between the theoretical and experimental position of the gap, which is less than 2% and is in the confident interval. We can thus define 1 pH as the uncertainty interval of this fitting procedure. Although the agreement is good, we see in the close-up that it is also not possible to have a perfect match between the gap frequency position **and** the gap wavevector position at the same time. After adjustment of L_0 to get a perfect match in frequency, there is still a small discrepancy of 0.6% error which is in our confidence interval. Moreover, we stress the fact that experimental points within the gap correspond to a very weak signal, which is not very suited to a precise fit. In Fig. 6.11, experimental data have been taken from sample S-TL D. From the fit, we extract $L_0 = 60.5$ pH, which must be compared to the previous value 58.7 pH extracted using the previous simpler model (without modulation). These two values are in good agreement. The former extracted value will be further used in Chapter 8 when the Josephson photonic crystals will be operated as traveling-wave amplifiers. Before turning to TWPAs, the next chapter is dedicated to experimental results obtained with the resonant Josephson parametric amplifiers designed at the early stage of this PhD.

Resonant Josephson parametric amplifier

7

Contents

This chapter is dedicated to the short SQUID array designed as a $\lambda/4$ resonator and operated as a resonant Josephson parametric amplifier (JPA). First, we address its performances by characterizing its gain, bandwidth, saturation and added noise. Then, we use this device to readout a superconducting qubit. These results have been obtained in collaboration with **Rémy Dassonneville** and **Vladimir Milchakov**. We conclude by quantifying the measurement efficiency of the qubit readout using our JPA in the measurement setup.

Link back to Table of contents →

7.1 Amplification

7.1.1 Effective model of the resonant mode

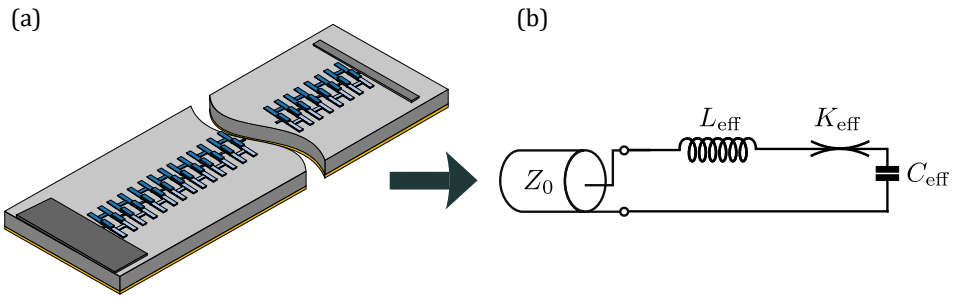

Figure 7.1 – **Mapping of the $\lambda/4$-Res to a nonlinear LC series resonator. (a)** 3D sketch of the resonant JPA based on an array of 80 SQUIDs. **(b)** Effective LC series nonlinear resonator. Effective parameters are calculated from the model developed in Section 2.6 with experimental values extracted from fits done in Section 6.1.

In Chapter 2 we have seen how to map a nonlinear $\lambda/4$ nonlinear resonator made of N junctions (or SQUIDs) to a nonlinear LC resonator. Close to one of its resonance, the resonator is described by three effective parameters: an inductance, a capacitance and a nonlinearity denoted as $L_{\text{eff}}, C_{\text{eff}}$ and K_{eff}, respectively. By plugging the experimental microscopic parameters extracted from the fits in Section 6.1, we calculate the effective parameters and find $L_{\text{eff}} = 21\,\text{nH}$, $C_{\text{eff}} = 24\,\text{fF}$ and an effective nonlinearity, being the self-Kerr coefficient of the first mode $K_{\text{eff}} = 80\,\text{kHz}$. As discussed in Chapter 2, K_{eff} is an important parameter to model the gain of the amplifier since it is proportional to the pump strength; it is also key to model the amplifier saturation.

From these calculated parameters, we define the effective resonant angular frequency $\omega_{\text{eff}} = 1/\sqrt{L_{\text{eff}}C_{\text{eff}}}$ and we find $\omega_{\text{eff}}/2\pi = 7.09\,\text{GHz}$. We also define the effective impedance $Z_{\text{eff}} = \sqrt{L_{\text{eff}}/C_{\text{eff}}}$. We eventually define the external quality factor as the impedance Z_{eff} to Z_0 ratio ($Z_0 = 50\,\Omega$ is the environment impedance) and find $Q_{\text{eff}} = 19$. The effective resonant frequency and quality factors are very close to the experimental frequency ($f_0 = 7.07\,\text{GHz}$) and experimental external quality factor ($Q_{\text{e}} = 19$) found from the fit of the experimental phase shift in Fig. 6.2.

7.1.2 Amplification at a single flux point

After modeling the JPA, we must compare the expected amplifier behavior to the experimental one. We measure the gain of the amplifier as a function of the signal frequency ω_{s} as shown in Fig. 7.2. Aside the amplification itself, the first

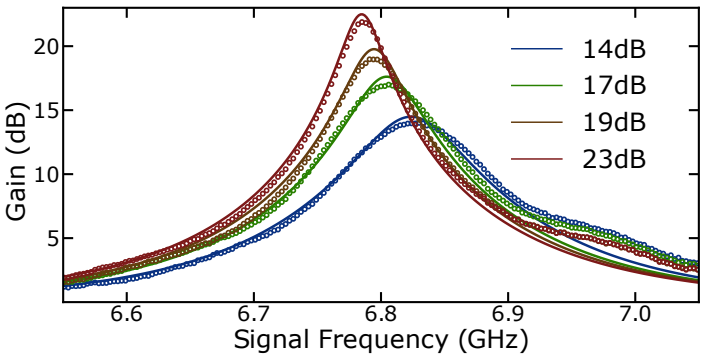

Figure 7.2 – **Gain *vs.* signal frequency.** Experimental (dots) and calculated (solid lines) gain at four different pump powers and frequencies. Theoretical pump settings are chosen as (from low gain to high gain): (−81.65 dBm, 6.83 GHz); (−81.12 dBm, 6.80 GHz); (−80.83 dBm, 6.79 GHz); (−80.57 dBm, 6.78 GHz). The bumps on the right tail of the experimental amplification curves are due to the normalization procedure and small losses at zero pump power.

remarkable feature of this figure is the constant drift towards lower frequencies when the maximum gain increases. This is explained by the fact that higher gains require larger pump strengths, shifting the resonance of the amplifier via the self-Kerr effect (negative sign). It means that having a precise gain G relies on a tuning of both the frequency and the pump power. Experimentally the best way to reach amplification is to pump first close to the linear resonance at very low power while probing the transmission with the VNA and to proceed iteratively:

— (i): increase the pump power until reaching a maximum gain.

— (ii): Decrease the pump frequency: the gain drops a bit.

— (iii): Repeat step (i) until reaching another maximum gain (at a lower frequency).

Once the amplifier gives the expected gain (typically around 20 dB), the best is to lock the pump frequency ω_p to a finite value and to play only with the pump power P_p in order to find the maximum gain at this particular pump frequency: the amplifier is optimally biased at the settings $(\omega_\mathrm{p}^\mathrm{opti}, P_\mathrm{p}^\mathrm{opti})$. Optimally biasing the amplifier has two advantages: the amplifier is stable and it becomes easier to compare the experimental gain with the theoretical expectation as the aforementioned protocol is easily translated to 'algorithmic' terms: for a given ω_p, which P_p maximizes the gain at zero detuning Δ ($\Delta = \omega_\mathrm{p} - \omega_\mathrm{s}$). This is how theoretical solid lines in Fig. 7.2 are obtained. There is thus no free parameter since the pump power is conditioned to maximize the gain (at a given ω_p). The agreement between experimental and theoretical data is good despite the absence of free

parameter. Both maximum gain $G_{\max}$ and -3 dB instantaneous bandwidth Δ_{bw} are well reproduced by the theory. We will see in Section 7.2.2 that this good agreement allows calibration of the input line of the setup and thus to infer the 1 dB compression point of the amplifier.

7.1.3 Amplification for different fluxes

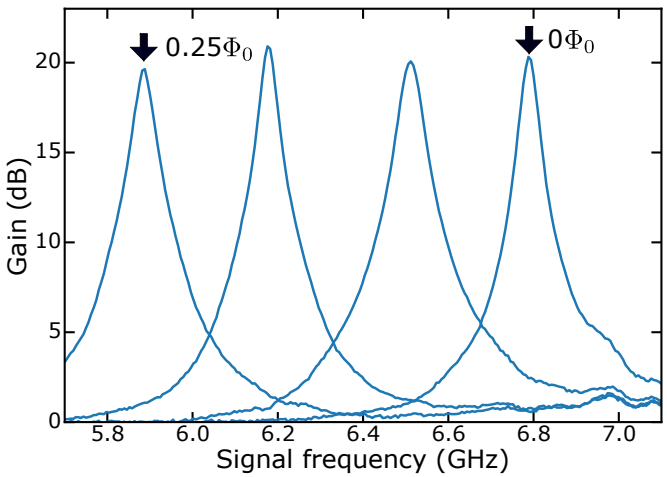

Figure 7.3 – **Gain of the amplifier for different flux bias configurations.** The flux $\Phi = 0.25\Phi_0$ is the lowest point – in frequency – where we could find a gain reaching 20 dB. This corresponds to a 900 MHz static bandwidth for fluxes between 0 and 0.25 Φ_0.

In Section 6.1, we have shown that threading the SQUID array with an external magnetic flux tunes the resonant frequency of the JPA. It means that the band where amplification occurs is actually much wider than the previously defined instantaneous bandwidth. In Fig. 6.3 we saw that the JPA resonance could be tuned from 7 GHz down to 4 GHz (circulator limit). In Fig. 7.3 we show the frequency band where we could reach 20 dB maximum gain. This band ranges between 6.8 GHz and 5.9 GHz. This 900 MHz wide band is what we call the static bandwidth of the amplifier (or its tunability). Of course, amplification occurs below 5.9 GHz, but a maximum gain above 20 dB cannot be reached. To our knowledge, there is no commonly accepted explanation for this fall-off in gain. A plausible explanation would be that by modulating the critical current I_c, it becomes similar to the pump current I_p and the assumption $I_p << I_c$ does not hold anymore. However, we did not further investigate this limitation of the static bandwidth.

7.1.4 Summary

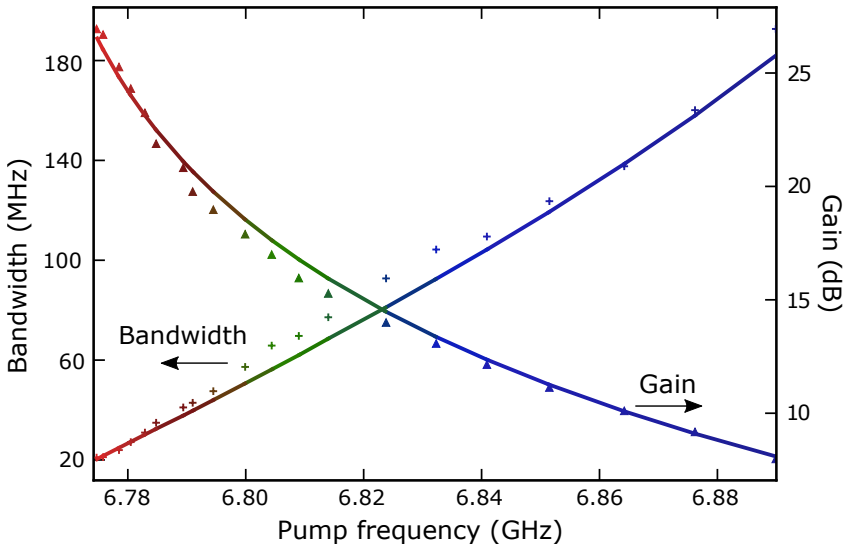

Figure 7.4 – **Summary of the amplifier gain performances.** Maximum gain $G_{\max}$ and -3 dB bandwidth Δ_{bw} found experimentally (symbols) and theoretically (solid lines) for optimal pumping condition as a function of the pump frequency.

We can proceed to a first summary of the amplifier performances. In Section 7.1.2, we have seen that the more we pump, the larger the Kerr shift, the higher the maximum gain. In Fig. 7.4 we plot the experimental maximum power gain $G_{\max} = G(\Delta \approx 0)$ and the -3 dB bandwidth Δ_{bw} found for each pump frequency. Δ_{bw} is extracted from a Lorentzian fit close to the gain peak. In the same figure, we plot the expected maximum gain and bandwidth for the optimal pump condition $(\omega_{\mathrm{p}}^{\mathrm{opti}}, P_{\mathrm{p}}^{\mathrm{opti}})$ as a function of $\omega_{\mathrm{p}}^{\mathrm{opti}}$. We see that the agreement between experiment and theory remains good for a large span in pump frequency. Up to now, the model accurately reproduces the amplifier performances. For both experiment and theory, we observe, as expected, a constant gain-bandwidth product.

The product $\Delta_{\mathrm{bw}}\sqrt{G_{\max}}$, which is almost constant, is found between 425 MHz and 450 MHz (depending on the gain). It must be compared to the bandwidth found during the linear characterization of the resonator in Chapter 6 $f_0/Q_{\mathrm{e}} = 375 \pm 20$ MHz. The agreement is good as we find a small discrepancy of 15% between these two values. This product is one of the figures of merit of the amplifier. It can also be expressed as an instantaneous bandwidth of 45 MHz for 20 dB gain.

Although this figure of merit is largely overcome by traveling-wave amplifiers it remains state-of-the-art for a resonant JPA. Putting aside impedance engineered JPA [34, 35], standard JPAs show gain-bandwidth product on the order of several

tens of megahertz to few hundreds of megahertz. In our case, this relatively high bandwidth is reach (without heavy engineering) thanks to the low external quality factor Q_e, easily tuned by a simple impedance mismatch between the standard $50\,\Omega$ transmission line galvanically connected to a Josephson metamaterial, having a 'naturally' large characteristic impedance.

7.2 Saturation

7.2.1 Motivation and protocol

Up to now, we have measured two out of four of the main figures of merit listed in Section 1.2. Saturation and noise performances of the amplifier are to be characterized. One of the interesting aspect of using an array of SQUID instead of a few SQUIDs is to dilute the Kerr nonlinearity and *in fine* to increase the saturation point of the JPA as studied in Section 2.4. Saturation will be characterized by precisely measuring the 1 dB compression point of the amplifier. It will allow to check whether nonlinearity dilution actually works in a resonant JPA and also if Kerr nonlinearity is indeed the main cause of gain compression in Kerr-based amplifiers.

To characterized the saturation point, the experimental protocol is as follow: the amplifier is first optimally biased according to pump setting $(\omega_p^{opti}, P_p^{opti})$. The gain is then continuously recorded on a small frequency span, while the signal power P_s sent by the VNA is steadily increased. Our JPA working in a four wave mixing fashion, maximum gain naturally occurs for $\Delta \approx 0$. We note that we record the gain via a continuous wave measurement, thus the recorded gain is **not** phase-sensitive, since the small frequency detuning between ω_s and ω_p is larger than the IF bandwidth of the recording instrument. We then plot the maximum gain G_{max}, taken at $(\omega_p^{opti}, P_p^{opti})$, as a function of P_s^{input}, the signal power at the input of the JPA. The main challenge in this protocol is to infer precisely P_s^{input}.

7.2.2 Calibration of the input line

As mentioned in Chapter 5, calibrating precisely the attenuation of a microwave line in a cryogenic setup can be tricky. We have shown that the theory developed previously gives good agreement with experimental data recorded in our setup as shown in Fig. 7.4. Moreover, the absence of free parameters leads us to compare the experimental pump power to the power required in the model to reach the same maximum gain. In Fig. 7.5, each point corresponds to the theoretical power (y-axis) and experimental power (x-axis) giving the same G_{max}. We then simply fit it with a linear law, where the slope corresponds to the attenuation of the microwave line. We find an attenuation of 73.4 dB. This value must be compared to the nominal attenuation in the lines inferred from the datasheets of the components used (coaxial cables, attenuators *etc.*). We find an attenuation of 74.7 dB. Both values are in good agreement, and we take their absolute difference 1.3 dB as the

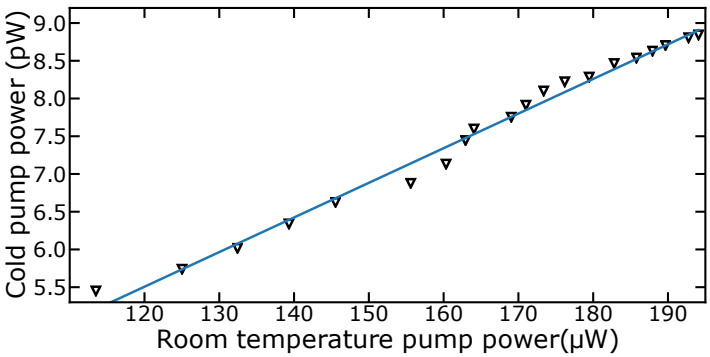

Figure 7.5 – **Expected signal power at the input of the JPA versus room temperature power sent from the pump.** The fitted slope returns an attenuation of 73.4 dB, in good agreement with the the nominal attenuation of the coaxial cables in the microwave setup (74.7 dB).

error bar. From now on, we directly translate the signal power sent from the VNA into the power at the input of the JPA $P_{\mathrm{s}}^{\mathrm{input}}$.

7.2.3 Gain *vs* signal power

We follow the experimental protocol previously described. We record the maximum gain G_{max} while sweeping up the signal power sent from the VNA P_{s} and translate it into the signal power at the input of the JPA $P_{\mathrm{s}}^{\mathrm{input}}$. In Fig. 7.6 we plot G_{max} *versus* $P_{\mathrm{s}}^{\mathrm{input}}$ obtained experimentally but also from our calculation based on the three effective parameters extracted from experimental data $\omega_{\mathrm{eff}}, Q_{\mathrm{eff}}$ and K_{eff}. We define G_{max}^{0} as the linear gain (for low signal input power). We see that for different G_{max}^{0} the agreement between theory and experimental data is good. To be precise, we allow the theoretical plots to be adjusted by ± 0.03 dBm in the pump power compared to $P_{\mathrm{p}}^{\mathrm{opti}}$. This is because such a small difference can lead to a difference of few tenth of decibels in G_{max}^{0}. We allow this adjustment because attenuation in the cables can fluctuate over a day. More precisely, pump settings were not updated between the moments where the gain profile (Fig. 7.2) was recorded to get $(\omega_{\mathrm{p}}^{\mathrm{opti}}, P_{\mathrm{p}}^{\mathrm{opti}})$ and the gain compression measurement was taken. These two records could be sometimes separated by few hours, up to a day. From Fig. 7.6 we can draw two conclusions.

First of all, the good agreement between experiment and theory shows that the assumptions we have done in Chapter 2 were right: the main reason for saturation in Kerr-based Josephson amplifiers is indeed the self Kerr effect induced by the signal power itself. The theoretical treatment was based on the two non ideal terms that we have added self-consistently, coming from the development of the cosine term of the Josephson potential. Furthermore, these non ideal terms are mainly depending on K_{eff}, that we calculated from the Lagrangian approach also

developed in Chapter 2. This shows that this treatment is correct, but also that K_{eff} is correctly estimated. Thus, the relatively simple treatment, considering only the highest non ideal terms, worked well.

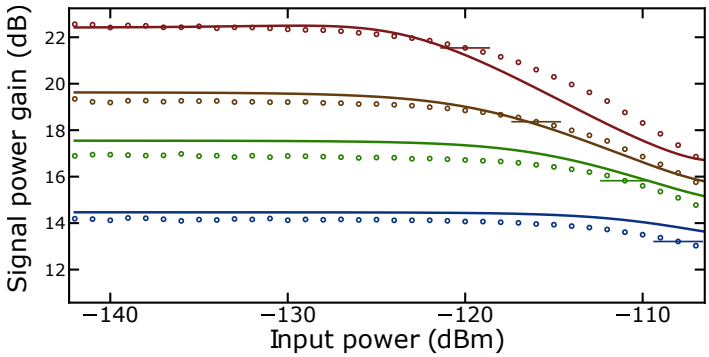

Figure 7.6 – **Summary of the amplifier's gain performances.** Maximum gain as a function of the signal input powerfor the four same pump parameters shown in Fig. 7.2. The pump powers for the theoretical curves (solid line) have been shifted by up to ± 0.03 dBm from the optimal pump power to account for the fact that a very small variation of pump power translates in a large variation of the gain as explained in the text. Such shifts are compatible with small drifts in the attenuation of the input line over the course of one day.

Second, from a performance point of view, our amplifier has a 1 dB compression point around -116 ± 1.3 dBm for $G^0_{\text{max}} = 19$ dB and -117 ± 1.3 dBm for $G^0_{\text{max}} = 20$ dB (from calculation we find -115 dBm). If we compare this value to previously reported 1 dB compression points with single junction/SQUID JPA, we see a clear improvement with our array JPA. In the literature, it is common to find 1 dB compression points between -135 dBm and -125 dBm for these devices [40, 117]. In the most conservative approach, it means an increase of about 10 dBm in the 1 dB compression point. However, if we consider the whole JPA ensemble and their different upgrades, impedance engineered JPAs have shown 1 dB compression points up to -108 dBm and -110 dBm [34, 35], almost 10 dBm above what we measured. The reason is the linear dependence of the 1 dB compression point with the amplifier bare bandwidth κ. More precisely, the 1 dB compression point scales as κ/K [72], where K is the JPA Kerr nonlinearity. While impedance engineered JPAs increase their 1 dB compression point by increasing κ, array-based JPAs enhance their saturation performances by lowering K. We emphasize that our array approach does not exclude impedance engineered JPAs. Arrays could be impedance engineered in order to benefit from both the bandwidth increase and the nonlinearity decrease.

7.2.4 Summary

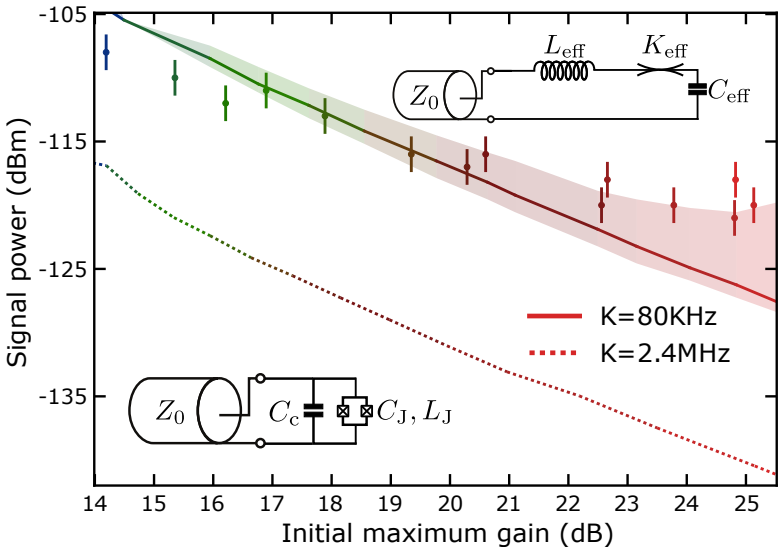

Figure 7.7 – **Summary of the amplifier saturation performances** 1-dB compression point as a function of the initial maximum gain. The shaded area below (above) the theoretical curve shows the effect of a shift of +0.03 dBm (-0.03 dBm) from the optimal pump power on the 1-dB compression point. The dashed line shows the calculated 1-dB compression point of a single-SQUID JPA, having same bandwidth and operating frequency.

We summarize the amplifier performance regarding saturation by plotting the 1 dB compression point $P_{1\,\text{dB}}$ as a function of the maximum gain G^0_{max} in Fig. 7.7. The first obvious trend is that $P_{1\,\text{dB}}$ is smaller as G^0_{max} increases. A higher gain requires a larger pump power. This shifts the JPA resonance to lower frequency, but also makes the JPA more sensitive to extra input power, shifting the optimal biasing point and leading to gain compression. On the same figure, we plot experimental and expected compression points of the JPA previously described. We see that the agreement is rather good for G^0_{max} around 20 dB maximum gain but there are larger discrepancies for lower and higher G^0_{max}. We also plot the compression point for an amplifier featuring the same effective parameters but the nonlinearity K_{eff}. In this fictional case, the effective Kerr coefficients is 2.4 MHz, which is the self Kerr coefficient calculated for a single junction JPA. As discussed in the previous subsection, for such amplifier the 1 dB compression point is expected to be much lower. According to our calculation, we expect $P_{1\,\text{dB}} = 130$ dBm (when $G^0_{\text{max}} = 20$ dB).

The shaded area below and above the solid line shows the compression point when the amplifier is under-biased ($P_{\text{p}} < P_{\text{p}}^{\text{opti}}$) and over-biased ($P_{\text{p}} > P_{\text{p}}^{\text{opti}}$).

As we previously explained in Chapter 2, when the amplifier is over-biased, the amplifier has a lower $G^0_{\max}$ and saturation happens for lower signal input power than when it is optimally biased. On the other hand, when the amplifier is under-biased, the amplifier has also a lower $G^0_{\max}$, however, higher input signal power is required to compress the gain as we observe a small 'bump' as shown in Fig. 2.11 where the gain increases a bit as P_s^{input} increases. Therefore, the shaded area corresponds to a shift of ± 0.03 dBm from P_p^{opti}, in the calculation of the compression point. It takes into account fluctuations in the attenuation of the setup as we previously explained. As we see, a small shift in the pump power can lead to $P_{1\,\text{dB}}$ quite different compared to the case where the amplifier is optimally biased.

7.3 JPA added noise

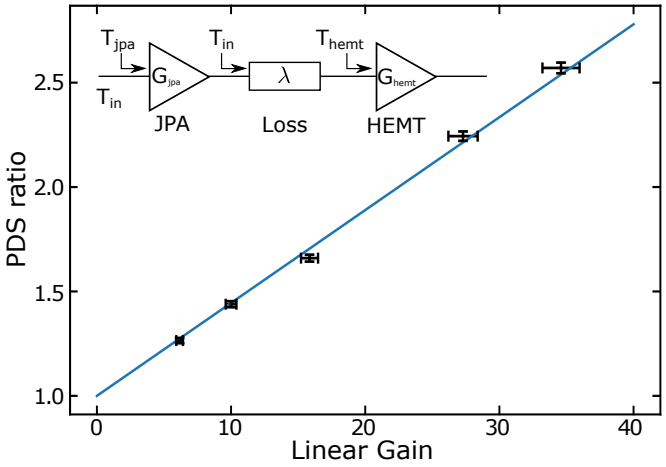

Figure 7.8 – **PSD ratio as a function of the JPA gain.** The fit function of the experimental data is in the main text. From this fit, we extract an intrinsic added noise $N_{\text{jpa}} = 0.55 \pm 0.25$ (the SQL is defined at 0.5 photon). **Inset:** simplified diagram of the amplification chain.

After having characterized three over four of the listed figures of merit, we logically now turn to the characterization of the JPA intrinsic noise. We characterized it on a physically different device compared to the previous sections. The two devices are nominally identical, except for the number of SQUID in the array since the currently characterized one is 70 SQUID long (instead of 80). We follow a standard experimental protocol: we measure the power spectral density (PSD) at the output of the whole measurement chain when the JPA is off and compare it to the case where it is operated with finite gain. This measurement chain consists of a JPA followed by a high electron mobility transistor (HEMT) amplifier as shown in the

inset of Fig. 7.8. At the output of the chain, when the JPA pump is off, the PSD (denoted PSD_{off}) is modeled as:

$$PSD_{\text{off}} = G_{\text{hemt}} k_{\text{b}} (T_{\text{hemt}} + T_{\text{in}}) \simeq k_{\text{b}} T_{\text{hemt}}, \tag{7.1}$$

where G_{hemt} is the HEMT gain and T_{hemt} its intrinsic noise. We assume that the input of the JPA is connected to a perfect $50\,\Omega$ resistance giving a vacuum noise of half a photon, $T_{\text{in}} = \hbar\omega_{\text{s}}/2k_{\text{b}} = 166\,\text{mK}$. We assume that the HEMT is much noisier than the vacuum noise ($T_{\text{hemt}} >> T_{\text{in}}$) and therefore T_{in} is discarded in Eq. (7.1).

When the JPA pump is on and set to give a gain G_{jpa}, the PSD increases because of the contribution of the amplified added noise of the JPA, $G_{\text{jpa}}(1-\lambda)k_{\text{b}}T_{\text{jpa}}$ with T_{jpa} the intrinsic noise temperature of the JPA. We model the inevitable losses in the cables between the output of the JPA and the input of the HEMT (see Appendix B) as a discrete attenuator with losses λ (its transmission is therefore 1-λ). The total PSD when the JPA pump is on, denoted PSD_{on}, reads:

$$PSD_{\text{on}} = G_{\text{hemt}} k_{\text{b}} \left[T_{\text{hemt}} + G_{\text{jpa}} \left(T_{\text{jpa}} + T_{\text{in}} \right) (1-\lambda) + \lambda T_{\text{in}} \right]. \tag{7.2}$$

In Eq. (7.2) we see three main noise components at the input of the HEMT: T_{hemt} for obvious reasons; $G_{\text{jpa}}(1-\lambda)(T_{\text{jpa}} + T_{\text{in}})$ which corresponds to the JPA (T_{jpa}) and vacuum (T_{in}) noise (the former being similar to the latter, T_{in} cannot be discarded this time) amplified by the JPA (G_{jpa}) and attenuated by the cables, modeled as a discrete attenuator with attenuation (1-λ). Finally we also consider vacuum noise coming from the second channel of the attenuator as described in Chapter 5. By assuming that the noise of the JPA does not depend on its gain, the PSD ratio, denoted R_{PSD} is:

$$\begin{aligned} R_{PSD} =& \frac{PSD_{\text{on}}}{PSD_{\text{off}}} = \frac{T_{\text{hemt}} + \lambda T_{\text{in}}}{T_{\text{hemt}} + T_{\text{in}}} + G_{\text{jpa}}(1-\lambda)\frac{T_{\text{jpa}} + T_{\text{in}}}{T_{\text{hemt}} + T_{in}} \\ \simeq& 1 + G_{\text{jpa}}(1-\lambda)\frac{T_{\text{jpa}} + T_{\text{in}}}{T_{\text{hemt}}}. \end{aligned} \tag{7.3}$$

In a precedent experiment [97], it has been shown that the ratio $T_{\text{hemt}}/(1-\lambda) = 8 \pm 2\,\text{K}$. The effect of losses in between the JPA and the HEMT is to increase the effective noise temperature of the HEMT, which goes from 4 K (suppliers' data sheets) to 8 K. The uncertainty of 2 K is coming from the difficulty to measure precisely the attenuation of the coaxial cables **in between** the HEMT and the JPA. To extract T_{jpa} we follow the following protocol: we measure experimentally R_{PSD} for different pump settings giving different G_{jpa}. We then fit it with Eq. (7.3), where all the parameters are known but T_{jpa}. We extract $T_{\text{JPA}} = 180\,\text{mK} \pm 90\,\text{mK}$. The large uncertainty is coming from the previously discussed uncertainty on the coaxial cables. In terms of added noise quanta, T_{JPA} is translated into $N_{\text{jpa}} = 0.55 \pm 0.25$. In that case, the standard quantum limit is defined as $N_{\text{sql}} = 0.5$. It means that our JPA can be considered as near quantum

limited. However, the uncertainty on the coaxial cables loss in between the JPA and the HEMT prevent us to claim that if the amplifier is strictly speaking quantum limited. In any case, our JPA noise is still an order of magnitude below the intrinsic noise of a HEMT, which is a clear advantage for quantum measurement.

We have finally characterized the four main figures of merit, as previously listed, of our SQUID array JPA. It displays high gain (up to 25 dB) and, when it is biased for $G_{\max} = 20\,\text{dB}$, a bandwidth and a 1 dB compression point of 45 MHz and $-117\,\text{dBm}$. Finally, we have shown that our amplifier is near quantum limited of noise and has an intrinsic noise an order of magnitude below the best microwave cryogenic amplifiers commercially available. To conclude, this amplifier is perfectly suited to the readout of a superconducting qubit. This is the topic of the next section.

7.4 Qubit readout

In this section, we report two superconducting qubit measurements enabled by our quantum limited JPA. Namely, high fidelity single-shot readout and continuous measurements, in real time, of its quantum state and consequently the record of a quantum jump between its excited and ground states. The quantum limited amplifier used to acquire the data is the 70 SQUID long JPA whose noise was calibrated in Section 7.3. The measured qubit was designed and fabricated by **R.D**. The measurement was carried out by **R.D.** and **V M**. The originality of this qubit resides on its readout mechanism, done in a 3D cavity architecture. It is based on a novel qubit-cavity coupling scheme relying on a cross-Kerr interaction between the qubit and the cavity. The qubit itself is designed as a transmon molecule circuit (two coupled transmons [28]) with two degrees of freedom called qubit and ancilla. The latter couples to the cavity field while the former has a cross-Kerr coupling with the mixture ancilla-cavity field. This coupling is meant to enable fast single-shot readout with high fidelity. The experimental results shown in this section were published by **R.D.** [102, 104].

7.4.1 Pump leakage

Before showing the main figures of merit of the readout measurements obtained with our JPA, it is important to highlight the experimental difficulties coming from the pumping scheme of our JPA. The price to pay for these easy-to-fabricate amplifiers (Chapter 4) is their relative difficult integration in a qubit readout setup. We must take into account that the amplifier is pumped from the same line used for the signal and is based on a four wave mixing process ($\omega_p \sim \omega_s$). It means that the pump tone easily leaks towards the qubit cavity and is resonant with it. It eventually scrambles the qubit state since the leakage can go up to few tens of pump photons **inside** the qubit cavity when using a standard setup as presented in Appendix B. Improvements in the microwave engineering of the setup are therefore required to avoid pump leakage. Three solutions are given:

— (i): two circulators between the cavity and the directional coupler (see Fig. B.1).

— (ii): Double pumping technique [118].

— (iii): Pump cancellation with destructive interference.

(i) is the easiest solution to implement. There are two ways to do it: either adding one more circulator in between the directional coupler and the cavity **or** invert the position of the directional coupler and the circulator at the input of the JPA. Both are not very good for the readout efficiency of the qubit η, also called the quantum efficiency. By definition [119], the quantum efficiency η is:

$$\eta = \frac{\kappa_{\text{out}}\eta_{\text{det}}}{\kappa}, \tag{7.4}$$

where $\kappa = \kappa_{\text{in}} + \kappa_{\text{out}}$ is the sum of the two damping rates of photon from the input and the output ports of the cavity, respectively, and $\eta_{\text{det}} = 1/(N_{\text{add}} + 1)$, called the detection efficiency, is the efficiency at which these photons are detected. N_{add} is the number of noise photons added by the amplification stage. In our case, $\kappa_{\text{in}} << \kappa_{\text{out}}$ and therefore $\eta \approx \eta_{\text{det}}$. Inferring precisely N_{add} is obviously hard, for the same reasons as inferring the attenuation between the JPA and the HEMT is not easy. Determining precisely N_{add} had not been carried out yet in the current setup. However, as we have seen previously, electrical loss before an amplifier tends to increase the effective noise temperature of an amplifier or equivalently the number of noise photons. This is why adding an extra lossy circulator (few tenth of decibel of attenuation) is detrimental to the detection efficiency because it adds extra noise photon. On the other hand, inverting the position of the directional coupler and the circulator keeps the number of circulators constant, but it is known that the voltage standing wave ratio (VSWR) of a directional coupler is higher than that of a circulator. The impedance matching is therefore poorer and standing waves are formed in between the coupler and the JPA, which is neither good for the amplification process nor the detection efficiency.

In order to avoid decreasing the detection efficiency, solution (ii) might be a good choice since it does not require any extra lossy microwave components. The idea is to send two pump tones with frequencies ω_{p1} and ω_{p2} detuned from each other such that $\omega_{\text{p1}} = \omega_{\text{p}}^{\text{opti}} + \Delta_{\text{p}}$ and $\omega_{\text{p2}} = \omega_{\text{p}}^{\text{opti}} - \Delta_{\text{p}}$ where Δ_{p} is on the order of few tens of megahertz. Neither of the two pump tones are then resonant with the qubit cavity. Yet, they can mix within the JPA itself such that it enables optimal pumping conditions. For a proper theoretical treatment, see references [63, 64]. This pumping scheme requires particular care in order to bias the JPA at its optimal condition. Unlike solution (i), the extra microwave components (IQ mixers typically) required for double pumping are at the 300 K stage. While the double pumping technique is not harmful to quantum efficiency [120], it is technically more difficult to implement. It requires much more care to adjust two pump tones (amplitude and phase) and an IQ mixer than simply adjusting a single pump tone propagating directly to the JPA. For having both tried during two different measurement sessions, **R.D.** and I never achieved to reach more than 15 dB/16 dB gain which was insufficient, given that we needed at least 20 dB of gain. The following data have been taken with 23 dB of gain.

We now turn to solution (iii), which has eventually been chosen as the best solution as it can reach very large gain, does not affect the efficiency, and it reduced the pump leakage down to $n_{\text{leakage}} = 2 \times 10^{-5}$ pump photons inside the cavity while reducing the coherence time of the qubit by only 1%. The idea is to send two pump tone via the two ports of the directional coupler. One is optimally biasing the JPA while the second one is set to interfere destructively with the first one. The qubit cavity sees in principle almost no pump photons. The exact protocol to follow is thoroughly described in [104]. It is by far the one requiring the greatest care and fine-tuning. But it allows us to obtain the data presented in the next subsections.

7.4.2 Fast single-shot high fidelity readout

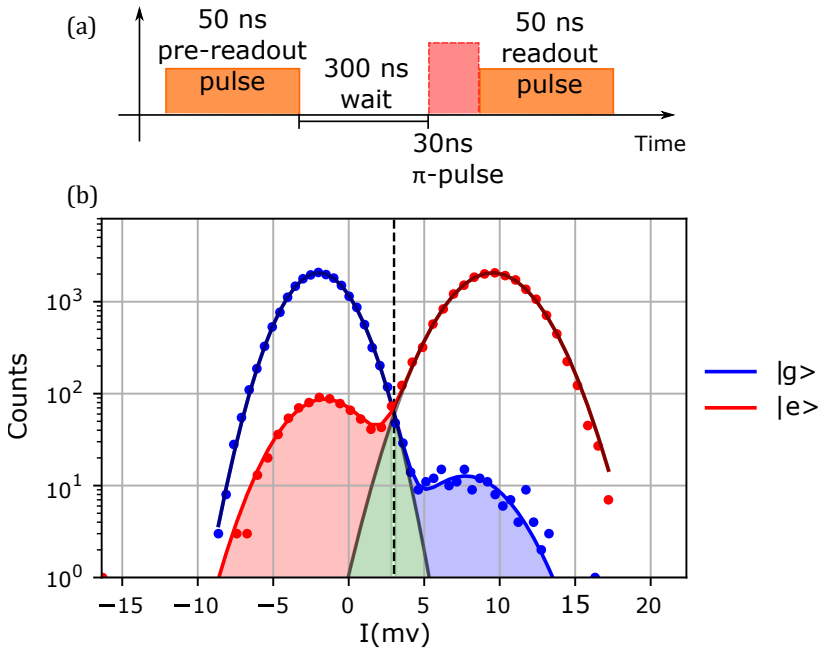

Figure 7.9 – **Single-shot readout (a)** Pulse sequence sketch. **(b)** Histogram of 50 ns single-shot measurement for qubit prepared in ground state (blue points) and excited state (red points) with heralding. The solid blue and red lines are fits with a double Gaussian model. Black line is a single Gaussian fit. The green area depicts the overlap error $\epsilon_{\text{o}} = 0.8\%$. The blue and red areas indicate the remaining error $\epsilon_{\text{r,g}} = 0.6\%$ and $\epsilon_{\text{r,e}} = 3.9\%$, respectively. It leads to a readout fidelity of 97.4%. Figure taken from [102] with the courtesy of **R. Dassonneville**.

In this section we present the fast, single-shot readout of a transmon molecule

qubit. In Fig. 7.9**(a)** we plot the sketch of the pulse sequence used for the readout of the qubit state. It consists in three pulses. The first one is the heralding pre-selection pulse. After 300 ns waiting time, a π-pulse is sent to excite the qubit in its excited state $|e\rangle$. Of course, no pulse is sent if we want to prepare the qubit in its ground state $|g\rangle$. Finally, the qubit state is inferred by a third 50 ns readout pulse. The outcome of the pulse sequence is shown in Fig. 7.9**(b)**. 24×10^3 single-shot readouts at frequency 7.028 GHz are plotted as an histogram in this figure. The outcomes of the readouts are fitted with double Gaussian and single Gaussian models. There are three sources of errors. The remaining errors of the excited state ($\epsilon_{\mathrm{r,e}} = 3.9\%$) and the ground state ($\epsilon_{\mathrm{r,g}} = 0.6\%$), highlighted by the red and blue shaded areas, respectively. The third one is the overlap error between the two states ($\epsilon_{\mathrm{o}} = 0.8\%$), highlighted by the shaded green area. We define the readout fidelity as:

$$F = 1 - \frac{P(e|g) + P(g|e)}{2} \approx 1 - \frac{\epsilon_{\mathrm{g}} + \epsilon_{\mathrm{e}}}{2}, \tag{7.5}$$

where $P(x|y)$ is the probability of reading out the x state while preparing the qubit into the y state. The quantity ϵ_{g} (ϵ_{e}) is the fraction of measured events of detecting the quadrature I above (below) the threshold value I_{th} when prepared in the g (e) state. From the measurements, we find $\epsilon_{\mathrm{g}} = \epsilon_{\mathrm{r,g}} + \epsilon_{\mathrm{o}}/2 = 1.0\%$ and $\epsilon_{\mathrm{e}} = \epsilon_{\mathrm{r,e}} + \epsilon_{\mathrm{o}}/2 = 4.3\%$. We therefore find a readout fidelity of 97.4% for a single-shot readout (of duration 50 ns). The overlap error being as low as 0.8% is a positive signature of the performances of the JPA and its ability to be, at least, near quantum limited. Our readout fidelity of 97.4% in 50 ns must be compared to current state-of-the-art high fidelity single-shot readout. For instance, standard scheme (transverse coupling between the qubit and the cavity) has reached fidelity as high as 99.6% with readout pulses of 88 ns [121]. It must be stressed that this readout mechanism has been first implemented more than ten years ago. As for longitudinal coupling [122, 123], it has been recently reported fidelity as high as 98.9% with readout times of duration 750 ns. Our cross-Kerr coupling qubit combined with a SQUID array JPA then reaches state-of-the-art single-shot readout fidelity. This original coupling scheme enables high fidelity single-shot readout, but the discrimination between the two qubit states could not be done without a quantum limited amplifier. Removing the JPA and having only the HEMT as the first amplifier would make the fidelity drops down to 65% for single-shot readouts.

7.4.3 Continuously monitored qubit measurement

We close this chapter with the continuous measurement of a single quadrature of the readout field. Continuously monitoring one quadrature of the readout field allows for following the qubit dynamics in real time, whether it is in its excited state or not. It also allows the measurement of quantum jumps [124] of the qubit from its excited state to its ground state.

The protocol to probe this continuous measurement follows the experimental sequence sketch shown in Fig. 7.10**(a)**. The qubit is either initialized in its excited state (π-pulse) or in its ground state (no pulse). A readout tone at frequency 7.028 GHz and amplitude $\bar{n} = 2$ photons is then sent for 1 µs in the cavity. The signal is also acquired a bit before and after the readout tone. In Fig. 7.10**(b-c)**, two typical continuous measurement records of the $I(t)$ quadrature are shown. Each red (blue) dot represents data recorded and integrated over 30 ns (corresponding to the resonator rising time) when the qubit was initially prepared in its excited (ground) state. Solid red (blue) lines corresponds to the average of one thousand records when the qubit was initially prepared in its excited (ground) state. The shaded areas correspond to the standard deviation around this mean value. We see that 50 ns after the π-pulse (t=0), it is already possible to discriminate between the excited and the ground state of the qubit, which is in agreement with what we observed in the previous subsection. We also observe a constant decay of the mean value of the $I(t)$ quadrature when the qubit is initially put in its excited state. It decays towards the ground state value. This decay corresponds to the qubit relaxation. The characteristic time T_{decay} corresponds to T_1, the relaxation time of the qubit. We also observe that at $t \approx T_{\text{decay}}$ it is not possible to discriminate between the excited and ground states anymore.

Finally, it is noteworthy that we can resolve a quantum jump (see Fig. 7.10 **(b)**). First experimentally observed in trapped ions, the first quantum jumps observation in superconducting qubit was realized in 2011 [125]. Recording quantum jumps with superconducting qubits is possible thanks to amplifiers such as the JPA reaching quantum limit of noise. The measurements must be quantum non-demolition (QND) in order to avoid scrambling the quantum state after measurement but the QND measurement must also be fast, taking place on a timescale much smaller than T_1. This is why amplifiers at the quantum limit of noise are essential. Very recently, a team from Yale has perfected their electronics and theoretical understanding of quantum jumps to enable their anticipation. They have been able to catch a qubit during its jumps and reverse its trajectory mid-flight [126].

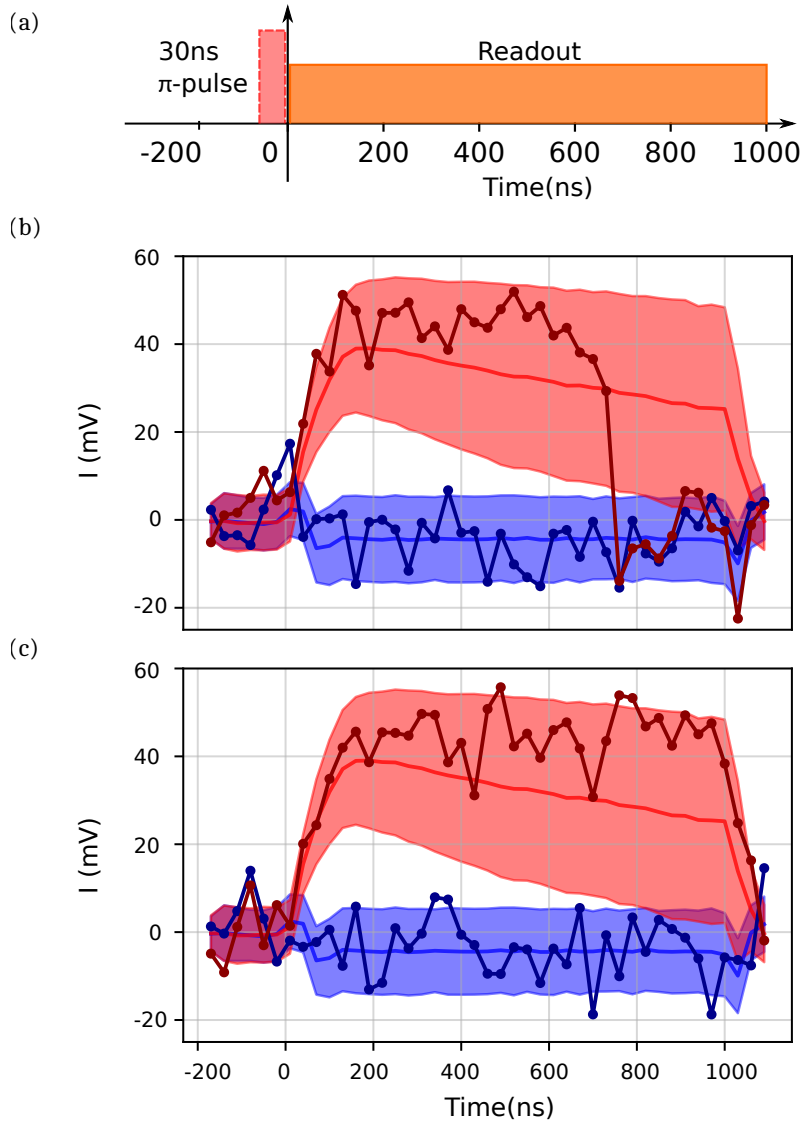

Figure 7.10 – **Continuous measurement records of the qubit state (a)** Experimental sequence sketch. **(b)** Quantum trajectory with a quantum jump. **(c)** Quantum trajectory without a quantum jump. Blue and red points refer to the case where the qubit is initially prepared in states $|g\rangle$ and $|e\rangle$, respectively (t = 0). Each point is measured with a 30 ns integration time. Solid lines are the averaged results over 1000 measurement records. Shaded areas mark +/- one standard deviation. Figure taken from [102] with the courtesy of **R. Dassonneville**.

Photonic crystal Josephson traveling wave parametric amplifier

8

Contents

This chapter is dedicated to the SQUID transmission lines introduced and characterized in Chapter 6 while they are operated as traveling-wave parametric amplifiers (TWPA). We follow the same logical order as for the resonant Josephson amplifiers. We will first examine the gain and bandwidth of the amplifier. Then, by calibrating the coaxial lines thanks to a good understanding of the physics of our amplifier, we will infer the gain saturation and the added noise of our TWPA.

Link back to Table of contents →

8.1 Presentation of the samples

Device	A	B
Total SQUID number N_J	2160	2184
Modulation period N_p	40	42
Length per SQUID a (µm)	3.3	3.3
Josephson modulation amplitude η	4%	2%
Ground capacitance modulation amplitude ζ	3%	2%
Gap position (GHz)	7.45	7.15
Gap width (MHz)	350	200
Josephson capacitance C_0 (fF)	485	485
Ground capacitance C_0^g (fF)	42.6	42.6
Zero-flux inductance L_0 (pH)	60.5 ± 1.1	61.7 ± 1.1

Table 8.1 – **Parameters of samples A and B.** The main nominal differences are the modulation amplitude η and the modulation period N_p, which reflects directly in the width and the frequency of their photonic gap.

Despite several batches of fabricated TWPA, we mostly present results of two samples, denoted A and B, coming from the fourth and last TWPA batch (see Table 6.1). Samples A and B main parameters are summarized in Table 8.1. Both samples have their SQUID arrays periodically modulated. All the reported parameters are taken from design or geometrical considerations but the zero-flux inductance L_0. It has been extracted from the dispersion fit as shown in Fig. 6.11 with the model developed in Section 3.5.

The only nominal differences between samples A and B are the number of SQUIDs per period N_p and their modulation amplitude, η and ζ. We measured a photonic gap larger and at higher frequency for sample A than for sample B. This observation is in good agreement with their design parameters (smaller N_p and larger η for sample A). Moreover, they were designed to have the same nominal mean Josephson inductance L_0 and we extract very close values within the uncertainty margin. This points towards a good control of our fabrication recipe and modeling for this batch. All data shown in this chapter were taken with the experimental setups shown in Fig. 5.3. We consider by default that data were taken with the configuration ①. We will specify when data were acquired with configuration ②.

8.2 Amplification in a bare SQUID array

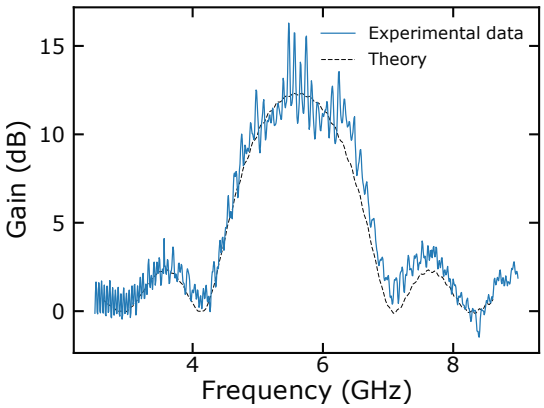

Figure 8.1 – **Gain profile taken with a bare TWPA.** Gain *vs.* frequency. The SQUID array is not modulated and both maximum gain and bandwidth are limited. Moreover, the gain suffers from important ripples.

Before studying data taken with the modulated SQUID arrays (samples A and B), we present some results of one of the very first fabricated TWPA. This version consists of a bare (*i.e.* no periodic modulation) array of 2063 SQUIDs. Its characteristic are reported in Table 6.1, in the 'batch 1' column. We show the amplification profile in a bare array as a reference for later results in order to have a grasp of the improvement provided by the periodic modulation.

Gain profile is plotted in Fig. 8.1. The pump frequency is $\omega_\mathrm{p}/2\pi \approx 5.6\,\mathrm{GHz}$. This pump frequency leads to the highest gain we could reach with this sample. We have about $\bar{G}_\mathrm{max} = 12\,\mathrm{dB}$ of mean maximum gain, without considering the ripples on top of the mean gain profile. From this maximum gain, we extract a $-3\,\mathrm{dB}$ bandwidth $\Delta_\mathrm{bw} = 1.6\,\mathrm{GHz}$. If we compare these figures of merit to the JPA's presented in Chapter 7, we obviously note an enhancement of the bandwidth by more than one order of magnitude, which is already remarkable. However, the maximum gain of 12 dB is one order of magnitude below that routinely provided by a JPA. Moreover, gain ripple is also an issue, even though they are in the present case only located very close to the pump frequency.

The theoretical expectation from the model developed in Sections 3.5 and 3.6 of the gain is superposed to the experimental data. As for the resonant JPA, to replicate experimental data, all the array parameters are fixed from the linear characterization and the pump frequency is the same as the experimental one. Only the pump power is a free parameter. We cannot, however, follow the exact same protocol as with resonant JPA by seeking the optimal pump power $P_\mathrm{p}^\mathrm{opti}$. Such optimal pump power does not exist in traveling-wave amplifier since the stronger the pump, the higher the gain it returns. Thus, the pump power P_p is

set to match the experimental maximum gain. The agreement between theory and experiment is good for a bare TWPA, with is a small discrepancy for frequencies higher than ω_p.

8.3 Amplification in the Josephson photonic crystal

In this section we present amplification profile from sample A, both forward gain and backward gain.

8.3.1 Unmatched amplification

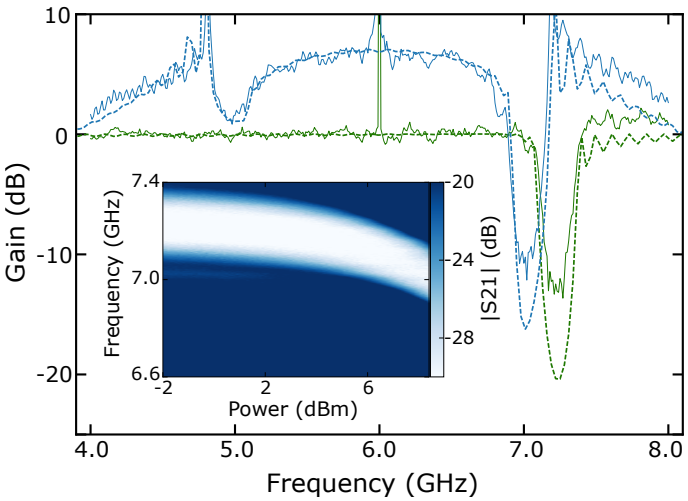

Figure 8.2 – **Unmatched amplification with a Josephson photonic crystal TWPA.** Gain with sample A for different pump powers ($\omega_p/2\pi = 6\,\text{GHz}$, green: $P_P = -83.8\,\text{dBm}$, blue: $P_P = -70.3\,\text{dBm}$). The gap is shifted by more than its width at large pump power. **Inset:** color map of the probe transmission versus probe frequency and pump power.

We first show amplification when the pump frequency $\omega_p/2\pi$ is far detuned from the gap frequency. In that case, the amplification process does not benefit from any phase matching correction. The outcome is shown in Fig. 8.2. This forward gain was taken with the configuration ②. In this figure, normalized gain (pumped on - pumped off) is plotted for two different pump powers. When the pump power is very low, no amplification occurs. The transmission is flat without any attenuation because losses are hidden by the normalization procedure (but they are still present as seen in Fig. 6.8).

When the pump power is large enough, amplification occurs and we also observe the displacement of the photonic gap. As already discussed Chapter 3, the

gap is displaced by few hundreds of megahertz, which also corresponds roughly to its own width (hence the non perturbative treatment in Section 3.5). Regarding amplification, the maximum gain reached is $G_{\max} = 7\,\mathrm{dB}$ for a bandwidth $\Delta_{\mathrm{bw}} = 1.75\,\mathrm{GHz}$. We have defined the bandwidth as the $-3\,\mathrm{dB}$ bandwidth within the band 5.0 GHz-7.0 GHz. We do see however that the amplification band is larger than 2 GHz but somehow interrupted by the photonic gap centered around 7 GHz. The transmission dip around 5 GHz, symmetric of the gap with respect to ω_{p}, is due to the idler being in the photonic gap when the signal is around 5 GHz. The signal gain depends on the **total** phase mismatch (also accounting for the idler's phase) as discussed in Section 3.4.3. As for the gain, the maximum reached with this sample is lower than for the previous sample presented in Section 8.2. The two samples have the same length (~ 2000 SQUIDs) and their junctions have the same nominal area. One SQUID array is modulated while the other is not, but it is pointless in this situation. The main difference is the thickness of their tunnel barrier. For the sample of this section, the junctions have been oxidized with 1 Torr while the previous bare array has been oxidized with 4 Torr. The difference in the oxidation pressure leads to a difference in the critical current density j_{c} of the junctions. A pressure of 4 Torr gives $j_{\mathrm{c}} \approx 25\,\mathrm{A\,cm^{-2}}$ while 1 Torr gives $j_{\mathrm{c}} \approx 35\,\mathrm{A\,cm^{-2}}$. Since the junctions in the bare array and the currently studied device have the same mean nominal area (see Table 6.1), a lower oxidation pressure leads to a smaller Josephson inductance. Aside from this difference, we do not have a solid answer to explain this difference of few decibels in the maximum gain between these two samples.

In the same figure, the expected gain profile is also plotted, superposed to the experimental data. Theoretical data have been obtained by modeling the TWPA with parameters in Table 8.1, solving the pump field (amplitudes and wavevector) and solving signal and idler amplitude. As explained previously, L_0 has been adjusted within less than 2% to perfectly match the gap frequency position. Once every parameter is fixed, the only free parameter between the green and the blue solid lines is the pump power at the input of the TWPA. We see that both the gap position, the maximum gain, and the bandwidth are in good agreement with experimental data. This good agreement between theory and experiments will be again used to infer the attenuation between the output of the VNA/RF source and the input of the TWPA, similarly to what has been done previously with the resonant JPA. This procedure will be explained in Section 8.5.

8.3.2 Matched amplification

We now turn to the situation where we pump very close to the gap to take advantage of the phase correction. The gain profile shown in Fig. 8.3 has been recorded with configuration ①. As expected, the maximum gain and the bandwidth are much higher than the two profiles previously shown in Fig. 8.1 and Fig. 8.2. Pump frequency is set to $\omega_{\mathrm{p}}/2\pi = 6.635\,\mathrm{GHz}$ while the magnetic flux is set to $\Phi/\Phi_0 = 0.2$, where Φ_0 is the magnetic flux quantum. Dielectric losses being dependent on the signal power, we specify the signal power $P_{\mathrm{s}} = -117\,\mathrm{dBm}$.

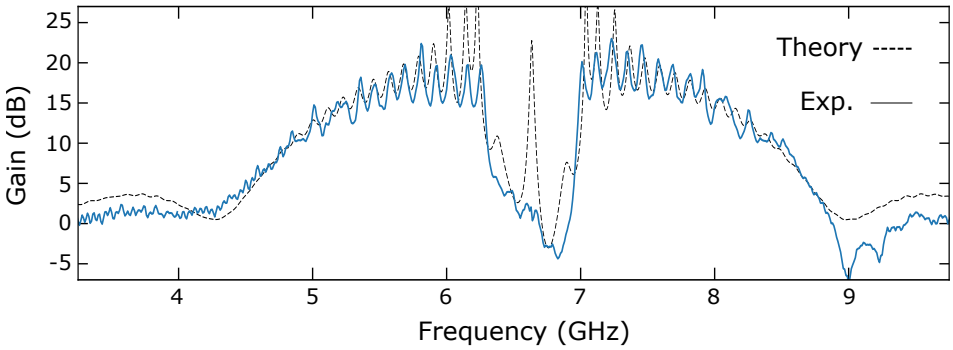

Figure 8.3 – **Amplification with a Josephson photonic crystal TWPA pumped close to the photonic gap.** Gain *vs.* frequency at magnetic flux $\Phi/\Phi_0 = 0.2$ and pump frequency 6.635 GHz. Theoretical gain profile (dashed black line) is obtained for a pump power $P_{\text{input}} = -70.2\,\text{dBm}$.

We reach a mean maximum gain around $\bar{G}_{\text{max}} \sim 18\,\text{dB}$ for a bandwidth $\Delta_{\text{bw}} = 3\,\text{GHz} - 0.75\,\text{GHz} = 2.25\,\text{GHz}$. We subtracted 750 MHz from the instantaneous bandwidth to account for the band gap where no amplification actually occurs. As expected, the gap has doubled its width compared to its 'linear' width as shown in Fig. 8.2 (solid green line). This is the exact same reason as for the atypical gain profile in Fig. 8.2 (solid blue line). We also observe high amplitude gain ripple. Their amplitudes are as high as 5 dB. With the same sample, compared to what is shown in Fig. 8.2, we note larger amplitude ripples when the maximum gain is higher. This can be easily explained by considering the TWPA and its environment as an amplifying Fabry-Pérot cavity. Even a small reflection coefficient at the input and output of the TWPA leads to unwanted gain ripple. The higher the gain, the higher the ripples amplitude.

We also superposed the theoretical gain profile. The protocol is the same as before: every parameters but the pump power are fixed. Once again, the general features are well reproduced by the theory: gap, maximum gain, bandwidth and ripples.

8.3.3 Backward amplification

As we discussed in Chapter 3, an important matter with Josephson photonic crystal is the possibility to have backward amplification. We have seen that if k_{p}, the pump wavevector, is very close to $G/2$, where G is the reciprocal lattice wavevector of the photonic crystal, a combination including backward signal and backward idler, with respect to a forward pump, could be in principle phase matched. We have shown theoretically that for realistic pump parameters leading to large forward amplification, backward amplification was very poorly matched. Naturally, we checked this prediction experimentally using the experimental setup

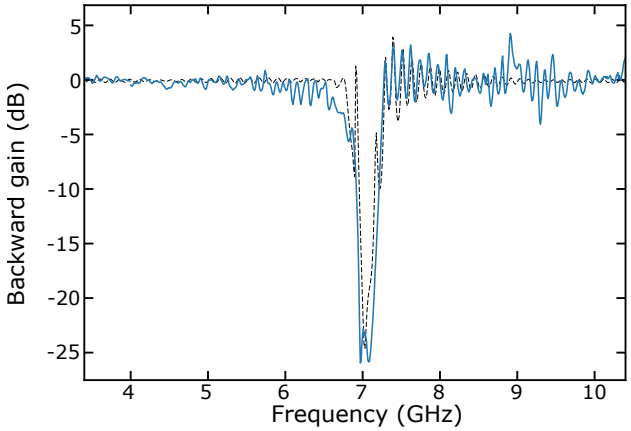

Figure 8.4 – **Backward amplification.** Backward gain *vs.* frequency measured with Φ/Φ_0=0.1 and pump frequency 6.9108 GHz. Expected gain (black dashed line) is plotted for a pump power $P_{\text{input}} = -71.4$ dBm.

configuration ② (see Fig. 5.3).

Backward amplification could be detrimental because a signal propagating from the input of the HEMT amplifier could be amplified by backward propagation through the TWPA and thereby excite the device under measurement. We can experimentally probe the opposite case where the signal is sent to the TWPA input towards the HEMT line while the pump is sent in the opposite direction. We are relying on symmetry arguments to consider that if no amplification is observed in the latter case, then no amplification would occur in the former case.

The protocol we follow is sufficiently conservative to be confident that backward amplification is kept minimal. At first, we probe forward gain, where pump and signal are co-propagating. Once optimal parameters are found for the pump (frequency and power), we unplug the pump source from the first line going to the TWPA input and plug it on the second line going directly to TWPA output. To find the maximum backward gain we fix the pump frequency and probe the signal backward gain while sweeping the pump power over a large span. The two coaxial lines have the same nominal attenuation but there is always a small discrepancy. In Fig. 8.4 the experimental backward amplification with the highest gain is plotted. In the same figure is plotted the expected backward amplification from the model. In the model, the pump is sent from one end of the array while the signal is sent from the other end (see Sections A.2.4 and 3.6).

In the worst case scenario, we do not measure more than 4 dB signal gain. We can see that higher gain is found for frequency higher than the gap frequency, in a relatively small band. Except for few peaks, almost no gain is found, which is an important point. We attribute this good performance to a good impedance matching between the setup and the TWPA but also to the fact that k_{p} is not

so close from $G/2$ and, as a consequence, phase matching is poor and backward amplification is not favorable. Moreover, regarding agreement between theory and experimental data, while the pump power is the only free parameter, we again observe a good agreement between experiments and theory. Not every ripple is reproduced by the theory, but close to the gap and for frequencies higher than the gap, the general behavior of the amplifier is well captured.

This is another proof, and perhaps the strongest, that the photonic crystal TWPA is indeed directional – **for amplification only**. No amplification occurs in the unwanted direction, but electrical signals can be transmitted in both directions anyway.

8.4 Flux response and *in-situ* tuning

In this section we extensively study with sample B in configuration ① the flux-tunability proposed by the SQUID array, and more precisely the *in-situ* impedance tuning of the array.

8.4.1 Gain *vs* flux

As shown in Table 8.1, sample B displays a smaller modulation amplitude as sample A. In Fig. 8.5**(a)-(c)**, three amplification profiles are plotted at three different magnetic flux. First, we note that the maximum gain is lower than that of sample A. Also a smaller bandwidth is found. We expect it since sample B has a smaller modulation amplitude leading therefore to a smaller distortion in the dispersion and eventually to a smaller phase correction. On the other hand, the forbidden band is smaller than for sample A in the amplification profile and is only 350 MHz wide. We are facing a fundamental trade-off between the amplifier performance and the width of the gap in the dispersion relation.

We observe that for a finite magnetic flux $\Phi/\Phi_0 \approx 0.3$, gain ripple is almost canceled. We used the same y-axis scale in Fig. 8.5**(a)-(c)** to emphasize the difference in ripples amplitude. The x-axis spans the same width in each figure, but it is centered at different frequencies. In addition to tune the ripples, threading the SQUID loops with a magnetic flux also shifts the frequency position of the gap, and therefore the frequency band where amplification occurs. It enables to tune the optimal pumping point frequency and therefore obtain an even larger usable bandwidth. To the best of our knowledge, this extra tunability was never implemented for a TWPA before.

As usual, the theory is superposed to experimental data, following the same procedure: for each flux point, the dispersion is fitted, $L_0(\Phi)$ is extracted, adjusted (within 2%), and P_p is let free. The agreement is rather good, maybe except for the gain profile show in panel **(a)** where there is a little discrepancy regarding the bandwidth. This is coming from an imperfect fit of the dispersion relation since it is the plasma frequency ω_Π that ultimately settles (after the phase correction) the bandwidth of a Josephson TWPA.

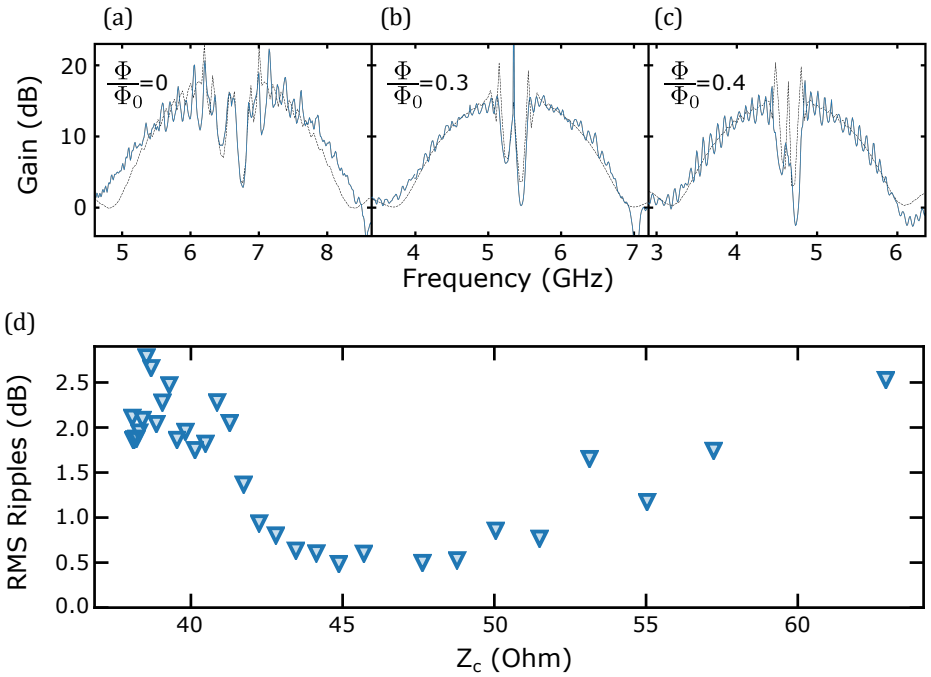

Figure 8.5 – **Flux response of the Josephson photonic crystal TWPA. (a)-(c)** Three gain profiles taken with device B at three different flux biasing points. Gain ripple evolve with the flux bias point. **(d)** Root mean square values of the ripples for 25 different flux biases. Each of this flux is converted to a characteristic impedance $\sqrt{L_0(\Phi)/C_0^{\mathrm{g}}}$. A local minimum is found for a small-signal impedance between 46 Ω and 49 Ω.

8.4.2 Flux sweetspot

In order to be more quantitative on the *in-situ* impedance tuning, we measured more than twenty-five gain profiles. Each were taken at different magnetic flux, and their gain ripple was systematically quantified. We ensured that each gain profile had the same maximum gain, since there is an obvious dependence between ripples amplitude and maximum gain displayed by the TWPA.

To quantify gain ripple, we go by the following protocol: each gain profile is fitted on a −3 dB band using a Savitzky-Golay filter [127], giving the gain G_{smooth} as a function of the signal frequency f. The photonic band gap is discarded. For each frequency, the standard deviation between G_{smooth} and G_{exp}, the experimentally

measured gain, is quantified by:

$$\sigma = \sqrt{\frac{\sum_f \left[G_{\text{exp}}(f) - G_{\text{smooth}}(f)\right]^2}{N}}, \tag{8.1}$$

where N is the number of frequency points. σ is therefore defined as the root mean square (RMS) value of the gain ripple and plotted in Fig. 8.5**(d)**. In this figure, σ is plotted as a function of the characteristic impedance $Z_c(\Phi)$, calculated from the linear inductance $L_0(\Phi)$, extracted from the fit of the linear dispersion relation at the corresponding flux. We have a convex shape and the presence of a sweet spot at a characteristic impedance Z_c between $46\,\Omega$ and $49\,\Omega$. Sweetspot does not occur for $Z_c = 50\,\Omega$ since we consider the small-signal impedance which does not account for the slight increase of the Josephson inductance when the TWPA is pumped. The precision and resolution we have on σ does not allow to get a better precision on the exact sweet spot. The fact that we cannot reach $\sigma \sim 0$, even when σ is close to its sweet spot tells us that we are still limited by some parasitic reflection, independent of the TWPA impedance. In our opinion, these parasitic reflections come from SMA connectors linking the coaxial cables and the PCB. But it could come from the chip carrier itself (box and PCB), or even wire bonding. Canceling these remaining parasitic reflections is going to be one of the first upgrades for the future TWPA generations.

8.5 Calibration

The last three sections have shown an overall good agreement between theory and experimental data and for different pumping conditions. We are now going to use this good agreement to precisely calibrate the main input line of configuration ②.

To calibrate the input line the protocol is the following: we pump the TWPA at a fixed frequency ω_p, detuned enough from the gap frequency. The gap being at 7.3 GHz at the working magnetic flux ($\Phi = 0.1\Phi_0$), we set $\omega_p = 6$ GHz. We start at very low pump power and steadily increase it: the maximum gain increases while the gap frequency is down shifted. The down shifting of the gap position is plotted in Fig. 8.6. It looks like Fig. 8.2, but this time more profiles are shown. Theoretical pump power is also progressively increased so that the model preferentially fits the frequency position of the gap. It turns out that the gain is also well reproduced. As done with the JPA in Section 7.2.2, the experimental and theoretical pump powers are then reported on the same figure as shown in the inset of Fig. 8.6. Each point corresponds to the power at room temperature (x-axis) and at cryogenic temperature (y-axis) required to shift the gap from the same frequency.

The linear regression is also plotted in the inset of Fig. 8.6. The slope of the fit gives the attenuation between the output of the RF source and the TWPA. An attenuation $A_{\text{tot}} = -78.8$ dB is found. Among these -78.8 dB of attenuation, intrinsic TWPA attenuation must be taken into account. At large power, TWPA losses are expected to be $A_{\text{twpa}} = \exp\left(-ik_p'' N_J a\right)$ (see Eq. (6.4) and Eq. (6.5)),

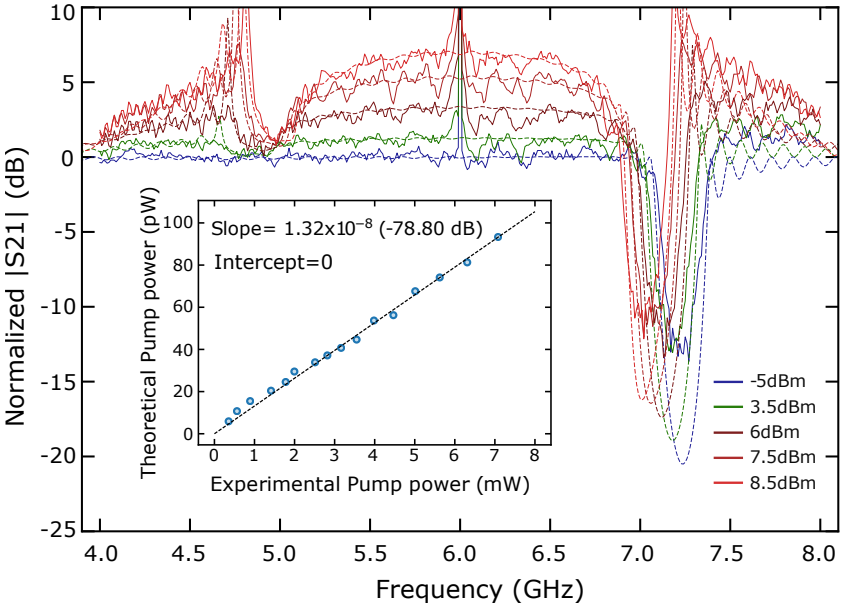

Figure 8.6 – **Calibration via cross modulation of the photonic gap.** Comparison between experiment (full lines) and theory (dashed lines) for a pump tone sent at 6 GHz at various power at a magnetic flux $\Phi = 0.1\Phi_0$. This figure is similar to Fig. 8.3**(a)**, but with more different pump powers, demonstrating the robustness of the model. **Inset:** experimental and theoretical pump power needed to get the same frequency shift of the gap. The linear fit gives an attenuation of the system $A_{\text{total}} = -78.8\,\text{dB}$.

where $k_{\text{p}}'' = -ik_{\text{p}}' \tan\delta/2$ is the imaginary part of the pump wavevector. We find $-3.7\,\text{dB}$. If we define A_{system} as the loss of the input line from the RF source to the TWPA input, then we have the equality $A_{\text{tot}} = A_{\text{system}} + A_{\text{twpa}}$. Therefore we calibrate the attenuation of the input line as $A_{\text{system}} = -75.1\,\text{dB}$. In the calculation of the pump attenuation A_{twpa}, we have chosen to take the full length of the TWPA ($N_{\text{J}} \times a$) in the exponential. We could have chosen only the half of this length as done in the supplementary material of [47]. Our choice leads to a lower system attenuation A_{system}. We consider that this choice is the most conservative one since a lower system attenuation leads to a lower system gain (see Section 8.7.3) and therefore to a higher experimental system noise (see Fig. 8.10) when the TWPA pump is on, as we will see later. We define the uncertainty of this calibration as the difference between this result and the expected attenuation from the nominal attenuation of the coaxial cables and microwave components in our microwave setup. In Chapter 5, we estimated the nominal attenuation to be$-75.6\,\text{dB}$. These two different calibrations gave consistent results. Second, the

uncertainty is defined as $\pm 0.5\,\mathrm{dB}$.

8.6 Saturation

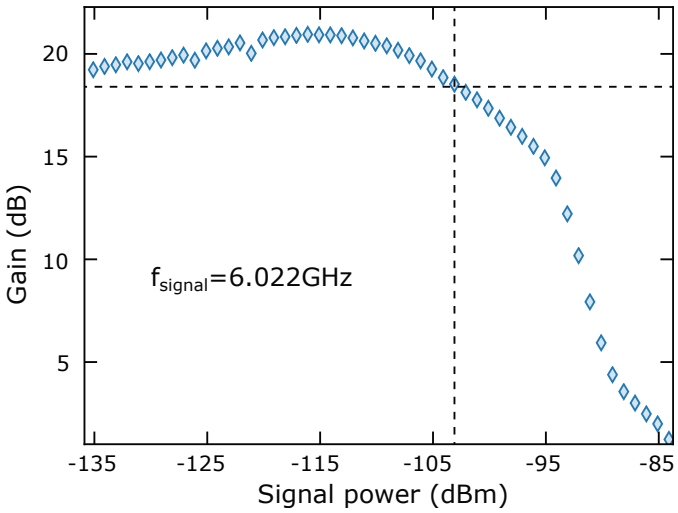

Figure 8.7 – **Gain compression.** Measured gain as a function of the signal power for $f_{\mathrm{signal}} = 6.022\,\mathrm{GHz}$. The gain is compressed by 1 dB when the input signal power is equal to $-103\,\mathrm{dBm}$.

The input line calibration allows now to quantify the gain compression of the TWPA. We recorded gain *versus* signal input power and inferred the 1 dB compression point. Though, we did not spend as much time as we did with JPA to understand precisely the gain compression mechanisms. The experimental protocol was to measure the TWPA gain on a large frequency band (more than 1 GHz), with an optimal pump setting (frequency and power) and to increase steadily the signal power. In Fig. 8.7, we plot the gain as a function of the signal power. Signal frequency is chosen in order to have a small-signal gain $G_0 \approx 20\,\mathrm{dB}$.

First of all, from this plot we infer the 1 dB gain compression $P_{1\,\mathrm{dB}} = -103 \pm 0.5\,\mathrm{dBm}$. It is obviously much higher than for the short array JPA characterized in Section 7.2. It is even more striking since, in the case of the TWPA, no particular care has been taken to improve this 1 dB compression point. It is more than one order of magnitude higher than the JPA. The most plausible reason is that a TWPA is intrinsically less nonlinear than a JPA, even though the latter has been designed to exhibit a very low nonlinearity. JPAs and TWPAs presented in this thesis are working in a four wave mixing fashion. Therefore we expect that gain saturation is directly related to their Kerr nonlinearity. For both, we can try to estimate their nonlinearity.

With a TWPA, the experimental protocol is the following. We probe the TWPA transmission S_{21} while we send a second strong tone at a fixed frequency, similarly to a two-tone spectroscopy. We follow the evolution of the transmitted signal phase as a function of the second tone power. In other words, we record the cross phase modulation of our $\chi^{(3)}$ nonlinear medium. Up to a certain power P_{d} (P_{d} is the power at which the TWPA transmission drops by several orders of magnitude see Section 3.2.3), the phase follows a linear trend with respect to the second tone power. By fitting this linear trend, the slope can be interpreted as the cross Kerr nonlinearity. For a second tone frequency set to 5 GHz and a probe frequency set to 7 GHz, we extract a cross phase modulation of $42\,\mathrm{rad\,nW^{-1}}$. With our JPA, in Chapter 7, we have found an effective self Kerr nonlinearity of 80 kHz (per unit photon) at 7 GHz. This translates to a 160 kHz (per unit photon) cross Kerr nonlinearity (see Chapter 2). It can be translated into radian per unit power since we can link the shift in radian $\Delta\theta$ to a small frequency shift $\Delta\omega$ using the analogy with the input-output theory of a linear resonator [128]:

$$\Delta\theta = 2\arctan(2\Delta\omega/\kappa) \sim 4\Delta\omega/\kappa, \tag{8.2}$$

where $\kappa/2\pi = 375\,\mathrm{MHz}$ is the bare bandwidth of the JPA. The shift in frequency $\Delta\omega = Kn$ is simply taken as the product of the nonlinearity K and the number of photons n. Roughly, the number of photon (in the linear case) is estimated to:

$$n = \frac{4}{\hbar\omega\kappa}P, \tag{8.3}$$

where P is the power in watt. Therefore, we have the following relation between a phase shift and the input power:

$$\Delta\theta = \underbrace{\frac{16K}{\hbar\omega\kappa^2}}_{\chi} P, \tag{8.4}$$

where χ is quantifying the nonlinear phase shift (in $\mathrm{rad\,W^{-1}}$) and is 15 times larger than for the TWPA. It could explain why TWPAs have higher saturation point, at least when operated in four wave mixing. Fabricating a traveling-wave amplifier implies having a much longer array of Josephson junctions/SQUID, which dilutes and decreases the intrinsic nonlinearity. If assume that the nonlinearity scales as the length of the array (or equivalently the number of unit cells), we expect a ratio $2000/80 \sim 25$ between our TWPA and our JPA. This number compares quite well with the measured ratio of nonlineairities. But of course, a more thorough investigation is required. The 1 dB compression point we find must be compared with existing TWPAs as well. In their article, C. Macklin *et. al* [47] report $P_{1\,\mathrm{dB}} = -98\,\mathrm{dBm}$ for a linear gain $G_0 \sim 22\,\mathrm{dB}$. This is better than our current TWPAs. We believe this difference could come from the power dependence of the photonic gap. In our case, large signal power shifts the gap frequency position whereas in their case gaps are not power dependent as they come from linear LC resonators.

Since pump frequency is set to a precise point close to the gap, if the latter is shifted, the former is not optimally biasing the amplifier anymore and gain compression occurs.

Another interesting feature visible in Fig. 8.7 is the gain increase happening at intermediate power (typically between −125 dBm and −105 dBm). This bump is frequency dependent: if the signal frequency is on a gain peak, its amplitude is higher than if the signal is on a gain dip. In Fig. 8.7, signal frequency is detuned from a gain peak: the bump amplitude is only 1.5 dB. If it was right on a gain peak, the bump amplitude would be $\sim$ 2.5 dBm. For people familiar with Kerr based resonant JPAs, this shape and this bump is typical from an under-biased JPA with an increase in the gain when signal power is increased. This is explained in Section 2.4. This is also thoroughly discussed by G. Liu *et. al.* [65]. In principle it could also be the case with a TWPA: the pump is not well set and a frequency shift of the gap could lead to a better pump biasing and therefore to a higher gain. Naturally, if it can happen, the opposite should also happen: gain saturation would occur for input signal lower than expected when the TWPA is over-biased. However, along the different gain compression measurements taken with sample A and B, we only recorded gain increase and never the opposite. Of course, this is not a smoking-gun proof to discard this hypothesis. In our opinion, this gain bump occurs because dielectric losses decrease when the signal power increases, which translates into a gain rise. However, we do not have enough experimental data to disprove one or the other hypothesis.

8.7 TWPA added noise

We conclude this chapter by characterizing the noise of our experimental microwave setup in presence of device A. This noise characterization is achieved thanks to the calibration of configuration ② in Section 8.5.

8.7.1 SNR improvement

The most direct measurement we can carry out is measuring the signal-to-noise ratio (SNR) when the TWPA pump is on and when it is off. Even if the calibration is slightly off, an improvement in the SNR is always a proof of the improvement of the noise performances of the measurement system. To quantify the SNR improvement, we record the power spectral density (PSD) of the system while sending a calibrated signal tone. The signal is sent from the VNA with a frequency $\omega_s/2\pi$ and a power $P_s = -60$ dBm. The PSD is recorded with a spectral analyzer FSQ26. Its resolution bandwidth is set to 20 kHz on a 1 MHz frequency windows. The recorded PSD is then normalized by the total amplification of the system G_{sys} starting from the TWPA. G_{sys} is inferred thanks the calibration of A_{system}.

Normalized PSD are plotted in Fig. 8.8. For both panels **(a)** and **(b)** we plot the normalized PSD when the TWPA pump is on and off. The PSD peaks (on and off) have the same value because the input of the TWPA is taken as the reference. It allows to directly infer the height of the peak (the SNR), the position of the

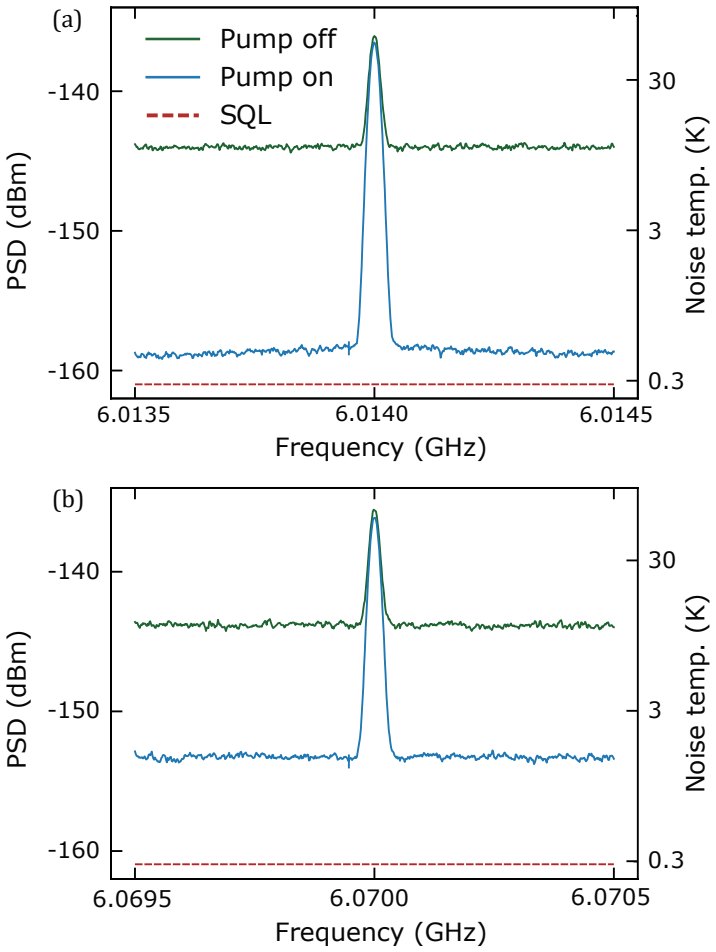

Figure 8.8 – **Signal-to-noise ratio improvement.** PSD normalised by the total system gain. An improvement of up to 15 dBm is observed. Gain ripple leads to different SNR whether the signal frequency is **(a)** on a gain peak or **(b)** on a gain dip. The red dashed line is the standard quantum limit of noise (SQL, defined as 1 photon).

noise floor (system noise) and therefore the improvement brought by the TWPA. The difference between panels **(a)** and **(b)** is the frequency $\omega_s/2\pi$ of the signal sent from the VNA. In the former, the signal is sent on a gain peak, while in the latter, the signal is sent on a gain dip.

The improvement of the SNR is better when the TWPA gain is higher, which is expected. We report up to 15 dBm improvement in panel **(b)**. 15 dBm improvement is only inferred by raw measurement, there is no assumption on the

calibrated attenuation. However, if we consider our calibration correct, the total added noise is very close to the standard quantum limit (SQL) (defined as 1 photon in this case) when the signal is close to a gain peak.

8.7.2 Noise calculation

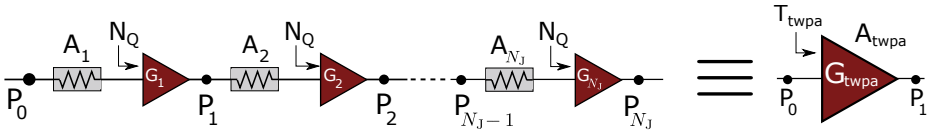

Figure 8.9 – **Circuit diagram of the TWPA as a cascade of attenuators and amplifier.** Every attenuator A_i is equals to $A_{\mathrm{twpa,lp}}/N_{\mathrm{J}}$ and every amplifier G_i is equals to $G_{\mathrm{twpa}}/N_{\mathrm{J}}$. We make the assumption that every amplifier is quantum limited with an input noise $T_{\mathrm{q}} = \hbar\omega_{\mathrm{s}}/2k_{\mathrm{b}}$.

Prior to show noise measurements with sample A, we calculate what we expect to be the TWPA added noise. We follow the approach from C. Macklin *et al.* [47, 129] to model a near quantum limited traveling-wave amplifier. The main idea is to model each elementary cell (in our case each SQUID) as an attenuator followed by an amplifier, respectively characterized by A_i and G_i, as shown in Fig. 8.9. They are respectively defined as:

$$A_i = \frac{A_{\mathrm{twpa,lp}}}{N_{\mathrm{J}}} \quad , \quad G_i = \frac{G_{\mathrm{twpa}}}{N_{\mathrm{J}}}. \tag{8.5}$$

It is important to stress that both G_{twpa} and $A_{\mathrm{twpa,lp}}$ were inferred **experimentally**. G_{twpa} is the normalized TWPA gain as plotted in Fig. 8.3 or in Fig. 8.2 for instance. In order to be as conservative as possible, attenuation is taken when it is the highest, in the low power saturation regime: $A_{\mathrm{twpa,lp}}$. At 6 GHz, we find $A_{\mathrm{twpa,lp}} = -5\,\mathrm{dB}$ (we found $-3.7\,\mathrm{dB}$ for high pump power). We model each cell as a quantum limited amplifier with an intrinsic noise temperature $T_{\mathrm{q}} = \hbar\omega_{\mathrm{s}}/2k_{\mathrm{b}}$ corresponding to half a signal photon. The noise temperature T_i of the amplifier after the i^{th} cell (on point P_i, see Fig. 8.9) is defined as:

$$T_i = \underbrace{T_{i-1}A_iG_i}_{\text{(i)}} + \underbrace{T_{\mathrm{q}}(1-A_i)G_i}_{\text{(ii)}} + \underbrace{T_{\mathrm{q}}(G_i-1)}_{\text{(iii)}}. \tag{8.6}$$

Each member in the right-hand of Eq. (8.6) corresponds to a different source of noise.

— (i): noise coming from the previous cell and being attenuated and amplified in the i^{th} cell. At P_0, the noise is $T_0 = T_{\mathrm{q}}$.

— (ii): Noise of the attenuator itself modeled as a beam splitter (likewise explained in Chapter 5 and in Fig. 5.2). We assume this noise to be quantum limited. It is then amplify by G_i.

— (iii): Quantum limited noise of the amplifier. Amplified by $(G_i - 1)$ since it is on idler's 'channel' (see Section 1.3).

As we can see in Eq. (8.6), the amount on noise after the i^{th} cell depends on the amount of noise generated by the previous cell T_{i-1} via the term (i). The noise at the output of the amplifier after the N_{J}^{th} cell, T_{N_J}, is the product of a cascaded noise, cell after cell. As usual, this amount of noise can be normalized by the actual gain of the amplifier $G_{\text{twpa}} \times A_{\text{twpa,lp}}$ (accounting for the intrinsic TWPA loss). The input-referred added noise $T_{\text{twpa}} = T_{\text{N}_\text{J}}/G_{\text{twpa}}A_{\text{twpa,lp}}$ is plotted in Fig. 8.10**(a)** (brown dotted line). We can see a very slight frequency dependence. This is because TWPA gain is not constant over frequency and suffers from gain ripple. Of course, higher gain leads to a lower noise and vice-versa. We assume though that attenuation is constant over the frequency band shown in Fig. 8.10**(a)**. In this model, fed with experimental data, we expect that the TWPA added noise is around 400 mK while the SQL is around 300 mK at 6 GHz. It seems that losses are indeed detrimental to TWPA efficiency, but it is not catastrophic, at least in our model.

8.7.3 Noise measurement

We eventually characterize experimentally the system noise when device A is included. Given our setup, we do not have direct access to the intrinsic noise of the TWPA alone. However, we do have access to the whole system noise, which corresponds to the noise of the amplification stage, consisting in the TWPA $(G_{\text{twpa}}, T_{\text{twpa}})$, the HEMT amplifier $(G_{\text{hemt}}, T_{\text{hemt}})$ with in-between an attenuator (A) modeling electrical losses (summarized in Fig. 8.10**(b)**). To extract the system noise we again measure the PSD at the output of the setup and we normalize it by the whole system gain G_{system}. The resolution bandwidth is set to 100 kHz. The experimental normalized PSD is plotted in Fig. 8.10**(a)**. Unlike the SNR measurements, we exclusively plot the PSD expressed as a temperature in kelvin. The system noise temperature is plotted when the TWPA pump is on and off.

The first observation is obviously a reduction of the system noise whenever the TWPA pump is on. It is only a confirmation of what we have observed in Fig. 8.8. When the TWPA pump is off, the system noise is around 15 K. This is slightly high for a standard cryogenic microwave setup with a HEMT amplifier. This is mostly due to our setup, configuration ②, which is not optimized in terms of noise of performances. There are different lossy microwave components before the HEMT input. $T_{\text{hemt,eff}} = 15\,\text{K}$ defines the HEMT effective noise temperature. When the TWPA pump is on, the most remarkable feature of the system noise temperature is its frequency dependence and the amplitude of the noise ripple. This is explained by the TWPA gain ripple, due to imperfect matching, parasitic reflection, *etc.* When the TWPA gain is too low to compensate for the effective

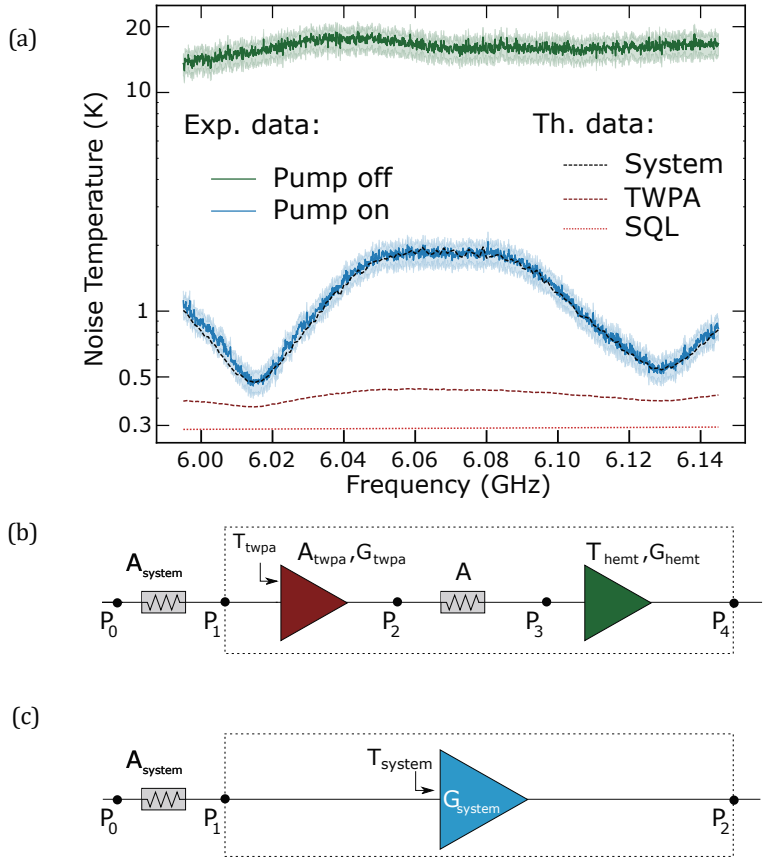

Figure 8.10 – **Amplifier added noise and schematics. (a)** Noise temperature of the TWPA. Measured PSD normalized by the system gain when the TWPA pump is off (green solid line) and on (blue solid line, the light blue shaded area corresponds to error bars). The red dotted line corresponds to the standard quantum limit (SQL) of noise. The brown dashed line refers to the intrinsic calculated noise of the TWPA, which is slightly above the SQL because of internal losses. The black dashed line is the total system noise temperature. It is higher than the TWPA intrinsic noise temperature because of the finite TWPA gain. Noise ripple are caused by TWPA gain ripple. **(b)** The system attenuation is A_{system}. Inside the dotted box, there is the TWPA, modeled as an attenuator combined with a lossless amplifier, followed by an unknown attenuation A and the rest of the chain (HEMT and room temperature amplifier), whose input noise is dominated by the HEMT noise. **(c)** Simpler modeling of the system as a single amplifier G_{system}, whose input noise T_{system} depends on whether or not the TWPA pump is turned on.

HEMT noise, noise temperature rises up to 2 K. On the contrary, when the TWPA gain is high, noise decreases as low as 0.5 K.

In order to check if experimental and theoretical noise are matched, we chose to calculate the whole input-referred system noise T_{system}. We start from the intrinsic noise amplifier calculated previously. Then, we simply model the output line, shown in panel **(b)**, into a meta amplifier $(G_{\text{system}}, T_{\text{system}})$ as shown in **(c)**. To compute the whole system noise T_{system} when the TWPA pump is on, we rely on the standard formula:

$$T_{\text{system}} = \underbrace{T_{\text{twpa}}}_{\text{calculated}} + \underbrace{\frac{T_{\text{hemt,eff}}}{G_{\text{twpa}}}}_{\text{measured}}. \tag{8.7}$$

The computed T_{system} is plotted in Fig. 8.10**(a)** in black dashed line. As stressed in Eq. (8.7), T_{system} is calculated from both experimental results and calculated data. It amounts to make the assumption that noise has two origins. First, in our TWPA, noise is exclusively coming from its dielectric losses. Second, it comes from the finite gain of the TWPA with respect to the HEMT noise. In panel **(a)**, we see a good agreement between the calculated and the measured system noise. It consequently means that our two assumptions on the origin of noise in our system are relevant.

In terms of performances, our TWPA does improve the system noise by reducing it from more than an order of magnitude. Our TWPA is obviously not quantum limited. Its intrinsic (calculated) noise is about 100 mK above the SQL. The only solution is to decrease TWPA dielectric losses. Additionally, to enhance the added noise of the whole system, it is necessary to cancel gain ripple by working on the microwave environment of the TWPA. However, most importantly our noise figures are *on par* with the very few published results on Josephson/kinetic inductance TWPA [47, 130].

Conclusion and perspectives 9

9.1 Conclusion

In this work we have modeled, developed, characterized and measured two different kind of near quantum-limited Josephson parametric amplifiers. Regarding low-noise performance, Josephson amplifiers are state-of-the-art microwave amplifiers and essential elements for circuit QED and quantum information experiments, which require to be always faster and with a better signal-to-noise ratio.

The first Josephson amplifier developed during this PhD was the Josephson parametric amplifier (JPA) based on a nonlinear resonator. This technology is now routinely used in many research teams working in circuit QED. Resonant JPAs are now declined in numerous versions, but there is still room for improvements. This work focused in particular on understanding the origin of gain saturation in four wave mixing, Kerr-based JPAs. After studying and developing a model to theoretically understand our JPA performances, we identified the self Kerr nonlinearity, true fuel in the amplification process, to instigate gain saturation.

We addressed this issue by decreasing the Kerr nonlinearity of the resonant structures. This was done by diluting the Kerr nonlinearity with the help of an array of Josephson junctions, instead of only one or few units as it is commonly done. In order to substantially dilute the nonlinearity, the array must be few hundreds microns long. Given the wave velocity of a Josephson metamaterial, it corresponds to a resonance in the gigahertz regime, right in our working range (4 GHz to 10 GHz). Therefore, one concrete achievement of this work was to account for propagating effects in the calculation of the nonlinearity and applying it to existing models considering Kerr nonlinearity as the source of gain saturation.

The implemented array JPAs showed good performances: they reach more than 20 dB signal power gain and exhibit bare bandwidth constant as high as 400 MHz. Their one decibel gain compression reach −117 dBm. The good agreement found between experimental and theoretical saturation data makes us confident in our approach to model our array JPAs and to infer nonlinearities in them. We report an effective Kerr nonlinearity of 80 kHz for the first mode of our Josephson

Link back to Table of contents →

metamaterial resonator, which is state-of-the-art for low nonlinear Josephson amplifiers.

The natural step-up after mastering propagation and amplification effects in Josephson arrays was to tackle traveling-wave parametric amplifiers (TWPA). We thus developed a fabrication recipe to go beyond the resonant amplification regime and reach the traveling-wave amplification regime. This design overcomes two well-known issues: impedance matching and phase matching. Whilst the first one is about microwave engineering, the latter is about waves' physics in a distributed, nonlinear medium several wavelength long. A subsequent issue to tackle was electrical loss in traveling-wave structures, somehow related to the first point.

The fabrication recipe we have developed for Josephson traveling-wave amplifiers is simple to implement yet surprisingly efficient. It is also very promising, since it goes beyond the fabrication of Josephson amplifiers only. Complexity wise, the recipe has only 3 steps. Additionally, the fabrication of the array has been kept the same with respect to the JPA fabrication. To impedance match the array, we drastically increased the shunt ground capacitance per unit length of the Josephson transmission lines by depositing on top of the array tens of nanometers of a dielectric via atomic layer deposition. A standard lithography step is done to deposit the metallic 'top-ground' on the dielectric while leaving the bonding pads uncovered. It ensures the bonding between the amplifier and the rest of the setup. This three-step fabrication recipe allows to fabricate a near $50\,\Omega$ Josephson transmission line. It also allows implementation of SQUIDs instead of single Josephson junctions. Last but not least, this recipe enables to the periodic modulation of the characteristic impedance of the SQUID transmission line. The main drawback of the top-ground deposition is loss of the transmitted signal through the nonlinear medium. In this work, we identified two kind of loss: conductor and dieletric loss. The first is coming from the relatively thin metallic top-ground. The second is coming from the atomically deposited dielectric layer. While the first was precisely identified and overcame, the latter is still under investigation and its precise origin is not fully understood. It clearly must be understood in the upcoming versions.

The second issue we tackled was the phase mismatch between the signal, the idler and the pump. It is coming from different strengths between the self phase modulation and the cross phase modulation in centrosymmetric nonlinear elements. To counter it, the dispersion relation must be locally distorted. It adds a phase offset to the pump wave and compensate for the initial phase mismatch. Unlike the previous Josephson TWPA, we did not open a stop-band with periodic resonators. Instead, we periodically modulated the characteristic impedance of the nonlinear transmission line to open a photonic band gap in the dispersion relation. The key point is that it does not add any complexity in the recipe: non modulated or a modulated array have equally complex fabrication. The drawback is an apparent weaker distortion of the dispersion relation and therefore a weaker correction of the pump phase leading to a lower gain. However, we have a direct control on the distortion through the amplitude of spatial modulation. On the other hand, a greater amplitude of modulation also comes with a larger

band gap, which reduced the effective instantaneous bandwidth of the amplifier. Further gap engineering could be an interesting challenge to focus on. In terms of figures of merit, our SQUID traveling-wave amplifier outperform our resonant JPA. We reach 18 dB of mean maximum gain, for 2.3 GHz instantaneous bandwidth and a one decibel compression point equals to −103 dBm at highest gain reached. In the best case, we measured a system noise down to 500 mK, at 6 GHz. At this frequency, one photon is equivalent to 300 mK. If we trust our model, our TWPA intrinsic noise is as low as 400 mK. Our TWPA also benefits from flux modulation, allowing for *in-situ* impedance tuning. For high gain, we report gain ripple as low as 5 dB amplitude.

Resonant JPA and TWPA are presently two approaches to quantum limited microwave signal amplification: the former has exclusive features such as squeezing or sub-single photon noise, while the latter has a higher gain-bandwidth product. However, TWPAs remain relatively new, less than 5 years old and numerous upgrades and optimizations are still to be done.

9.2 Perspectives

To conclude, we give some perspectives and ideas to follow in order to improve the current version of our TWPA; but also to explore new angles of research. We focus in this section on four more or less near term projects.

9.2.1 Four wave mixing TWPA optimization

The most urgent matter for upgrading TWPAs is to enhance the quality of the deposited dielectric. As we mentioned in Chapter 4 and Chapter 6, depositing amorphous silicon instead of alumina did little dielectric losses mitigation. It seems it is coming from the hydrogen concentration used during the deposition of amorphous silicon. In principle, amorphous silicon has a loss tangent low enough to completely cancel signal attenuation. A loss tangent as low as 10^{-5} was reported [99] while a loss tangent in the order of 10^{-3} would already be enough to keep an attenuation above −1 dB for frequencies below 10 GHz.

The second most important upgrade would be to improve the impedance environment of the TWPA. The chip carrier, printed circuit board and their connections must be optimized for TWPA purposes. As shown in Chapter 5, the geometry of the box itself is ill-designed since a parasitic resonance occurs at 10 GHz, no matter the microwave geometry (CPW or stripline). This needs to be improved if we want to optimize our amplifiers. This geometry (carriers and connectors) was not originally intended for traveling-wave amplification purposes. We would need specific microwave connectors with a tapered shape and a good ground continuity between the coaxial cables and the PCB.

Finally, some improvement could be done to reduce the width of the photonic gap. In order to avoid having a too large forbidden band, a thorough gap engineering of the dispersion relation could provide larger gain. Gap engineering would

sharpen the gap edges and therefore get a larger phase correction while reducing the width of the photonic gap.

9.2.2 Low frequency amplification

The emergence of silicon, spin-based qubits as a serious candidate for quantum computing is bringing original readout schemes. For instance, reflectometry readouts with CMOS-based devices [131] asks for extremely low frequency readouts, typically between 100 MHz and 900 MHz. For now, readout happening in this frequency range has very poor detection efficiency since up to very recently no quantum limited amplifier existed in this range. It has been reported in July 2019 a Josephson-based (resonant) amplifier [132] working around 500 MHz.

In principle, reaching quantum limited amplification with a TWPA should be much easier than with a resonant JPA since we know that a traveling-wave amplifier can be pumped at any frequency to expect amplification, unlike a resonant JPA where amplification only occurs close to a resonance. During the last months of my PhD, we have supplied TWPAs to a team working at the Néel Institute on CMOS based qubit (**David Niegemann** and **Matias Urdampilleta**). Their readout frequency is around 500 MHz. However, making a TWPA working in this frequency range is not as straightforward as we expected. First of all, it seems that having a good impedance matching between the resonator and the TWPA is not simple. Some engineering tricks are necessary, requiring more components and leading to signal attenuation. Moreover, pumping so close from the edge of the dispersion relation (frequencies at stake are very low) is not trivial and a very narrow bandwidth and low gain are found. Eventually, a gain of only few decibels is found which is not worth given the complexity of the eventual microwave setup. To make it worth, gap engineering and dispersion engineering are necessary. The first is required to improve the phase matching and the maximum gain. The second is to avoid higher order photon generation, highly detrimental for the amplifier performances. It is much more probable that in our case it is needed since we pump at very low frequency, in the linear region of the dispersion. Therefore, a low plasma frequency could be a solution.

9.2.3 Three wave mixing TWPA

This project has already been taken over by **Arpit Ranadive**, a graduate student who arrived in the institute in November 2018. As we have seen in Chapter 2, amplification is not necessary relying on a four wave mixing process and three wave mixing is possible, also for traveling-wave amplification. To implement traveling-wave, three wave mixing amplification, the unit cell cannot be a single Josephson junction or a SQUID. The nonlinearity must be engineered in order to mute the fourth order Kerr nonlinearity and to enhance the third order nonlinearity. RF SQUIDs are a very promising candidate for that. The key point is that flux tuning is needed to thread the loop and discard the former while enhancing the latter. We have experimentally proven that our current fabrication method allows to

homogeneously thread a millimeter long SQUID transmission line.

Three wave mixing TWPA could be in principle the most advanced quantum limited amplifier, combining all the advantages of the existing four wave mixing TWPAs while discarding their main drawback: no more photonic gap. Three wave mixing would allow a complete detuning of the pump frequency from the working band. The first samples are being tested and this project is currently in progress.

9.2.4 Josephson transmission line as a platform for quantum optics experiments

We conclude this section with the most basic physics perspective of the Josephson transmission line. This project is also already carried by a newly arrived post-doctoral fellow **Martina Esposito**. The goal of this project seeks to reproduce basic experiments done in quantum optics with a distributed nonlinear medium (such as nonlinear fiber optics) with the Josephson transmission lines we are able to fabricate. There are already some theoretical proposals [133] to engineer original quantum states in such structures. Up to now, we have been able to measure second and third harmonics generation (SHG and THG), which are classical nonlinear effects. Quantum optics experiments, such as triplet photon generation or single/multi mode squeezing generation, could be envisioned. However, we are for now limited by dielectric losses when probing such interesting states: the dissipation within our structures is still too high.

The end ☺

Appendices

Calculations

A

A.1 Derivation of the degenerate parametric amplifier Hamiltonian

We first start with a Kerr-like potential:

$$\begin{aligned} U_{\mathrm{a}}(t) &= -U_{\mathrm{a}}^{0}\cos\left(x_{\mathrm{a}}^{\mathrm{zpf}}\left(\hat{a}+\hat{a}^{\dagger}\right)\right) \\ &\approx -U_{\mathrm{a}}^{0}\left[1-\frac{1}{2!}\left(x_{\mathrm{a}}^{\mathrm{zpf}}\left(\hat{a}+\hat{a}^{\dagger}\right)\right)^{2}+\frac{1}{4!}\left(x_{\mathrm{a}}^{\mathrm{zpf}}\left(\hat{a}+\hat{a}^{\dagger}\right)\right)^{4}\right]. \end{aligned} \tag{A.1}$$

We expand the last two terms of the right-hand side of Eq. (A.1):

$$(\hat{a}+\hat{a}^{\dagger})^{2} = \hat{a}^{2}+\hat{a}\hat{a}^{\dagger}+\hat{a}^{\dagger}\hat{a}+\hat{a}^{\dagger 2}, \tag{A.2a}$$

$$\begin{aligned} (\hat{a}+\hat{a}^{\dagger})^{4} = {} & \hat{a}^{\dagger 4}+\hat{a}^{\dagger 3}\hat{a}+\hat{a}^{\dagger 2}\hat{a}\hat{a}^{\dagger}+\hat{a}^{\dagger 2}\hat{a}^{2}+\hat{a}^{\dagger}\hat{a}\hat{a}^{\dagger 2}+\hat{a}^{\dagger}\hat{a}\hat{a}^{\dagger}\hat{a}+\hat{a}^{\dagger}\hat{a}^{2}\hat{a}^{\dagger}+\hat{a}^{\dagger}\hat{a}^{3} \\ & +\hat{a}\hat{a}^{\dagger 3}+\hat{a}\hat{a}^{\dagger 2}\hat{a}+\hat{a}\hat{a}^{\dagger}\hat{a}\hat{a}^{\dagger}+\hat{a}\hat{a}^{\dagger}\hat{a}^{2}+\hat{a}^{2}\hat{a}^{\dagger 2}+\hat{a}^{2}\hat{a}^{\dagger}\hat{a}+\hat{a}^{3}\hat{a}^{\dagger}+\hat{a}^{4}. \end{aligned} \tag{A.2b}$$

Now that we have the expression of the linear and nonlinear parts of the potential, we can simplify it. To do so, we perform a change of frame using the unitary transformation $R(t) = \exp\left(i\left(\omega_{\mathrm{p}}p^{*}p+\omega_{\mathrm{p}}\hat{a}^{\dagger}\hat{a}\right)t\right)$. The rotated Hamiltonian is given by:

$$\hat{H}'_{\mathrm{4WMD}} = \hat{R}(t)\hat{H}_{\mathrm{4WMD}}R^{\dagger}(t)+i\hbar\dot{\hat{R}}(t)\hat{R}^{\dagger}(t). \tag{A.3}$$

To calculate the first term of the right-hand side of Eq. (A.3), we recall the expansion of an exponantial term in the Taylor series:

$$e^{i\hat{K}}\hat{\mathcal{O}}e^{-i\hat{K}} = \hat{\mathcal{O}}+i\left[\hat{K},\hat{\mathcal{O}}\right]+\frac{i^{2}}{2!}\left[\hat{K},\left[\hat{K},\hat{\mathcal{O}}\right]\right]+\frac{i^{3}}{3!}\left[\hat{K},\left[\hat{K},\left[\hat{K},\hat{\mathcal{O}}\right]\right]\right]+\cdots. \tag{A.4}$$

Link back to Table of contents →

For instance, if $\hat{\mathcal{O}} = \hat{a}$ and $\hat{K} = \omega_\mathrm{p} t \left(p^* p + \hat{a}^\dagger \hat{a}\right)$, we obtain:

$$\hat{R}\hat{a}\hat{R}^\dagger = e^{i\left(\omega_\mathrm{p} p^* p + \omega_\mathrm{p} \hat{a}^\dagger \hat{a}\right)t} \hat{a} e^{-i\left(\omega_\mathrm{p} p^* p + \omega_\mathrm{p} \hat{a}^\dagger \hat{a}\right)t} = \hat{a} + \left[\omega_\mathrm{p} \left(p^* p + \hat{a}^\dagger \hat{a}\right) t, \hat{a}\right] + \cdots . \tag{A.5}$$

The general form of the commutator between $\hat{a}^\dagger \hat{a}$ and $\hat{a}$ gives $\left[\gamma \hat{a}^\dagger \hat{a}, \hat{a}\right] = -\gamma \hat{a}$. We therefore have the relation:

$$e^{i\gamma \hat{a}^\dagger \hat{a}} \hat{a} e^{-i\gamma \hat{a}^\dagger \hat{a}} = \hat{a} \left(1 - i\gamma - \frac{1}{2!}(i\gamma)^2 - \frac{1}{3!}(i\gamma)^3 - ...\right) = \hat{a} e^{-i\gamma}. \tag{A.6}$$

Following the same procedure with $\hat{\mathcal{O}} = \hat{a}^\dagger$, $\hat{\mathcal{O}} = \hat{a}^\dagger \hat{a}$, and $\hat{\mathcal{O}} = \hat{a}^{\dagger 2} \hat{a}^2$, we can demonstrate that:

$$\begin{aligned} e^{i\gamma \hat{a}^\dagger \hat{a}} \hat{a}^\dagger e^{-i\gamma \hat{a}^\dagger \hat{a}} &= \hat{a}^\dagger e^{i\gamma}, \\ e^{i\gamma \hat{a}^\dagger \hat{a}} \hat{a}^\dagger \hat{a} e^{-i\gamma \hat{a}^\dagger \hat{a}} &= \hat{a}^\dagger \hat{a}, \\ e^{i\gamma \hat{a}^\dagger \hat{a}} \hat{a}^{\dagger 2} \hat{a}^2 e^{-i\gamma \hat{a}^\dagger \hat{a}} &= \hat{a}^{\dagger 2} \hat{a}^2. \end{aligned} \tag{A.7}$$

We can deduce that any term from Eqs. (A.2a) and (A.2b) with an unbalanced number of creation and annihilation terms will have an extra phase term after rotation of the frame of study. Therefore, if we consider that these terms oscillate very rapidly and have in average a zero value, we can discard them. This is the rotating wave approximation (RWA). Therefore with this in mind and the commutation relation of the creation/annihilation operators ($[\hat{a}, \hat{a}^\dagger] = 1$), Eqs. (A.2a) and (A.2b) now read:

$$(\hat{a} + \hat{a}^\dagger)^2 \overset{\mathrm{RWA}}{=} \hat{a}\hat{a}^\dagger + \hat{a}^\dagger \hat{a} = 2\hat{a}^\dagger \hat{a} + 1, \tag{A.8a}$$

$$(\hat{a} + \hat{a}^\dagger)^4 \overset{\mathrm{RWA}}{=} \hat{a}^{\dagger 2} \hat{a}^2 + \hat{a}^\dagger \hat{a} \hat{a}^\dagger \hat{a} + \hat{a}^\dagger \hat{a}^2 \hat{a}^\dagger + \hat{a}\hat{a}^{\dagger 2} \hat{a} + \hat{a}\hat{a}^\dagger \hat{a}\hat{a}^\dagger + \hat{a}^2 \hat{a}^{\dagger 2} = C \hat{a}^{\dagger 2} \hat{a}^2. \tag{A.8b}$$

If we consider the full Hamiltonian $\hat{H}_{4\mathrm{WMD}}$ made of the pump, the signal and their interaction, we have:

$$\begin{aligned} \hat{R}\hat{H}_{4\mathrm{WMD}}\hat{R}^\dagger &= \hat{R}\hat{H}_\mathrm{p}\hat{R}^\dagger + \hat{R}\hat{H}_\mathrm{s}\hat{R}^\dagger + \hat{R}\hat{H}_\mathrm{int}\hat{R}^\dagger, \\ &\overset{\mathrm{RWA}}{=} \hbar\omega_\mathrm{p} p^* p + \hbar\omega_0 \hat{a}^\dagger \hat{a} - U_\mathrm{a}^0 \hat{a}^{\dagger 2} \hat{a}^2 + \hbar g(\hat{a} p^* + \hat{a}^\dagger p). \end{aligned} \tag{A.9}$$

We must now calculate the second term of Eq. (A.3). We expand again an exponantial term in the Taylor series:

$$\frac{\mathrm{d}e^{i\hat{K}}}{\mathrm{d}t} e^{-i\hat{K}} = i\frac{\mathrm{d}\hat{K}}{\mathrm{d}t} + \frac{i^2}{2!}\left[\hat{K}, \frac{\mathrm{d}\hat{K}}{\mathrm{d}t}\right] + \frac{i^3}{3!}\left[\hat{K}, \left[\hat{K}, \frac{\mathrm{d}\hat{K}}{\mathrm{d}t}\right]\right] + \cdots . \tag{A.10}$$

It is straightforward that for $\hat{K} = \omega_{\mathrm{p}} t \left(p^* p + \hat{a}^\dagger \hat{a}\right)$, we have $\frac{\mathrm{d}\hat{K}}{\mathrm{d}t} = \omega_{\mathrm{p}} \left(p^* p + \hat{a}^\dagger \hat{a}\right)$ and $\frac{\mathrm{d}K}{\mathrm{d}t}$ commutes with $\hat{K}$. Therefore, the Hamiltonian in the new rotating frame of study is simplified into:

$$\hat{H}'_{\mathrm{4WMD}} = \hbar(\omega_0 - \omega_{\mathrm{p}})\hat{a}^\dagger \hat{a} - U_{\mathrm{a}}^0 \hat{a}^{\dagger 2}\hat{a}^2 + \hbar\left(\hat{a}\epsilon^* + \hat{a}^\dagger \epsilon\right), \tag{A.11}$$

where we consider $\epsilon = gp$ the pump amplitude. The next unitary transformation to perform is a displacement of the nonlinear cavity, caused by the strong pump tone. The displacement operator is defined as $\hat{D}(\alpha) = \exp\left(\alpha\hat{a}^\dagger - \alpha^*\hat{a}\right)$ where α is a complex number and the classical part of the intra-resonator field. The displaced Hamiltonian reads:

$$\hat{H}''_{\mathrm{4WMD}} = \hat{D}^\dagger(\alpha)\hat{H}'_{\mathrm{4WMD}}\hat{D}(\alpha) - i\hbar\dot{\hat{D}}(\alpha)\hat{D}^\dagger(\alpha). \tag{A.12}$$

By using again the expansion Eq. (A.4), we show that:

$$\hat{D}^\dagger(\alpha)\hat{a}\hat{D}(\alpha) = \hat{a} + \alpha, \tag{A.13}$$

$$\hat{D}^\dagger(\alpha)\hat{a}^\dagger\hat{D}(\alpha) = \hat{a}^\dagger + \alpha^*. \tag{A.14}$$

Since the displacement operator is unitary ($\hat{D}^\dagger(\alpha)\hat{D}(\alpha) = \hat{D}(\alpha)\hat{D}^\dagger(\alpha) = 1$), the Hamiltonian reads:

$$\hat{D}^\dagger(\alpha)\hat{H}'_{\mathrm{4WMD}}\hat{D}(\alpha) = \hbar(\omega_0 - \omega_{\mathrm{p}})\underbrace{(\hat{a}^\dagger + \alpha^*)(\hat{a} + \alpha)}_{(1)} - U_{\mathrm{a}}^0\underbrace{(\hat{a}^\dagger + \alpha^*)^2(\hat{a} + \alpha)^2}_{(2)}$$
$$+ \hbar\underbrace{\left((\hat{a} + \alpha)\,\epsilon^* + \left(\hat{a}^\dagger + \alpha^*\right)\epsilon\right)}_{(3)}. \tag{A.15}$$

We expand term by term. For the first one:

$$(1) = \hat{a}^\dagger\hat{a} + \underbrace{\hat{a}^\dagger\alpha + \hat{a}\alpha^*}_{\text{will simplify with (3)}} + \underbrace{|\alpha|^2}_{\text{constant}}. \tag{A.16}$$

For term (2), it can be written as :

$$(2) = \underbrace{|\alpha|^4}_{\text{constant}} + \underbrace{2|\alpha|^2(\alpha\hat{a}^\dagger + \alpha^*\hat{a})}_{\text{will simplify with (3)}} + 4|\alpha|^2\hat{a}^\dagger\hat{a} + \alpha^2\hat{a}^{\dagger 2} +$$
$$\alpha^{*2}\hat{a}^2 + \underbrace{2(\hat{a}^{\dagger 2}a\alpha + \alpha^*\hat{a}^\dagger\hat{a}^2) + \hat{a}^{\dagger 2}\hat{a}^2}_{\text{higher order terms}}. \tag{A.17}$$

The first term $|\alpha|^4$ of Eq. (A.17) is a constant and can be dropped. The third term can be put with the first term of Eq. (A.15): it is the nonlinear Kerr frequency shift produced by the pump. The two next terms are the terms of interest for amplification since they lead to the four wave mixing process. Finally, the last terms are higher order terms that can be discarded for now (see Section 2.4 to treat them). To cancel the extra pump terms denoted (3), we must consider the evolution of the resonator field in the Heisenberg picture:

$$\frac{\mathrm{d}\hat{a}}{\mathrm{d}t} = \frac{i}{\hbar}\left[\hat{H}''_{\mathrm{4WMD}}, \hat{a}\right], \tag{A.18}$$

where $\hat{H}''_{\mathrm{4WMD}}$ is the displaced Hamiltonian. In the semi-classical steady-state case the pump amplitude reads:

$$\epsilon = \left(\omega_{\mathrm{p}} - \omega_0 + 2\frac{U_{\mathrm{a}}^0}{\hbar}|\alpha|^2\right)\alpha. \tag{A.19}$$

We see that ϵ is proportional to α, therefore terms in $\epsilon\alpha^*$ (and $\epsilon^*\alpha$) can be discarded since they are constants. The two other pump terms are written:

$$\epsilon\hat{a}^\dagger = \left(\omega_{\mathrm{p}} - \omega_0 + 2\frac{U_{\mathrm{a}}^0}{\hbar}|\alpha|^2\right)\alpha\hat{a}^\dagger, \tag{A.20a}$$

$$\epsilon^*\hat{a} = \left(\omega_{\mathrm{p}} - \omega_0 + 2\frac{U_{\mathrm{a}}^0}{\hbar}|\alpha|^2\right)\alpha^*\hat{a}. \tag{A.20b}$$

The last pump terms are canceled with the previous calculated terms. Still in the steady-state and by dropping all constant terms, the pumped and displaced Hamiltonian in Eq. (A.12) reads:

$$\hat{H}''_{\mathrm{4WMD}} = \hbar(\omega_0 - \omega_p + 4\frac{U_{\mathrm{a}}^0}{\hbar}|\alpha|^2)\hat{a}^\dagger\hat{a} - U_{\mathrm{a}}^0\alpha^2\hat{a}^{\dagger 2} - U_{\mathrm{a}}^0\alpha^{*2}\hat{a}^2. \tag{A.21}$$

We recognize Eq. (2.21a) if we define $K = -2U_{\mathrm{a}}^0/\hbar$ and $\lambda = K\alpha^2$.

A.2 Derivation for traveling-wave amplification

A.2.1 Gain in a bare Josephson array

In this section we detail the calculations for the coupled equations between the pump, the signal and the idler in Eq. (3.27) (O'Brien *et. al* model) and leading to the expression of the signal power gain shown in Eqs. (3.35) and (3.49) for a Josephson TWPA. In order to stay consistent, we will use only the formalism of Section 3.5. We treat the array as a non modulated, bare Josephson array. We

start from the array Lagrangian of the system (from Eq. (3.46))

$$\mathcal{L} = \frac{\hbar^2}{(2e)^2}\left[\sum_n \frac{C(\dot{\phi}_{n+1}-\dot{\phi}_n)^2 + C^{\mathrm{g}}\dot{\phi}_n^2}{2} + \sum_n \frac{1-\cos\left(\phi_{n+1}-\phi_n\right)}{L}\right]. \tag{A.22}$$

We use the Euler-Lagrange equation and we consider that there is **no** spatial modulation of the Josephson array. For every site n between 1 and N_J, we have

$$\begin{aligned} &\forall n \in [1, N_{\mathrm{J}}]: \qquad \frac{\partial \mathcal{L}}{\partial \phi_n} - \frac{\mathrm{d}}{\mathrm{d}t}\left(\frac{\partial \mathcal{L}}{\partial \dot{\phi}_n}\right) = 0, \\ \leftrightarrow \quad &\forall n \in [1, N_{\mathrm{J}}]: \qquad C\left(2\ddot{\phi}_n - \ddot{\phi}_{n+1} - \ddot{\phi}_{n-1}\right) + C^{\mathrm{g}}\ddot{\phi}_n + \\ &\qquad\qquad \frac{1}{L}\left(\sin\left(\phi_n - \phi_{n+1}\right) + \sin\left(\phi_n - \phi_{n-1}\right)\right) = 0. \end{aligned} \tag{A.23}$$

After expanding the nonlinear term up to the third order, we obtain :

$$\begin{aligned} 2\phi_n - \phi_{n-1} - \phi_{n+1} - \frac{1}{6}\left(\left(\phi_n - \phi_{n-1}\right)^3 + \left(\phi_n - \phi_{n+1}\right)^3\right) \\ + LC\left(2\ddot{\phi}_n - \ddot{\phi}_{n-1} - \ddot{\phi}_{n+1}\right) + LC^g\ddot{\phi}_n = 0. \end{aligned} \tag{A.24}$$

For the superconducting phase ϕ_n , we use the standard ansatz where the solution is a sum of three monocromatic waves: the strong pump, the signal and the idler fulfilling frequency conservation $2\omega_{\mathrm{p}} = \omega_{\mathrm{s}} + \omega_{\mathrm{i}}$. Their amplitude is denoted A_{j} and varies slowly, their wavevector is k_{j}, where j=p,s,i is an index standing for pump, signal and idler, respectively.

$$\phi_n(t) = A_{\mathrm{p}}(n)e^{ik_{\mathrm{p}}n - i\omega_{\mathrm{p}}t} + A_{\mathrm{s}}(n)e^{ik_{\mathrm{s}}n - i\omega_{\mathrm{s}}t} + A_{\mathrm{i}}(n)e^{ik_{\mathrm{i}}n - i\omega_{\mathrm{i}}t} + \mathrm{c.c.}. \tag{A.25}$$

For convenience, we define $\Psi_{\mathrm{j}} = k_{\mathrm{j}}n - \omega_{\mathrm{j}}t$. The phase difference is expressed as:

$$\phi_n(t) - \phi_{n+1}(t) = \sum_{\mathrm{j=p,s,i}}\left[A_{\mathrm{j}}(n) - A_{\mathrm{j}}(n+1)e^{ik_{\mathrm{j}}}\right]e^{i\Psi_{\mathrm{j}}} + \mathrm{c.c.}. \tag{A.26}$$

Then, we assume that the wavelength λ is much longer than the unit cell size a. Therefore, we use the continuum approximation and the index n related to the cell is replaced by a continuous position x. Now, if we consider that $A_{\mathrm{j}}(n+1) \approx$

$A_\mathrm{j}(x+a) \approx A_\mathrm{j}(x) + a\frac{\mathrm{d}A_\mathrm{j}}{\mathrm{d}x} + \frac{a^2}{2}\frac{\mathrm{d}^2A_\mathrm{j}}{\mathrm{d}x^2}$, Eq. (A.26) can be written as

$$\phi_n(t) - \phi_{n+1}(t) \approx \sum_{\mathrm{j=p,s,i}} \left[A_\mathrm{j}(x) - \left(A_\mathrm{j}(x) + a\frac{\mathrm{d}A_\mathrm{j}}{\mathrm{d}x} + \frac{a^2}{2}\frac{\mathrm{d}^2A_\mathrm{j}}{\mathrm{d}x^2} \right) e^{ik_\mathrm{j}} \right] e^{i\Psi_\mathrm{j}} + \mathrm{c.c.},$$

$$\approx \sum_{\mathrm{j=p,s,i}} \left[-2i \sin\left(\frac{k_\mathrm{j}}{2}\right) e^{ik_\mathrm{j}/2} A_\mathrm{j}(x) - a\frac{\mathrm{d}A_\mathrm{j}}{\mathrm{d}x} e^{ik_\mathrm{j}} - \frac{a^2}{2}\frac{\mathrm{d}^2A_\mathrm{j}}{\mathrm{d}x^2} e^{ik_\mathrm{j}} \right] e^{i\Psi_\mathrm{j}} + \mathrm{c.c.}. \tag{A.27}$$

We do the same with $A_\mathrm{j}(n-1) \approx A_\mathrm{j}(x-a) \approx A_\mathrm{j}(x) - a\frac{\mathrm{d}A_\mathrm{j}}{\mathrm{d}x} + \frac{a^2}{2}\frac{\mathrm{d}^2A_\mathrm{j}}{\mathrm{d}x^2}$. It yields:

$$\phi_n(t) - \phi_{n-1}(t) \approx$$

$$\sum_{\mathrm{j=p,s,i}} \left[2i \sin\left(\frac{k_\mathrm{j}}{2}\right) e^{-ik_\mathrm{j}/2} A_\mathrm{j}(x) + a\frac{\mathrm{d}A_\mathrm{j}}{\mathrm{d}x} e^{-ik_\mathrm{j}} - \frac{a^2}{2}\frac{\mathrm{d}^2A_\mathrm{j}}{\mathrm{d}x^2} e^{-ik_\mathrm{j}} \right] e^{i\Psi_\mathrm{j}} + \mathrm{c.c.}. \tag{A.28}$$

We use from now on the dimensionless coordinate $x \leftarrow x/a$. Assuming slowly varying amplitude, we drop the second derivatives of the wave amplitudes. It follows:

$$2\phi_n(t) - \phi_{n+1}(t) - \phi_{n-1}(t) \approx$$

$$\sum_{\mathrm{j=p,s,i}} \left[4\sin^2\left(\frac{k_\mathrm{j}}{2}\right) A_\mathrm{j} - 2i \sin\left(k_\mathrm{j}\right) \frac{\mathrm{d}A_\mathrm{j}}{\mathrm{d}x} e^{ik_\mathrm{j}} \right] e^{i\Psi_\mathrm{j}} + \mathrm{c.c.}. \tag{A.29}$$

For now, we can write the linear part of Eq. (A.24) as:

$$LC^g \ddot{\phi}_n + 2\phi_n - \phi_{n-1} - \phi_{n+1} + LC\left(2\ddot{\phi}_n - \ddot{\phi}_{n-1} - \ddot{\phi}_{n+1}\right) \approx$$

$$\sum_{\mathrm{j=p,s,i}} \left[-\omega_\mathrm{j}^2 LC^g A_\mathrm{j}(x) + 4\sin^2\left(\frac{k_\mathrm{j}}{2}\right)(1 - \omega_\mathrm{j}^2 LC) A_\mathrm{j}(x) \right.$$

$$\left. + 2i\left(\omega_\mathrm{j}^2 LC - 1\right)\sin\left(k_\mathrm{j}\right)\frac{\mathrm{d}A_\mathrm{j}}{\mathrm{d}x} \right] e^{i\Psi_\mathrm{j}} + \mathrm{c.c.}. \tag{A.30}$$

The two first terms of the right-hand side of Eq. (A.30) cancel each other if we assume that the dimensionless wavevector is small ($k_\mathrm{j} \ll 1$) and the dispersion relation of the array is defined as $k_\mathrm{j} = \omega_\mathrm{j}\sqrt{LC^\mathrm{g}/(1 - \omega_\mathrm{j}^2 LC)}$ (k_j is dimensionless).

The right-hand side of Eq. (A.30) simplifies to:

$$\sum_{\mathrm{j=p,s,i}} 2i\left(\frac{\omega_{\mathrm{j}}^2}{\omega_{\Pi}^2}-1\right)\sin\left(k_{\mathrm{j}}\right)\frac{\mathrm{d}A_{\mathrm{j}}}{\mathrm{d}x}e^{i\Psi_{\mathrm{j}}}+\mathrm{c.c.}, \tag{A.31}$$

where $\omega_{\Pi}=(LC)^{-1/2}$. For the third order nonlinear term, it reads:

$$\left(\phi_n-\phi_{n+1}\right)^3=\left[\sum_{\mathrm{j=p,s,i}}\left[-2i\sin\left(\frac{k_{\mathrm{j}}}{2}\right)e^{ik_{\mathrm{j}}/2}A_{\mathrm{j}}(x)+\frac{\mathrm{d}A_{\mathrm{j}}}{\mathrm{d}x}e^{ik_{\mathrm{j}}}\right]e^{i\Psi_{\mathrm{j}}}+\mathrm{c.c.}\right]^3. \tag{A.32}$$

Assuming again the slowly varying amplitude, but this time to neglect the first derivatives, we can simplify Eq. (A.32) to:

$$\left(\phi_n-\phi_{n+1}\right)^3\approx\left[\sum_{\mathrm{j=p,s,i}}-2i\sin\left(\frac{k_{\mathrm{j}}}{2}\right)e^{ik_{\mathrm{j}}/2}A_{\mathrm{j}}(x)e^{i\Psi_{\mathrm{j}}}+\mathrm{c.c.}\right]^3, \tag{A.33a}$$

$$\left(\phi_n-\phi_{n-1}\right)^3\approx\left[\sum_{\mathrm{j=p,s,i}}2i\sin\left(\frac{k_{\mathrm{j}}}{2}\right)e^{-ik_{\mathrm{j}}/2}A_{\mathrm{j}}(x)e^{i\Psi_{\mathrm{j}}}+\mathrm{c.c.}\right]^3. \tag{A.33b}$$

We must now keep only terms rotating at $e^{-i\omega_{\mathrm{p}}t}, e^{-i\omega_{\mathrm{s}}t}, e^{-i\omega_{\mathrm{i}}t}$ for the pump, the signal and the idler amplitudes, respectively. Assuming the pump is the only strong amplitude, it yields:

$$i\sin\left(k_{\mathrm{p}}\right)\left(1-\frac{\omega_{\mathrm{p}}^2}{\omega_{\Pi}^2}\right)\frac{\mathrm{d}A_{\mathrm{p}}}{\mathrm{d}x}+4\left|A_{\mathrm{p}}\right|^2A_{\mathrm{p}}\sin^4\left(k_{\mathrm{p}}/2\right)=0, \tag{A.34a}$$

$$\begin{aligned}i\sin\left(k_{\mathrm{s}}\right)\left(1-\frac{\omega_{\mathrm{s}}^2}{\omega_{\Pi}^2}\right)\frac{\mathrm{d}A_{\mathrm{s}}}{\mathrm{d}x}+8\left|A_{\mathrm{p}}\right|^2A_{\mathrm{s}}\sin^2\left(k_{\mathrm{p}}/2\right)\sin^2\left(k_{\mathrm{s}}/2\right)\\+4A_{\mathrm{p}}^2A_{\mathrm{i}}^*\sin^2\left(k_{\mathrm{p}}/2\right)\sin\left(k_{\mathrm{i}}/2\right)\sin\left(k_{\mathrm{p}}-k_{\mathrm{i}}/2\right)=0.\end{aligned} \tag{A.34b}$$

While Eq. (A.34a) describes the pump propagation, Eq. (A.34b) describes the signal propagation. To get the idler propagation, the index s and i must be swapped (s↔i). We solve the pump straightforwardly by defining the pump nonlinearity γ_{p}

$$A_{\mathrm{p}}=\left|A_{\mathrm{p}}\right|e^{i\gamma_{\mathrm{pp}}x},\ \gamma_{\mathrm{pp}}=\frac{4|A_{\mathrm{p}}|^2\sin^4\left(k_{\mathrm{p}}/2\right)\omega_{\Pi}^2}{\sin(k_{\mathrm{p}})\left(\omega_{\Pi}^2-\omega_{\mathrm{p}}^2\right)}. \tag{A.35}$$

For the signal and idler equations, it is efficient to rewrite it by defining a set of new variables:

$$\tilde{A}_\mathrm{s} = A_\mathrm{s} e^{-i\gamma_\mathrm{sp} x},\ \gamma_\mathrm{sp} = \frac{8|A_\mathrm{p}|^2 \sin^2(k_\mathrm{p}/2) \sin^2(k_\mathrm{s}/2)\, \omega_\Pi^2}{\sin(k_\mathrm{s})\left(\omega_\Pi^2 - \omega_\mathrm{s}^2\right)}, \tag{A.36a}$$

$$(\mathrm{s} \leftrightarrow \mathrm{i}). \tag{A.36b}$$

By defining the usual linear phase shift as $\Delta k_\mathrm{l} = 2k_\mathrm{p} - k_\mathrm{s} - k_\mathrm{i}$ and the nonlinear one $\Delta k = \Delta k_\mathrm{l} + 2\gamma_\mathrm{pp} - \gamma_\mathrm{sp} - \gamma_\mathrm{ip}$, we have a system of two coupled equations for the signal and idler amplitudes:

$$\frac{\mathrm{d}\tilde{A}_\mathrm{s}}{\mathrm{d}x} = i\gamma_\mathrm{si}\tilde{A}_\mathrm{i}^* e^{i\Delta k x},\quad \gamma_\mathrm{si} = \frac{4|A_\mathrm{p}|^2 \sin^2(k_\mathrm{p}/2) \sin(k_\mathrm{i}/2) \sin(k_\mathrm{p} - k_\mathrm{i}/2)\, \omega_\Pi^2}{\sin k_\mathrm{s}\left(\omega_\Pi^2 - \omega_\mathrm{s}^2\right)}, \tag{A.37a}$$

$$\frac{\mathrm{d}\tilde{A}_\mathrm{i}^*}{\mathrm{d}x} = -i\gamma_\mathrm{is}\tilde{A}_\mathrm{s} e^{-i\Delta k x},\quad \gamma_\mathrm{is} = \frac{4|A_\mathrm{p}|^2 \sin^2(k_\mathrm{p}/2) \sin(k_\mathrm{s}/2) \sin(k_\mathrm{p} - k_\mathrm{s}/2)\, \omega_\Pi^2}{\sin k_\mathrm{i}\left(\omega_\Pi^2 - \omega_\mathrm{i}^2\right)}. \tag{A.37b}$$

There are several ways to solve these coupled equations. Here, we differentiate a second time Eqs. (A.37a) and (A.37b) and cancel the $\tilde{A}_\mathrm{i}^*$ ($\tilde{A}_\mathrm{s}$) terms with Eq. (A.37a) (Eq. (A.37b)). Since we study a bare array, we consider that no dispersion engineering is done to address the phase matching issue. Therefore we assume a large phase mismatch $\Delta k^2/4 > \gamma_\mathrm{si}\gamma_\mathrm{is}^*$. Hence we define a positive gain coefficient $g = \sqrt{\Delta k^2/4 - \gamma_\mathrm{si}\gamma_\mathrm{is}^*}$. After solving the second order differential equation, we obtain the general expression for the signal and idler amplitudes:

$$\tilde{A}_\mathrm{s}(x) = e^{i\Delta k x/2}\left(a_{s1} e^{igx} + a_{s2} e^{-igx}\right), \tag{A.38a}$$

$$\tilde{A}_\mathrm{i}^*(x) = e^{-i\Delta k x/2}\left(a_{i1} e^{igx} + a_{i2} e^{-igx}\right). \tag{A.38b}$$

To determine the different coefficients, we must use the boundary conditions. We already know that $a_{s1} + a_{s2} = \tilde{A}_\mathrm{s}(0)$ and $a_{i1} + a_{i2} = \tilde{A}_\mathrm{i}(0) = 0$. To get two more equations, we differentiate Eqs. (A.38a) and (A.38b) and get the equality with Eqs. (A.37a) and (A.37b) for $x = 0$. It yields $a_{s1} - a_{s2} = -\tilde{A}_\mathrm{s}(0)\Delta k/2g$ and $a_{i1} = -\tilde{A}_\mathrm{s}(0)\gamma_\mathrm{is}/2g$. We eventually find for the amplitudes:

$$\tilde{A}_\mathrm{s}(x) = \tilde{A}_\mathrm{s}(0) e^{i\Delta k x/2}\left(\cos(gx) - \frac{i\Delta k}{2g}\sin(gx)\right), \tag{A.39a}$$

$$\tilde{A}_\mathrm{i}^*(x) = -i\tilde{A}_\mathrm{s}(0) e^{-i\Delta k x/2}\frac{\gamma_\mathrm{is}^*}{g}\sin(gx). \tag{A.39b}$$

A.2.2 Linear dispersion relation

In this subsection, we detail the derivation of the linear dispersion relation Eq. (3.55). We start with the linear coupled equations for the pump amplitudes in Eq. (3.54):

$$\left[\frac{\omega_\mathrm{p}^2}{\omega_\Pi^2\ell_\mathrm{cs}^2}-k_\mathrm{p}^2\left(1-\frac{\omega_\mathrm{p}^2}{\omega_\Pi^2}\right)\right]A+\left[\frac{\zeta}{2}\frac{\omega_\mathrm{p}^2}{\omega_\Pi^2\ell_\mathrm{cs}^2}+\frac{\eta}{2}k_\mathrm{p}(G-k_\mathrm{p})\left(1-\frac{\omega_\mathrm{p}^2}{\omega_\Pi^2}\right)\right]B=0, \tag{A.40a}$$

$$\left[\frac{\zeta}{2}\frac{\omega_\mathrm{p}^2}{\omega_\Pi^2\ell_\mathrm{cs}^2}+\frac{\eta}{2}k_\mathrm{p}(G-k_\mathrm{p})\left(1-\frac{\omega_\mathrm{p}^2}{\omega_\Pi^2}\right)\right]A+\left[\frac{\omega_\mathrm{p}^2}{\omega_\Pi^2\ell_\mathrm{cs}^2}-(G-k_\mathrm{p})^2\left(1-\frac{\omega_\mathrm{p}^2}{\omega_\Pi^2}\right)\right]B=0. \tag{A.40b}$$

Leaving the trivial solution $A=B=0$ apart, we get the solution by solving the determinant of the system:

$$\begin{aligned}\left[\frac{\omega_\mathrm{p}^2}{\omega_\Pi^2\ell_\mathrm{cs}^2}-k_\mathrm{p}^2\left(1-\frac{\omega_\mathrm{p}^2}{\omega_\Pi^2}\right)\right]\left[\frac{\omega_\mathrm{p}^2}{\omega_\Pi^2\ell_\mathrm{cs}^2}-(G-k_\mathrm{p})^2\left(1-\frac{\omega_\mathrm{p}^2}{\omega_\Pi^2}\right)\right]\\ -\left[\frac{\zeta}{2}\frac{\omega_\mathrm{p}^2}{\omega_\Pi^2\ell_\mathrm{cs}^2}+\frac{\eta}{2}k_\mathrm{p}(G-k_\mathrm{p})\left(1-\frac{\omega_\mathrm{p}^2}{\omega_\Pi^2}\right)\right]^2=0.\end{aligned} \tag{A.41}$$

Dividing by $(1-\omega_\mathrm{p}^2/\omega_\Pi^2)/l_\mathrm{cs}^2$ yields:

$$\begin{aligned}\left(-\frac{\omega_\mathrm{p}^2}{\omega_\Pi^2-\omega_\mathrm{p}^2}+k_\mathrm{p}^2l_\mathrm{cs}^2\right)\left(-\frac{\omega_\mathrm{p}^2}{\omega_\Pi^2-\omega_\mathrm{p}^2}+(G-k_\mathrm{p})^2l_\mathrm{cs}^2\right)-\\ \left(\frac{\zeta}{2}\frac{\omega_\mathrm{p}^2}{\omega_\Pi^2-\omega_\mathrm{p}^2}+\frac{\eta}{2}k_\mathrm{p}(G-k_\mathrm{p})l_\mathrm{cs}^2\right)^2=0.\end{aligned} \tag{A.42}$$

From now on we define the variable $\kappa_\omega^2=\omega_\mathrm{p}^2/(\omega_\Pi^2-\omega_\mathrm{p}^2)$. It eventually leads to:

$$\begin{aligned}\kappa_\omega^4-\kappa_\omega^2l_\mathrm{cs}^2\left(2k_\mathrm{p}^2+G^2-2k_\mathrm{p}G\right)+k_\mathrm{p}^2\left(G-k_\mathrm{p}\right)^2l_\mathrm{cs}^4-\\ \left(\frac{\zeta}{2}\kappa_\omega^2+\frac{\eta}{2}\left(Gk_\mathrm{p}-k_\mathrm{p}^2\right)l_\mathrm{cs}^2\right)^2=0.\end{aligned} \tag{A.43}$$

To get through the calculation, we define $\mathcal{K} = k_\mathrm{p} l_\mathrm{cs} - G l_\mathrm{cs}/2$ and $\kappa_\mathrm{g} = G l_\mathrm{cs}/2$. The simplified equation can be written as:

$$\left(\kappa_\omega^4 - 2\kappa_\omega^2\left(\mathcal{K}^2 + \kappa_\mathrm{g}^2\right) + \mathcal{K}^4 - 2\kappa_\mathrm{g}^2\mathcal{K}^2 + \kappa_\mathrm{g}^4\right) - \left(\frac{\zeta}{2}\kappa_\omega^2 + \frac{\eta}{2}\left(\kappa_\mathrm{g}^2 - \mathcal{K}^2\right)\right)^2 = 0. \tag{A.44}$$

We can define $u^2 = \zeta\kappa_\omega^2/2 + \eta\kappa_\mathrm{g}^2/2$. It yields a biquadratic equation in $\mathcal{K}$:

$$(1 - \frac{\eta^2}{4})\mathcal{K}^4 - 2(\kappa_\omega^2 + \kappa_\mathrm{g}^2 - \frac{\eta}{2}u^2)\mathcal{K}^2 + (\kappa_\omega^2 - \kappa_g^2)^2 - u^4 = 0. \tag{A.45}$$

We therefore defined the determinant Δ of Eq. (A.45) as:

$$\Delta = 4D \quad \text{where} \quad D = \left[4\kappa_\omega^2\kappa_\mathrm{g}^2 + u^4 + \frac{\eta^2}{4}\left(\kappa_\omega^2 - \kappa_\mathrm{g}^2\right)^2 - \eta\left(\kappa_\omega^2 + \kappa_\mathrm{g}^2\right)u^2\right]. \tag{A.46}$$

We first solve for $\mathcal{K}^2$ and then naturally get an analytical expression of $\mathcal{K}$ as a function of the angular frequency ω_p:

$$\mathcal{K} = \mathrm{sign}(\kappa_\omega - \kappa_\mathrm{g})\sqrt{\frac{\left(\kappa_\omega^2 - \kappa_\mathrm{g}^2\right)^2 - u^4}{\kappa_\omega^2 + \kappa_\mathrm{g}^2 - \eta u^2/2 + \sqrt{D}}}. \tag{A.47}$$

We eventually find the expression of the linear dispersion relation as shown in Eq. (3.55):

$$k = \frac{\mathrm{sign}\left(\kappa_\omega - \kappa_\mathrm{g}\right)}{\ell_\mathrm{cs}}\sqrt{\frac{\left(\kappa_\omega^2 - \kappa_\mathrm{g}^2\right)^2 - u^4}{\kappa_\omega^2 + \kappa_\mathrm{g}^2 - \eta u^2/2 + \sqrt{D}}} + \frac{G}{2}. \tag{A.48}$$

A.2.3 Carried power

In this subsection, we derive the expression of the power carried by the pump in the SQUID array as shown in Eq. (3.61). We start from the general expression for the power P from the Lagrangian of the system $\mathcal{L}$:

$$P = \frac{\mathrm{d}\,\mathcal{L}}{\mathrm{d}t} = \frac{\hbar^2}{(2e)^2}\sum_{n=1}\left[C_{n+1/2}\left(\dot{\phi}_n - \dot{\phi}_{n+1}\right)\left(\ddot{\phi}_n - \ddot{\phi}_{n+1}\right) + C^\mathrm{g}_{n+1/2}\dot{\phi}_n\ddot{\phi}_n\right]$$

$$+ \frac{\hbar^2}{(2e)^2}\sum_{n=1}\left[\frac{\left(\dot{\phi}_n - \dot{\phi}_{n+1}\right)\sin\left(\phi_n - \phi_{n+1}\right)}{L_{n+1/2}}\right]. \tag{A.49}$$

To simplify it, we use the Euler-Lagrange equation:

$$\begin{aligned} &\forall n \in [1, N_\mathrm{J}]: \qquad \frac{\partial \mathcal{L}}{\partial \phi_n} - \frac{\mathrm{d}}{\mathrm{d}t}\left(\frac{\partial \mathcal{L}}{\partial \dot{\phi}_n}\right) = 0, \\ \leftrightarrow \quad &\forall n \in [1, N_\mathrm{J}]: \qquad C_{n+1/2}\left(\ddot{\phi}_n - \ddot{\phi}_{n+1}\right) + C_{n-1/2}\left(\ddot{\phi}_n - \ddot{\phi}_{n-1}\right) + C_n^\mathrm{g}\ddot{\phi}_n \\ &\qquad\qquad \frac{\sin\left(\phi_n - \phi_{n+1}\right)}{L_{n+1/2}} + \frac{\sin\left(\phi_n - \phi_{n-1}\right)}{L_{n-1/2}} = 0. \end{aligned} \tag{A.50}$$

By multiplying each side of Eq. (A.50) by $\dot{\phi}_n$, we see that we can cancel every terms from Eq. (A.49). It only remains three terms in the sum for $n = 1$:

$$\begin{aligned} P &= \frac{\hbar^2}{(2e)^2}\left[C_{3/2}\left(\ddot{\phi}_1 - \ddot{\phi}_2\right) + C_n^\mathrm{g}\ddot{\phi}_1 + \frac{\sin\left(\phi_n - \phi_{n+1}\right)}{L_{3/2}}\right]\dot{\phi}_1, \\ P &= \frac{\hbar^2}{(2e)^2}\left[C_{1/2}\left(\ddot{\phi}_0 - \ddot{\phi}_1\right) + \frac{\sin\left(\phi_0 - \phi_1\right)}{L_{1/2}}\right]\dot{\phi}_1. \end{aligned} \tag{A.51}$$

We recall that the Josephson inductance and capacitance are modulated with the relation as defined in Eq. (3.52). For $n = 0$, we have $L_{1/2}^{-1} = L_0^{-1}(1 + \eta\cos(G/2))$ and $C_{1/2} = C_0(1 + \eta\cos(G/2))$. Moreover, we recall that $\omega_\Pi^2 = (L_0 C_0)^{-1}$, where η is the small spatial modulation amplitude. Dimensionless G is very small and $\cos(G/2) \approx 1$. The carried power reads:

$$P = \frac{\hbar^2}{(2e)^2 L_0}\left[\omega_\Pi^{-2}\left(\ddot{\phi}_0 - \ddot{\phi}_1\right)(1+\eta) + \sin\left(\phi_0 - \phi_1\right)(1+\eta)\right]\dot{\phi}_1. \tag{A.52}$$

The prefactor is equal to the Josephson energy $E_\mathrm{J} = \hbar^2/(2e)^2 L_0$. We expand the nonlinearity in the Taylor series $\sin(x) = x - x^3/6$:

$$P = E_\mathrm{J}\left[\omega_\Pi^{-2}\left(\ddot{\phi}_0 - \ddot{\phi}_1\right)(1+\eta) + \left(\left(\phi_0 - \phi_1\right) - \frac{\left(\phi_0 - \phi_1\right)^3}{6}\right)(1+\eta)\right]\dot{\phi}_1. \tag{A.53}$$

We consider the temporal depedence of the superconducting phase $\phi_n(t)$ to be $e^{-i\omega_\mathrm{p}t}$. We factorize by $(\phi_0 - \phi_1)$, and drop the very small term $(\phi_0 - \phi_1)^2\eta$. We reach the intermediate form for the carried power:

$$P = E_\mathrm{J}\left[(1+\eta)\left(1 - \frac{\omega_\mathrm{p}^2}{\omega_\Pi^2}\right) - \frac{\left(\phi_0 - \phi_1\right)^2}{6}\right]\dot{\phi}_1\left(\phi_0 - \phi_1\right). \tag{A.54}$$

The full expression of $\phi_n(t)$ is $\phi_n(t) = \left(Ae^{ikn} + Be^{i(k-G)n}\right) e^{-i\omega_p t} + \text{c.c.}$ (see Section 3.5.2 and Eq. (3.53)). We now derive the expression of $\phi_0 - \phi_1$ and $\dot{\phi}_1$:

$$\begin{aligned} \phi_0 - \phi_1 &= \left(A(1-e^{ik}) + B(1-e^{-i(G-k)})\right) e^{-i\omega_p t} + \text{c.c.}, \\ \dot{\phi}_1 &= -i\omega_p (A + Be^{-iG}) e^{ik} e^{-i\omega_p t} + \text{c.c.}. \end{aligned} \tag{A.55}$$

Since k and G are small, we can simplify the expression. It yields:

$$\begin{aligned} P = 2\omega_p E_J \times \\ \left[(1+\eta)\left(1 - \frac{\omega_p^2}{\omega_\Pi^2}\right) - \frac{1}{6}\left[|kA + (k-G)B|^2 - (kA + (k-G)B)^2 e^{-2i\omega_p t} + \text{c.c.}\right]\right] \times \\ \left[(k - \frac{G}{2})|A+B|^2 + \frac{G}{2}\left(|A|^2 - |B|^2\right) - \right. \\ \left. \frac{1}{2}\left[\left(A^2 k + B^2(k-G) + AB(2k-G)\right) e^{-2i\omega_p t} + \text{c.c.}\right]\right]. \end{aligned} \tag{A.56}$$

We drop all fast rotating terms and we eventually find the following expression for the power carried by the pump:

$$\begin{aligned} P = 2\omega_p E_J \left[(1+\eta)\left(1 - \frac{\omega_p^2}{\omega_\Pi^2}\right) - \frac{|kA + (k-G)B|^2}{2}\right] \\ \times \left[(k - \frac{G}{2})|A+B|^2 + \frac{G}{2}\left(|A|^2 - |B|^2\right)\right]. \end{aligned} \tag{A.57}$$

A.2.4 Matrix representation

To get the signal power gain in our Josephson photonic crystal as shown in Figs. 3.14 and 3.16, we need to solve for every site n of the modulated array Eqs. (3.63a) and (3.63b) in order to get the signal and the idler amplitude. We define the $2N+2$ amplitude vector $\mathbf{\Phi}$ as:

$$\mathbf{\Phi}^t = \frac{1}{A_{\text{in}}^s}(\phi_0^s, \phi_1^s, ..., \phi_{N+1}^s, \bar{\phi}_0^i, \bar{\phi}_1^i, ..., \bar{\phi}_{N+1}^i), \tag{A.58}$$

where A_{in}^s is the input signal amplitude and N is the junction/SQUID number. ϕ_n^s (ϕ_n^i) is the signal (idler) amplitude at site n. We use the notation $\bar{\phi}_n^i \equiv (\phi_n^i)^*$. We want to numerically solve the system $\hat{A}_\Phi \mathbf{\Phi} = \mathbf{b}$, where $\hat{A}_\Phi$ is a $2(N+1) \times$

$2(N+1)$ matrix encoding Eqs. (3.63a) and (3.63b) for the $N+1$ sites (signal and idler). The vector $\mathbf{b}$ of dimension $2(N+1)$ accounts for the initial conditions and describes where the signal is initially sent from. It is defined as:

$$\mathbf{b}^{\mathrm{t}} = (2i\bar{\omega}_{\mathrm{s}}/l_{\mathrm{cs}}, 0, 0, ..., 0), \tag{A.59a}$$

$$\mathbf{b}^{\mathrm{t}} = (0, 0, ..., 0, 2i\bar{\omega}_{\mathrm{s}}/l_{\mathrm{cs}}, 0, ..., 0). \tag{A.59b}$$

Eq. (A.59a) accounts for a forward amplification (pump and signal sent from site 0) whereas Eq. (A.59b) corresponds to the backward amplification (pump is sent from site 0 while signal is sent from site N). $\bar{\omega}_{\mathrm{s}} = \omega_{\mathrm{s}}/\omega_{\Pi}$ is the reduced signal frequency. To build the $\hat{A}_{\Phi}$ matrix, we need first to define five vectors. We denote them as $\mathbf{D}_0$, $\mathbf{D}_1$, $\mathbf{D}_N$, $\mathbf{D}_{N+1}$, and $\mathbf{D}_{N+2}$ of dimension $2(N+1)$, $2N+1$, $N+2$, $N+1$ and N, respectively. Before, we introduce compact notations:

$$\mathcal{C}_n^{\mathrm{s,i}} = [1+\zeta\cos(Gn)]\,\frac{\bar{\omega}_{\mathrm{s,i}}}{l_{\mathrm{cs}}} \quad , \quad \mathcal{V}_{n+1/2} = \left[1+\eta\cos\left(G\left(n+\frac{1}{2}\right)\right)\right](\partial\phi^{\mathrm{P}}_{n+1/2})^2,$$

$$\mathcal{G}^{\mathrm{s,i}}_{n+1/2} = \left[1+\eta\cos\left(G\left(n+\frac{1}{2}\right)\right)\right](1-\bar{\omega}^2_{\mathrm{s,i}} - |\partial\phi^{\mathrm{P}}_{n+1/2}|^2) \quad , \quad \mathcal{Z}^{\mathrm{s,i}} = j\frac{\bar{\omega}_{\mathrm{s,i}}}{l_{\mathrm{cs}}}\frac{Z_{\mathrm{c}}}{Z_{\mathrm{TL}}}.$$

We can now define the vectors as:

$$\mathbf{D}_0 = (\underbrace{\mathcal{C}^{\mathrm{s}}_0 + \mathcal{Z}^{\mathrm{s}} - \mathcal{G}^{\mathrm{s}}_{1/2} \quad , \quad \mathcal{C}^{\mathrm{s}}_1 - \mathcal{G}^{\mathrm{s}}_{1/2} - \mathcal{G}^{\mathrm{s}}_{3/2} \quad , \quad \cdots \quad , \quad \mathcal{C}^{\mathrm{s}}_N - \mathcal{G}^{\mathrm{s}}_{N-1/2} + \mathcal{Z}^{\mathrm{s}}}_{N+1},$$

$$\underbrace{\mathcal{C}^{\mathrm{i}}_0 - \mathcal{Z}^{\mathrm{i}} - \mathcal{G}^{\mathrm{i}}_{1/2} \quad , \quad \mathcal{C}^{\mathrm{i}}_1 - \mathcal{G}^{\mathrm{i}}_{1/2} - \mathcal{G}^{\mathrm{i}}_{3/2} \quad , \quad \cdots \quad , \quad \mathcal{C}^{\mathrm{i}}_N - \mathcal{G}^{\mathrm{i}}_{N-1/2} - \mathcal{Z}^{\mathrm{i}}}_{N+1}), \tag{A.60a}$$

$$\mathbf{D}_1 = (\underbrace{\mathcal{G}^{\mathrm{s}}_{1/2}\ ,\ \mathcal{G}^{\mathrm{s}}_{3/2}\ ,\ \cdots\ ,\ \mathcal{G}^{\mathrm{s}}_{N-1/2}}_{N},\ 0\ ,\ \underbrace{\mathcal{G}^{\mathrm{i}}_{1/2}\ ,\ \mathcal{G}^{\mathrm{i}}_{3/2}\ ,\ \cdots\ ,\ \mathcal{G}^{\mathrm{i}}_{N-1/2}}_{N}), \tag{A.60b}$$

$$\mathbf{D}_N = (0\ ,\ \underbrace{\mathcal{V}_{1/2}\ ,\mathcal{V}_{3/2},\ ,\ \cdots\ ,\ \mathcal{V}_{N-1/2}}_{N}\ ,\ 0), \tag{A.60c}$$

$$\mathbf{D}_{N+1} = -(\underbrace{\mathcal{V}_{1/2}\ ,\ \mathcal{V}_{1/2}+\mathcal{V}_{3/2}\ ,\ \mathcal{V}_{3/2}+\mathcal{V}_{5/2}\ ,\ \cdots\ ,\ \mathcal{V}_{N-3/2}+\mathcal{V}_{N-1/2}\ ,\ \mathcal{V}_{N-1/2}}_{N+1}), \tag{A.60d}$$

$$\mathbf{D}_{N+2} = (\underbrace{\mathcal{V}_{1/2}\ ,\ \mathcal{V}_{3/2}\ ,\ \mathcal{V}_{5/2}\ ,\ \cdots\ ,\ \mathcal{V}_{N-3/2}\ ,\ \mathcal{V}_{N-1/2}}_{N}). \tag{A.60e}$$

We build the matrix from these vectors. The notation $\mathbf{D}_0[n]$ means the n^{th} element of vector $\mathbf{D}_0$. First entry of a vector is taken at 0. Once the matrix is built, we can solve the linear system $\hat{A}_{\Phi}\Phi = \mathbf{b}$ with a numerical solver. We have chosen the solver **spsolve** from the **scipy.sparse.linalg** python library. Solutions found are for instance plotted in Fig. 3.14. The $\hat{A}_{\Phi}$ matrix reads:

$$
\begin{pmatrix}
D_0[0] & D_1[0] & 0 & 0 & \cdots & 0 & D_N[0] & D_{N+1}[0] & D_{N+2}[0] & 0 & \cdots & 0 & 0 & 0 \\
D_1[0] & D_0[1] & D_1[1] & 0 & \cdots & 0 & 0 & D_N[1] & D_{N+1}[1] & D_{N+2}[1] & \cdots & 0 & 0 & 0 \\
0 & D_1[1] & D_0[2] & D_1[2] & \cdots & 0 & 0 & 0 & D_N[2] & D_{N+1}[2] & \cdots & 0 & 0 & 0 \\
\cdots & \cdots & \cdots & \cdots & \cdots & \cdots & \cdots & \cdots & \cdots & \cdots & \cdots & \cdots & \cdots & \cdots \\
\cdots & \cdots & \cdots & \cdots & \cdots & \cdots & \cdots & \cdots & \cdots & \cdots & \cdots & \cdots & \cdots & \cdots \\
\cdots & \cdots & \cdots & \cdots & \cdots & \cdots & \cdots & \cdots & \cdots & \cdots & \cdots & \cdots & \cdots & \cdots \\
D_N^*[0] & 0 & 0 & 0 & \cdots & D_1[N-1] & D_0[N] & D_1[N] & 0 & 0 & \cdots & D_N[N\text{-}1] & D_{N+1}[N\text{-}1] & D_{N+2}[N\text{-}1] \\
D_{N+1}^*[0] & D_N^*[1] & 0 & 0 & \cdots & 0 & D_1[N] & D_0[N+1] & D_1[N+1] & 0 & \cdots & 0 & D_N[N] & D_{N+1}[N] \\
D_{N+2}^*[0] & D_{N+1}^*[1] & D_N^*[2] & 0 & \cdots & 0 & 0 & D_1[N+1] & D_0[N+2] & D_1[N+2] & \cdots & 0 & 0 & D_N[N+1] \\
\cdots & \cdots & \cdots & \cdots & \cdots & \cdots & \cdots & \cdots & \cdots & \cdots & \cdots & \cdots & \cdots & \cdots \\
\cdots & \cdots & \cdots & \cdots & \cdots & \cdots & \cdots & \cdots & \cdots & \cdots & \cdots & \cdots & \cdots & \cdots \\
\cdots & \cdots & \cdots & \cdots & \cdots & \cdots & \cdots & \cdots & \cdots & \cdots & \cdots & \cdots & \cdots & \cdots \\
0 & 0 & 0 & 0 & \cdots & D_N^*[N*1] & 0 & 0 & 0 & 0 & \cdots & D_0[2N\text{-}1] & D_1[2N\text{-}1] & 0 \\
0 & 0 & 0 & 0 & \cdots & D_{N+1}^*[N\text{-}1] & D_N^*[N] & 0 & 0 & 0 & \cdots & D_1[2N\text{-}1] & D_0[2N] & D_1[2N] \\
0 & 0 & 0 & 0 & \cdots & D_{N+2}^*[N\text{-}1] & D_{N+1}^*[N] & D_N^*[N+1] & 0 & 0 & \cdots & 0 & D_1[2N] & D_0[2N+1]
\end{pmatrix}
$$

blue elements describes the signal amplitude
red elements describes the idler amplitude
green elements carry information about boundary conditions.

Link back to ToC →

Experimental setup

B

In this appendix, we succinctly present the experimental microwave setup for the large dilution refrigerator in the qubit readout experiment. It is shown in Fig. B.1. There are three RF sources SMB 100A. The first one sending a frequency f_1 (on the left hand of the figure) is meant for qubit excitation (and modulated with f_{if}, IF stands for intermediate frequency). The second one, on the right-hand side of the arbitrary waveform generator (AWG) Tabor, is used for readout and sends a signal of frequency f_2. It is split in two: the first one is modulated with the AWG DC tone and is heading to the qubit. The second one is used for down-converting the pulsed signal which went through the qubit cavity. The latter is down-converted with an IQ-mixer in two DC signals for each signal's quadrature and thereafter amplified by room temperature amplifiers. The third RF source is used as a pump for the Josephson parametric amplifier (JPA). The pump frequency is denoted f_3.

It is a standard microwave circuit for qubit readout based on homodyne detection. Here, homodyne means that f_2 and the frequency of the signal going to the qubit cavity are equal, or equivalently that signals acquired by the digitizer are DC (or zero-frequency). The vector network analyzer (ZNB 20) is used to monitor the JPA for an optimal pump biasing. This standard setup can be upgraded by sending a second pump tone towards the fourth directional coupler port in order to cancel the main pump tone, as explained in Section 7.4.1. To do so, the signal of frequency f_3 is split and sent to the two directional coupler ports.

Link back to Table of contents →

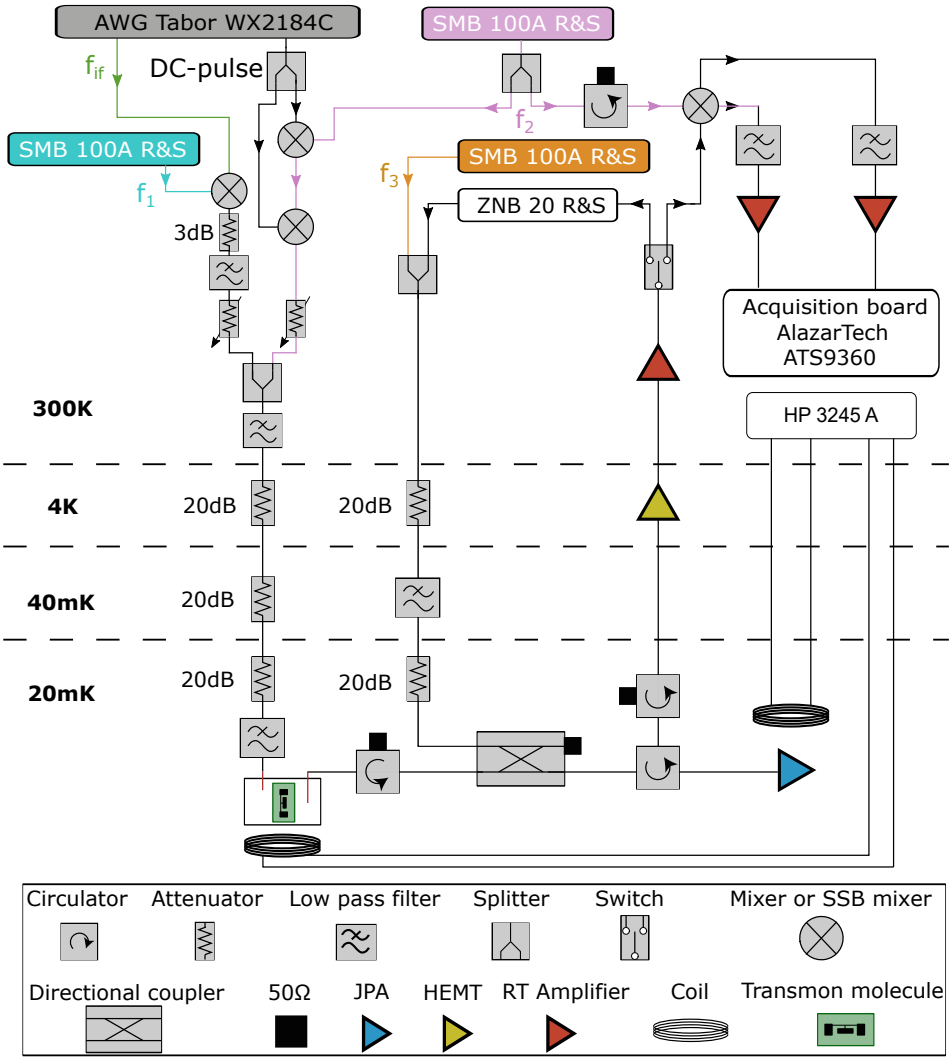

Figure B.1 – **Experimental setup in the large dilution refrigerator.**

Bibliography

[1] F. Arute, K. Arya, R. Babbush, D. Bacon, J. C. Bardin, R. Barends, R. Biswas, S. Boixo, F. G. Brandao, D. A. Buell, et al., Nature **574**, 505 (2019), URL https://doi.org/10.1038/s41586-019-1666-5.
(Cited on page 1.)

[2] J. Preskill, arXiv preprint (2012), URL https://arxiv.org/abs/1203.5813.
(Cited on page 1.)

[3] M. H. Devoret, J. M. Martinis, and J. Clarke, Phys. Rev. Lett. **55**, 1908 (1985), URL https://link.aps.org/doi/10.1103/PhysRevLett.55.1908.
(Cited on page 1.)

[4] Y. Nakamura, C. D. Chen, and J. S. Tsai, Phys. Rev. Lett. **79**, 2328 (1997), URL https://link.aps.org/doi/10.1103/PhysRevLett.79.2328.
(Cited on page 1.)

[5] C. M. Caves, Phys. Rev. D **26**, 1817 (1982), URL https://link.aps.org/doi/10.1103/PhysRevD.26.1817.
(Cited on pages 1 and 5.)

[6] H. Heffner, Proceedings of the IRE **50**, 1604 (1962), URL https://ieeexplore.ieee.org/document/4066904.
(Cited on page 1.)

[7] H. A. Haus and J. A. Mullen, Phys. Rev. **128**, 2407 (1962), URL https://link.aps.org/doi/10.1103/PhysRev.128.2407.
(Cited on page 1.)

[8] K. S. Thorne, Rev. Mod. Phys. **52**, 285 (1980), URL https://link.aps.org/doi/10.1103/RevModPhys.52.285.
(Cited on page 1.)

[9] M. Tse, H. Yu, N. Kijbunchoo, A. Fernandez-Galiana, P. Dupej, L. Barsotti, C. D. Blair, D. D. Brown, S. E. Dwyer, A. Effler, et al., Phys. Rev. Lett. **123**, 231107 (2019), URL https://link.aps.org/doi/10.1103/PhysRevLett.

123.231107.
(Cited on page 1.)

[10] J. Clarke, IEEE Transactions on Electron Devices **27**, 1896 (1980), URL https://ieeexplore.ieee.org/abstract/document/1480920.
(Cited on page 1.)

[11] N. Calander, T. Claeson, and S. Rudner, Journal of Applied Physics **53**, 5093 (1982), URL https://doi.org/10.1063/1.331342.
(Cited on page 1.)

[12] A. Smith, R. Sandell, J. Burch, and A. Silver, IEEE Transactions on Magnetics **21**, 1022 (1985), URL https://ieeexplore.ieee.org/document/1063665.
(Cited on page 1.)

[13] H. K. Olsson and T. Claeson, Journal of Applied Physics **64**, 5234 (1988), URL https://doi.org/10.1063/1.342409.
(Cited on page 2.)

[14] B. Yurke, L. R. Corruccini, P. G. Kaminsky, L. W. Rupp, A. D. Smith, A. H. Silver, R. W. Simon, and E. A. Whittaker, Phys. Rev. A **39**, 2519 (1989), URL https://link.aps.org/doi/10.1103/PhysRevA.39.2519.
(Cited on page 2.)

[15] B. Yurke, P. G. Kaminsky, R. E. Miller, E. A. Whittaker, A. D. Smith, A. H. Silver, and R. W. Simon, Phys. Rev. Lett. **60**, 764 (1988), URL https://link.aps.org/doi/10.1103/PhysRevLett.60.764.
(Cited on page 2.)

[16] R. Movshovich, B. Yurke, P. G. Kaminsky, A. D. Smith, A. H. Silver, R. W. Simon, and M. V. Schneider, Phys. Rev. Lett. **65**, 1419 (1990), URL https://link.aps.org/doi/10.1103/PhysRevLett.65.1419.
(Cited on page 2.)

[17] M. Sweeny and R. Mahler, IEEE Transactions on Magnetics **21**, 654 (1985), URL http://ieeexplore.ieee.org/document/1063777/.
(Cited on page 2.)

[18] A. L. Cullen, Nature **181**, 332 (1958), URL http://www.nature.com/articles/181332a0.
(Cited on page 2.)

[19] B. Yurke, M. L. Roukes, R. Movshovich, and A. N. Pargellis, Applied Physics Letters **69**, 3078 (1996), URL https://doi.org/10.1063/1.116845.
(Cited on pages 2 and 4.)

[20] J. D. Teufel, T. Donner, D. Li, J. W. Harlow, M. S. Allman, K. Cicak, A. J. Sirois, J. D. Whittaker, K. W. Lehnert, and R. W. Simmonds, Nature **475**, 359 (2011), URL https://doi.org/10.1038/nature10261.
(Cited on page 2.)

[21] J. Stehlik, Y. Y. Liu, C. M. Quintana, C. Eichler, T. R. Hartke, and J. R. Petta, Physical Review Applied **4**, 014018 (2015), URL https://link.aps.org/doi/10.1103/PhysRevApplied.4.014018.
(Cited on page 2.)

[22] A. Bienfait, J. J. Pla, Y. Kubo, M. Stern, X. Zhou, C. C. Lo, C. D. Weis, T. Schenkel, M. L. W. Thewalt, D. Vion, et al., Nature nanotechnology **11**, 253 (2015), URL http://dx.doi.org/10.1038/nnano.2015.282.
(Cited on page 2.)

[23] N. Du et al ADMX Collaboration, Physical Review Letters **120**, 151301 (2018), URL https://doi.org/10.1103/PhysRevLett.120.151301.
(Cited on page 2.)

[24] M. H. Devoret and R. J. Schoelkopf, Science **339**, 1169 (2013), ISSN 0036-8075, URL https://science.sciencemag.org/content/339/6124/1169.
(Cited on page 2.)

[25] D. Vion, A. Aassime, A. Cottet, P. Joyez, H. Pothier, C. Urbina, D. Esteve, and M. H. Devoret, Science **296**, 886 (2002), URL https://doi.org/10.1126/science.1069372.
(Cited on page 2.)

[26] A. Blais, R.-S. Huang, A. Wallraff, S. M. Girvin, and R. J. Schoelkopf, Phys. Rev. A **69**, 062320 (2004), URL https://link.aps.org/doi/10.1103/PhysRevA.69.062320.
(Cited on page 2.)

[27] A. Wallraff, D. I. Schuster, A. Blais, L. Frunzio, R. S. Huang, J. Majer, S. Kumar, S. M. Girvin, and R. J. Schoelkopf, Nature **431**, 162 (2004), URL https://doi.org/10.1038/nature02851.
(Cited on page 2.)

[28] J. Koch, T. M. Yu, J. Gambetta, A. A. Houck, D. I. Schuster, J. Majer, A. Blais, M. H. Devoret, S. M. Girvin, and R. J. Schoelkopf, Physical Review A **76**, 042319 (2007), URL https://link.aps.org/doi/10.1103/PhysRevA.76.042319.
(Cited on pages 2, 41, and 160.)

[29] I. Siddiqi, R. Vijay, F. Pierre, C. M. Wilson, M. Metcalfe, C. Rigetti, L. Frunzio, and M. H. Devoret, Phys. Rev. Lett. **93**, 207002 (2004), URL https://link.aps.org/doi/10.1103/PhysRevLett.93.207002.
(Cited on pages 2 and 35.)

[30] V. E. Manucharyan, E. Boaknin, M. Metcalfe, R. Vijay, I. Siddiqi, and M. Devoret, Phys. Rev. B **76**, 014524 (2007), URL https://link.aps.org/doi/10.1103/PhysRevB.76.014524.
(Cited on pages 2, 35, and 53.)

[31] F. Mallet, F. R. Ong, A. Palacios-Laloy, F. Nguyen, P. Bertet, D. Vion, and D. Esteve, Nature Physics **5**, 791 (2009), URL https://doi.org/10.1038/nphys1400.
(Cited on page 2.)

[32] M. A. Castellanos-Beltran and K. W. Lehnert, Applied Physics Letters **91**, 083509 (2007), URL https://doi.org/10.1063/1.2773988.
(Cited on pages 2 and 42.)

[33] M. A. Castellanos-Beltran, K. D. Irwin, G. C. Hilton, L. R. Vale, and K. W. Lehnert, Nature Physics **4**, 928 (2008), URL https://doi.org/10.1038/nphys1090.
(Cited on pages 2, 42, and 125.)

[34] J. Y. Mutus, T. C. White, R. Barends, Y. Chen, Z. Chen, B. Chiaro, A. Dunsworth, E. Jeffrey, J. Kelly, A. Megrant, et al., Applied Physics Letters **104**, 263513 (2014), URL https://doi.org/10.1063/1.4886408.
(Cited on pages 2, 153, and 156.)

[35] T. Roy, S. Kundu, M. Chand, A. Vadiraj, A. Ranadive, N. Nehra, M. P. Patankar, J. Aumentado, A. Clerk, and R. Vijay, Applied Physics Letters **107**, 262601 (2015), URL https://doi.org/10.1063/1.4939148.
(Cited on pages 2, 125, 153, and 156.)

[36] X. Zhou, V. Schmitt, P. Bertet, D. Vion, W. Wustmann, V. Shumeiko, and D. Esteve, Phys Rev B **89**, 214517 (2014), URL https://link.aps.org/doi/10.1103/PhysRevB.89.214517.
(Cited on pages 2 and 24.)

[37] G. Liu, T. C. Chien, X. Cao, O. Lanes, E. Alpern, D. Pekker, and M. Hatridge, Applied Physics Letters **111**, 202603 (2017), URL https://doi.org/10.1063/1.5003032.
(Cited on page 2.)

[38] T. Yamamoto, K. Inomata, M. Watanabe, K. Matsuba, T. Miyazaki, W. D. Oliver, Y. Nakamura, and J. S. Tsai, Applied Physics Letters **93**, 042510 (2008), URL https://doi.org/10.1063/1.2964182.
(Cited on page 2.)

[39] N. Bergeal, F. Schackert, M. Metcalfe, R. Vijay, V. Manucharyan, L. Frunzio, D. Prober, R. Schoelkopf, S. Girvin, and M. Devoret, Nature **465**, 64 (2010), URL https://doi.org/10.1038/nature09035.
(Cited on pages 2 and 25.)

[40] N. Roch, E. Flurin, F. Nguyen, P. Morfin, P. Campagne-Ibarcq, M. H. Devoret, and B. Huard, Phys. Rev. Lett. **108**, 147701 (2012), URL https://link.aps.org/doi/10.1103/PhysRevLett.108.147701.
(Cited on pages 2, 25, and 156.)

[41] C. Eichler, Y. Salathe, J. Mlynek, S. Schmidt, and A. Wallraff, Phys. Rev. Lett. **113**, 110502 (2014), URL https://link.aps.org/doi/10.1103/PhysRevLett.113.110502.
(Cited on pages 2 and 29.)

[42] N. Frattini, V. Sivak, A. Lingenfelter, S. Shankar, and M. Devoret, Physical Review Applied **10**, 054020 (2018), URL https://link.aps.org/doi/10.1103/PhysRevApplied.10.054020.
(Cited on page 2.)

[43] B. Abdo, F. Schackert, M. Hatridge, C. Rigetti, and M. Devoret, Applied Physics Letters **99**, 162506 (2011), URL https://doi.org/10.1063/1.3653473.
(Cited on page 2.)

[44] F. Lecocq, L. Ranzani, G. A. Peterson, K. Cicak, R. W. Simmonds, J. D. Teufel, and J. Aumentado, Phys. Rev. Applied **7**, 024028 (2017), URL https://link.aps.org/doi/10.1103/PhysRevApplied.7.024028.
(Cited on page 2.)

[45] B. H. Eom, P. K. Day, H. G. Leduc, and J. Zmuidzinas, Nature Physics **8**, 623 (2012), URL https://doi.org/10.1038/nphys2356.
(Cited on pages 2, 53, and 66.)

[46] T. C. White, J. Y. Mutus, I. Hoi, R. Barends, B. Campbell, Y. Chen, Z. Chen, B. Chiaro, A. Dunsworth, E. Jeffrey, et al., Applied Physics Letters **106**, 242601 (2015), URL https://doi.org/10.1063/1.4922348.
(Cited on pages 2, 53, and 66.)

[47] C. Macklin, K. O'Brien, D. Hover, M. E. Schwartz, V. Bolkhovsky, X. Zhang, W. D. Oliver, and I. Siddiqi, Science **350**, 307 (2015), URL https://doi.org/10.1126/science.aaa8525.
(Cited on pages 2, 53, 66, 74, 144, 177, 179, 182, and 185.)

[48] A. B. Zorin, M. Khabipov, J. Dietel, and R. Dolata, 2017 16th International Superconductive Electronics Conference (ISEC) pp. 1–3 (2017), URL https://ieeexplore.ieee.org/abstract/document/8314196.
(Cited on pages 2, 33, and 66.)

[49] A. Miano and O. A. Mukhanov, IEEE Transactions on Applied Superconductivity **29**, 1 (2019), URL https://ieeexplore.ieee.org/document/8666769.
(Cited on page 2.)

[50] A. Gilmour, *Klystrons, traveling wave tubes, magnetrons, crossed-field amplifiers, and gyrotrons* (Artech House, 2011).
(Cited on page 3.)

[51] J. Copeland and A. A. Haeff, IEEE Spectrum **52**, 38 (2015), ISSN 1939-9340, URL https://ieeexplore.ieee.org/document/7226611.
(Cited on page 3.)

[52] T. Mimura, K. Joshin, S. Hiyamizu, K. Hikosaka, and M. Abe, Japanese Journal of Applied Physics **20**, L598 (1981), URL https://doi.org/10.1143/2Fjjap.20.l598.
(Cited on page 3.)

[53] A. A. Clerk, M. H. Devoret, S. M. Girvin, F. Marquardt, and R. J. Schoelkopf, Rev. Mod. Phys. **82**, 1155 (2010), URL https://link.aps.org/doi/10.1103/RevModPhys.82.1155.
(Cited on pages 5 and 7.)

[54] J. Claudon, Ph.D. thesis, Université Grenoble Alpes (2005), URL http://www.theses.fr/2005GRE10116.
(Cited on pages 9 and 132.)

[55] G. Agrawal, *Nonlinear fiber optics; 5th ed.*, Optics and Photonics (Elsevier, Burlington, MA, 2012).
(Cited on pages 11, 33, 34, 53, and 55.)

[56] L. Planat, R. Dassonneville, J. P. Martínez, F. Foroughi, O. Buisson, W. Hasch-Guichard, C. Naud, R. Vijay, K. Murch, and N. Roch, Phys. Rev. Applied **11**, 034014 (2019), URL https://link.aps.org/doi/10.1103/PhysRevApplied.11.034014.
(Cited on page 12.)

[57] L. Planat, E. Al-Tavil, J. P. Martínez, R. Dassonneville, F. Foroughi, S. Léger, K. Bharadwaj, J. Delaforce, V. Milchakov, C. Naud, et al., Phys. Rev. Applied **12**, 064017 (2019), URL https://link.aps.org/doi/10.1103/PhysRevApplied.12.064017.
(Cited on page 12.)

[58] L. Planat, A. Ranadive, R. Dassonneville, J. Puertas Martínez, S. Léger, C. Naud, O. Buisson, W. Hasch-Guichard, D. M. Basko, and N. Roch, Phys. Rev. X **10**, 021021 (2020), URL https://link.aps.org/doi/10.1103/PhysRevX.10.021021.
(Cited on page 12.)

[59] D. C. Burnham and D. L. Weinberg, Phys. Rev. Lett. **25**, 84 (1970), URL https://link.aps.org/doi/10.1103/PhysRevLett.25.84.
(Cited on page 18.)

[60] E. Flurin, Theses, Ecole normale supérieure - ENS PARIS (2014), URL https://tel.archives-ouvertes.fr/tel-01241123.
(Cited on pages 19 and 25.)

[61] D. Walls and G. J. Milburn, *Quantum Optics* (Springer-Verlag Berlin Heidelberg, 2008).
(Cited on page 19.)

[62] A. Roy and M. Devoret, Comptes Rendus Physique **17**, 740 (2016), ISSN 1631-0705, quantum microwaves / Micro-ondes quantiques, URL http://www.sciencedirect.com/science/article/pii/S1631070516300640.
(Cited on page 20.)

[63] S. Boutin, D. M. Toyli, A. V. Venkatramani, A. W. Eddins, I. Siddiqi, and A. Blais, Physical Review Applied **8**, 054030 (2017), URL https://link.aps.org/doi/10.1103/PhysRevApplied.8.054030.
(Cited on pages 21, 26, 27, and 161.)

[64] Q. Ficheux, Theses, École normale supérieure - ENS PARIS (2018), URL https://tel.archives-ouvertes.fr/tel-02098804.
(Cited on pages 21 and 161.)

[65] G. Liu, T.-C. Chien, X. Cao, O. Lanes, E. Alpern, D. Pekker, and M. Hatridge, Applied Physics Letters **111**, 202603 (2017), https://doi.org/10.1063/1.5003032, URL https://doi.org/10.1063/1.5003032.
(Cited on pages 25 and 180.)

[66] N. E. Frattini, U. Vool, S. Shankar, A. Narla, K. M. Sliwa, and M. H. Devoret, Applied Physics Letters **110**, 222603 (2017), URL https://doi.org/10.1063/1.4984142.
(Cited on pages 25 and 33.)

[67] J. Bourassa, F. Beaudoin, J. M. Gambetta, and A. Blais, Physical Review A **86**, 013814 (2012), URL https://link.aps.org/doi/10.1103/PhysRevA.86.013814.
(Cited on pages 26 and 27.)

[68] P. Winkel, I. Takmakov, D. Rieger, L. Planat, W. Hasch-Guichard, L. Grünhaupt, N. Maleeva, F. Foroughi, F. Henriques, K. Borisov, et al., Phys. Rev. Applied **13**, 024015 (2020), URL https://link.aps.org/doi/10.1103/PhysRevApplied.13.024015.
(Cited on pages 29, 96, and 132.)

[69] J. Heinsoo, C. K. Andersen, A. Remm, S. Krinner, T. Walter, Y. Salathé, S. Gasparinetti, J.-C. Besse, A. Potočnik, A. Wallraff, et al., Phys. Rev. Applied **10**, 034040 (2018), URL https://link.aps.org/doi/10.1103/PhysRevApplied.10.034040.
(Cited on page 33.)

[70] S. Kundu, N. Gheeraert, S. Hazra, T. Roy, K. V. Salunkhe, M. P. Patankar, and R. Vijay, Applied Physics Letters **114**, 172601 (2019), URL https://doi.org/10.1063/1.5089729.
(Cited on page 33.)

[71] A. B. Zorin, Phys. Rev. Applied **6**, 034006 (2016), URL https://link.aps.org/doi/10.1103/PhysRevApplied.6.034006.
(Cited on pages 33 and 66.)

[72] C. Eichler and A. Wallraff, EPJ Quantum Technology **1**, 2 (2014), URL https://doi.org/10.1140/epjqt2.
(Cited on pages 37, 42, and 156.)

[73] W. Wustmann and V. Shumeiko, Phys. Rev. B **87**, 184501 (2013), URL https://link.aps.org/doi/10.1103/PhysRevB.87.184501.
(Cited on page 41.)

[74] D. M. Pozar, *Microwave engineering* (John Wiley & Sons, 2009).
(Cited on pages 43, 44, 47, 71, 102, 103, 107, 139, and 142.)

[75] T. Weißl, B. Küng, E. Dumur, A. K. Feofanov, I. Matei, C. Naud, O. Buisson, F. W. J. Hekking, and W. Guichard, Phys. Rev. B **92**, 104508 (2015), URL https://link.aps.org/doi/10.1103/PhysRevB.92.104508.
(Cited on pages 44 and 132.)

[76] T. Weißl, Ph.D. thesis, Université Grenoble Alpes (2014), URL http://www.theses.fr/2014GRENY038.
(Cited on pages 45, 48, 63, and 138.)

[77] Y. Krupko, V. D. Nguyen, T. Weißl, E. Dumur, J. Puertas, R. Dassonneville, C. Naud, F. W. J. Hekking, D. M. Basko, O. Buisson, et al., Phys Rev B **98**, 094516 (2018), URL https://link.aps.org/doi/10.1103/PhysRevB.98.094516.
(Cited on pages 47 and 131.)

[78] V. D. Nguyen, Theses, Université Grenoble Alpes (2018), URL https://tel.archives-ouvertes.fr/tel-02052403.
(Cited on page 47.)

[79] A. Metelmann and A. A. Clerk, Phys. Rev. Lett. **112**, 133904 (2014), URL https://link.aps.org/doi/10.1103/PhysRevLett.112.133904.
(Cited on page 53.)

[80] O. Yaakobi, L. Friedland, C. Macklin, and I. Siddiqi, Phys. Rev. B **87**, 144301 (2013), URL https://link.aps.org/doi/10.1103/PhysRevB.87.144301.
(Cited on page 59.)

[81] K. O'Brien, C. Macklin, I. Siddiqi, and X. Zhang, Phys. Rev. Lett. **113**, 157001 (2014), URL https://link.aps.org/doi/10.1103/PhysRevLett.113.157001.
(Cited on pages 61, 66, 74, and 85.)

[82] J. A. Armstrong, N. Bloembergen, J. Ducuing, and P. S. Pershan, Phys. Rev. **127**, 1918 (1962), URL https://link.aps.org/doi/10.1103/PhysRev.127.1918.
(Cited on page 63.)

[83] A. Fay, Ph.D. thesis, Université Joseph-Fourier - Grenoble I (2008), URL https://www.theses.fr/2008GRE10071.
(Cited on page 65.)

[84] C. Bockstiegel, J. Gao, M. R. Vissers, M. Sandberg, S. Chaudhuri, A. Sanders, L. R. Vale, K. D. Irwin, and D. P. Pappas, Journal of Low Temperature Physics **176**, 476 (2014), URL https://doi.org/10.1007/s10909-013-1042-z.
(Cited on page 66.)

[85] M. R. Vissers, R. P. Erickson, H. S. Ku, L. Vale, X. Wu, G. C. Hilton, and D. P. Pappas, Applied Physics Letters **108**, 012601 (2016), URL https://doi.org/10.1063/1.4937922.
(Cited on page 66.)

[86] L. Ranzani, M. Bal, K. C. Fong, G. Ribeill, X. Wu, J. Long, H. S. Ku, R. P. Erickson, D. Pappas, and T. A. Ohki, Applied Physics Letters **113**, 242602 (2018), URL http://aip.scitation.org/doi/10.1063/1.5063252.
(Cited on page 66.)

[87] M. T. Bell and A. Samolov, Phys. Rev. Applied **4**, 024014 (2015), URL https://link.aps.org/doi/10.1103/PhysRevApplied.4.024014.
(Cited on page 66.)

[88] W. Zhang, W. Huang, M. E. Gershenson, and M. T. Bell, Phys. Rev. Applied **8**, 051001 (2017), URL https://link.aps.org/doi/10.1103/PhysRevApplied.8.051001.
(Cited on page 66.)

[89] N. Ashcroft and N. Mermin, *Solid State Physics* (Saunders College, Philadelphia, 1976).
(Cited on page 66.)

[90] F. Lecocq, Theses, Université de Grenoble (2011), URL https://tel.archives-ouvertes.fr/tel-00601382.
(Cited on page 95.)

[91] J. Puertas, Theses, Université Grenoble Alpes (2018), URL https://tel.archives-ouvertes.fr/tel-01839210.
(Cited on pages 95, 97, and 119.)

[92] G. J. Dolan, Applied Physics Letters **31**, 337 (1977), URL https://doi.org/10.1063/1.89690.
(Cited on page 95.)

[93] J. P. Martínez, S. Léger, N. Gheeraert, R. Dassonneville, L. Planat, F. Foroughi, Y. Krupko, O. Buisson, C. Naud, W. Hasch-Guichard, et al., npj Quantum Information **5**, 19 (2019), URL https://doi.org/10.1038/s41534-018-0104-0.
(Cited on pages 97 and 139.)

[94] S. Léger, J. Puertas-Martínez, K. Bharadwaj, R. Dassonneville, J. Delaforce, F. Foroughi, V. Milchakov, L. Planat, O. Buisson, C. Naud, et al., Nature communications **10**, 1 (2019), URL https://doi.org/10.1038/s41467-019-13199-x.
(Cited on pages 97 and 139.)

[95] V. Ambegaokar and A. Baratoff, Phys. Rev. Lett. **10**, 486 (1963), URL https://link.aps.org/doi/10.1103/PhysRevLett.10.486.
(Cited on page 100.)

[96] C. Deng, M. Otto, and A. Lupascu, Applied Physics Letters **104**, 043506 (2014), URL https://doi.org/10.1063/1.4863686.
(Cited on pages 105 and 135.)

[97] E. Dumur, Ph.D. thesis, University Grenoble Alpes (2015), URL https://www.theses.fr/2015GREAY003.
(Cited on pages 107, 134, 135, and 159.)

[98] E. Al-Tavil, Master's thesis, Université Grenoble Alpes (2019), master thesis supervised by Nicolas Roch, Nanophysique Grenoble 2019.
(Cited on pages 109, 133, and 137.)

[99] A. D. O'Connell, M. Ansmann, R. C. Bialczak, M. Hofheinz, N. Katz, E. Lucero, C. McKenney, M. Neeley, H. Wang, E. M. Weig, et al., Applied Physics Letters **92**, 112903 (2008), URL https://doi.org/10.1063/1.2898887.
(Cited on pages 109, 110, and 189.)

[100] M. V. Schneider, The Bell System Technical Journal **48**, 1421 (1969), ISSN 0005-8580, URL https://ieeexplore.ieee.org/document/6772165.
(Cited on pages 113 and 142.)

[101] H. A. Wheeler, Proceedings of the IRE **30**, 412 (1942), ISSN 0096-8390, URL https://doi.org/10.1109/JRPROC.1942.232015.
(Cited on pages 113 and 142.)

[102] R. Dassonneville, T. Ramos, V. Milchakov, L. Planat, E. Dumur, F. Foroughi, J. Puertas, S. Leger, K. Bharadwaj, J. Delaforce, et al., Phys. Rev. X **10**, 011045 (2020), URL https://link.aps.org/doi/10.1103/PhysRevX.

10.011045.
(Cited on pages 118, 160, 162, and 165.)

[103] F. Pobell, *Matter and methods at low temperatures*, vol. 2 (Springer, 2007).
(Cited on page 119.)

[104] R. Dassonneville, Theses, Université Grenoble Alpes (2019), URL https://tel.archives-ouvertes.fr/tel-02274266.
(Cited on pages 119, 160, and 162.)

[105] G. Catelani, J. Koch, L. Frunzio, R. J. Schoelkopf, M. H. Devoret, and L. I. Glazman, Phys. Rev. Lett. **106**, 077002 (2011), URL https://link.aps.org/doi/10.1103/PhysRevLett.106.077002.
(Cited on page 121.)

[106] K. Serniak, M. Hays, G. de Lange, S. Diamond, S. Shankar, L. D. Burkhart, L. Frunzio, M. Houzet, and M. H. Devoret, Phys. Rev. Lett. **121**, 157701 (2018), URL https://link.aps.org/doi/10.1103/PhysRevLett.121.157701.
(Cited on page 121.)

[107] L. Spietz, K. W. Lehnert, I. Siddiqi, and R. J. Schoelkopf, Science **300**, 1929 (2003), ISSN 0036-8075, URL https://science.sciencemag.org/content/300/5627/1929.
(Cited on page 125.)

[108] N. Masluk, I. Pop, A. Kamal, Z. Minev, and M. Devoret, Physical Review Letters **109**, 137002 (2012), URL https://link.aps.org/doi/10.1103/PhysRevLett.109.137002.
(Cited on page 132.)

[109] V. V. Sivak, S. Shankar, G. Liu, J. Aumentado, and M. H. Devoret, Phys. Rev. Applied **13**, 024014 (2020), URL https://link.aps.org/doi/10.1103/PhysRevApplied.13.024014.
(Cited on page 132.)

[110] W. A. Phillips, Reports on Progress in Physics **50**, 1657 (1987), URL https://iopscience.iop.org/article/10.1088/0034-4885/50/12/003.
(Cited on page 135.)

[111] A. Megrant, C. Neill, R. Barends, B. Chiaro, Y. Chen, L. Feigl, J. Kelly, E. Lucero, M. Mariantoni, P. J. J. O'Malley, et al., Applied Physics Letters **100**, 113510 (2012), URL https://doi.org/10.1063/1.3693409.
(Cited on page 135.)

[112] C. Müller, J. H. Cole, and J. Lisenfeld, Reports on Progress in Physics **82**, 124501 (2019), URL https://iopscience.iop.org/article/10.1088/1361-6633/ab3a7e.
(Cited on page 135.)

[113] J. Kreikebaum, K. O'Brien, and I. Siddiqi, arXiv preprint (2019), URL https://arxiv.org/abs/1909.09165.
(Cited on page 139.)

[114] S. K. Tolpygo, V. Bolkhovsky, T. J. Weir, L. M. Johnson, M. A. Gouker, and W. D. Oliver, IEEE Transactions on Applied Superconductivity **25**, 1 (2015), ISSN 1051-8223, URL https://doi.org/10.1109/TASC.2014.2374836.
(Cited on page 144.)

[115] C. Hutter, E. A. Tholén, K. Stannigel, J. Lidmar, and D. B. Haviland, Phys. Rev. B **83**, 014511 (2011), URL https://link.aps.org/doi/10.1103/PhysRevB.83.014511.
(Cited on page 144.)

[116] H. J. McGuinness, M. G. Raymer, C. J. McKinstrie, and S. Radic, Physical Review Letters **105**, 093604 (2010), URL https://link.aps.org/doi/10.1103/PhysRevLett.105.093604.
(Cited on page 144.)

[117] S. Jebari, F. Blanchet, A. Grimm, D. Hazra, R. Albert, P. Joyez, D. Vion, D. Estève, F. Portier, and M. Hofheinz, Nature Electronics **1**, 223 (2018), URL https://doi.org/10.1038/s41928-018-0055-7.
(Cited on page 156.)

[118] N. Roch, M. E. Schwartz, F. Motzoi, C. Macklin, R. Vijay, A. W. Eddins, A. N. Korotkov, K. B. Whaley, M. Sarovar, and I. Siddiqi, Phys. Rev. Lett. **112**, 170501 (2014), URL https://link.aps.org/doi/10.1103/PhysRevLett.112.170501.
(Cited on page 161.)

[119] J. Gambetta, A. Blais, M. Boissonneault, A. A. Houck, D. I. Schuster, and S. M. Girvin, Phys. Rev. A **77**, 012112 (2008), URL https://link.aps.org/doi/10.1103/PhysRevA.77.012112.
(Cited on page 161.)

[120] A. Kamal, A. Marblestone, and M. Devoret, Phys. Rev. B **79**, 184301 (2009), URL https://link.aps.org/doi/10.1103/PhysRevB.79.184301.
(Cited on page 161.)

[121] T. Walter, P. Kurpiers, S. Gasparinetti, P. Magnard, A. Potočnik, Y. Salathé, M. Pechal, M. Mondal, M. Oppliger, C. Eichler, et al., Phys. Rev. Applied **7**, 054020 (2017), URL https://link.aps.org/doi/10.1103/PhysRevApplied.7.054020.
(Cited on page 163.)

[122] F. Lecocq, J. Claudon, O. Buisson, and P. Milman, Phys. Rev. Lett. **107**, 197002 (2011), URL https://link.aps.org/doi/10.1103/PhysRevLett.

107.197002.
(Cited on page 163.)

[123] N. Didier, J. Bourassa, and A. Blais, Phys. Rev. Lett. **115**, 203601 (2015), URL https://link.aps.org/doi/10.1103/PhysRevLett.115.203601.
(Cited on page 163.)

[124] N. B. D. phil., The London, Edinburgh, and Dublin Philosophical Magazine and Journal of Science **26**, 1 (1913), URL https://doi.org/10.1080/14786441308634955.
(Cited on page 163.)

[125] R. Vijay, D. H. Slichter, and I. Siddiqi, Physical Review Letters **106**, 110502 (2011), URL https://doi.org/10.1103/PhysRevLett.106.110502.
(Cited on page 164.)

[126] Z. Minev, S. Mundhada, S. Shankar, P. Reinhold, R. Gutiérrez-Jáuregui, R. Schoelkopf, M. Mirrahimi, H. Carmichael, and M. Devoret, Nature p. 1 (2019), URL https://doi.org/10.1038/s41586-019-1287-z.
(Cited on page 164.)

[127] A. Savitzky and M. J. E. Golay, Analytical Chemistry **36**, 1627 (1964), URL https://doi.org/10.1021/ac60214a047.
(Cited on page 175.)

[128] A. Palacios-Laloy, Ph.D. thesis, Université Pierre et Marie Curie - Paris VI (2010), URL https://tel.archives-ouvertes.fr/tel-00815078.
(Cited on page 179.)

[129] C. S. Macklin, Ph.D. thesis, University of California, Berkeley (2015), URL https://escholarship.org/uc/item/41d554wg.
(Cited on page 182.)

[130] N. Zobrist, B. H. Eom, P. Day, B. A. Mazin, S. R. Meeker, B. Bumble, H. G. LeDuc, G. Coiffard, P. Szypryt, N. Fruitwala, et al., Applied Physics Letters **115**, 042601 (2019), URL https://doi.org/10.1063/1.5098469.
(Cited on page 185.)

[131] M. Urdampilleta, D. J. Niegemann, E. Chanrion, B. Jadot, C. Spence, P.-A. Mortemousque, L. Hutin, B. Bertrand, S. Barraud, R. Maurand, et al., Nature nanotechnology **14**, 737 (2018), URL https://doi.org/10.1038/s41565-019-0443-9.
(Cited on page 190.)

[132] S. Schaal, I. Ahmed, J. A. Haigh, L. Hutin, B. Bertrand, S. Barraud, M. Vinet, C.-M. Lee, N. Stelmashenko, J. W. A. Robinson, et al., Phys. Rev. Lett. **124**, 067701 (2020), URL https://link.aps.org/doi/10.1103/PhysRevLett.124.067701.
(Cited on page 190.)

[133] A. L. Grimsmo and A. Blais, npj Quantum Information **3**, 20 (2017), URL https://doi.org/10.1038/s41534-017-0020-8.
(Cited on page 191.)